School of Physics and Astronomy
The Raymond and Beverly Sackler
Faculty of Exact Sciences
Tel Aviv University

בית הספר לפיזיקה ולאסטרונומיה
הפקולטה למדעים מדויקים
ע״ש ריימונד ובברלי סאקלר
אוניברסיטת תל אביב

Research Thesis for a Degree "Doctor of Philosophy"

COHERENT CONTROL OF ULTRAFAST NONLINEAR INTERACTION IN METAMATERIALS

Submitted to the Senate of Tel Aviv University by

Eyal Bahar

The work was carried out under the supervision of

Prof. Haim Suchowski

July 2022

Abstract

The last decades have witnessed remarkable progress in our ability to control and shape light-matter interaction. The use of ultrafast lasers with artificial optical materials has been a major contributor to the development of the field. Such artificial optical materials are designed to manipulate and enhance the interaction. Control over the amplitude and phase of electromagnetic oscillations in nano-optical interaction has been widely demonstrated, obtained by the design of the nanoparticle's geometrical configuration, materials and environment. These nanoparticles can be structured into arrays, named metasurfaces, enhancing the cross section of the interaction. Such artificially made materials offer optical surfaces with a custom designed frequency response and spatial configuration. Hence, these metasurfaces enable the possibility of miniaturizing traditional optical elements as well as realizing new functionalities. The great degree of freedom in their design, down to the individual nanostructure, provides a vast playground to explore novel physical phenomena in nanoscale optical interaction. In recent years, the prospect of actively controlling metamaterials' optical response, enabling on-demand manipulation of the light-matter interaction, has gained much attention. Such capabilities would enable a new dimension of controllability and intriguing physical phenomena. However, most metasurfaces used today, including in research, are designed in such a way that their optical properties are set in stone during their fabrication. In this dissertation, we theoretically and experimentally explore fundamental aspects of control over nonlinear optical interaction, in systems that combine ultrafast pulses and nano-optical materials, such as nanostructures and waveguides. Specifically, we focus on the manipulation of the coherent dynamics via spatial or temporal modulation and research novel methods for control over the ultrafast nonlinear optical response in plasmonic nanostructures and silicon photonic waveguides.

Coherent control is a quantum mechanics-based method for controlling dynamical processes in matter by electromagnetic radiation. Coherent control methods are often used to solve the problem of efficiently steering a quantum system from an initial state to a final state. In atomic and molecular systems, coherent control has found vast applications in enhancing nonlinear phenomena by control over the quantum interference existing in the multiple eigenstate interaction. For multiphoton excitation, a main tactic to steer a system to a desired optimal state is obtained by tailoring the phase of an incident ultrashort laser pulse. The phase of the pulse affects the interaction by modifying the interference between the multiple path-ways of the interaction. Hence, the phase can be tailored to induce destructive interference between pathways leading to an unwanted final states or to induce constructive interference for desired states. The approach and schemes of coherent control have also been demonstrated for mathematically analogous systems such as nonlinear frequency conversion. In such systems, the geometrical configuration

of a waveguide can be designed to modify the phase of the propagating light through the waveguide, manipulating the interaction outcome dictated by phase-matching interference.

This dissertation is comprised as follows: we start by a comprehensive introduction in Chapter 1 that serves as the background for the key ideas integrated in this dissertation. The introduction presents the subjects of nonlinear optics, four-wave-mixing (section 1.1), metasurfaces (section 1.2), quantum coherent control in plasmonics (section 1.3) and the various experimental, numerical and fabrication methods used in our research (section 1.4). In Chapter 2, which is the body of this article-based thesis, we present three peer-reviewed publications, each focused on different aspects of integrating a coherent control approach in ultrafast nano optics. In Chapter 3, we provide an outlook and propose future research directions continuing the findings presented in this dissertation.

In the **First** article, we share our achievements in nonlinear frequency conversion, where we study the optical frequency conversion of broadband ultrafast pulses in modulated optical waveguides and find a highly applicable coherent control method for efficient broadband conversion. In the article, we present the concept adiabatic four-wave-mixing frequency conversion in $\chi^{(3)}$ materials, a coherent control approach for nonlinear frequency conversion in spatially designed centrosymmetric waveguides. In a joint collaboration with the Moses's group from Cornell University, we developed an approach that offers a route to side step the conventional efficiency-bandwidth trade-off usually found in frequency conversion schemes in $\chi^{(3)}$ materials. Furthermore, we suggest a generalized scheme, supported by numerical calculations and simulations, suitable for implementation in Silicon-photonic devices as well as in optical fibers. In the **second** article, we present our experiments on coherent control of second harmonic generation in the nanostructures, obtained by pulse shaping pulses on the 100 fs regime. In the plasmonic case, it is considered a narrowband regime since the spectral pulse width is narrow relative to the plasmonic line-width. We demonstrate control by implementing a V-shaped spectral phase and show that the quadratic nonlinear power-law response, commonly expected by second-harmonic-generation, has a complex structure strongly influenced by order of arrival of the pulse frequencies. **Finally**, in the third article, we focus on a main challenge in coherent control of metallic nanostructures -   manifested by their ultrafast sub 20 fs dephasing times. Such short dephasing in plasmonic system time has limited the capability to coherently control the ultrafast dynamics, prior to our work. Demonstration of corner-stone coherent control schemes, such as enhancement of nonlinear excitation via pathways interference, has so far remained elusive. By pulse shaping broadband sub 10 fs pulses, within the plasmonic lifetime, we demonstrate coherent control in plasmonic nanostructures and show that the optimal nonlinear plasmonic excitation is not obtained by maximally compressed pulses. The optimal pulse is obtained when the pulse is stretched according to bandwidth characteristics of the plasmonic resonance and pulse. Alongside

our experimental demonstrations, we provide a theory predicting the enhancement to the second harmonic emission and predicts the optimal pulse shape that outperforms the transform limited pulse, based on the pulse and plasmonic characteristics.

The findings and developments of this dissertation enables new and exciting research and applications opportunities in ultrafast optics and nanophotonics.

Table of contents

List of publications, conferences and awards

Scholar.google/Eyal-Bahar

Linkedin/eyal-bahar

Peer-Reviewed Publications

- Levanon, A., Dahan, A., Nagler, A., Lifshitz, E., Bahar, E., Mrejen, M. and Suchowski, H., 2017. Pulse shaping of broadband adiabatic SHG from a Ti-sapphire oscillator. Optics Letters, 42(15), pp.2992-2995.

- Bahar, E., Ding, X., Dahan, A., Suchowski, H. and Moses, J., 2018. Adiabatic four-wave mixing frequency conversion. Optics Express, 26(20), pp.25582-25601.

- Bahar, E., Arieli, U., Mrejen, M. and Suchowski, H., 2020. Coherent control of the noninstantaneous nonlinear power-law response in resonant nanostructures. Physical Review B, 101(3), p.035141.

- Suchowski, H., Dahan, A., Bahar, E., Moses, J. and Ding, X., Ramot at Tel Aviv University Ltd and Cornell University, 2021. Generation of broadband coherent laser pulses based on adiabatic four-wave mixing in waveguides and fiber. U.S. Patent Application 17/055,554.

- Bahar, E., Arieli, U., Stern, M.V. and Suchowski, H., 2022. Unlocking coherent control of ultrafast plasmonic interaction. Laser & Photonics Reviews, 16(7), p.2100467.

- Korman, S., Bahar, E., Arieli, U. and Suchowski, H., 2022. Spatio-temporal ultrafast pulse shaping at the femtosecond–nanometer scale. Optics Letters, 47(17), pp.4279-4282.

Conference Presentations

- Cleo 2021, Peer reviewed speaker, Online, 2021.
- GRS Quantum Control of Light and Matter, Invited talk, USA. 2019
- Cleo Europe 2019, Peer reviewed speaker, Munich, Germany. 2019
- Cleo USA 2019, Accepted speaker, San Jose, California, USA. 2019
- GRC Quantum Control of Light and Matter, Poster presentation, USA. 2019
- Oasis 7, Poster presentation, Tel Aviv, Israel. 2019
- Nanometa 2019, Poster presentation, Seefeld, Austria. 2019
- Nano-IL, Poster presentation, Jerusalem, Israel. 2018
- Ultrafast Phenomena, Poster presentation, Hamburg, Germany. 2018
- GRC Quantum Control of Light and Matter, Poster presentation, USA. 2017

Awards

- **Unique Excellence Award** - Tel-Aviv University Center for Nanoscience and Nanotechnology 2021
- **Excellence in Research** Award - Tel-Aviv University, Physics department 2022
- **Excellence in Research** Award - Tel-Aviv University, Physics department 2021
- **Excellence in Research** Award **-** The Levi Yeshayahu Scholarship, TAU, 2019
- **Excellence in Teaching** Award - Tel-Aviv University, Physics department 2021
- **Excellence in Teaching** Award - The Cohen Ann and Moris Scholarship, TAU 2019
- **Excellence in Teaching** Award - Waidman Paul Scholarship, 2018

1 **Introduction**

In 1875, Prof. John Kerr (Glasgow, UK) demonstrated that by application of strong DC fields, the refractive index of a number of solids and liquids can be slightly modified (*1*). This phenomenon, now known as the (DC) Kerr effect, was the first nonlinear optical effect to be observed, leading eventually to the rich plethora of science and applications corner-stoned by nonlinear optics, ranging from nuclear physics and quantum computing to chip design and vision-correcting surgery.

In a different area of research, in 1967, Manykin and Afanas'ev (*2*) were probably the first to suggest that modifying the optical phase of a pulse can be used to control physical processes and interaction in materials. Such schemes have been extensively studied and developed by phase modulation techniques for control over coherent interaction. Since then, quantum coherent control has been widely demonstrated for atomic, molecular and even larger systems (*3–7*) leading to groundbreaking capabilities in atomic and molecular research as well as remarkable sensing devices such as nuclear magnetic resonance (used for MRI). In my PhD research, I pushed to combine nonlinear optical phenomena with coherent control by pulse shaping ultrafast broadband pulses to study electronic and photonic dynamics in nanophotonic materials, metamaterials and 2D materials.

Following the great success of coherent control experiments in the atomic and molecular regime, many researchers apply these methods in more complex systems. Examples can be found in the manipulation of photocurrents in bulk semiconductors (*8*), nonlinear optical enhancement (*9*), superconducting Van der Waals control (*10*), quantum information processing (*11*) and more. The concepts of coherent control have been applied also to other systems, such as integrated photonics (*12–15*) and nonlinear optics (*5*, *16–18*). Adiabatic frequency conversion (*19*), an example for other systems where the concepts of coherent control have been successfully applied, is a robust method for broadband optical frequency conversion. Adiabatic frequency conversion has demonstrated robust broadband optical frequency conversion, implementing an analogy of rapid-adiabatic passage by modulating the *material's* contribution to the optical interaction, where the phase of the interaction is modified by modulating the geometrical path in which the optical fields propagates through (*19*).

During my PhD research, I contributed uniquely to these research topics by utilizing our state-of-the-art resources to the coherent control realm. Across several projects, I utilize our sub-10 femtosecond (fs) pulses or 100 fs near-IR optical parametric oscillator to study nonlinear optical interaction. To research nonlinear interaction in nanoscale regimes and ultrafast speeds, I designed and fabricated custom nanostructured metasurfaces and applied cutting-edge optical techniques. Such efforts enable us to deepen our research capabilities of coherent control and nonlinear phenomena in complex nano-systems. While we used plasmonic nanostructures as a use-case (*20*, *21*), the constructed apparatus can be used in general for a variety of materials and configurations. In addition, I applied novel theoretical approaches. Supported by numerical calculations and simulating, modeling plasmonic interaction (*20*, *21*), adiabatic frequency conversion (*22*) and complimentary simulations for control. In my first project, which was carried out in collaboration with Dr. Xiaoyue Ding from the group of Prof. Jeffery Moses, Cornell, we expanded the theory of adiabatic frequency conversion for centrosymmetric $\chi^{(3)}$ materials (such as Silicon photonics and optical fibers). In my next projects, I applied a novel approach to nonlinear plasmonic excitation and experimentally researched the coherent mechanism of plasmonic excitations via second harmonic generation, expanding corner-stone schemes of coherent control from atomic systems to nanostructured resonant interaction. In this thesis, I first provide a short introduction overviewing key-topics in my research. Next, I present three published Peer-review articles - focused on studying coherent control of nonlinear optical phenomena in artificially designed materials. Each of the articles is self-contained in its scientific introduction, content and objective list – but all constructively provide insight on applying coherent control and nonlinear optics in the artificially designed materials. Finally, I discuss future research directions and outlook.

1.1 **Nonlinear optics**

Nonlinear optics regards the interaction between electromagnetic waves through a mediator media. It is a well-established field of research, owing to the first observation of Bloembergen's work in 1960 (*23*), and is already implemented in dozens of applications, e.g. laser sources and detectors (*24–26*), optical communication and computation (*27*), spectroscopy (*28*), microscopy (*29*) and more (*30, 31*).

The results of nonlinear interaction may lead to the generation of waves at new frequencies, by a "wave-mixing" process (*30*), amplification of the electromagnetic field, or by changing of the physical properties of the material itself. Conventional nonlinear optics is based on nonlinear processes that occur in bulk materials, where the induced polarization of the material is nonlinear with the electric field of light, such as in second harmonic generation (SHG) where the materials polarizability is quadratic with the incoming field $P_{material}(t) \sim E(t)_{EM}^2$. Since the polarization takes part in the electromagnetic wave equation as the source term, the wave equation becomes nonlinear and as a result, new phenomena emerge. Comprehensive and rigorous treatment of standard nonlinear optics can be found in "Nonlinear optics" by Boyd (*30*).

In recent years the research field of nonlinear optics in nanostructures and metamaterials is flourishing (*32–37*). The interest in this field was greatly motivated by the high degree of tunability offered by metamaterials along with the capability to concentrate electromagnetic energy within small volumes. This makes easy to obtain and spatially control extremely high field intensities, that are essential to efficient nonlinear interaction. Combined with the advances in ultrafast physics in the past two decades, scientists now understand that nonlinear optical dynamics is much richer with ultrafast time dependencies, phase-related geometrical factors, electron cloud formations and hot electron dynamics – all affected by the dynamics of the initial photo-excited carriers. In this sections, I will go over key ideas of nonlinear optics applied and studied in my Thesis. I will start by describing the general three-wave mixing theory focusing on SHG. Then I will introduce ultrafast nonlinear optics, emphasizing the materials response function and its coherent contribution to the nonlinear process in instantanoues and non-instantaneous interaction. Last, I will shorty discuss four-wave-mixing in the context of the theory and background emphasizing its importance and limitations in nonlinear frequency conversion and the concept of adiabatic four-wave mixing.

1.1.1 Three-wave mixing and second harmonic generation

In this section, I will briefly go over the text-book description of nonlinear optics by three-wave mixing as can be found, for example, in Ref (*30*). I also introduce the response function of the media participating in the nonlinear second order process. First, I will introduce the response function for in the instantaneous response approximation, suitable to describe far-from resonance interaction. Next, I introduce the non-instantaneous approach for a resonant interaction.

Three wave mixing, which includes the process of SHG, is usually introduced by the second order term of the nonlinear polarization of a material, described by a power-series expansion. An example for this treatment can be illustrated by the following power series where P is the material's polarization and E is the electric field inducing this polarization:

$$P(E) = \chi^{(1)}E + \underbrace{\chi^{(2)}E^2 + \chi^{(3)}E^3 + \cdots}_{P_{NL}} \qquad (1)$$

By introducing these nonlinear terms to Maxwell's wave equations and focusing on the second order interaction contributions for an incoming two wave interaction source with ω_1 and ω_2, the most known processes of three wave mixing are manifested. These include an expression, which constitutes as a source term of the electromagnetic wave equation to new fields at frequencies $(2\omega_1, 2\omega_2, \omega_1 \pm \omega_2, 0)$. The different quadratic processes emerging are classified by their resulting frequencies: SHG: $(\omega, \omega \to 2\omega)$, sum and difference frequency generation: $(\omega_1, \omega_2 \to \omega_1 \pm \omega_2)$, optical rectification: $(\omega, -\omega \to 0)$, Pockels effect $(\omega, 0 \to \omega)$ and spontaneous parametric down conversion $(\omega_1 + \omega_2 \to \omega_1, \omega_2)$ (*30*). For clarity, since we deal with fs sources that are inherently broad, the term SHG is used in this thesis to describe both SHG and sum frequency generation combined. Additionally, we note that surface SHG is possible even for materials which do not exhibit SHG in the bulk (*38*).

1.1.2 Instantaneous vs non-instantaneous SHG

The nonlinear polarizability, induced by a pulse of an electromagnetic field interacting with a material, might certainly be dependent on the accumulation of past events and evolution of the interaction. Due to the Fourier relations and since the response of all natural materials to light is dispersive, the temporal response of a material is dictated to

be non-instantaneous, meaning that it is dependent on the accumulation of past events in the interaction. The expression describing the polarizability under the assumptions of a perturbative approach, phase-matched free interaction and causality, may be described as (*30*)[1]:

$$P_{NL}(t) \propto \int_{-\infty}^{t} \chi^{(2)}(t-\tau)E^2(\tau)d\tau \qquad (2)$$

In the second and third articles that comprise the main body of this thesis, the second order response function and its non-instantaneous ultrafast structure are put to focus theoretically and experimentally, researching the ultrafast coherent electronic dynamics and the ultrashort excitation evolution.

1.1.2.1 **Instantaneous interaction**

A general nonlinear interaction can be instantaneous or non-instantaneous. Since all natural materials are dispersive to light and due to the frequency-time Fourier relation, an instantaneous nonlinear interaction is an approximation assuming that the dispersion is small for the bandwidth of light taking part in the interaction. To put this into context, instantaneous interaction is best suitable to describe a pulse that experiences a response from the material that does not evolve over time. In contrast, a non-instantaneous interaction describes a response that evolves with a lasting effect that decays slower or on the same time scale as the pulse duration.

Until recent years, the approximation of SHG as an instantaneous process has been widely applied for many systems and has shown great accuracy in describing SHG in bulk, inorganic materials and some semiconductor systems, far from their resonances. However, it is not suitable for describing the nonlinear interaction in many other physical systems like organic materials, metallic nanostructures or other nanophotonic structures.

In the case of a weak dependency of the nonlinear polarization on frequency components, this SHG process translates to the frequency domain as follows[2]:

$$E_{SHG}(\omega) \propto \tilde{\chi}^{(2)} \int E(\Omega)E(\omega-\Omega)d\Omega \qquad (3)$$

---

[1] This expression is a direct result of comining the equation 1.1.2 from Ref [30], with the approach that includes causaility, as described in equation 1.6.1 in Ref [30].
[2] The Fourier transform of Eq 1.1.2 in Ref [30].

In the case of Gaussian spectral pulse, the analysis of this simple convolution integral results in a shift and contraction of the Gaussian spectrum such that the new Gaussian is centered at double the frequency and with double the variance. This mathematical operation reflects that the medium only serves as a passive mediator for the interaction. A material that is approximated to have a constant susceptibility only determines the amplitude for the nonlinear interaction, meaning, the medium has *no differential effect* on the interaction process itself. Moreover, it does not take into consideration the effect of the pulse on the material itself. This is mathematically evident in the treatment of the $\chi^{(2)}$ term which has been assumed to be weakly dependent on frequency. By Fourier analysis this treatment translates to a $\chi^{(2)}(t - \tau)$ that is non vanishing only for $t = \tau$, meaning that the response of the materials is instantaneous.

1.1.2.2 **Non-Instantaneous interaction**

The weak dependency on frequency assumption is inaccurate when describing the interaction near a resonant frequency of a material. To have an example in mind for a frequency-dependency system, the Lorentizan-shaped resonance, corresponding to a resonant harmonic oscillator, can be considered. In this case, the response function in the frequency domain is $\chi^{(1)}(\omega) = \frac{1}{2\pi} \frac{\Gamma}{(\omega-\omega_r)^2 + \frac{1}{2}\Gamma}$, where ω_r is the resonant frequency and Γ is the linewidth. This expression translates in the time domain to a response functions with an exponentially decaying oscillation $\chi^{(1)}(t) = e^{-\Gamma\pi|t|} \cdot e^{-2\pi i \omega_r t}$. Note, that the response function for second order processes, $\chi^{(2)}$ is not generally dictated to correspond to the first order linear response $\chi^{(1)}$. However, For conventional nonlinear crystals, it has been shown empirically that the second order response can be accurately predicted by the first order response, by what is known as "Miller's Rule" (*39*). By Miller's rule, second order response is described to be $\chi^{(2)}(\omega) \sim \chi^{(1)}\left(\frac{\omega}{2}\right)\chi^{(1)}\left(\frac{\omega}{2}\right)\chi^{(1)}(\omega)$. This relation can also be fully derived theoretically by assuming a nonlinear oscillator model (*30*). Historically, the empirical findings of Miller strongly contributed to the development and acceptance of the nonlinear oscillator model as an acceptable description for instantaneous optical interaction in crystals.

In the case of a non-instantaneous interaction, for any general second order response function, $\chi^{(2)}$, the interaction can further analyzed in the time domain to be as follows (See equation 1.6.7 in Ref(30)):

$$E_{SHG}(t) \propto \int_0^\infty \int_0^\infty \chi^{(2)}(\tau_1, \tau_2)E(t-\tau_1)E(t-\tau_2)d\tau_1 d\tau_2 \qquad (4)$$

Reflecting the requirement of causality that $\chi^{(2)}(\tau_1, \tau_2)$ vanishes for either negative τ_i. For the *frequency picture* process, it can be shown that this translates to:

$$E_{SHG}(\omega) \propto \int_{-\infty}^\infty \chi^{(2)}(\omega, \Omega_1, \omega - \Omega_1)E(\Omega_1)E(\omega - \Omega_1)d\Omega_1 \qquad (5)$$

Here, in the case where $\chi^{(2)}(\omega, \Omega_1, \omega - \Omega_1)$ is not simply approximated to be constant, the generation of ω depends not only on the fields but also on the frequency dependent response of the material $\chi^{(2)}$. Since this weighted convulsion is complex to comprehend, $\chi^{(2)}$ is commonly approximated as weakly depending of frequency and therefore assumed as constant. This directly corresponds to an instantaneous response, as such assumption naturally translates back to the time domain assumption that $\chi^{(2)}(-\tau_1, -\tau_2)$ is constant. If not assuming a weakly dependent $\chi^{(2)}(\omega, \Omega_1, \omega - \Omega_1)$, the material indeed has a non-instantaneous response function which depends on past events, where each frequency contributes differently, according to the response function.

1.1.3   Broadband frequency conversion limitations

In my PhD research, my first research project was focused on broadband frequency conversion of ultrafast pulses in FWM by coherent control methods. We studied coherent control of FWM by spatial modulation in nanometer systems, and introduced the concept of adiabatic frequency conversion in FWM, which we find broadly applicable to $\chi^{(3)}$ nonlinear platforms. We tackled a common problem in the paradigm of frequency conversion schemes and suggested a route to overcome the usual efficiency-bandwidth trade-off commonly restricting broadband FWM frequency conversion. This will be covered in Section 2, in the first published article comprising this dissertation. In the next

section, we describe the progress made and the limitations in *three-wave-mixing* adiabatic frequency conversion, a central motivation for developing the FWM theory.

Efficient and robust frequency conversion of broadband optical pulses is essential for fields ranging from pure science to technology industries, including integrated photonics for telecommunications and the next generation of computers (*40, 41*), environmental detection devices (*42*), optical signal processing for applications such as encoding and encryption (*43*), as well as strong field applications such as X-ray generation and multidimensional spectroscopies for understanding the fundamental ultrafast dynamics of molecules (*44, 45*). In recent years, much effort has been invested in developing schemes to efficiently convert broader and broader optical spectra. Yet the common paradigm of nonlinear frequency conversion with constant phase matching includes a restrictive trade-off between the conversion efficiency and its bandwidth. Recent demonstrations of the adiabatic frequency conversion concept in three-wave mixing processes introduced the ability to sidestep the efficiency-bandwidth trade-off in sum-frequency generation (SFG) and difference-frequency generation (DFG) (*18, 19, 46, 47*), dramatically increasing the available bandwidth while also ensuring a high conversion efficiency. Application of this concept in a periodically poled quasi-phase-matched media allowed the generation of phase and amplitude-controlled, octave-spanning, coherent mid-IR light sources (*48, 49*). Moreover, the amplitude and phase transferability of adiabatic frequency conversion enables arbitrary amplitude and phase tunability by pulse shaping prior to conversion. This allowed the arbitrary shaping of single-cycle pulses and promises great flexibility for ultrafast spectroscopic applications (*49*).

1.1.4 **Efficient and broadband frequency conversion by Four-wave-mixing**

Similar to three-wave mixing, if we consider the impinging electric field to be consisted of the frequencies ω_1, ω_2 and ω_3, we find that the third-order susceptibility $\chi^{(3)}$ will give rise to new frequencies, which suits all the combinations of three photons at the input frequencies (See Figure 1). All these processes are not bound to the symmetry constraint that exists in second-order nonlinearity, thus their versatility stimulates their potential to be incorporated in various optical schemes. The third-order nonlinearity of

materials is responsible for various interesting and important phenomena such as four-wave-mixing (FWM), intensity dependent refractive index, self-focusing and self-phase modulation (*30*) in a range of materials including Silicon and Fiber optics (Silica), for example. Importantly, such phenomena are also existing in silicon photonic waveguides, which hold promising ground for nonlinear phenomena as their nanoscale configuration has great impact in modulating the nonlinear interaction by varying the intensity profile and phase accumulated during propagation.

Traditional platforms for frequency conversion using three-wave mixing processes are limited to devices based on specialized materials engineered and grown specifically for the application, whether for ultrashort pulses or for single-frequency sources. In contrast, the ubiquitous presence of cubic optical nonlinearities enables all devices employing light propagation the capacity for frequency conversion via FWM. Recent examples include optical parametric gain and frequency conversion in Silicon waveguides used for telecommunications (*40*, *50–52*), supercontinuum generation in optical fibers

Three-wave mixing (TWM) **Four-wave mixing (FWM)**

$$\omega_{SHG}^{(idler)} = \omega_A^{(pump)} + \omega_B^{(pump)}$$

$$\omega_{SHG} = 2\omega_{pump\,A} - \omega_{pump\,B}$$

Energy conservation

$\omega_B^{(pump)}$ $\omega_{TWM}^{(idler)}$ $\omega_A^{(pump)}$

$\omega_A^{(pump)}$ $\omega_B^{(pump)}$ $\omega_{FWM}^{(idler)}$ $\omega_A^{(pump)}$

Phase mismatching

k_{idler} k_A k_B

k_{idler} k_A k_A $-k_B$

$$\Delta k = k_{idler} - k_B - k_A$$

$$\Delta k = k_{idler} - k_B - 2k_A$$
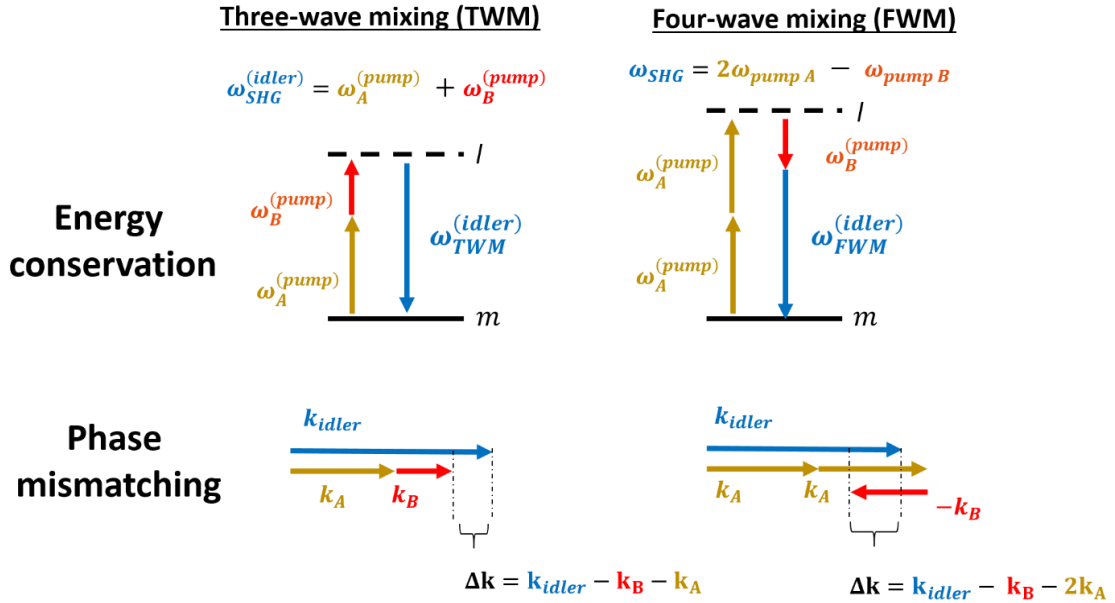
Figure 1. Nonlinear conversion by three or four wave mixing. The figure illustrates the similarity of three and four mixing in generating new frequencies by a particular three and four wave mixing processes that yield a frequency of ω_3, mixing ω_1 and ω_2. Four wave mixing, which is a third order nonlineairty, is not bound to the symmetry constraint that exists in second-order nonlinearity, making its attractive as it is highly applicable in various optical schemes and materials. In the illustration, the total produced frequency is the same, but the phase mismatch is different. The phase (momentum) is determined by the dispersion relation of the materials, $k = 2 \times n(\omega) \times \frac{\omega}{c}$. For detailed analysis on nonlinear optical processes see Ref. [30].

made from a wide range of materials and with a diverse set of structures (*53–55*), dielectric and semiconductor microresonators used for supercontinuum or frequency comb generation (*56–59*), and gas filled capillaries used for spectral broadening or parametric amplification of ultrashort pulses (*60*, *61*). In each of these technologies, FWM frequency conversion has been employed. Like all nonlinear frequency conversion methods, applications of FWM to the generation of broadband light sources are limited by a trade-off between efficiency and bandwidth. Furthermore, the commonly used technique for frequency conversion, cascaded FWM (*62–65*), does not allow flexible control of the spectral phase of the converted light.

1.1.4.1 **Adiabatic FWM**

In the past three decades, developing schemes to efficiently convert broader and broader optical spectra has gained much attention. Yet, the common paradigm of having a phase-matching condition that remains constant along the optical axis includes a restrictive tradeoff between the conversion efficiency and its bandwidth.

In recent years, a new direction in frequency conversion has emerged - *three-wave-mixing* adiabatic frequency conversion - a method that is based on adiabatic evolution of the nonlinear optics dynamics (*66*). Such method was demonstrated to overcome the tradeoff between conversion efficiency and bandwidth (*18*), offering the use of SU(2) dynamical symmetry including the analogous mechanism of Landau-Zener adiabatic transition (*19*, *67*). In the past few years, the fully nonlinear regime in *three-wave-mixing* received special attention (*19*, *49*, *68–75*). An extensive analysis on ultrafast adiabatic three-wave-mixing can be found in a thesis by Asaf Dahan Ref. (*76*) and related articles (*17*, *77*). The adiabatic conversion dramatically increases the available bandwidth in three-wave-mixing applications while also ensuring high conversion efficiency. Realization of this concept to three-wave mixing in a periodically poled quasi-phase-matched waveguides enabled the generation octave-spanning, ultrafast mid-IR light sources, allowing coherent amplitude and phase tunability by pulse shaping prior to conversion, providing great flexibility for spectroscopic applications (*74*).

While very promising, *three-wave mixing*, in practice, is limited to asymmetric crystals possessing quadratic nonlinearity, which means that any realization is based on specialized materials engineered and grown specifically for the application. In contrast, the omnipresence of cubic optical nonlinearities in all natural crystal-like materials

employing light propagation mean that all materials have a capacity for frequency conversion – by *FWM*. Examples of FWM frequency conversion application can found for research and telecommunications in optical amplifiers, Silicon and various semiconductor waveguides as well as for photonics applications including highly nonlinear and photonic crystal fibers (*56*, *64*, *78–81*). However, like all nonlinear frequency conversion, application of FWM to the generation of broadband light sources are limited in bandwidth, and are further limited by the natural trade-off between efficiency and bandwidth in nonlinear conversion.

Our theory for FWM, which we find broadly applicable to numerous nonlinear platforms, is explained extensively with supporting simulations in the first published article comprising this thesis. In the mentioned article, we show the conditions in which photon transfer in a FWM process can be understood by analogy to population transfer in a two-level quantum atom. Those are the conditions under which a fully adiabatic, one-to-one transfer of photons between frequencies becomes possible, corresponding to the probability of an electron to populate the ground or excited state in a two-level atom. In the right conditions, we show that FWM shares the same mathematical form as a two-level atomic system. Hence, rapid adiabatic passage (RAP), a method can be used to asymptotically achieve full population transfer (*82*), should also exist in FWM (where the population transfer is from the fundamental frequency to the target conversion frequency). In a nutshell, if the effective wave-vector mismatch is swept from large positive value to large negative value (or vice-versa) adiabatically, the signal wave (initial state) shall fully convert to the idler wave (target state) without back-conversion. This can be achieved by nano-scale modulations the waveguide or sweeping the doping period of a doped optical fiber. A more extensive description is presented in the first article of this thesis, along with a full simulation showing the theoretical implementations of this technique and the parameters needed to obtains its realizations (The simulation code can be found in Appendix A).

1.2 Optical metasurfaces and nanostructures

In the last two decades, there has been significant advancements in the ability to control light using optically thin structured materials, called metasurfaces. These 2D optical materials are commonly made of subwavelength nanostructures (NSs), which allow control over the properties of light interacting with them by controlling their size

and geometry (*83*). NSs and metasurfaces enable the manipulation of waves in the optical far field and can be used as optical elements for beam shaping, holography and more. In the near-field regime, such nanoscale characteristics enables geometrical control over the energy distribution, a highly beneficial attribute for various processes, such as nonlinear generation of new frequencies (*32*, *33*, *84–87*), surface-enhanced Raman scattering (*88–90*), enhancement of Purcell factors (*91–93*), and enhancement of the chirality formation of molecules (*94–96*).

NSs can be used to locally control the amplitude, phase and polarization of transmitted and reflected light with very high efficiency. Hence, metasurfaces offer previously unavailable properties, enabling miniaturizing traditional optical elements and realizing new functionalities. The nanostructured building blocks are fundamentally important as they have been shown to support intriguing physical phenomena such as hybrid light-matter states (*97*, *98*), electron wave function tunneling (*99*, *100*), single molecules interaction (*101*, *102*), negative refraction (*103*), to name a few. Thanks to the great flexibility in design that directly control their optical and physical properties, NSs provide a playground for exploration of complex optical observations along with fundamental physical phenomena, which appear in completely different physical systems. Specifically, analogies between the energy-dependent coherent pseudo-electronic states in condensed matter systems and the allowed real-electronic states in atomic and molecular systems are now being put to focus.

During my PhD research, we focused on metallic nanoparticles that support resonances associated pseudo-electronic oscillations, called localized plasmon resonances (LPRs). These resonances lead to enhancement and localization of the electromagnetic field in the vicinity of a metallic nanoparticle, along with enhanced absorption cross sections. Since metasurfaces are composed of nanoparticle arrays, the net optical response usually depends on the individual nanoparticle response, defined by its material and morphology, the geometry of the array and the surrounding media. We focused on the ultrafast nonlinear optical response when interacting LPR, and research how ultrafast modulation of the phase of the incoming pulse may modulated the excitation and nonlinear optical response during LPR excitation. In the next sections, we will give a short introduction to the concept of LPR, provide discuss the ultrafast regime and parallel process that emerge during LPR excitation (section 1.2.2), and discuss two main theoretical approaches in analyzing the non-instantaneous structure of the LPR in nonlinear optical interaction.

1.2.1 **Localized plasmonic resonance**

The optical response of a nanoparticle to an applied electromagnetic field is usually described in a steady state description. Although such description is naturally inappropriate when considering ultrafast interaction, understanding it provides great insight on the mechanism behind plasmonic excitation. In some cases, such descriptions can serve as a leading element in a description capturing the full response. An example for this can be found in the use of Miller's rule (*30*) , which by the measuring the steady state linear response predict the nonlinear dynamics as well (see section 1.1.2 for more information). In addition, it can produce key variables such as the resonant frequency and linewidth which can then be placed in a coupled mode equation predicting the full dynamics.

The traditional approach for defining the optical response consists the frequency-dependent polarizability $\alpha(\omega)$, which relates the inducing electric field $\boldsymbol{E}_{in}(\omega)$ to the induced polarization $\boldsymbol{P}(\omega)$ through the relation $\boldsymbol{P}(\omega) = \alpha(\omega)\boldsymbol{E}_{in}(\omega)$. The main mechanism determining $\alpha(\omega)$ is the collective electron oscillations in metallic nanoparticles, called localized surface plasmon (LSP). Surface plasmons are coherent modes of collective oscillations of the free electrons on a metal-dielectric interface (*104*). These localized electron oscillations, can give rise to enhanced electromagnetic near fields and absorption amplitudes, through a resonance known as the localized surface plasmonic resonance (LSPR). Illustrative analysis that captures important features of the LSPR is based on a driven harmonic oscillator model (*105*), which results in a Lorentzian solution for the polarizability:

$$\alpha(\omega) = \frac{A_0}{\omega_r^2 - \omega^2 + i\gamma\omega} \qquad (6)$$

Where A_0 is the amplitude, ω_r is the resonance frequency and γ is the damping constant. In the driven harmonic oscillator model, a restoring force is exerted by the positive ions in the metal, which attract the electrons displaced by the electric field. The phase of the collective electron motion relative to the phase of the electrical driving force determines the relative phase and amplitude of the scattered light. The above description depicts the mechanism of plasmonic resonances only qualitatively. To achieve a more complete description, numerical calculations using electromagnetic simulation tools can be used.

In NS characterization and as preparation for experiments, the fundamental properties of the plasmonic NS are usually obtained by far field measurements measuring extinction and scattering. The extinction and scattering cross sections can be calculated from the particle's polarizability, according to (*106*):

$$\sigma_{ext} = \sigma_{abs} + \sigma_{sca} \tag{7}$$

$$\sigma_{abs} = 4\pi k \cdot Imag\{\alpha\} \tag{8}$$

$$\sigma_{sca} = \frac{8\pi}{3} k^4 |\alpha|^2 \tag{9}$$

1.2.2 Photo-induced electronic dynamics in metallic NS's

Collective electronic dynamics in metallic structures restricted to a confined nanometer configuration give rise to new physical phenomena such as the localized surface plasmon resonance (*107*). This can be described, to first approximation, by the motion of the electrons, driven by an external light's electric field, periodically displaced with respect to the lattice ions. The result is an electron oscillator, whose resonance is called a localized surface plasmon and whose resonant frequency is determined by the type of the materials (restoring force, effective mass of the electron), and geometrical configuration (confinement).

The common depiction of light-matter interaction in metallic *NSs* is Illustrated in Figure 2. The first consist of the collective oscillation of surface electrons participating in the resonant surface plasmon excitation (*108–110*). After excitation, energy is transferred to the metal electrons through inter and intraband transitions, creating a highly non-thermal distribution of electrons (*110–112*). The electron population then decays through electron–electron interactions, creating a hot electron distribution within a few hundred fs, followed by a further relaxation via electron–phonon scattering on the
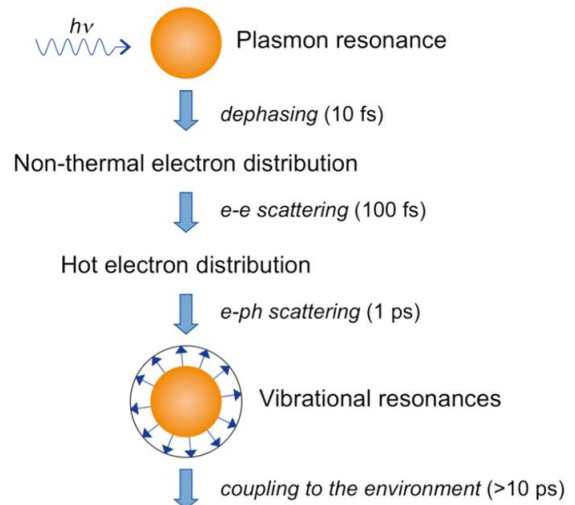

Figure 2. Sequence of events and approximate time scales following absorption of photons by a metal nanoparticle. Figure adopted from Ref. (109).

22

timescale of a few picoseconds (*111*). In the spectral domain, the excited electron as well as the hot plasmonic electrons, induce changes to the plasmonic resonance of the NS by modifying the spectral response of NSs and effecting the dielectric constant of the metal.

As the photon-induced collective electronic dynamics are fundamentally evolving with and as a result of the plasmonic excitation, an elemental understanding of the plasmonic excitation is crucially needed to understand the full evolution of the noninstantnous response following initial excitation. Furthermore, the collective electronic oscillation decoherece is strongly dependent on the plasmonic lifetime as well as to other competing processes that might interfere with coherence and induced changes to the plasmonic oscillation such as hot electronic dynamics.

The nonlinear non-instantaneous optical response and optical generation in the plasmonic nonlinear dynamics is at the heart of this Thesis. For a nonlinear plasmonic interaction within the plasmonic lifetime, the coherent structure of the pulse is shown to be crucial in determining the final outcome the interaction. Such non-instantaneous response in the nonlinear optical response is not fully understood or described in the literature and is the main focus of research brought forward in second and third articles that are in the main body of the thesis (see Chapter 2). The two relevant optical models, Miller's rule and the 3-level model, are adequately introduced in each of the articles and are extensively described in textbooks such as in Refs. (*30*) and (*113*) and are experimentally and theory compared and discussed in the second and third articles that comprise the main body of this thesis. Since both are mentioned throughout the articles on several occasions, a short description is given in the next sections. For context: in the second article (see 2.2), we find that the non-instantaneous response captured by Miller's rule (see 1.2.2.1 and Ref. (*30*)) does not predict results that fits with experiment. However we are able to fit predictions made using a 3-level systems with only one fitted parameters (see 1.2.2.2 and extensively in the manuscripts). In the third article (see 2.3), we use the optimal phase as the 3-level model prescribes and indeed find it to produce the optimal second harmonic emission in our experiments with no need to fit over parameters.

1.2.2.1 **Non-instantaneous response captured in Miller's rule**

For a bulk, far from resonance interaction, the empirical rule known as "Miller's rule" has shown great accuracy in describing the second order response function for SHG (*39*). It predicts the second order response by multiplication of the first order response of

the fundamental waves involved. This empirical rule was the basis for the nonlinear oscillator model, and can actually be fully derived by the nonlinear-oscillator model, solve in a perturbative expansion. The identification of the empirical rule with the theoretical perturbative solution benchmarks the relation of SHG as a second order excitation (*30*). We will not go into detail but simply describe this rule and show it can also be described as the modified field according to the linear response.

The Miller rule describes the nonlinear response to be:

$$\chi^{(2)}(\omega = \Omega_1 \pm \Omega_2, \Omega_1, \Omega_2) \propto \chi^{(1)}(\Omega_1)\chi^{(1)}(\Omega_2)\chi^{(1)}(\omega = \Omega_1 \pm \Omega_2) \quad (10)$$

Which means that the linear response determines the nonlinear response. If substituting this relation in Equation (4) (section 1.1.2.2) and assuming the second order response is weakly dependent on frequency and can be approximated as a proportionality factor, we obtain the following :

$$E_{SHG}(\omega) \propto \int_{-\infty}^{\infty} \chi^{(1)}(\Omega_1)E(\Omega_1)\chi^{(1)}(\omega - \Omega_1)E(\omega - \Omega_1)d\Omega_1 \quad (11)$$

Which by Fourier transform shows:

$$E_{SHG}(t) \propto \left(\chi^{(1)}(t)E(t)\right)^2 \quad (12)$$

Suggesting the second order susceptibility is directly related to the linear response by modifying the field strength in the materials and only then interacting directly.

An explicit expression for the nonlinear polarization can be obtained for the nonlinear oscillator model by setting the linear response to be:

$$\chi^{(1)}(\omega) = \frac{K_0}{\omega_r^2 - \omega^2 - 2i\omega\gamma} \quad (13)$$

where K_0 is a strength parameter that depends on the materials effective electric charge density and effective mass and γ is dependent on the resonant linewidth and corresponds to losses in the interaction. In the frequency picture, substituting Eq 14 into Eq 12, this yields a second order excitations that reads:

$$E_{SHG}(\omega) \propto \int_{-\infty}^{\infty} \frac{E(\Omega)E(\omega - \Omega)}{(\omega_r^2 - \Omega^2 - 2i\Omega\gamma)(\omega_r^2 - (\omega - \Omega)^2 - 2i(\omega - \Omega)\gamma)} \, d\Omega \quad (14)$$

.

1.2.2.2 **Non-instantaneous response in the resonant three level system**

Beyond the nonlinear oscillator model, other models can be better suited such as the perturbative description that arises from a three level dynamics. The non-instantaneous response for a near-resonant strongly interacting nonlinear process has no perturbative description which is widely accepted.

The three level system model is based on a couple mode interaction, which can rearranged to follow a Schrödinger like equation (*114*). The ground state would be the relaxed state of the system, the first level is these resonant level of the medium and the excited is the second harmonic excited level we are probing to be excited.

The Hamiltonian (lossless) which would describe this system is

$$H(\omega_{SHG}) = \begin{pmatrix} 0 & \mu_{12}E(t) & \mu_{13}E(t) \\ \mu_{21}E(t) & \omega_R & \mu_{23}E(t) \\ \mu_{31}E(t) & \mu_{32}E(t) & \omega_{SHG} \end{pmatrix}$$

Where $\mu_{ij}E(t) = \langle i| V(t)|j\rangle$.

The Hamiltonian can be perturbatively solved, by time dependent perturbation theory which would give:

$$C^{(2)}(\omega_{SHG}) \propto \mu_{12}^2 \int_{-\infty}^{\infty} \frac{E(\Omega)E(\omega_{SHG}-\Omega)}{\omega_R - \Omega + i\Gamma} d\Omega \qquad (15)$$

Where $C^{(2)}$ is the second order probability amplitude for transitioning to the third state. For a far from resonance pulse, this expression approaches the conventional instantaneous expression. However, for a near resonance interaction, it has a different form including a phase shift. An important limitation in the validity and application of this model is that described the system for a a given SHG frequency ω $_{SHG}$. While the calculation can be repeated for a range of ω_{SHG}, any interaction between the frequencies is not included.

1.3 **Quantum coherent control in plasmonic interaction**

During my PhD research, and as provided in this dissertation, I have connected ideas of coherent control from atomic systems to nonlinear optical generation in metamaterials. The following section comprises of many of the ideas and findings we have uncovered during my PhD work. Mainly, we will briefly discuss key notions, conclusions and observations crucial in connecting coherent control of nonlinear optical

phenomena in NSs. Section 1.3 is organized as follows: First, I will provide background for coherent control and its application. I focus on a key research direction of experimentally corner-stoned by the group of Prof. Yaron Silberberg (RIP) and describe a main challenge and limitations in implementing coherent control in extreme ultrafast systems, such as plasmonic systems. In section 1.3.1 we describe the context in which coherent control of nonlinear response in NSs is addressed in this dissertation. In sections 1.3.1.1-1.3.1.2 we discuss the general motivation of shaping light to control plasmonic response. In section 1.3.1.3 we present our understanding and analysis on the fundamental importance of laser range to resonant linewidth in realizing coherent control. The ideas are discussed and general and emphasized for plasmonic systems studied during my PhD. In 1.3.1.4 we provide an approach to describe the enhancement mechanism and its limitations.

Coherent control is a quantum mechanics-based method for controlling dynamical processes by electromagnetic radiation (*6*). The basic principle of coherent control in the optical domain is to control quantum interference phenomena, typically by shaping the phase of laser pulses to control coherent excitation pathways in matter (*113*). In the last few decades, coherent control has offered exceptional capabilities and remarkable observations across scientific disciplines from superresoluation to medicine (*7*, *115–117*). Control in the optical domain, which gained popularity since the development of ultrafast lasers, provides a unique approach to actively control ultrafast nonlinear dynamics in atomic, molecular and condensed matter systems (*5*, *118*). Following the profound advances in ultrafast and nonlinear imaging and spectroscopic capabilities enabled by pulse-shaping schemes, recent applications are emerging in neuroscience, high harmonic generation, and quantum information processing (*119–121*). Despite its great success, coherent control is still in its infancy for systems that exhibit complex spatiotemporal dynamics such as nanophotonics and atomic layered materials.

In essence, the field of coherent control came to life as a solution for efficiently steering a quantum system from an initial state to a final state (*113*). Furthermore, coherent control has found vast application in enhancing nonlinear phenomena. Nonlinear phenomena can be intensified by interaction with multiple eigenstates of a system to achieve a excitation that is enhanced by quantum interference (*122–124*). In the field of optics, coherent control refers to the capability of precisely shaping laser fields to manipulate the outcome of certain light–matter interactions by exploiting the coherent properties of the system. The laser pulse actively steers the excitation process towards the

desired target by inducing constructive interference between excitation pathways leading to desired final state and by destructive interference among those leading to unwanted final states. A corner stone scheme in coherent control is the work of Dudovitch et al. (*122*). In this work, the authors demonstrated how pulse shaping may be used to induce constructive interference between the various pathways leading to higher two-photon absorption. First, they point out an inherent destructive interference that occurs between all the two-photon pathways, shown in a theoretical framework describing resonant two-photon absorption (TPA). The expression used for evaluating the TPA rate (amplitude) corresponds to

$$TPA \sim \int \frac{E(\omega)E(\omega_{eg}-\omega)}{\omega_r - \omega}d\omega \qquad (16)$$

The destructive interference is manifested by the denominator, which changes sign during the integration over frequencies that are larger that ω_r (see Figure 2, right, path A vs Path B). The destructive interference originates from the resonant state that contributes a positive or negative weight to the amplitude, depending on the frequency. Second, they show to enhance the absorption by *excluding* some of the frequencies (by filtering them out of the pulse). The absorption is enhanced by filtering frequencies with that induce amplitudes with opposite sign, increasing the final amplitude obtained in the integration of the TPA rate equation. They further show how to overcome the inherent interference by applying phase mask to the pulse. The phase mask they apply is a pi-step function centered around the resonant frequency. Effectively, this mathematically translates into multiplying the amplitudes of pathways from frequencies larger than the resonant
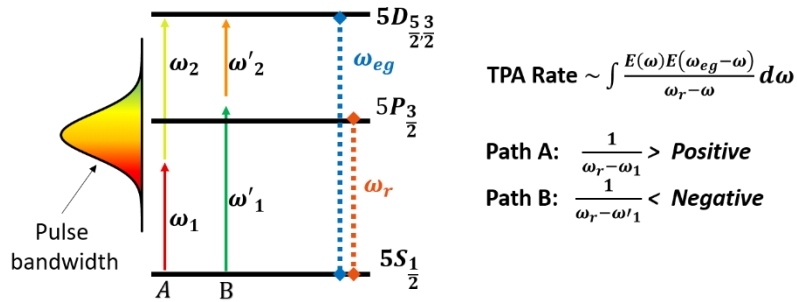
Figure 3. Destructive interference in broadband two-photon absorption (TPA). **Left**: a schematic of a two level system, where the excited level is assumed to lead to absorption (not shown). Two frequency pairs out of the broadband pulse, path A and path B, are shown leading to the same excited state (5D) with energy proportional to ω_{eg}. For Path A, the leading frequency ω_1 is smaller than the resonant state (5P) with energy proportional to ω_r. For path B it is larger $\omega'_1 > \omega_r$. **Right**: A simplified equation for the TPA rate is shown to sum over all frequency pairs. For Path A, the denominator will be positive while for Path B it will negative, meaning that both contribution would cancel out (if the sign of the numerator does not change).

frequency by a minus sign. In effect, cancelling almost all of the destructive interference that originates in the denominator. In the atomic case, an enhancement factor of 7 was demonstrated (*122*). This corner-stone work demonstrates the importance and great potential that coherent control by pulse shaping has.

However, there exists a major challenge in coherent control by pulse shaping in plasmonic systems. As interference is fundamentally related to phase, coherent control is only applicable to systems that retain the phase information for a sufficiently long time, relative to the pulses temporal duration. The so called dephasing or coherence time is defined as time undertaking the system to lose its phase memory of phase-relation. In atomic systems, this time is usually indicated as the T_2 time (*125*), and is related to the electron collision rate in plasmonic systems The condition for coherent control to be effective is thus $T_2 > \tau_{pulse}$ or in the spectral representation $\sigma_{pulse} > \sigma_{res}$, where σ_i (i={pulse, res}) is the full width at half maximum of the characteristic frequency of the system and pulse. Systems with coherence time shorter than the pulse duration are elusive to coherent control and are accessible only by high order nonlinear interaction. Plasmonic NSs exhibit coherence time less than 20 fs and resonant bandwidth larger than 100 nanometers, meaning that to fully examine coherent control of plasmonic NSs requires pulses of durations shorter than 10 fs or greater than 200 nanometers in bandwidth. Beyond the challenge of creating such extreme sort pulses, the challenge is intensified by needing to have a robust, reliable, high fidelity apparatus of such a wide bandwidth pulse, capable of controlling the pulse and delivering precise alterations to its shape with few-fs sensitivity.

1.3.1 Coherent Control of Nonlinear Response in Nanostructures

The optical response due to plasmonic dynamics in NSs, such as the localized plasmonic resonance, was introduced in section 1.2. Beyond the steady-state collective oscillations, the ultrafast nonlinear collective electronic dynamics are yet to be probed experimentally to the full extent. The main limitation was that previous experiments were carried out with pulse width longer than the plasmonic lifetime, which is approximately 20 fs. Pulse shaping has recently been used, as a tool to study plasmonic systems (*20, 126–132*), revealing novel spatio-temporal effects (*133–136*) as well as utilizing their nonlinear optical response for subwavelength control. Experiments probing only the linear response are commonly restricted, by their inherent linearity, to view only single photon

responses. Studying nonlinear properties by light-matter interaction can probe non-instantaneous response by its multiphoton interaction that consist of the material's relaxation mechanisms and phase differences in the electronic dynamics in these systems, as can be seen by in the nonlinear response (for example, by the SHG non-instantaneous response described in section 1.1.2.2).

In the course of this dissertation, the ultrafast coherent structure of the plasmonic response is put to focus and tested through its impact on non-instantaneous nonlinear second harmonic non-instantaneous response function (such as described in section 1.1.2.2). In particular, we examine both theoretically and experimentally the structure of the second order response function and its non-instantaneous plasmonic response. Our observations and achievements are brought forth in the second and third published articles that comprise the main body of the dissertation.

As the coherent structure of the phase response tightly corresponds to the ultrafast coherent electronic dynamics, our achievements focus on demonstrating coherent control of the nonlinear response of the plasmonic nanostructured light-matter interactions leading to an enhanced nonlinear response of the SHG field. Successfully demonstrating coherent control over the nonlinear interaction outcome provides crucial evidence that substantiate and evaluate the validity of the steady state approximation, as well as the analogy of the plasmonic excitation as a resonant Eigen-mode of the system. Furthermore, the ability to control, on demand, the interaction of light and matter is obviously very attractive, interesting and desired capability for both research and application. Plasmonic NSs, which hold the promise to confine, route, and control light at the nanoscale, constitute a rapidly de-cohering system. Hence corner stone coherent control schemes, such as the two-photon optimization by Dudovitch et al. (*122*) discussed in section 1.3, have yet to been tested in plasmonic systems.

1.3.1.1 **Shaping light rather than geometry for controlled plasmonic interaction**

Recent advances in fabrication techniques of plasmonic NSs allow for unprecedented control of optical, electric, mechanical or quantum mechanical properties (*137–143*). However, studying the electronic dynamics in NSs materials by variation in fabrication designs has two main disadvantages: First, the long, complex, error-prone and commonly expensive fabrication processes, which for novel designs results in very

difficult to reproduce fabrication procedures. Second, once fabricated, these engineered materials have fixed qualities which are commonly unchangeable. On the *light* side, controlling the interaction outcome by pulse shaping has proved to be possible through relatively easy techniques which are also commonly very versatile and flexible. Implementing a spatial-spectral profile to an electromagnetic pulse has enabled to dynamically drive, steer and control the interaction process to enhance, suppress or tailor the effective interaction process. Furthermore, controlling the interaction by pulse shaping allows for unique profound understanding of light-matter interaction unraveling overlooked phenomena (*122*) precise control by quantum pathway selection (*3*) and other desired controllable knobs (*144*).

1.3.1.2 **Non instantaneous resonant interaction in nanostructures**

Quantum mechanics should, in principle, be capable to describe any electromagnetic interaction. However, it is unsuitable for describing most phenomena in fault to its immense complexity. Furthermore, many phenomena are well described by use of semi-classical models which are more intuitive and provide better insight and fundamental understanding of the phenomena in focus. In this context, it can be said that in systems such as the interaction of light in NSs, the nonlinear SHG owing to the interaction in gold NSs is not completely understood. In the past two decades, the *geometrical* contribution for SHG from NSs has been studied extensively (*84*, *145–147*) and has been successfully described under the framework of the nonlinear scattering theory (*85*). However, even with the geometrical analysis, the semi-classical models that the geometrical approach relies on does not capture the temporal dynamics of the interaction, including the non-instantaneous contribution that is inherent to-resonant-phenomena. To study this aspect, we designed a set of experiments directed specifically for studying non-instantaneous effects. We have developed a model describing this interaction by the use of a 3-level resonant system, which takes into the consideration the spectral response introduced to the interaction process by the material which arise due to the plasmonic decay. The resonant 3-level model, was found suitable to predict our experimental observations and consistent throughout our experiments in several optical intensity regimes and timescales. In the second published article comprising this dissertation, we studied the nonlinear power-law response. We fully describe the 3-level model and how we use it to predict plasmonic interaction and dynamics. In the article, we

use the 3-level model and its solution via a high-order perturbative expansion, to fully describe and predict the complex nonlinear power law modulation we experimentally observed by a coherently controlled pump-probe experiment. Furthermore, we use the 3-level model to provide an intuitive explanation to the phenomena. The 3-level model is described in depth yet again with focus on the complex structure of the solution obtained by the interfering second order term with the forth order terms in a perturbative expansion, captured experimentally by optimization via coherent control. In the next section, we will discuss the importance of the relation of the bandwidth of the laser source to the resonant linewidth in coherent control. This ratio is the main factor why observations of SHG enhancement via coherent control in plasmonic have been elusive in the past.

1.3.1.3 **The importance of laser spectral range to resonant linewidth ratio**

During our research on coherent control of SHG in plasmonic interaction, we realized the importance of the relation of the bandwidth of the laser source to the resonant linewidth. The ratio is crucial in enabling any meaningful enhancement to SHG by pulse shaping or any other coherent control over the non perturbative plasmonic dynamics. For example, in the case of a 130-fs, as used during our experiments presented in the second publication in this dissertation, the ratio of pulse spectral range to the resonant linewidth was only $\frac{\sigma}{\Gamma_r} \approx \frac{25}{100} = 0.25$. This small ratio describes the small portion that the pulse spectrum overlaps with the resonant linewidth.

Resonant interaction is commonly accompanied by a spectral phase shift in the response function. The spectral profile consists of the effective response of a system, which is affected by the electronic affinity to absorb and exchange energy with electromagnetic fields as well as the electronic dynamics of system following the interaction that correspond to the duration of the electromagnetic pulse. Demonstrating by spectral pulse shaping a stronger SHG emission, which is superior to the emission achieved by a transform-limited pulses (where the peak intensity is the highest) is counter-intuitive from the perspective of any common textbook in nonlinear optics. Especially in the era of hybrid nanophotonics, understanding the impact of resonant interaction in nanostructured systems is crucial for analyzing the physical structure and dynamics in the sub 20-fs regime.

In any ~ 100 fs near-IR laser, the relatively narrow spectral bandwidth of the pulse does not enable significant enhancement by spectral shaping the excitation in resonant NS's. This can be understood by examining the ratio of the pulse's spectral range relative to the resonant linewidth (see Figure 6), which provides an intuitive and quantitative measure for the potentiality of enhancement by pulse shaping.

In the case of a 130-fs pulse, as used in the experiments presented in the second publication in this dissertation, the spectral to resonant linewidth was small, $\frac{\sigma}{\Gamma_r} \approx \frac{25}{100} = 0.25$. With such a small ratio, the spectral phase differences added by the resonant NS are small. Thus, canceling it by additively inversing the phase accumulated, via the pulses spectral phase, should not yield much enhancement. However, a source such as the OPCPA Venteon dual system, which was used in the experiments described the third publication, provides a sub 10 fs pulses that holds a spectral range that is ~ 10 times larger than the 130 fs source. This significantly larger spectrum, in addition to the narrowing of the resonant linewidth due to a higher frequency LSPR (centered at 750 nm rather than 1450 nm), yields a ratio of laser bandwidth to resonant bandwidth of $\frac{\sigma}{\Gamma_r} \approx 3$, which is 12 times greater than the ratio of the narrowband case.
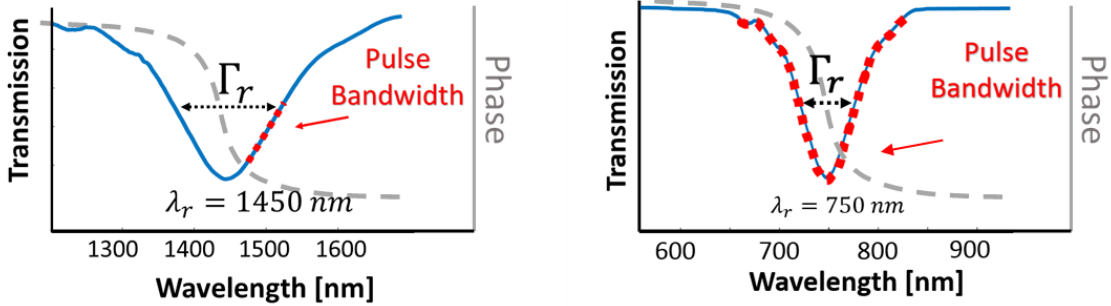
Figure 4. Resonant split ring resonator transmission spectrum and phase (blue line, gray dashed line) and pulse full width (dashed red) showing the different overlap of pulse bandwidth with resonant linewidth. (Left) LSPR at 1450 nm, 130 fs pulse with spectral bandwidth of 30. (Right) LSPR at 750 nm, 6 fs pulse with spectral bandwidth of ~ 200 nm.

1.3.1.4 Intuitive depiction of the enhancement mechanism

We developed a method to analyze and visualize the importance of this ratio. Using parameters that correspond to plasmonic bandwidth, we analyzed our interaction by a

geometrical representation of the excitation. Our analysis unraveled why our attempts to observe SHG *emission* enhance in a 130 fs source failed, and provided a firm theoretical stand that such observations will be enabled by a sub 20 fs pulse. Furthermore, it allowed us to intuitively understand and connect the complex contribution of the field to the coherent interference of the interaction. The summary of our exploration and the key ideas extract from it are describe in the following section.

In order to fully appreciate the importance of this ratio difference, consider a resonant SHG interaction described by the resonant 3-level system with SHG intensity for a specific frequency ω_{SHG} as follows:

$$|E(\omega_{SHG})| \propto \left| \int \frac{E(\Omega)E(\omega_{SHG} - \Omega)}{\omega_R - \Omega + i\Gamma_R} d\Omega \right| \tag{17}$$

$$\rightarrow \left| \sum_n \frac{E(\Omega_n)E(\omega_{SHG} - \Omega_n)}{\omega_R - \Omega_n + i\Gamma_R} \right| \rightarrow |z_1 + z_2 + \cdots z_n|$$

Each complex term of this sum, z_i, represents the amplitude and phase of the interaction between two specific frequencies $\{\Omega_n, \omega_{SHG} - \Omega_n\}$ which contribute to SHG signal at ω_{SHG}. If we now consider the geometric picture of this sum depicted on the complex 2D plane, then *addition* corresponds to connecting the arrow each z_i represents. This picture allows us to observe the frequency domain picture of the interaction process. Shown in Figure 5, the blue arrows represent each term in the sum, while the red line is the absolute value of this complex sum, which will be the final intensity this process yields for this given frequency, $|E(\omega_{SHG})|$. Please note that the phase each term has two contributors: the phase added by the electric field phase and the phase added by the imaginary part of the weight function, $1/(\omega_R - \Omega_n + i\Gamma_R)$, which represents the materials response to the excitation. In this model, the maximal intensity possible for this process is when all terms in the sum have the same phase, i.e. for all z_i, angle(z_i)=constant. In this ideal case, this would result in having all blue arrows pointing in the same direction, thus the total blue arrow would be straight and exactly equal in length to its absolute value (red arrow). The calculation in the frequency domain interaction process is plotted in Figure 5(a), for a range/linewidth ratio of 5 and for a phaseless electric field (transform limited pulse), resulting in a very curved interaction process. The curvature of the blue curve is due to the phase introduced by the interacting medium which changes for each

component in the sum [see Eq. (17)]. This curvature implies that if we introduce a spectral phase to the process through the electric filed, we could "straighten" the blue arrows, and result in a stronger intensity SHG simply by applying a phase to the pulse. In contrast, in Figure 5 (b), the range/linewidth ratio is 0.5, resulting in a very small curvature, such that even if we apply a phase, the "straightened" arrow would not be much greater than the un-straighten one.

The non-instantaneous contribution inherent to nonlinear resonant dynamics is well known in atomic and molecular systems, which is of particular importance in multiphoton processes (*3*). Enhancement by orders of magnitude of electronic transitions in atomic systems (*122, 144*) as well as for large organic molecules (*148, 149*) has been enabled by spectrally shaping the pulse to be compatible with the non-instantaneous response in resonant mediated interactions, via coherent control schemes. However, for resonant NSs, applying such pulse shaping methods to enhance nonlinear processes have been so far limited, since, these require the interacting pulse spectrum to be much broader than the resonant linewidth, which is typically not fulfilled for NSs. Therefore, pulse shaping has been mostly shown for controlling the *linear* response in plasmonic systems (*150–154*) or for multicolor SHG imaging (*155*).
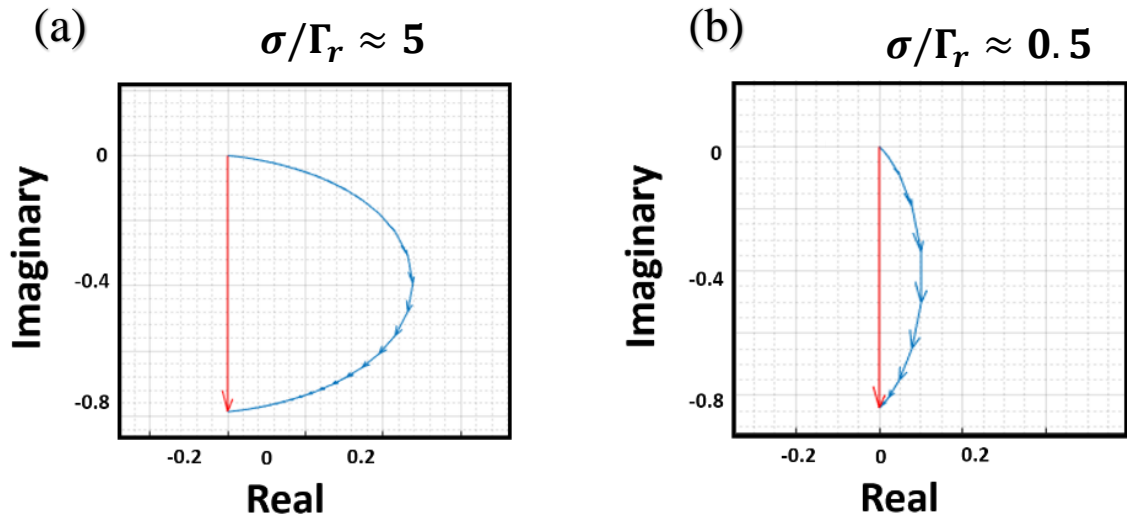
Figure 5. Geometric picture in the complex plane plots of resonant SHG showing the potential of coherent control for different range/linewidth ratios (a) Broad bandwidth interaction - ratio of 5 showing the interaction process is not efficient since each step in the process interferes with the previous one. (b) Narrow bandwidth interaction - ratio of 0.5 showing that this effect is less prominent for smaller ratios. Both electric fields are with no spectral phase (Transform limited pulses).

1.4 **Methods**

1.4.1 **Experimental methods**

1.4.1.1 **Pulse shaping**

Pulse shaping is a concept aimed to describe the capability of shaping the temporal or spatial waveform of electromagnetic pulses. Dynamical coherent control over ultrafast interactions requires accurate pulse shaping of ultrafast optical pulses, a task which becomes increasingly difficult as the pulse duration is shortened and as the regime become smaller. Fidelity and accuracy in pulse shaping is absolutely crucial in determining in researching novel phenomena in ultrafast nanoscale optical nonlinearities. During my PhD research, we have complied several pulse shaping devices with increasing complexity as we applied pulse shaping down to the sub 10 fs regime and down to the individual NS. In the following section, I will introduce the topic of optical pulse shaping and go over the key ideas that challenged us during my research and how we implemented our solution to obtain sub-10 fs pulse shaping for high fidelity reliable coherent control in the nano regime.

1.4.1.2 **Basic Optical Pulse shaping**

Pulse shaping is a concept aimed to describe the capability of shaping the temporal or spatial waveform of electromagnetic pulses. Full modulation of optical fs pulses cannot be conventionally achieved by electronic modulation as they are limited to electronic timescales that are much slower than optical frequencies. To produce a flexible frequncy-dependent dispersion mask, optical pulse shaping requires manipulation of the optical path with a combination of using spatio-temporal coupling. In such a method, the desired dispersion can be obtained by controlling static, spatial dependencies. The simplest of pulse shaping techniques might be to just place a highly-dispersive element in the optical path. Such implementation would stretch the pulse both in space and time, lowering its peak intensity but retaining its overall energy. The amount of stretching would directly

correspond to the dispersion-coefficient of the medium and the optical path of the material. A more controllable pulse shaper, but still simple, would be to place a grating pair, inserting spatial dispersion by the diffraction at the first gratings, later to be translated to temporal dispersion by propagating in air and inverting the spatial dispersion by the second grating (*156*, *157*). A more precise and programmable pulse shaping apparatus is obtained by constructing a 4f –grating-based-pulse shaper and place a spatial light modulator in its Fourier plane (*158*). Such pulse-shaper, enables to induce different phase to each wavelength separately. This allows to produce almost arbitrary pulse shapes, as the spectral phase function corresponds directly to the temporal shape, by Fourier Transform. Hence this would allow, ideally, any pulse shape that can be achieved by the Fourier Transform. The relation between the spectral phase applied by the SLM is given by:

$$E_{in}(t) \xrightarrow{FFT} E_{in}(\omega) \xrightarrow{SLM} E_{in}(\omega) \times e^{i \cdot \phi_{SLM}(\omega)} \xrightarrow{FFT} E_{out}(t) \,.$$

1.4.1.3 **Spatiotemporal coupling in the 4f pulse shaper SLM**

Constructing a 4f optical system (*159*) results in a mapping of the frequency components into a spatial map. Inserting a spatial-light modulator at the Fourier plane of such configuration enables to modulate the temporal profile of the pulse by applying a spatial phase mask. This may be used for phase compensation and pulse compression to obtain higher peak-intensity, or could be used for pulse shaping for coherent control (*20*, *122*, *133*).

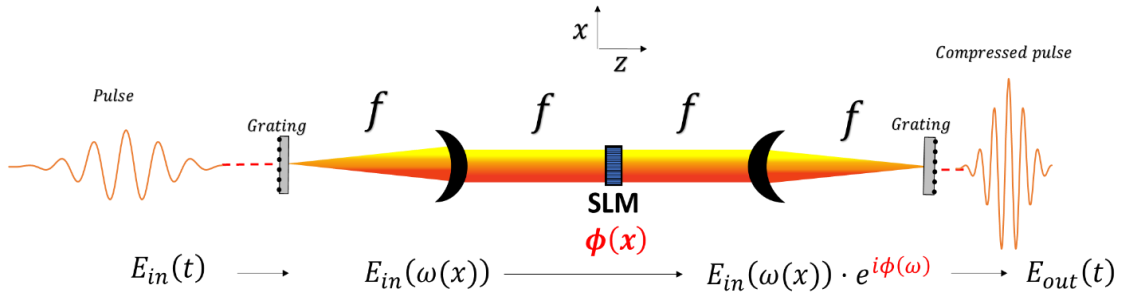Figure 6. Single pass configuration. A 4f pulse shaper consisting of a spatial light modulator in its Fourier plane, applying a spectral phase to compress pulse duration (for example a quadratic phase). The grating, placed one focal length from a lens, project the incoming pulses frequency components into a spatial distribution allowing for a spatial mask to act as a spectral mask $\phi(\omega(x))$.

Previous works describing a grating pair for introducing spatiotemporal effects can be traced originally to the work performed in 1984 by Martinez et al (*156*). This apparatus is the basis for achieving a Fourier plane in the 4f system, decoupling the frequencies in space and allowing for a spatial mask to be used as a spectral mask. These studies, were the first to show that a anti parallel pair of refracting gratings could provide spectral dispersion with both positive and negative coefficients (natural vs anomalous dispersion) (*157*, *160*, *161*). In these papers, Martinez describes the spatiotemporal coupling of a grating pair showing that a spectral dispersion originating from spatial mask is intimately connected to spatial dispersion (commonly resulting in a front pulse tilt). He further suggests introducing a mirror after the grating pair and revisit the pair to achieve a double amount of spectral dispersion but cancel the spatial effect. Although this simple set-up provides a way to use spatiotemporal coupling to introduce a purely spectral phase, complete cancellation of the spectral effect is generally not possible for a pulse that accumulated an arbitrary spatiotemporal phase while in between the grating pair. Therefore, incorporating a SLM to the Fourier plane of a 4f mirrored grating system (see Figure 6), introduces a spatiotemporal phase that ultimately affects both the temporal and spatial profiles. In the mentioned research, they have roughly calculated and speculated that unlike the case of a simple grating pair, arbitrary phases added by the SLM could not be canceled out by a use of a mirror. This problem was mostly not revisited, mainly because these parasitic effects are negligible when performing experiments in uniform bulk materials. However in 2011, Brink et al. has demonstrated the importance of these effects in the nano regime (*162*) and experimentally demonstrated that adding a mirror to obtain a double-pass configuration can diminish spatiotemporal effects by at least an order of magnitude. The construction of the double pass configuration was proved crucial in the experiments present in the second article comprising the main body of this dissertation, where low power required strong spatial focus, which enhances the parasitic phenomena. Hence the double-pass enabled the high spatial precision needed to observe the non-instantaneous coherent effect.

1.4.1.4 **Pulse shaping sub 10 fs pulses**

Dynamical coherent control over extreme ultrafast interactions is unquestionably very challenging as it requires pulse shaping extremely ultrashort pulses. In the spectral domain, the challenge translates to precise and delicate manipulation of the spectral phase

function of the driving pulse over a sizable bandwidth, as dictated by Fourier transform. In such systems, delicate dispersion management is essential since even the dispersion induced by the propagation in air significantly hinders the fidelity and temporal resolution extreme ultrafast processes demand, such as plasmonic excitations. Furthermore, any conventional strong focusing elements, commonly used in nano-optical systems, such as high NA immersion objective lens', further complicates the spectral shape of the pulse as they are immensely dispersive as well as contribute considerably to high order terms in the spectral phase. These obstacles in coherent control application are typically addressed by utilizing the pulse shaper itself as a compensation mask. However, such implementations substantially lower fidelity of the applied spectral mask, restricting the resolution and accuracy of the spatial light modulator (SLM). As a result, these impede controllability, narrowing the coherent control landscape and inhibiting the realization of control over ultrafast processes within the excitation lifetimes.

To address these challenges, which are critically required for extreme ultrashort plasmonic lifetimes, allowing for our SLM to solely be used as an active dynamical coherent control device, we carefully designed a dispersionless pulse shaper set up, effectively freeing the SLM from dispersion management. Our set up consists of a carefully constructed mirror-based (parabolic mirror, f = 500 mm) 4f pulse shaper (Plane Ruled reflective grating, 1200 G/mm Newport, Richardson) SLM, (Jenoptik 640d) accompanied by a custom-made chirped mirror set-up (Laser Quantum), tunable CaF2
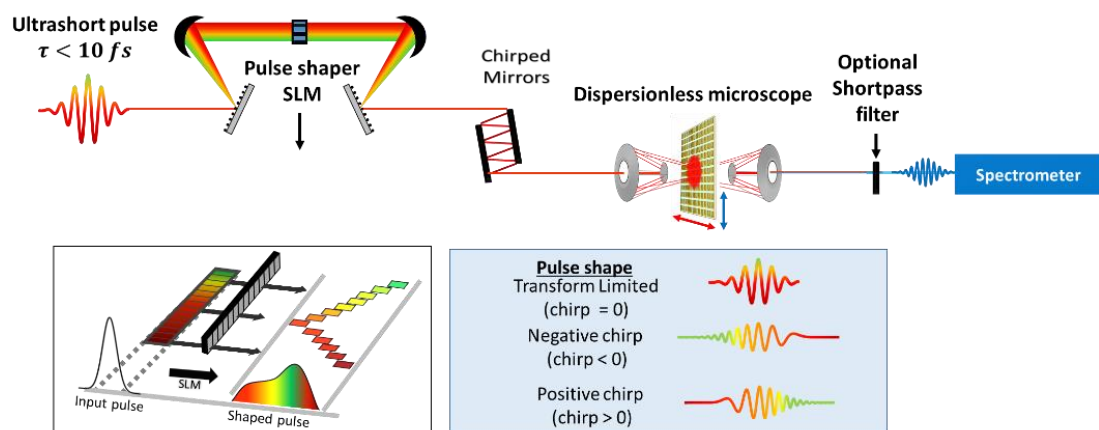
Figure 7. The experimental setup. A sub-10 fs pulse passes through a 4f pulse shaper consisting of a spatial light modulator (SLM, See left Inset). The shaped pulses interact with an array of gold NSs, producing SHG emission. The mirror-based setup frees the SLM from dispersion management of the pulse and is used only for CC. The interaction can be coherently controlled externally by manipulating the pulse's spectral phase to reroute the accumulative excitation-pathways to constructively interfere. For example, the SLM can be used to stretch pulse by negative or positive chirp (see right Inset).

ultrafast wedge pair followed by a mirror-based objective lenses (Edmund optics, infinity corrected 15X NA 0.28 and Thorlabs, LMM-15X-UVV, infinity corrected 15X, 0.30 NA). The beam was maximally focused to a diameter of ~ 10 micrometers at FWHM.

1.4.1.5 Frequency-resolved optical gating (FROG)

Frequency-resolved optical gating (FROG) is a general method for measuring the spectral phase of ultrashort laser pulses, which range from sub fs to hundreds of picoseconds (*163*, *164*). FROG is a spectrally resolved autocorrelation, which allows the use of a phase-retrieval algorithm to retrieve the precise pulse intensity and phase vs. time. FROG and autocorrelation share the idea of combining a pulse with itself in a nonlinear medium. Auto correlators measure a pulse by measuring the intensity of the nonlinear signal field as a function of pulse delay. Estimating the pulse length requires assuming a pulse shape, and the phase of the pulse electric field cannot be measured at all. FROG extends this idea by measuring the spectrum of the signal at each delay (hence "frequency-resolved"), instead of just the intensity. This measurement creates a spectrogram of the pulse, which can be used to retrieve, via analytical or iterative calculation, the complex electric field as a function of time. Since FROG depends on an auto correlated pulse interacting in a nonlinear crystal, the set-up configuration depends on temporal duration of the pulse and resolution of the retrieval, pulse wavelengths, intensities etc.
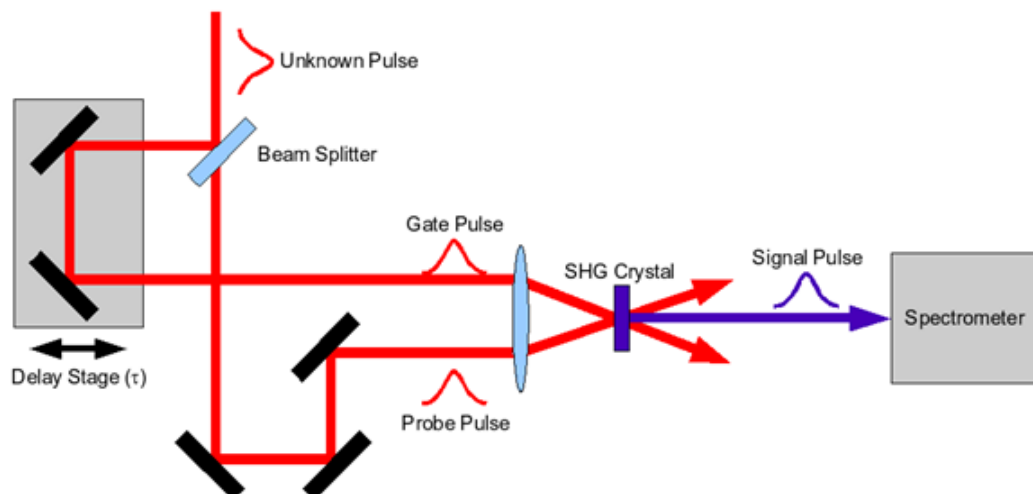

Figure 8. A schematic of a typical experimental, multishot SHG FROG setup. Figure adopted from Ref. (*164*).

1.4.1.6 Microscopic spectroscopy

For linear characterization of the metasurfaces studied at this thesis, various microscopic spectroscopies setup was used including a commercial FTIR system for the NIR NS experiments. For the NIR-vis samples, the setup comprised an off the shelf illumination source (Thorlabs Compact Stabilized Broadband Light Source), half-wave plate (λ/2) and a polarizer (P) to control the beam power and polarization, sample on a motorized rotational stage (Thorlabs PRM1Z8), objective lens (Obj.), tube lens (TL), iris at the image plane, 4f system, polarizer (P) and an imaging spectrometer (IS) with a cooled back-illuminated EMCCD detector (IsoPlane, Pixis camera).

The measurements procedure started with obtaining a focused and clear magnified image of the studied sample. The image was taken with the IS in a standard camera mode and with an open iris. Then, the iris was adjusted to transmit only light passing through the studied sample, and the IS was used in a spectrometer mode. For measurements that exceeded the spectral range of the IS (~350-1050 nm), fiber coupled spectrometer for the near-infrared (Ocean Optics NIRQ512, spectral range 900-1700 nm) was used. Transmission measurements were calculated according to $T = \frac{I_{sample} - I_{background}}{I_{refrence} - I_{background}}$, where sample, reference and background are the spectrometer counts for light passing through the sample, reference, and with no light, respectively. The reference measurements were performed on the substrate without the metasurfaces. The background counts were reduced by cooling the detector of the spectrometer (internal fan). Measurements with good signal to noise ratios were achieved by adjusting the acquisition rates, source power, and the spectrometer temperature to assure negligible influence of the background signal.

1.4.1.7 SHG measurements

The SHG measurements were performed in the setup shown in Figure 1.5. A short-pass filters was placed after the sample and between the tube lens and imaging system. The spectral range operation of the filters was adjusted to block residual SHG on the incident beam, and FF from entering the spectrometer. The FF source for the SHG measurements was an ultrafast pulsed source, either a sub 10 fs pulsed fs (Venteon dual, sub 10 fs, repetition rate 80 MHz centered at 850 nm) or an OPO pumped by a Titanium Sapphire laser (ORIA OPO, pulse width ~150 fs, repetition rate 80 MHz, spectral range 1000-1600 nm). The incident beam waist in the experiments was focused down to minimal
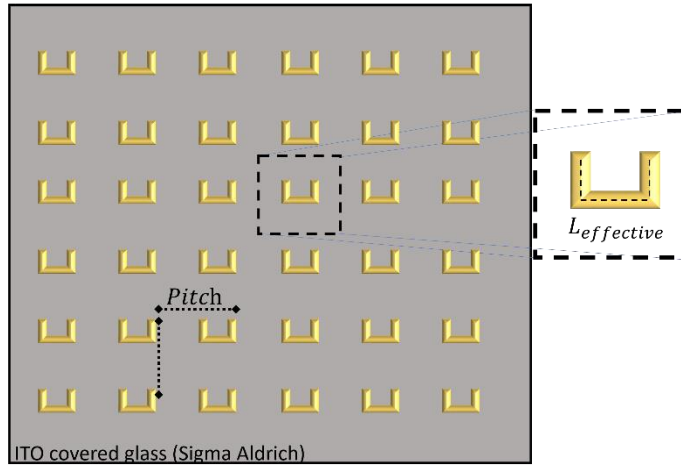
Figure 9. Illustration of a sample containing plasmonic nanostructures. Each sample is a 50 by 50 micrometer array containing nanostructures sharing their effective length. The effective lengths used in experiments range in 100 – 700 nm, producing LPR's in the range of 700 - 1600 nm. The pitch in both axes was set to be equal and ranged in 500, 700 and 800 showing no significant pitch–related effects in the pulse shaping experiments.

spot size of ~2-20 μm with an average power going up to ~1 mW. The spot size varied based on the objective lends (Edmund optics, infinity corrected 15X NA 0.28 and 20X Mitutoyo Plan Apo NIR) as as on incoming waist of the beam, and laser source (ORIA vs Venteon).

1.4.2 **Fabrication techniques**

NSs were fabricated on an ITO covered glass (Sigma Aldrich). The samples were first covered with PMMA-A4 polymer and spin-coated for one minute at 7,000 RPM. The electron beam (Raith150) used was a 10 kV beam, aperture 6 mm WD, and a dose was deposited in single-pixel lines. Samples were then developed in MIBK/IPA (1:3) for 1 min and rinsed in isopropanol for 20 s. A concentration of 40 nm of gold was then evaporated on the sample with an E-Beam Evaporator (VST evaporator). Lift-off was performed with acetone and followed with a final wash in isopropanol. NS arrays of 50x50 micrometer. In each array the nanostructured were to design to have equal effective length (See Figure 9). The NSs are asymmetric, allowing for inline SHG, where the asymmetry ratio used in all experiments was of 0.16-0.2 to maximize nonlinear emission (*85*). The samples were also measured for different pitch, 500 - 800 nm, the variations of pitch values did not show any significant effect beyond enhanced absorption crossection.

1.4.3 **Numerical Simulations**

During my PhD research, I have developed two core types of simulations. The first is focused on the adiabatic FWM and uses a 4'th order Runge-Kutta ODE method for solving a Maxwell's-equations-based 4 coupled wave equations predicting spatiotemporal FWM (FWM) in waveguides (Main Matlab script attached in Appendix A). The second deals with the effect of spectral phase coherent control on resonant structures (Main Matlab script attached in Appendix B). The simulation predicts the effects of pulse shaping in plasmonic mediated SHG and based on the perturbative expansion of a 3 level systems. Each of these simulation tools enabled detailed explorations of the studied dynamics.

For the adiabatic FWM, it is natural to observe the interaction by integrating forward each step during the propagation of light in the waveguide. The interaction is instantaneous and is centered around the peak power of the incoming light and since energy conversion must hold, the full set of equations can be verifying for each step and produce a window to the spatiotemporal evolution of energy exchange between frequencies. Detailed description of the numerical simulation for the adiabatic FWM are central to the first published article.

The numerical simulation for the plasmonic interaction provides a direct connection between the experimental ability to reconfigure the SLM and control the pulse shape and the ability to calculate the produced SHG. It provided a convenient tool to study the complex relation between pulse shape and interaction. The prediction, made in the frequency domain, enables direct insertion of the spectral phase of the pulse. This corresponds to the SLM that is reconfigured to applied a spectral phase target. Furthermore, the main characteristics that were scanned over in the experiments are direct parameters in the simulation, such as the NSs resonant wavelength and linewidth. This allowed on-demand comparison between simulation and experiment and enabled an easy method to predict how variations in the pulse shape should affect the SHG. Description of the plasmonic SHG simulations are detailed in second and third article comprising the main body of the dissertation.

In addition, for research over plasmonic mediated nonlinear optical interaction, I have programed a graphic user interface (GUI) which enables to easily switch between several models prediction nonlinear optical generation. More specifically, models that predict SHGs by instantaneous, non-instantaneous resonant 3-level system or non-

instantaneous nonlinear oscillator model. The simulations can be loaded with a computer-generated Gaussian spectrum of choice or a measured spectrum as input, for a more accurate prediction based on spectral measurements of the pulse pre-interaction. The GUI enables the user to write, in free text, the phase function applied by the spectral shaper. Such spectral shaper corresponds to an ideal double-pass 4f SLM. The GUI also enables the user to scan over a parameters and easily produce a 2D map of the scan and spectrum. An example of the use of this GUI and its versatility is placed in Figure 9. In Figure 9a, a computer generated spectrum of a sub 10 fs Gaussian pulse is placed as input and is simulated to interact with a resonant level under the framework of a two-photon resonant three-level interaction. This interaction is than simulated for a transform limited pulse and for a pulse with spectral phase of $\tan^{-1}\left(\frac{\Gamma}{\omega - \omega_0}\right)$ showing up to 100% enhancement of SHG. In Figure 9b, the same interaction is predicted for a measured spectrum of a sub 10 fs, as measured in the lab before any nonlinear interaction. The ease of use and speed of this GUI based simulator played an essential role in assisting the research and data analysis of experiments.
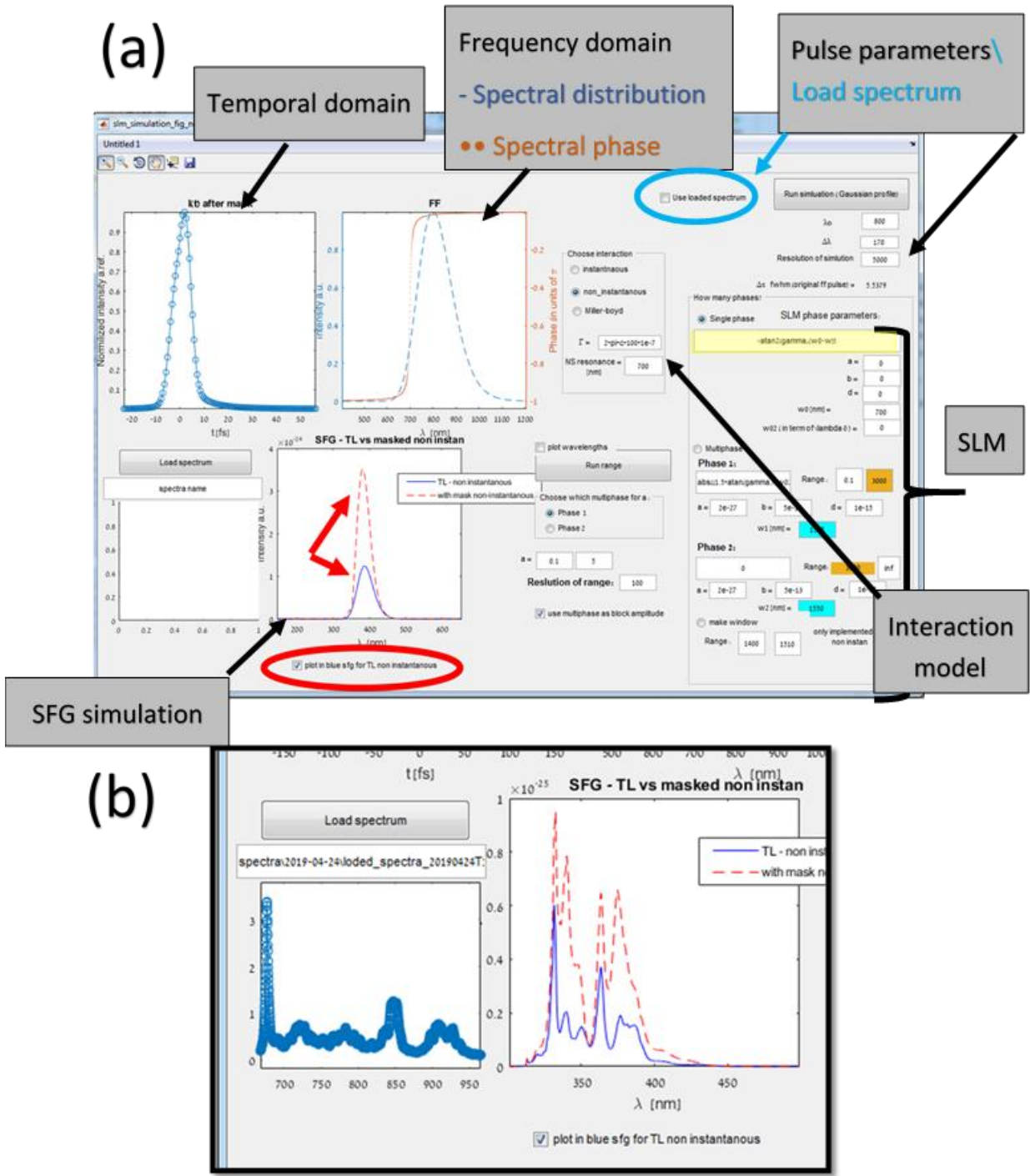
Figure 10. An example of the versatility of the graphical user interface designed to aid in researching the nonlinear optical generation in plasmonic interaction. (a) An input pulse centered at 800 nm with 170 nm bandwidth, corresponding to a sub 10 fs pulse, is placed as input for the simulation. A non-instantaneous model based of the resonant 3 level systems is selected for the simulation with selected linewidth and resonant frequency. The SFG prediction is then presented for a transform limited pulse with no spectral phase (blue) and for a pulse shape as input at the "SLM" section (red dashed). (b) The same as (a) but this time the laser spectrum input is a measured spectrum input to the simulations.

2 Published Manuscripts

In this chapter, we present key results obtained over the course of my PhD work, in the form of three peer-reviewed scientific papers. In the first paper, in section 2.1, a collaboration with the group of Prof. Jeffery Moses, Cornell University, we show a novel method for broadband FWM frequency conversion. In particular we expand the concept of 'Adiabatic frequency conversion' for centrosymmetric $\chi^{(3)}$ materials. Our approach suggests a rout for near-100% efficiency in nonlinear frequency conversion, and provide applicable schemes for materials such as Silicon photonics and optical fibers. The adiabatic method is a spatiotemporal coherent control scheme that enables to side step the usual bandwidth-efficiency commonly found in nonlinear frequency conversion, as we show in the supporting simulations reinforcing the theory. In the second paper, in section 2.2, we demonstrate coherent control of the nonlinear power-law response in plasmonic NSs by pulse shaping. In particular, we show that the power-law of the SHG can be coherently controlled by applying a v-shaped phase mask to the pulse. Finally, in section 2.3we demonstrate direct coherent control of the second harmonic emission in plasmonic , interaction. By constructing an apparatus capable of providing high-fidelity pulse shaping of sub fs pulses, we are able to interact within the lifetime of the plasmonic excitation. This enables us to demonstrate corner-stone coherent control schemes in plasmonic systems tht have been previously unattainable. We demonstrate to enhance SHG beyond the maximal value usually expected by maximally compressing the pulse. Our demonstration ofenhancement via stretching the pulse stands in contrary to the common perception in nonlinear plasmonics, which is based on analysis of non-resonant interaction, where the greatest nonlinear response is usually obtained by maximizing the pulse peak intensity. The findings and developments presented in this chapter promote the understanding of optical interaction in nanophotonic platforms and will potentially lead to new and exciting developments in the ultrafast dynamics of condensed matter systems.

2.1 Adiabatic four-wave-mixing frequency conversion

Check for updates

Adiabatic four-wave mixing frequency conversion

EYAL BAHAR,[1,3] XIAOYUE DING,[2,3] ASAF DAHAN,[1] HAIM SUCHOWSKI,[1] AND JEFFREY MOSES[2,*]

[1] *Raymond and Beverly Sackler School of Physics and Astronomy, Tel Aviv University, Tel Aviv 69978, Israel*
[2] *School of Applied and Engineering Physics, Cornell University, Ithaca, NY 14853, USA*
[3] *These authors contributed equally to this work*
[*] *moses@cornell.edu*

Abstract: We introduce the concept of adiabatic four-wave mixing (AFMW) frequency conversion in cubic nonlinear media through an analogy to dynamics in quantum two-level systems. Rapid adiabatic passage in four-wave mixing enables coherent near-100% photon number down-conversion or up-conversion over a bandwidth much larger than ordinary phase-matching bandwidths, overcoming the normal efficiency-bandwidth trade-off. We develop numerical methods to simulate AFWM pulse propagation in silicon photonics and fiber platforms as examples. First, we show that with a longitudinally varying silicon waveguide structure, a bandwidth of 70 nm centered at 1820 nm can be generated with 90% photon number conversion. Second, we predict the broadband generation of nanojoule energy, 4.2-5.2 μm mid-infrared light in a short, linearly tapered fluoride step-index fiber. We expect the AFWM concept to be broadly applicable to cubic nonlinear platforms, for applications as diverse as bright ultrafast light pulse generation, sensing, and conversion between telecommunications bands.

References and links

1. M. A. Foster, A. C. Turner, R. Salem, M. Lipson, and A. L. Gaeta, "Broad-band continuous-wave parametric wavelength conversion in silicon nanowaveguides," Opt. Express **15**, 12949–12958 (2007).
2. J. Leuthold, C. Koos, and W. Freude, "Nonlinear silicon photonics," Nat. Photonics **4**, 535–544 (2010).
3. M. G. Allen, "Diode laser absorption sensors for gas-dynamic and combustion flows," Meas. Sci. Technol. **9**, 545–562 (1998).
4. J. Wang, J. Sun, and Q. Sun, "Proposal for all-optical switchable or/xor logic gates using sum-frequency generation," IEEE Photonics Technol. Lett. **19**, 541–543 (2007).
5. D. Polli, P. Altoè, O. Weingart, K. M. Spillane, C. Manzoni, D. Brida, G. Tomasello, G. Orlandi, P. Kukura, R. A. Mathies, M. Garavelli, and G. Cerullo, "Conical intersection dynamics of the primary photoisomerization event in vision," Nature. **467**, 440–443 (2010).
6. T. Popmintchev, M.-C. Chen, D. Popmintchev, P. Arpin, S. Brown, S. Ališauskas, G. Andriukaitis, T. Balčiunas, O. D. Mücke, A. Pugzlys, A. Baltuška, B. Shim, S. E. Schrauth, A. Gaeta, C. Hernández-García, L. Plaja, A. Becker, A. Jaron-Becker, M. M. Murnane, and H. C. Kapteyn, "Bright coherent ultrahigh harmonics in the kev x-ray regime from mid-infrared femtosecond lasers," Science. **336**, 1287–1291 (2012).
7. H. Suchowski, D. Oron, A. Arie, and Y. Silberberg, "Geometrical representation of sum frequency generation and adiabatic frequency conversion," Phys. Rev. A **78**, 063821 (2008).
8. H. Suchowski, V. Prabhudesai, D. Oron, A. Arie, and Y. Silberberg, "Robust adiabatic sum frequency conversion," Opt. Express **17**, 12731–12740 (2009).
9. H. Suchowski, B. D. Bruner, A. Ganany-Padowicz, I. Juwiler, A. Arie, and Y. Silberberg, "Adiabatic frequency conversion of ultrafast pulses," Appl. Phys. B **105**, 697–702 (2011).
10. J. Moses, H. Suchowski, and F. X. Kärtner, "Fully efficient adiabatic frequency conversion of broadband ti: sapphire oscillator pulses," Opt. Lett. **37**, 1589–1591 (2012).
11. H. Suchowski, P. R. Krogen, S.-W. Huang, F. X. Kärtner, and J. Moses, "Octave-spanning coherent mid-ir generation via adiabatic difference frequency conversion," Opt. Express **21**, 28892–28901 (2013).
12. P. Krogen, H. Suchowski, H. Liang, N. Flemens, K.-H. Hong, F. X. Kärtner, and J. Moses, "Generation and multi-octave shaping of mid-infrared intense single-cycle pulses," Nat. Photonics **11**, 222–226 (2017).
13. M. Charbonneau-Lefort, B. Afeyan, and M. M. Fejer, "Optical parametric amplifiers using chirped quasi-phase-matching gratings i: practical design formulas," J. Opt. Soc. Am. B **25**, 463–480 (2008).

14. C. Phillips and M. Fejer, "Efficiency and phase of optical parametric amplification in chirped quasi-phase-matched gratings," Opt. Lett. **35**, 3093–3095 (2010).
15. C. Phillips and M. Fejer, "Adiabatic optical parametric oscillators: steady-state and dynamical behavior," Opt. Express **20**, 2466–2482 (2012).
16. C. Heese, C. R. Phillips, B. W. Mayer, L. Gallmann, M. M. Fejer, and U. Keller, "75 mw few-cycle mid-infrared pulses from a collinear apodized appln-based opcpa," Opt. Express **20**, 26888–26894 (2012).
17. O. Yaakobi, L. Caspani, M. Clerici, F. Vidal, and R. Morandotti, "Complete energy conversion by autoresonant three-wave mixing in nonuniform media," Opt. Express **21**, 1623–1632 (2013).
18. A. Markov, A. Mazhorova, H. Breitenborn, A. Bruhacs, M. Clerici, D. Modotto, O. Jedrkiewicz, P. di Trapani, A. Major, F. Vidal, and R. Morandotti, "Broadband and efficient adiabatic three-wave-mixing in a temperature-controlled bulk crystal," Opt. Express **26**, 4448–4458 (2018).
19. M. A. Foster, A. C. Turner, J. E. Sharping, B. S. Schmidt, M. Lipson, and A. L. Gaeta, "Broad-band optical parametric gain on a silicon photonic chip," Nature **441**, 960–963 (2006).
20. Y. Ding, J. Xu, H. Ou, and C. Peucheret, "Mode-selective wavelength conversion based on four-wave mixing in a multimode silicon waveguide," Opt. Express **22**, 127–135 (2014).
21. I. Agha, M. Davanço, B. Thurston, and K. Srinivasan, "Low-noise chip-based frequency conversion by four-wave-mixing bragg scattering in sinx waveguides," Opt. Lett. **37**, 2997–2999 (2012).
22. S. Coen, A. H. L. Chau, R. Leonhardt, J. D. Harvey, J. C. Knight, W. J. Wadsworth, and P. S. J. Russell, "Supercontinuum generation by stimulated raman scattering and parametric four-wave mixing in photonic crystal fibers," J. Opt. Soc. Am. B **19**, 753–764 (2002).
23. C. R. Petersen, U. Møller, I. Kubat, B. Zhou, S. Dupont, J. Ramsay, T. Benson, S. Sujecki, N. Abdel-Moneim, Z. Tang, D. Furniss, A. Seddon, and O. Bang, "Mid-infrared supercontinuum covering the 1.4–13.3 μm molecular fingerprint region using ultra-high na chalcogenide step-index fibre," Nat. Photonics **8**, 830–834 (2014).
24. K. Yin, B. Zhang, L. Yang, and J. Hou, "15.2 w spectrally flat all-fiber supercontinuum laser source with> 1 w power beyond 3.8 μm," Opt. Lett. **42**, 2334–2337 (2017).
25. C. Y. Wang, T. Herr, P. Del'Haye, A. Schliesser, J. Hofer, R. Holzwarth, T. Hänsch, N. Picqué, and T. J. Kippenberg, "Mid-infrared optical frequency combs at 2.5 μm based on crystalline microresonators," Nat. Commun. **4**, 1345 (2013).
26. P. Del'Haye, O. Arcizet, A. Schliesser, R. Holzwarth, and T. J. Kippenberg, "Full stabilization of a microresonator-based optical frequency comb," Phys. Rev. Lett. **101**, 053903 (2008).
27. A. G. Griffith, R. K. Lau, J. Cardenas, Y. Okawachi, A. Mohanty, R. Fain, Y. H. D. Lee, M. Yu, C. T. Phare, C. B. Poitras, A. L. Gaeta, and M. Lipson, "Silicon-chip mid-infrared frequency comb generation," Nat. Commun. **6**, 6299 (2015).
28. S. B. Papp, K. Beha, P. Del'Haye, F. Quinlan, H. Lee, K. J. Vahala, and S. A. Diddams, "Microresonator frequency comb optical clock," Optica. **1**, 10–14 (2014).
29. M. Nisoli, S. De Silvestri, and O. Svelto, "Generation of high energy 10 fs pulses by a new pulse compression technique," Appl. Phys. Lett. **68**, 2793–2795 (1996).
30. D. Faccio, A. Grün, P. K. Bates, O. Chalus, and J. Biegert, "Optical amplification in the near-infrared in gas-filled hollow-core fibers," Opt. Lett. **34**, 2918–2920 (2009).
31. J. Fatome, S. Pitois, and G. Millot, "20-ghz-to-1-thz repetition rate pulse sources based on multiple four-wave mixing in optical fibers," IEEE J. Quantum Electron. **42**, 1038–1046 (2006).
32. C. McKinstrie, S. Radic, M. Raymer, and L. Schenato, "Unimpaired phase-sensitive amplification by vector four-wave mixing near the zero-dispersion frequency," Opt. Express **15**, 2178–2189 (2007).
33. A. C. S Jr, J. C. Boggio, A. Rieznik, H. Hernandez-Figueroa, H. Fragnito, and J. Knight, "Highly efficient generation of broadband cascaded four-wave mixing products," Opt. Express **16**, 2816–2828 (2008).
34. T. T. Ng, J. L. Blows, J. T. Mok, R. W. McKerracher, and B. J. Eggleton, "Cascaded four-wave mixing in fiber optical parametric amplifiers: application to residual dispersion monitoring," J. Light. Technol. **23**, 818–826 (2005).
35. K. Inoue, "Tunable and selective wavelength conversion using fiber four-wave mixing with two pump lights," IEEE Photonics Technol. Lett. **6**, 1451–1453 (1994).
36. C. McKinstrie, J. Harvey, S. Radic, and M. Raymer, "Translation of quantum states by four-wave mixing in fibers," Opt. Express **13**, 9131–9142 (2005).
37. G. Agrawal, *Nonlinear Fiber Optics* (Academic Press, 2012).
38. B. W. Shore, *The Theory of Coherent Atomic Excitation* (Wiley, 1996).
39. T. Rickes, L. Yatsenko, S. Steuerwald, T. Halfmann, B. Shore, N. Vitanov, and K. Bergmann, "Efficient adiabatic population transfer by two-photon excitation assisted by a laser-induced stark shift," The J. Chem. Phys. **113**, 534–546 (2000).
40. H. Kogelnik, "Theory of dielectric waveguides," in *Integrated Optics,* T. Tamir, ed. (Springer Berlin Heidelberg, 1975), pp. 13–81.
41. R. W. Boyd, *Nonlinear optics* (Academic Press, 2003).
42. A. Levanon, A. Dahan, A. Nagler, E. Lifshitz, E. Bahar, M. Mrejen, and H. Suchowski, "Pulse shaping of broadband adiabatic shg from a ti-sapphire oscillator," Opt. Lett. **42**, 2992–2995 (2017).
43. J. B. Christensen, J. G. Koefoed, B. Bell, C. McKinstrie, and K. Rottwitt, "Shape-preserving and unidirectional frequency conversion by four-wave mixing," Opt. Express **26**, 17145–17157 (2018).

44. A. C. Turner, C. Manolatou, B. S. Schmidt, M. Lipson, M. A. Foster, J. E. Sharping, and A. L. Gaeta, "Tailored anomalous group-velocity dispersion in silicon channel waveguides," Opt. Express **14**, 4357–4362 (2006).

45. L. Tong, J. Lou, and E. Mazur, "Single-mode guiding properties of subwavelength-diameter silica and silicon wire waveguides," Opt. Express **12**, 1025–1035 (2004).

46. Y. Tang, L. G. Wright, K. Charan, T. Wang, C. Xu, and F. W. Wise, "Generation of intense 100 fs solitons tunable from 2 to 4.3 μm in fluoride fiber," Optica **3**, 948–951 (2016).

47. L. D. Landau, "Zur theorie der energieubertragung ii," Phys. Sov. Union **2**, 46–51 (1932).

48. C. Zener, "Non-adiabatic crossing of energy levels," Proc. Royal S. L. A **137**, 696–702 (1932).

49. A. M. Heidt, Z. Li, J. Sahu, P. C. Shardlow, M. Becker, M. Rothhardt, M. Ibsen, R. Phelan, B. Kelly, S. U. Alam, and D. J. Richardson, "100 kw peak power picosecond thulium-doped fiber amplifier system seeded by a gain-switched diode laser at 2 μm," Opt. Lett. **38**, 1615–1617 (2013).

50. G. Krauss, S. Lohss, T. Hanke, A. Sell, S. Eggert, R. Huber, and A. Leitenstorfer, "Synthesis of a single cycle of light with compact erbium-doped fibre technology," Nat. Photonics **4**, 33–36 (2010).

51. M. S. Habib, C. Markos, O. Bang, and M. Bache, "Soliton-plasma nonlinear dynamics in mid-ir gas-filled hollow-core fibers," Opt. Lett. **42**, 2232–2235 (2017).

52. T. Tanemura, C. S. Goh, K. Kikuchi, and S. Y. Set, "Highly efficient arbitrary wavelength conversion within entire c-band based on nondegenerate fiber four-wave mixing," IEEE Photonics Technol. Lett. **16**, 551–553 (2004).

53. H. McGuinness, M. Raymer, C. McKinstrie, and S. Radic, "Quantum frequency translation of single-photon states in a photonic crystal fiber," Phys. Rev. Lett. **105**, 093604 (2010).

54. Q. Li, M. Davanço, and K. Srinivasan, "Efficient and low-noise single-photon-level frequency conversion interfaces using silicon nanophotonics," Nat. Photonics **10**, 406–414 (2016).

55. S. Clemmen, A. Farsi, S. Ramelow, and A. L. Gaeta, "Ramsey interference with single photons," Phys. Rev. Lett. **117**, 223601 (2016).

56. S. Clemmen, A. Farsi, S. Ramelow, and A. L. Gaeta, "All-optically tunable buffer for single photons," Opt. Lett. **43**, 2138–2141 (2018).

57. C. Joshi, A. Farsi, S. Clemmen, S. Ramelow, and A. L. Gaeta, "Frequency multiplexing for quasi-deterministic heralded single-photon sources," Nat. Commun. **9**, 847 (2018).

1. Introduction

Efficient and robust frequency conversion of broadband optical pulses is essential for fields ranging from pure science to technology industries, including integrated photonics for telecommunications and the next generation of computers [1, 2], environmental detection devices [3], optical signal processing for applications such as encoding and encryption [4], as well as strong field applications such as X-ray generation and multidimensional spectroscopies for understanding the fundamental ultrafast dynamics of molecules [5, 6].

In recent years, much effort has been invested in developing schemes to efficiently convert broader and broader optical spectra. Yet the common paradigm of nonlinear frequency conversion with constant phase matching includes a restrictive trade-off between the conversion efficiency and its bandwidth. Our recent demonstrations of the adiabatic frequency conversion concept in three-wave mixing processes introduced the ability to sidestep the efficiency-bandwidth trade-off in sum-frequency generation (SFG) and difference-frequency generation (DFG) [7–10], dramatically increasing the available bandwidth while also ensuring a high conversion efficiency. Application of this concept in aperiodically poled quasi-phase-matched media allowed the generation of phase- and amplitude-controlled, octave-spanning, coherent mid-IR light sources [11, 12]. Moreover, the amplitude and phase transferability of adiabatic frequency conversion enables arbitrary amplitude and phase tunability by pulse shaping prior to conversion. This allowed the arbitrary shaping of single-cycle pulses and promises great flexibility for ultrafast spectroscopic applications [12]. Broadband optical parametric amplification (OPA) and optical parametric oscillation (OPO) have also been investigated to show greatly enhanced conversion efficiency in aperiodically poled quasi-phase-matched media and nonuniform media [13–18]. Though the adiabatic frequency conversion concept is very promising, the traditional platforms for frequency conversion using three-wave mixing processes are limited to devices based on specialized materials engineered and grown specifically for the application, whether for ultrashort pulses or for single-frequency sources.

In contrast, the ubiquitous presence of cubic optical nonlinearities enables all devices employing

light propagation the capacity for frequency conversion via four-wave mixing (FWM). Recent examples include optical parametric gain and frequency conversion in silicon waveguides used for telecommunications [1, 19–21], supercontinuum generation in optical fibers made from a wide range of materials and with a diverse set of structures [22–24], dielectric and semiconductor microresonators used for supercontinuum or frequency comb generation [25–28], and gas filled capillaries used for spectral broadening or parametric amplification of ultrashort pulses [29, 30]. In each of these technologies, FWM frequency conversion has been employed. Like all nonlinear frequency conversion methods, applications of FWM to the generation of broadband light sources are limited by a trade-off between efficiency and bandwidth. Furthermore, the commonly used technique for frequency conversion, cascaded FWM [31–34], does not allow flexible control of the spectral phase of the converted light.

Here, we introduce the concept of adiabatic frequency conversion in FWM, which we find broadly applicable to $\chi^{(3)}$ nonlinear platforms. We develop a theoretical framework for rapid adiabatic passage in FWM, analogous to the dynamics of quantum two-level systems. We show that a conversion efficiency asymptotically approaching 100% over broad bandwidth can be achieved if the adiabatic condition is met, overcoming the traditional efficiency-bandwidth trade-off in common FWM frequency conversion processes. As examples, we apply the theory to silicon photonics and step-index fibers, two of the $\chi^{(3)}$ nonlinear platforms most widely used in applications, using generalized pulsed beam propagation simulations. We find near-100% photon conversion efficiency can be achieved by a simple longitudinal tuning of waveguide dimensions, generating broad bandwidths in either near-IR or mid-IR wavelength ranges. We expect FWM frequency conversion in many other platforms and at many other wavelengths would benefit from this process in a similar fashion.

The article is organized as follows. In Section 2, we present the SU(2) symmetry present in FWM frequency conversion under the strong pump approximation, which illuminates the similarity of photon conversion in FWM to population exchange in two-level systems. We then discuss the conditions for achieving rapid adiabatic passage in FWM. Compared to adiabatic evolution in $\chi^{(2)}$ media, several new characteristics are observed. In Section 3, we present generalized propagation equations for FWM derived from Maxwell's equations. We develop numerical methods capturing the full frequency- and time-domain nonlinear pulse propagation effects for waveguided interactions, including exact broadband dispersion, self- and cross-phase modulation, and the FWM process used for adiabatic frequency conversion. We focus on particular features of broadband pulse propagation in waveguided media that may be essential for a given application of adiabatic four wave mixing (AFWM), such as the evaluation of accurate relative strengths of nonlinear effects over a large frequency range as well as the capture of additional parasitic degenerate and non-degenerate FWM processes.

In Section 4, we numerically solve the generalized equations in order to explore silicon photonic devices and optical fiber platforms for realizing AFWM. For silicon photonic devices, we show generation of a 70-nm bandwidth centered at 1820 nm with a photon conversion efficiency greater than 90%. Our solution, which does not require a strong pump condition, is the first solution that allows such wide spectral widths with high conversion efficiency. For step-index fibers, we present the optimal fiber parameters for phase matching AFWM frequency conversion. By modeling a tapered commercially available fluoride step-index fiber, we predict that nanojoule energy, 4.2-5.2 μm broadband mid-IR pulses could be realized by an all-fiber based system, being among the most energetic mid-IR fiber sources in this spectral range. Because the AFWM mechanism is fundamental, we believe our findings will open new routes for achieving energetic and broadband generation over large frequency ranges where other methods suffer from either low spectral power or narrow bandwidth due to the efficiency-bandwidth trade-off, such as frequency conversion in on-chip photonic devices for telecom and innovative computers, as well as fiber-based down-conversion (mid-IR) and up-conversion (UV) sources for high-repetition-rate

spectroscopy or low-repetition-rate high-intensity applications.

2. Concepts and theory

We begin by introducing the concept of AFWM underlying the new broadband and efficient FWM frequency conversion paradigm. To establish an intuitive physical picture, we make an analogy between FWM frequency conversion and coupled two-level systems through demonstration of SU(2) symmetry present in FWM processes under the strong pump approximation. We then establish the adiabatic condition for achieving AFWM. In the following sections, we will explore the more general nonlinear dynamics of broadband pulsed waves in a waveguided geometry.

2.1. Analogy to population transfer in a two-level system possessing SU(2) symmetry

As in three-wave mixing processes [7], under certain conditions photon transfer in a FWM process can be understood by analogy to population transfer in a two-level quantum atom possessing SU(2) symmetry. These are the conditions under which a fully adiabatic, one-to-one transfer of photons between frequencies becomes possible. Consider FWM in a $\chi^{(3)}$ nonlinear medium by the schemes shown in Fig. 1(a), commonly known as four-wave mixing Bragg scattering (FWM-BS) [35, 36], and Fig. 1(b), with initial photon numbers n_A, n_B, n_{Sig}, and n_{Idl}, for $Pump_A$, $Pump_B$, Signal, and Idler waves, respectively. When satisfying the conditions $n_A, n_B \gg n_{Sig}, n_{Idl}$ under either scheme, an exchange of n photons will leave the four waves with approximate photon numbers n_A, n_B, $n_{Sig} - n$, and $n_{Idl} + n$. An exchange of photons between four waves is thus approximately reduced to a one-to-one photon number transfer between the signal and idler waves, resembling population exchange in a two-level system. Experimentally, these conditions can be met if the intensities of the two pumps are assumed to be much stronger than those of the signal and idler waves.
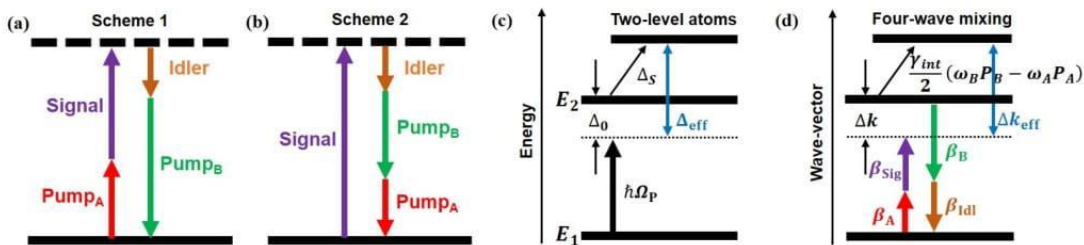
Fig. 1. Energy diagrams of two schemes of four-wave mixing, and the analogy between two-level atoms and FWM. **(a)** Annihilation of *Signal* and *Pump A* photons allows creation of *Idler* and *Pump B* photons. This scheme is known as four-wave mixing Bragg scattering. **(b)** Annihilation of a *Signal* photon allows creation of *Pump A*, *Pump B*, and *Idler* photons. In both cases, when pump intensities are much larger than those of the signal and idler, signal and idler photons are exchanged through coupled equations of motion possessing SU(2) symmetry, analogously to population transfer in coupled two-level quantum systems. **(c),(d)** Analogy between Stark-chirped two-level atomic systems with field-free energies E_1, E_2 and four-wave mixing. $\hbar\Omega_P$ is the coupling pump's photon energy in two-level atomic systems. $\beta'_i s$ (i = A,B,Sig,Idl) are wave-vectors of the four waves in FWM. Energy detuning Δ_0 corresponds to phase mismatch Δk, while Stark-induced energy shift Δ_S corresponds to Kerr-induced nonlinear phase modulation $\frac{\epsilon_0 \chi^{(3)} \gamma_{int}}{2} (\omega_B P_B - \omega_A P_A)$. The effective energy detuning Δ_{eff} is analogous to effective phase mismatch Δk_{eff}.

To mathematically demonstrate the concept, we start with simplified nonlinear Schrödinger equations under strong pump and plane, continuous wave (cw) approximations:

$$i\frac{dA_A}{dz} = \omega_A \epsilon_0 \chi^{(3)} \left(\frac{\mu_{A,A}}{2}|A_A|^2 + \mu_{A,B}|A_B|^2 \right) A_A,$$

$$i\frac{dA_B}{dz} = \omega_B \epsilon_0 \chi^{(3)} \left(\mu_{A,B}|A_A|^2 + \frac{\mu_{B,B}}{2}|A_B|^2 \right) A_B,$$

(1)

$$i\frac{dA_{Sig}}{dz} = \omega_{Sig}\epsilon_0\chi^{(3)}\left[\left(\mu_{Sig,A}|A_A|^2 + \mu_{Sig,B}|A_B|^2\right)A_{Sig} + \gamma_{int}A_A^\dagger A_B A_{Idl}e^{i\Delta kz}\right],$$

$$i\frac{dA_{Idl}}{dz} = \omega_{Idl}\epsilon_0\chi^{(3)}\left[\left(\mu_{Idl,A}|A_A|^2 + \mu_{Idl,B}|A_B|^2\right)A_{Idl} + \gamma_{int}A_A A_B^\dagger A_{Sig}e^{-i\Delta kz}\right].$$

(2)

The waves are assumed to be linearly polarized and copolarized. The superscript † denotes a complex conjugate, A_i is the electric field envelope and $\mu_{i,j}$ (with i, j = A,B, Sig, Idl) and γ_{int} are nonlinear coupling coefficients for the two non-degenerate pumps (A,B), signal (Sig), and idler (Idl) waves [37]. The field envelopes are defined by $E_i = A_i e^{i(\omega t - \beta z)}$, where E_i are electric fields of the mixing waves normalized to their power P_i such that, $P_i = |E_i|^2 = |A_i|^2$, for i = A,B. For the sake of analytical simplicity, the transverse field distribution has been taken as wavelength-independent and ignored in this section under the plane wave approximation. $\Delta k = \beta_A + \beta_{Sig} - \beta_B - \beta_{Idl}$ is the wave-vector mismatch arising from dispersion of the propagation constants of the waveguided $\chi^{(3)}$ nonlinear medium. Under the undepleted pump approximation, the pump magnitudes are approximately constant, and their envelopes acquire only phase modulations due to self- and cross-phase modulation (SPM, XPM) during propagation, and thus their powers, P_i, remain constant. The phases of Pump A and Pump B are modulated by $\omega_A \epsilon_0 \chi^{(3)} \left(\frac{\mu_{A,A}}{2} P_A + \mu_{A,B} P_B \right)$ and $\omega_B \epsilon_0 \chi^{(3)} \left(\mu_{B,A} P_A + \frac{\mu_{B,B}}{2} P_B \right)$, accordingly. SPM and XPM between signal and idler waves are ignored due to their small amplitudes compared to the pumps. However, the signal and idler waves experience XPM from the pump waves, $\omega_{Sig}\epsilon_0\chi^{(3)} \left(\mu_{Sig,A} P_A + \mu_{Sig,B} P_B \right)$ and $\omega_{Idl}\epsilon_0\chi^{(3)} \left(\mu_{Idl,A} P_A + \mu_{Idl,B} P_B \right)$, as well as a mutual power transfer. By further approximating the nonlinear coupling coefficient to be wavelength-independent, i.e. $\mu_{i,j} = \gamma_{int}$, and introducing normalized amplitudes $C_{Sig} = \frac{A_{Sig}\exp\left(i\frac{1}{2}\left(-\Delta k + \epsilon_0\chi^{(3)}\gamma_{int}\left(2\omega_{Sig}(P_A+P_B)+\frac{1}{2}(\omega_A P_A - \omega_B P_B)\right)\right)z\right)}{\sqrt{\omega_{Sig}\epsilon_0\chi^{(3)}\gamma_{int}|A_A||A_B|}}$

and $C_{Idl} = \frac{A_{Idl}\exp\left(i\frac{1}{2}\left(\Delta k + \epsilon_0\chi^{(3)}\gamma_{int}\left(2\omega_{Idl}(P_A+P_B)-\frac{1}{2}(\omega_A P_A - \omega_B P_B)\right)\right)z\right)}{\sqrt{\omega_{Idl}\epsilon_0\chi^{(3)}\gamma_{int}|A_A||A_B|}}$, the coupled amplitude equations (CAEs) for the signal and idler waves (2) can be rearranged into the form:

$$i\frac{dC_{Sig}(z)}{dz} = \frac{\Delta k_{eff}}{2} \cdot C_{Sig}(z) + \frac{\kappa}{2} \cdot C_{Idl}(z),$$

(3)

$$i\frac{dC_{Idl}(z)}{dz} = \frac{\kappa}{2} \cdot C_{Sig}(z) - \frac{\Delta k_{eff}}{2} \cdot C_{Idl}(z),$$

(4)

where the effective wave-vector mismatch is $\Delta k_{eff} = \Delta k + \frac{\epsilon_0\chi^{(3)}\gamma_{int}}{2}(\omega_B P_B - \omega_A P_A)$ and the coupling strength between the two waves is $\kappa = 2\epsilon_0\chi^{(3)}\sqrt{\omega_{Sig}\omega_{Idl}\gamma_{int}^2 P_A P_B}$. This set of CAEs describing the wave mixing resembles the form of the SU(2) symmetric time-dependent Schrödinger equations of a coupled two-state atom except that time evolution in the quantum model has now become z propagation in the $\chi^{(3)}$ nonlinear medium. Whereas in an optically driven two-level atom, an effective energy detuning of the driving laser frequency from resonance, Δ_{eff}, is a sum of the detuning in the coupled two-level system, $\Delta_0 = E_2 - E_1 - \hbar\Omega_P$, and a field-induced Stark shift, Δ_s, the quantity analogous to the effective detuning for an exchange of the signal and idler wave amplitudes is an effective wave-vector mismatch, Δk_{eff}, which is a sum of the intrinsic wave-vector mismatch (i.e., when phase modulations are ignored), $\Delta k = \beta_{Sig} + \beta_A - \beta_{Idl} - \beta_B$, and XPM-induced phase modulations $\frac{\epsilon_0\chi^{(3)}\gamma_{int}}{2}(\omega_B P_B - \omega_A P_A)$ that

become important at high pump intensities. The coupling strength between the signal and idler states, κ, analogous to the interaction strength in two-level systems, depends on both the signal and idler's angular frequencies $\omega_{\mathrm{Sig}}, \omega_{\mathrm{Idl}}$, nonlinear coupling coefficient γ_{int} and the two pump intensities P_A, P_B. The analogous quantities are summarized in Table 1 and are depicted in Figs. 1(c)–1(d).

Table 1. **Analogy of FWM to a coupled 2-level atom**

Parameter	2-level atom	Four-wave mixing
Evolution parameters	time	z axis
Frequency detuning / Phase mismatch	Δ_0	Δk
Stark shift	Δ_S	$\frac{\epsilon_0 \chi^{(3)} \gamma_{int}}{2} (\omega_B P_B - \omega_A P_A)$
Coupling coefficient	Ω_R	$\kappa = 2\epsilon_0 \chi^{(3)} \sqrt{\omega_{\mathrm{Sig}} \omega_{\mathrm{Idl}} \gamma_{int}^2 P_A P_B}$
Generalized "Rabi" frequency	Ω	$\sqrt{\kappa^2 + \Delta k_{\mathrm{eff}}^2}$

2.2. Adiabatic passage

Having identified a close analogy, the evolution dynamics of FWM under the undepleted pump approximation and with a photon exchange as drawn in Figs. 1(a)–1(b) can be expected to follow the known dynamics of SU(2) symmetric coupled two-level atomic systems. The simplest analogy is the case of constant Δk_{eff}, in which the difference between signal and idler photon numbers oscillates at the (spatial) Rabi frequency, $\Omega = \sqrt{\kappa^2 + \Delta k_{\mathrm{eff}}^2}$. As is the case in experimental atomic physics, Rabi flopping can be used to achieve a complete population inversion (in this case meaning all signal photons are converted to idler photons, or vice-versa, depending on which field has a nonzero initial amplitude), but only if the coupling lasts for exactly one-half of a Rabi oscillation ($z = \pi/\Omega$) and the detuning (Δk_{eff}) is zero. Thus, the final population is highly sensitive to the experimental parameters and is wavelength dependent. This solution is characterized by the well known efficiency-bandwidth trade-off: if the experiment is tuned perfectly for one signal-idler wavelength pair, i.e., $\Delta k_{\mathrm{eff}} = 0$ and the medium length $L = \pi/\Omega$, it will be improperly tuned for other signal-idler wavelength pairs, since Δk_{eff} is wavelength dependent. Broadband conversion is only achieved in the low conversion efficiency limit, i.e., when $L \ll \pi/\Omega$.

A second example is rapid adiabatic passage (RAP), which can be used to asymptotically achieve 100% population transfer from an initial state to a target state through a slowly swept energy detuning. Since the CAEs of our FWM model shares the same mathematical form as a two-level atomic system, RAP should also exist in FWM: if the effective wave-vector mismatch is swept from large positive value to large negative value (or vice-versa) adiabatically, the signal wave (initial state) shall fully convert to the idler wave (target state) without back-conversion. It can be shown that for our CAEs (3) and (4), the condition required for adiabatic following in AFWM is [38]:

$$|\dot{\kappa}\Delta k_{\mathrm{eff}} - \kappa \Delta \dot{k}_{\mathrm{eff}}| \ll \left(\kappa^2 + \Delta k_{\mathrm{eff}}^2\right)^{\frac{3}{2}}, \tag{5}$$

where the derivatives are with respect to propagation distance, z. Additionally, to ensure a robust adiabatic conversion, $|\Delta k_{\mathrm{eff}}| \gg \kappa$ is required at both the beginning and end of the photon exchange, i.e., the coupling between waves at the entrance and exit of the medium should be insignificant.

Nearly 100% photon conversion efficiency is expected to be achieved between signal and idler waves through AFWM if the adiabatic condition (5) is fulfilled, as has been demonstrated in $\chi^{(2)}$ nonlinear media using a swept wave-vector mismatch created by aperiodically poled

gratings [10, 11]. Moreover, a RAP-like frequency transfer can occur for each frequency within a broadband signal pulse in a single nonlinear medium [8, 9], and greater than octave-spanning bandwidths have been achieved through adiabatic three-wave mixing [11, 12]. The process is also expected to exhibit a linear transfer function of spectral phase and amplitude if the pump pulses have a relatively narrow bandwidth compared to the signal and idler pulses, as has also been demonstrated for RAP in three-wave mixing [12], offering a simple route towards arbitrary pulse shaping of the generated idler through pre-conversion amplitude and phase shaping of the signal.

We note that the distinguishing features of the driven two-level system analogy for FWM versus three-wave mixing include: first, that two nondegenerate pump waves are required to achieve SU(2) symmetric frequency conversion between signal and idler waves rather than one pump wave, and second, that the effective wave-vector mismatch Δk_{eff} is not only dependent on propagation constants β_i, but also on Kerr-induced nonlinear phase modulations $\frac{\epsilon_0 \chi^{(3)} \gamma_{int}}{2} (\omega_{\text{B}} P_{\text{B}} - \omega_{\text{A}} P_{\text{A}})$. These features allow a wide range of possible implementations of RAP that are unique to the FWM system, including the possibility of a swept effective wave-vector mismatch derived from longitudinally increasing or decreasing phase modulations imparted by the two non-degenerate pumps (achieved through group-velocity walk-off, for example), an analogy of Stark-chirped rapid adiabatic passage [39]. In the case that a waveguided structure is used for the FWM interaction, RAP can be achieved through a longitudinal sweep of the waveguide dispersion, or by width modulation of the waveguide core. Two examples of waveguide-enabled AFWM are presented in Section 4.

3. Generalized propagation model

Here we develop a generalized analytical framework for rigorous numerical treatment of FWM processes that captures arbitrary time-dependent ultrashort pulses propagating in longitudinally-variant waveguides of a $\chi^{(3)}$ nonlinear medium. The analysis is suitable for arbitrary mode profiles and arbitrary waveguide geometries or material assuming the waveguide modes have negligible components in the direction of propagation. In Section 4, we apply the generalized framework to treat the AFWM frequency conversion scheme. Let us start with the nonlinear dynamical equations for propagation of an optical pulse in a waveguided system [37, 40],

$$\frac{dA(z,\omega)}{dz} = -i\omega \int \int \bar{P}_{NL}(x,y,\omega) \cdot \left(\vec{E}_{0t}^{\,\dagger} e^{i\beta(z,\omega)z} \right) dx dy, \qquad (6)$$

where $\bar{P}_{NL}$ is the nonlinear polarization, the subscript $()_t$ stands for the transverse electric field, $()_{0t}$ refers to the transverse mode of the electric field profile of the waveguide, $\beta(z,\omega)$ is the propagation constant inside the waveguide, and $A(z,\omega)$ is the field amplitude spectral density for the transverse electric field, which is related to the electric field in time and space through an inverse Fourier transform:
$$\vec{E}_t(x,y,z,t) = \int_{-\infty}^{\infty} \frac{d\omega}{2\pi} \frac{1}{2} \overbrace{\left[A(z,\omega) + A^{\dagger}(z,-\omega) \right] \vec{E}_{0t}(x,y,z,\omega) e^{-i\beta(z,\omega)z}}^{\equiv \bar{E}_t(x,y,z,\omega)} e^{i\omega t}.$$
In the case of centrosymmetric material, where the dependence of the nonlinearity on frequency is weak, the 3rd-order nonlinear coefficient tensor is $\chi^{(3)} = \chi^{(3)}_{xxxx} = \chi^{(3)}_{yyyy} = \frac{\chi^{(3)}_{\{yyxx\}}}{3}$, where the $_{\{\}}$ stands for all permutations [41], and the nonlinear polarization takes the form $\bar{P}_{NL,k} = \epsilon_0 \chi^{(3)} \sum_{j \in x,y} \bar{E}_j(x,y,z,\omega) * \bar{E}_j(x,y,z,\omega) * \bar{E}_k(x,y,z,\omega)$, where $*$ stands for the convolution product. This yields the equation

$$\frac{dA(z,\omega)}{dz} = -i\omega \chi^{(3)} e^{i\beta(z,\omega)z} \iint \sum_{k \in x,y} \bar{P}_{NL,k} \cdot \left(\vec{E}_{0t,k}(x,y,z,\omega)^{\dagger} \right) dx dy. \qquad (7)$$

In this article, we focus our investigation on FWM Scheme 1 from Fig. 1(a) with non-degenerate pump wavelengths. We wish to obtain a set of equations for describing the scheme, as in Eq.(1),(2), where the field amplitude spectral density now takes the form of an optical pulse. The spectral density is $A(z, \omega) = A_A(z, \omega) + A_B(z, \omega) + A_{Sig}(z, \omega) + A_{Idl}(z, \omega)$, where the $A_i(z, \omega)$ are the envelopes for field components centered around carrier frequency ω_i. We choose to ignore the polarization component corresponding to third-harmonic generation, due to the large phase mismatch of the process in our investigated platforms. We also ignore attenuation because of the short lengths of the platforms.

We first discuss implementations where non-overlapping spectral components among four waves can be approximated. By further approximating the transverse modes of the electric field profiles to those at their central wavelengths, Eq. (7) yields a set of four nonlinear coupled equations. For example, for the signal wave we obtain,

$$
\frac{dA_{Sig}(z, \omega)}{dz} = -i\omega\epsilon_0 \chi^{(3)} e^{i\beta_{Sig}(\omega)z} \times
$$

$$
\Big[\gamma_{int} A_B(\omega) e^{-i\beta_B(\omega)z} * A_{Idl}(\omega) e^{-i\beta_{Idl}(\omega)z} * A_A^\dagger(-\omega) e^{-i\beta_A(\omega)z} +
$$

$$
\frac{\mu_{Sig,Sig}}{2} A_{Sig}(\omega) e^{-i\beta_{Sig}(\omega)z} * A_{Sig}^\dagger(-\omega) e^{i\beta_{Sig}(\omega)z} * A_{Sig}(\omega) e^{-i\beta_{Sig}(\omega)z} +
$$

$$
\mu_{Sig,Idl} A_{Idl}(\omega) e^{-i\beta_{Idl}(\omega)z} * A_{Idl}^\dagger(-\omega) e^{i\beta_{Idl}(\omega)z} * A_{Sig}(\omega) e^{-i\beta_{Sig}(\omega)z} + \qquad (8)
$$

$$
\mu_{Sig,A} A_A(\omega) e^{-i\beta_A(\omega)z} * A_A^\dagger(-\omega) e^{i\beta_A(\omega)z} * A_{Sig}(\omega) e^{-i\beta_{Sig}(\omega)z} +
$$

$$
\mu_{Sig,B} A_B(\omega) e^{-i\beta_B(\omega)z} * A_B^\dagger(-\omega) e^{i\beta_B(\omega)z} * A_{Sig}(\omega) e^{-i\beta_{Sig}(\omega)z} \Big].
$$

The z-dependence of A_i and β_i (i = A,B,Sig,Idl) was dropped from the notation for clarity (e.g., $A(\omega) = A(z, \omega)$), and we defined the following overlap integrals of the electric field transverse profiles: $\gamma_{int} = \frac{1}{2} \iint dxdy \Big[(\vec{E}_B \cdot \vec{E}_{Idl})(\vec{E}_A \cdot \vec{E}_{Sig}) + (\vec{E}_B \cdot \vec{E}_A)(\vec{E}_{Idl} \cdot \vec{E}_{Sig}) + (\vec{E}_{Idl} \cdot \vec{E}_A)(\vec{E}_B \cdot \vec{E}_{Sig}) \Big]$ and $\mu_{i,j} = \frac{1}{2} \iint dxdy \left(|\vec{E}_i|^2 |\vec{E}_j|^2 + 2|\vec{E}_i \cdot \vec{E}_j|^2 \right)$. These overlap integrals are evaluated at the center wavelengths of each mixing wave. Due to the convolution product naturally appearing in these equations, it is more natural to introduce them in the time domain [42]. We define $B_i(z, \omega) = A_i(z, \omega) e^{-i\beta_i(z, \omega)z}$, and deduce a time-domain version of the four nonlinear coupled equations. For example, the equation for $B_{Sig}(z, t)$ is,

$$
i\frac{dB_{Sig}(z, t)}{dz} =
$$

$$
+ \mathcal{F}^{-1}\Big[\beta_{Sig}(z, \omega) B_{Sig}(z, \omega) \Big] \leftarrow \text{Dispersion}
$$

$$
+ \varepsilon_0 \chi^{(3)} \mathcal{F}^{-1}\Big[\omega\mathcal{F}\Big[\gamma_{int} B_B(z, t) B_{Idl}(z, t) B_A^\dagger(z, t) \Big] \Big] \leftarrow \text{FWM} \qquad (9)
$$

$$
+ \varepsilon_0 \chi^{(3)} \mathcal{F}^{-1}\Big[\omega\mathcal{F}\Big[\sum_{\nu \in A,B,Idl} \mu_{Sig,\nu} |B_\nu(z, t)|^2 B_{Sig}(z, t) \Big] \Big] \leftarrow \text{XPM}
$$

$$
+ \varepsilon_0 \chi^{(3)} \mathcal{F}^{-1}\Big[\omega\mathcal{F}\Big[\frac{\mu_{Sig,Sig}}{2} |B_{Sig}(z, t)|^2 B_{Sig}(z, t) \Big] \Big] \leftarrow \text{SPM,}
$$

where $\mathcal{F}$ is the Fourier transform operator. The first term can be understood as the dispersion dynamics, second term is the exchange of energy between the four waves, and the third and fourth terms are the cross- and self-phase modulations, respectively. Cast in this way, the γ_{int} and $\mu_{i,j}$ overlap factors can be understood as the frequency dependent nonlinear coupling coefficients, which enables accurate evaluation of nonlinear frequency conversion strength in FWM. Eq. (9) mimics the traditional form of FWM processes by capturing phase-matched

3rd-order nonlinearities [37], i.e., those that are automatically phase matched (namely SPM and XPM), as well as non-degenerate FWM, which will be arranged to be phase matched in the applications of AFWM investigated below. However, Eq. (9) has improvements over the traditional form by capturing exact dispersion and self-steepening effect through the use of the Fourier transform operator rather than Taylor expansions. Under the above approximations, this is the general form of a FWM process depicted by Fig. 1(a), Scheme 1.

To consider implementations where the four waves do have overlapping spectral components, such as in the case of supercontinuum generation, or, as in our work, near-octave-spanning bandwidth generated by AFWM in optical fibers, we follow the same Fourier transform steps from Eq. (7) to Eq. (9), but maintain a single pulse simulation without splitting the spectral density or temporal envelope into four fields. To guarantee generality in optical fibers, we also include Stimulated Raman Scattering (SRS) and spontaneous emission. This results in a supercontinuum-like $(1 + 1)$-D generalized nonlinear Schrödinger equation (GNLSE):

$$
i\frac{dB(z,t)}{dz} = \mathcal{F}^{-1}\left(\beta(z,\omega)B(z,\omega)\right) + \varepsilon_0\chi^{(3)}\cdot
$$
$$
\mathcal{F}^{-1}\left(\omega \cdot \gamma_{int} \cdot \mathcal{F}\left\{(1-f_R)\left|B(z,t)\right|^2 \cdot B(z,t) + f_R B(z,t) \cdot \int_0^\infty h_R(t')|B(z,t-t')|^2 dt'\right\}\right),
$$
(10)

where $B(z,t)$ is a single-field envelope with a frequency grid covering all four mixing waves. $B(0,t) = A_A(0,t)e^{i(\omega_A-\omega_0)t} + A_B(0,t)e^{i(\omega_B-\omega_0)t} + A_{Sig}(0,t)e^{i(\omega_{Sig}-\omega_0)t}$ is the sum of all input field envelopes, where ω_0 is the carrier frequency of the single-field envelope and here is chosen to be the center frequency of the frequency grid. A one-photon-per-mode noise seed with random phase is superimposed onto each spectral point in the frequency grid to simulate vacuum noise. The propagation constant $\beta(z,\omega)$ is numerically solved at each z-step for each frequency grid point, given the fiber geometry and material properties at the position. Thus, although Eq. (10) mimics the traditional form of GNLSE in treating supercontinuum generation [37], it has the advantage over the traditional form in that the chromatic dispersion term (first term on the right-hand side (RHS)) captures exact dispersion across the simulated frequency grid without making the Taylor series approximation. Moreover, due to the wide simulated spectral bandwidth, we use the frequency dependent nonlinear coefficient $\omega \cdot \gamma_{int}$ to account for the self-steepening effect. The dispersion of $\chi^{(3)}$ is ignored.

As opposed to the coupled-field model above, the single-field model captures all possible FWM terms involving two created photons and two annihilated photons through the second term on the RHS. This includes not only the desired FWM-BS of Scheme 1 $(\omega_A + \omega_{Sig} = \omega_B + \omega_{Idl})$ and SPM/XPM $(\omega_i + \omega_j = \omega_i + \omega_j)$, but also, when combined with the vacuum noise seed, it captures unintended parametric FWM interactions, such as other FWM-BS processes, modulation instability and parametric amplification by degenerate and non-degenerate FWM, which can produce both new and overlapping Fourier components. Only third harmonic generation and other $3 \to 1$ and $1 \to 3$ photon interactions (Scheme 2) are excluded, which are expected to be minimal due to large wave-vector mismatch. However, in this model, the overlap factor γ_{int} must be treated as a constant across the frequency grid of the simulation to ensure conservation of photon number. Thus, while the model can capture all relevant parasitic processes, it cannot handle any differences in their relative strength that are due to the dispersion of the overlap factor. The last term on the RHS represents SRS, which is described by the convolution integral between the Raman response function $h_R(t)$ and the total intensity of the field. f_R represents the delayed Raman response's fractional contribution to nonlinear polarization.

In Section 4.1, Eq. (9) and the corresponding equations for the other three field components are numerically solved to capture the complex propagation dynamics of AFWM in a structured silicon photonics waveguide, where broad but non-overlapping pulse bandwidths and a highly modulated, longitudinally varying waveguide structure are employed. The inclusion of an overlap integral for
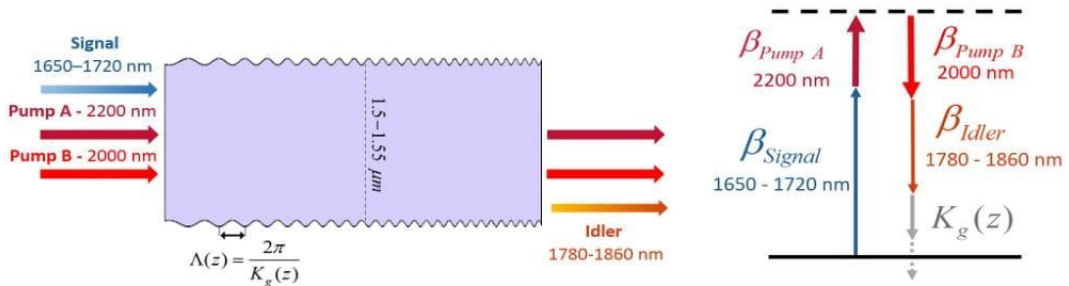
Fig. 2. Adiabatic frequency conversion in silicon photonics. (Left) The scheme allows an efficient broadband conversion of signal to idler waves (or vice-versa) by adiabatically changing the wave-vector mismatch through a chirped modulation of the width along the propagation direction. (Right) Momentum matching diagram (see Fig. 1(d)) illustrating the use of a variable effective momentum, $K_g(z)$, to longitudinally sweep the wave-vector mismatch. We have shown a near 100% conversion efficiency of an incoming signal spanning from 1.65-1.72 μm to an idler spanning from 1.78-1.86 μm.

each type of wave-mixing process allows accurate capture of their relative nonlinear coupling strengths. In Section 4.2, to capture AFWM in tapered optical fibers where the conversion bandwidth is nearly octave spanning, we find it is necessary to employ a single-field numerical framework using Eq. (10) to allow for capture of parasitic and unintended phase-matched FWM processes. Simulations for both platforms are described in the next section.

4. Potential platforms and simulations

In this section, we employ numerical investigations of broadband pulse propagation to illustrate how AFWM can be achieved in both silicon photonics structures and optical fibers, which are two platforms with broad interest to science and technology. For illustration of the AFWM concept, we choose to investigate broadband down-conversion as the application, and find conditions for efficient conversion in both platforms. We assume a fundamental mode evolution along the optical waveguides.

Eq. (5) suggests that AFWM can be achieved by longitudinal variation of either the effective wave-vector mismatch, Δk_{eff}, or the coupling strength, κ. Here, we explore straightforward control of the adiabatic condition through the waveguide geometry, which presents a controllable knob for tuning the propagation constants through waveguide dispersion and for tuning the overlap factors. Thus, in the following examples, we explore the use of longitudinal variations to the waveguide geometry to achieve the adiabatic condition of Eq. (5). Two distinct approaches are investigated. In the case of silicon waveguides, an aperiodic quasi-phase matching (QPM) approach is employed, utilizing cyclic modulations of the waveguide width to modulate the nonlinear coupling coefficients. This gives rise to a longitudinally varying effective momentum that can be used to offset the wave-vector mismatch. In the case of optical fibers, a linear variation of fiber core diameter is used to achieve a monotonic longitudinal sweep of Δk_{eff} through its effect on the waveguide dispersion.

4.1. AFWM in silicon photonics devices

Thanks to recent technological advances, control of the wave-vector mismatch parameter for realizing AFWM in silicon photonics might be achieved by several methods. One approach is to longitudinally sweep the width of the waveguide from one end to the other, thereby producing an adiabatic sweep of Δk_{eff} from a large positive value to a large negative one (or vice versa) through the contribution of the waveguide dispersion to the effective refractive index of the material. A second approach would be to apply a small periodic change in waveguide width

with a longitudinal chirp to the period (as illustrated in Fig. 2). This approach adds an effective momentum, $K_g(z) = 2\pi/\Lambda(z)$, to the effective wave-vector mismatch, Δk_{eff}, derived from the resulting modulation of the nonlinear coupling coefficient. Thus, the period of width modulations, $\Lambda(z)$, can serve as a highly tunable knob for controlling wave-vector mismatch. We define a wave-vector mismatch of the modulated process, $\Delta k_{\text{mod}}(z) = \Delta k_{\text{eff}}(z) + K_g(z)$. In this expression, we have explicitly included the longitudinal variation of Δk_{eff}, which is due to the cyclic variation in waveguide dispersion also arising from the modulation in width. As discussed below, the waveguided structure is designed to ensure that this variation has a negligible magnitude compared to the longitudinal sweep of Δk_{mod} imparted by $K_g(z)$.

Our numerical simulations are of Eq. (9) with no further approximations. However, in order to gain intuition regarding the physical mechanism prominent in the adiabatic width modulation scheme, the effective momentum from the QPM process can be derived in the following way. Assume the FWM has a periodically varying nonlinear coupling coefficient in the longitudinal direction: $\gamma_{int} = \gamma_{avg} \left[1 + s \cdot \cos \left(K_g(z) \cdot z \right) \right], s < 1$. This represents the nonlinear coupling coefficient of a silicon waveguide with width modulation period $\Lambda(z)$. γ_{avg} is the average nonlinear coupling coefficient, while s is half the maximum difference in coupling strength due to the width modulation. Rewriting the cosine in terms of two exponents, $2 \cdot \cos \left(K_g(z) \cdot z \right) = \exp \left(i K_g(z) \cdot z \right) + \exp \left(-i K_g(z) \cdot z \right)$, will result in three terms, the unmodulated average term, and the two modulated terms contributing momenta $\pm K_g(z)$. The second term only further increases the wave-vector mismatch and thus plays an insignificant role for the intended FWM process. The first term, however, reduces the wave-vector mismatch for the intended process and offers a controllable wave-vector mismatch offset. The overall wave-vector mismatch of the modulated process reduces to $\Delta k_{\text{mod}}(z) = \Delta k_{\text{eff}}(z) + K_g(z), K_g(z) = 2\pi/\Lambda(z)$, which enables the possibility of tuning the $\Delta k_{\text{mod}}(z)$ by scanning the effective momentum $K_g(z)$. This can be achieved by longitudinally chirping the waveguide width modulation period $\Lambda(z)$.

Our numerical simulations were based on the 4th-order Runge-Kutte method. Conversion efficiency was evaluated by the photon conversion ratio (PCR) parameter, defined as:

$$\text{PCR} = \frac{\text{idler final spectral density}}{\text{signal input spectral density}} \times \frac{\omega_{\text{Sig}}}{\omega_{\text{Idl}}}, \tag{11}$$

where ω_{Idl} and ω_{Sig} are the frequencies of each signal-idler pair. This definition is inherently normalized such that complete conversion of signal to idler without parasitic effects corresponds to a PCR of 1. We compare the performance of an adiabatic structure with chirped $\Lambda(z)$ to a standard QPM approach of using a constant-valued $\Lambda(z)$ chosen to phase match the carrier frequency. We find that the adiabatic structure results in a PCR that is larger than 0.9 for a broad range of frequencies, while the PCR of the standard QPM approach does not converge due to non-uniform conversion-back-conversion dynamics during propagation.

In the framework of a silicon waveguide compatible for an on-chip device, the minimum and maximum widths of the waveguide are set as restrictions. We simulated a Si rectangular waveguide with a tunable width restricted to the range 1.5-1.55 μm and with a constant height of 380 nm. Under these width restrictions, a monotonic sweep of the width of the waveguide would not yield the desired crossing of zero phase mismatch, and therefore the periodicity of a cyclic width variation is used as the knob for tuning the total modulated wave-vector mismatch, Δk_{mod}, along the waveguide. To realize efficient energy transfer, Δk_{mod} is varied longitudinally while fulfilling the condition presented in Eq. (5) (substituting Δk_{mod} for Δk_{eff}), by varying $1/\Lambda(z)$ from 2/mm to 20/mm. We choose to demonstrate this method by converting a signal ranging in wavelength from 1650-1720 nm to an idler of 1780-1860 nm. As another design consideration, in general one must be careful not to use a range of waveguide widths so large as to phase match unintended (parasitic) frequency conversion processes (as investigated in [43], for example). This can be avoided by setting the waveguide's length and modulation limits to be suitable for only the intended process. In the presented simulation of the silicon photonic waveguide, the
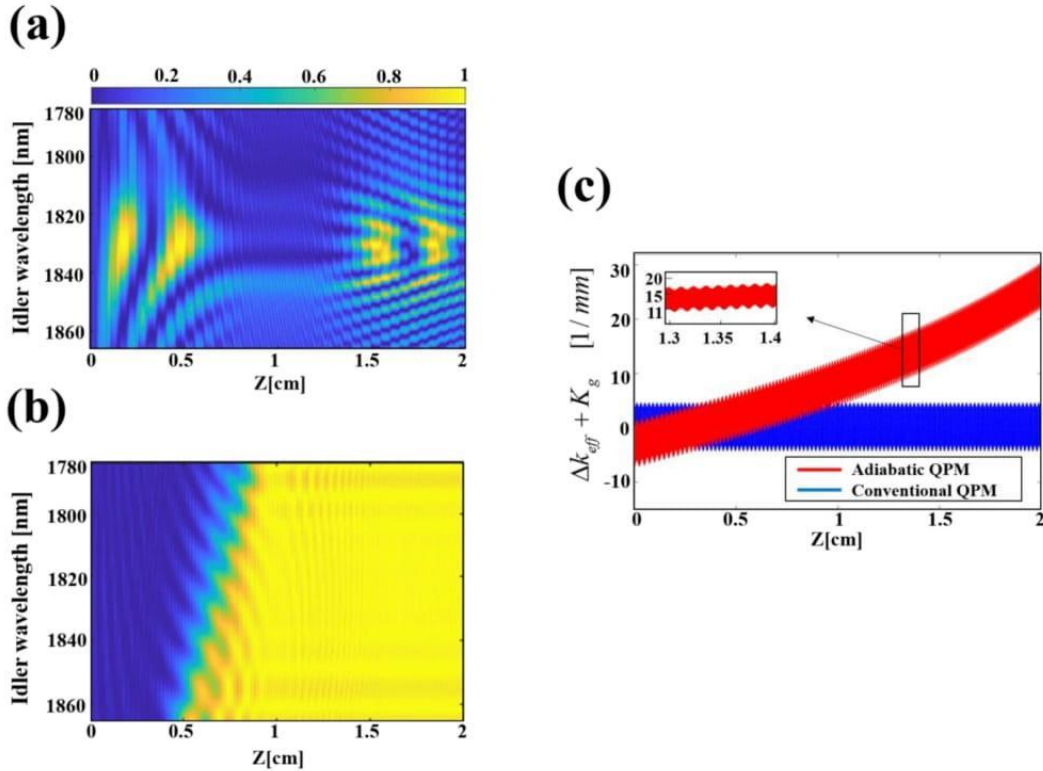
Fig. 3. Simulation results for an adiabatically modulated Si waveguide and for the standard periodic QPM approach. (a) Pseudocolor plot of idler intensity (arb. units) versus wavelength for the standard case of a periodic width modulation (i.e., constant-valued K_g) chosen to phase match only the central carrier wavelength. Efficiency is highly non-uniform and displays conversion-back-conversion cycles. (b) Pseudocolor plot of idler intensity (arb. units) versus wavelength for the adiabatic case, which shows nearly full and highly uniform conversion for all wavelengths included in the simulation. As expected, the locations where each wavelength has its rapid conversion jump are separated longitudinally. (c) The sum of effective phase mismatch and added momenta, $\Delta k_{\mathrm{mod}}(z)$, a multi-valued function corresponding to the wide range of signal (and corresponding idler) wavelengths. The overall shift is due to the longitudinal variation of $K_g(z)$, the effective momentum of the modulated waveguide, while the smaller oscillations are due to the modulation of the propagation constants due to the changing waveguide dispersion.

phase-matching conditions are restricted such that the modulated total phase mismatch of the desired scheme (i.e., $\omega_{\mathrm{Idl}} = \omega_{\mathrm{Sig}} + \omega_A - \omega_B$) crosses zero but is very large for the undesired scheme (i.e., $\omega_{\mathrm{Idl}} = \omega_{\mathrm{Sig}} - \omega_A + \omega_B$).

The FWM process is stimulated by the presence of two stronger narrow-band radiation sources centered at 2000 and 2200 nm. Our numerical simulations employed 1-ps Gaussian pump pulses with each having as little as 10-pJ energy, easily achieved from an oscillator. In this extremely low-energy scenario, the signal pulse energies, which are 60 fs at FWHM when compressed to be Fourier transform limited, can be as high as 0.5 pJ, with simulation results remaining the same (i.e., the conversion efficiency is > 90% for all wavelengths,). Our simulation results remain the same when pump and signal pulses are scaled together to much higher energies, for example with both pump pulses stretched to 5 ps with an energy of 10 nJ per pulse and with a signal pulse stretched to 500 fs with a pulse energy as high as 1 nJ. The simulated results presented in this section are for 1-ps, 10-pJ Gaussian pump pulses co-propagating with a 60-fs, 0.1-pJ
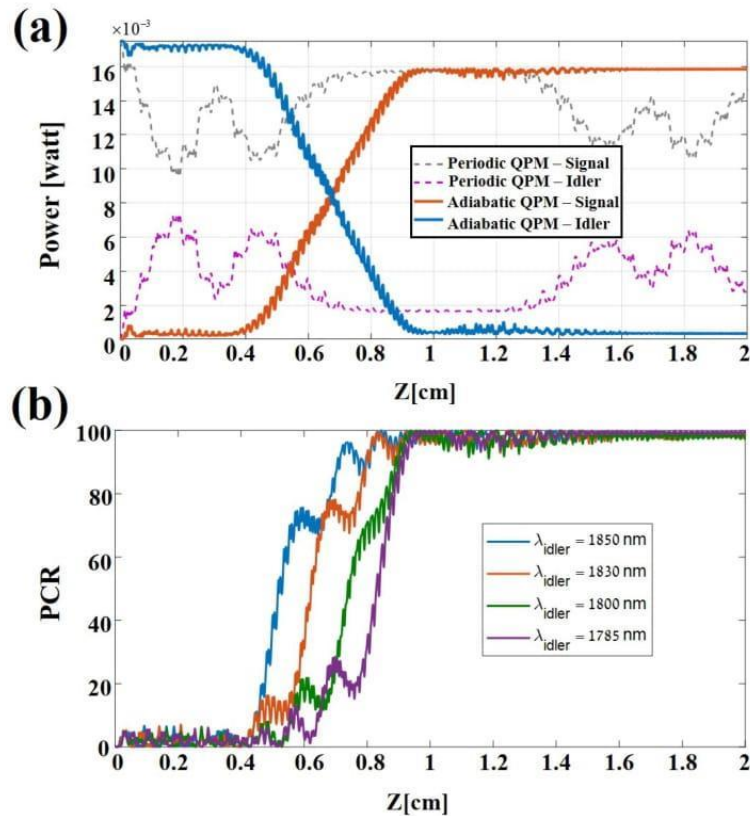
Fig. 4. (a) Integrated idler and signal powers during propagation in periodic and aperiodic (adiabatic) waveguides, illustrating signal-to-idler energy transfer. For the adiabatic evolution there is convergence of energy transfer from signal (blue) to idler (orange), while the conventional QPM case (gray, purple) shows unwanted back-conversion with efficiency that is non-uniform and highly sensitive to the initial conditions. (b) Efficiency vs. propagation length for various idler wavelengths in the adiabatic waveguide (corresponding to cross-sections of Fig. 3(a)). Illustrating evolution of an adiabatic nature, convergence is apparent for each wavelength, with rapid conversion taking place at a different location corresponding to the zero-crossing of the QPM wave-vector mismatch.

Gaussian Signal pump pulse. The group dispersion of our waveguide was analyzed according to the method of [44]. The dispersion obtained does not have a zero-dispersion wavelength (ZDW) between the fields and accurately matches previous reports [45], with group dispersion ranging from -1500 to -1000 [ps $\cdot$ km^{-1} $\cdot$ nm^{-1}].

For a waveguide with no modulation of width (results not shown), the wave-vector mismatch is always large and the conversion efficiency is poor (PCR < 0.04). For the waveguide with width modulated periodically to achieve QPM of the central idler wavelength (i.e., the conventional QPM approach), the efficiency is non-uniform and is highly sensitive to initial conditions, resulting in an output that is selective in wavelength [Fig. 3(a)]. In contrast, for the AFWM (adiabatic QPM) structure, all wavelengths gradually converge to a final state value close to full efficiency [Fig. 3(b)]. Induced oscillations in phase mismatch can been seen in the inset of Fig. 3(c). These oscillations, which are also present for the conventional QPM case, are the manifestation of the change in effective index due to modulation in that particular step. The width of the plotted modulated wave-vector mismatch is due to the broad bandwidth of the signal, since Δk_{eff} is wavelength dependent and takes a slightly different value for each wavelength. In addition, the QPM wave-vector mismatch is shifted from zero due to the XPM term in Δk_{eff}.

Figure. 4(a) illustrates the total conversion efficiency along the waveguide for a signal wavelength range spanning from 1650 to 1720 nm. As can be seen, pulses are converted with very high efficiency and converge to a final value, whereas the efficiency of the conventional QPM approach does not converge due to back-conversion. Furthermore, the intensities during propagation of the broadband signal and idler in the adiabatic frequency conversion scheme exhibit a robustness and superiority of power transfer when compared to the conventional QPM periodic scheme. Energy is shifted in an adiabatic manner and converges to a final state. In Fig. 4(b), the idler intensity is plotted for selected wavelengths in order to emphasize the convergence of the adiabatic solution to a final state for all wavelengths. It is worth noting that this type of structure can accommodate the conversion of a different idler range by an appropriate change to the designed width modulation periods, i.e., such that Δk_{mod} will contain a zero-crossing for each signal-idler pair while fulfilling Eq. (5).

4.2. AFWM in step-index fibers

In this section, we investigate the feasibility of AFWM frequency conversion in the simplest and most common fiber platform, step-index optical fibers (SIF). To achieve the longitudinal variation in Δk_{eff} needed for AFWM, we explore the use of a fiber taper to longitudinally sweep the waveguide dispersion contribution to the propagation constants. Our goal is to employ a long enough fiber with an adiabatic taper rate satisfying Eq. (5) to achieve efficient AFWM frequency conversion for an infrared bandwidth approaching a full octave.

As before, we focus our investigation on FWM Scheme 1 from Fig. 1(a). In the application modeled below, the second harmonic of $\mathrm{Pump_A}$ is used as $\mathrm{Pump_B}$. A signal with its wavelength between $\mathrm{Pump_A}$ and $\mathrm{Pump_B}$ is used to generate an idler wave with a longer wavelength than the three input waves. Given the wavelengths of typical modern pulsed lasers, this scheme would be convenient for near-IR and mid-IR generation. We investigate the cases where ω_A corresponds to 1.03, 1.55, or 2.0 μm. For applications in solid-core fibers involving four well-separated frequencies, the typical beam intensity (as limited by the laser damage threshold) is usually low enough to make the contribution to wave-vector mismatch from nonlinear phase modulations, $\frac{\epsilon_0 \chi^{(3)} \gamma_{int}}{2} (\omega_B P_B - \omega_A P_A)$, much smaller than that from the propagation constants β_i (i.e., the intrinsic wave-vector mismatch). Therefore, we approximate $\Delta k_{\mathrm{eff}} \approx \beta_A + \beta_{\mathrm{Sig}} - \beta_B - \beta_{\mathrm{Idl}}$, and explore the conditions for which $\Delta k_{\mathrm{eff}} = 0$.

We consider a fiber with only one ZDW, as is the case for most commonly used SIFs. As is typically the case for FWM-BS processes, a symmetric placement of the four mixing frequencies around the ZDW enables phase matching [35, 43]. As shown below, while phase matching can be achieved in other configurations, the broadest bandwidth is achievable in symmetric configuration, which is a successful approach even in the case of FWM frequencies separated by multiple octaves. Plots of propagation constant β against optical frequency ω are shown in Fig. 5 for $\mathrm{Pump_A}$ wavelengths corresponding to (a) Yb-doped, (b) Er-doped, and (c) Tm-doped fiber lasers, in either standard silica fiber, $\mathrm{ZrF_4}$ fiber (Thorlabs P1-23Z models), and $\mathrm{InF_3}$ fiber (Thorlabs P1-32F models), respectively. We define average propagation constants $\beta_{M_1} = (\beta_A + \beta_{\mathrm{Sig}})/2$ and $\beta_{M_2} = (\beta_B + \beta_{\mathrm{Idl}})/2$. Achieving $\Delta k_{\mathrm{eff}} = 0$ thus requires $\beta_{M_1} = \beta_{M_2}$. If all four mixing waves are located on one side of the ZDW [Fig. 5(a)], the condition $\beta_{M_1} = \beta_{M_2}$ cannot be achieved, a consequence of the group-velocity dispersion $\beta'' = d^2\beta/d\omega^2 > 0$ for all frequencies. For typical single-mode fiber core radii ($\sim$2-8 μm), the ZDW (~ 1.27 μm) is longer than any wavelength of the four waves involved, and there is no phase matching for a wide idler range, as shown in Fig. 5(d). A similar conclusion can be drawn if all four waves lie within the $\beta'' < 0$ region. In contrast, if one wave is on the opposite side of the ZDW with respect to the other three waves [Fig. 5(b)], phase matching becomes possible, but only within a narrow range of parameters. As seen in Fig. 5(e), narrowband phase-matching conditions are achieved for only a small range of core radii.

Finally, if there are two waves on each side of the ZDW [Fig. 5(c)], the chance that $\beta_{M_1} = \beta_{M_2}$
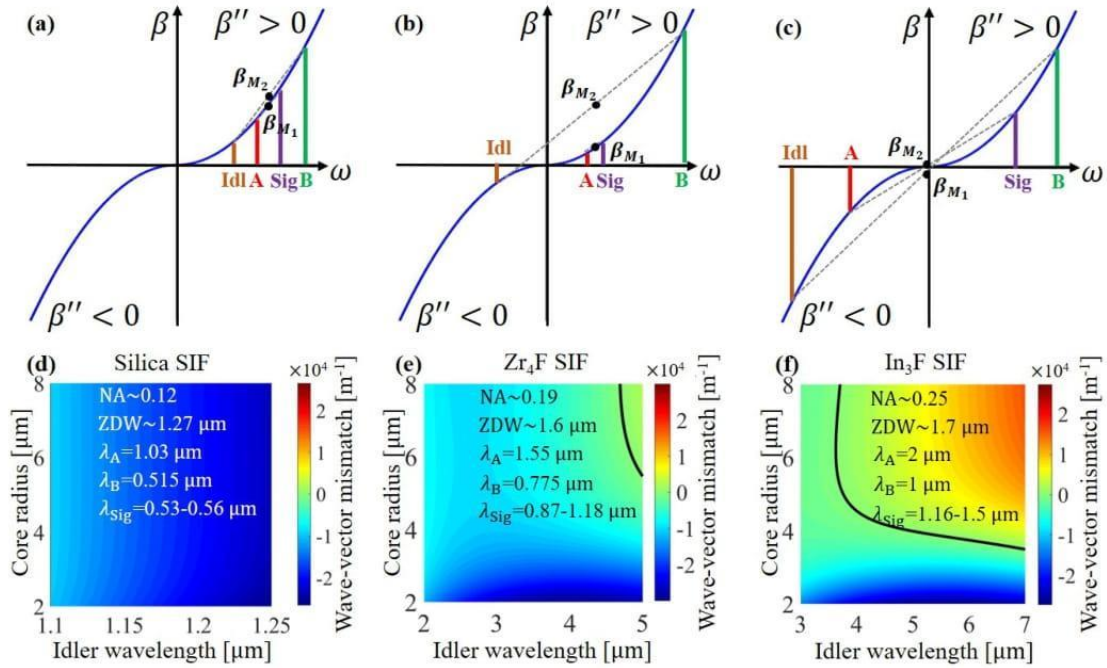
Fig. 5. The relative positions of the ZDW and optical wavelengths determine the likelihood of a broad phase-matching bandwidth for AFWM in SIF. Top row: Propagation constants of the four mixing waves where $\omega_A + \omega_{Sig} = \omega_B + \omega_{Idl}$ and $2\omega_A = \omega_B$, for three cases. The y-axis lies at the ZDW. Achieving $\Delta k_{eff} = 0$ requires $\beta_{M_1} = \beta_{M_2}$, where $\beta_{M_1} = (\beta_A + \beta_{Sig})/2$ and $\beta_{M_2} = (\beta_B + \beta_{Idl})/2$. Bottom row: wavevector mismatch versus fiber core radius and idler wavelength for laser parameters corresponding to each case. (a),(d) Case for a standard silica SIF where all four waves are on one side of the ZDW. No phase matching is possible. (b),(e) Case where one frequency is on the opposite side of the ZDW from the other three. Narrowband phase matching under limited conditions is possible. The black curve represents contour zero ($\Delta k_{eff} = 0$). (c),(f) Case where there are two waves on each side of the ZDW. Phase matching is probable in this case, and gives rise to conditions where an octave-spanning idler wave covering 3.5-7 μm can be phase matched in an AFWM process in a tapered fiber.

becomes much higher. As seen in Fig. 5(f), an octave-spanning range of idler wavelengths can be phase matched over a core radius range spanning 3.5-7 μm. In an untapered fiber, Δk_{eff} will equal zero for only one idler frequency, and the conversion bandwidth will be limited to the standard phase-matching bandwidth. In contrast, a tapered fiber with an adiabatic taper rate according to Eq. (5) over this range of core radii could be used to achieve AFWM over the full octave-spanning wavelength range, offering a route to dramatically increase the conversion bandwidth. We conclude that a ZDW lying between pairs of interacting wavelengths maximizes the possibility for a broad AFWM conversion bandwidth in a tapered SIF.

To examine AFWM in tapered SIF with ultrashort pulses, we numerically solved the (1 + 1)-D GNLSE representing Scheme 1 $(\omega_A + \omega_{Sig} = \omega_B + \omega_{Idl})$, Eq. (10), as discussed in Section 3. The frequency grid used in the simulation covers a multi-octave bandwidth spanning from 450 nm to 9 μm. Analytical eigenvalue equations for SIF are used to determine the longitudinally varying propagation constant $\beta(z, \omega)$ [37]. We found SRS to be negligible due to the short length of the fiber simulated and the low Raman gain for fluoride fibers with picosecond transform-limited (TL) pump durations [46]. Therefore, SRS terms in Eq. (10) were ignored. The GNLSE numerical simulation captures both intended and unintended FWM processes, giving guidance for choosing parameters that deliver optimal AFWM without exciting significant parasitic effects

upon generation of the desired idler wave.

Motivated by its wide potential AFWM frequency conversion bandwidth, we investigated fiber parameters corresponding to Figs. 5(c) and 5(f). The transparency range of Thorlabs P1-32F fibers is listed as 310 nm to 5.5 μm (for attenuation < 3 dB/m). Therefore, we expect a lower than 0.25 dB attenuation (> 95% transmission) in this spectral range if a short ($\sim$cm) fiber is used. We chose intensity, chirp rate, and fiber length to optimize the generation of mid-IR light by AFWM while maintaining an insignificant amount of parasitic effects. The simulated fiber has a core radius taper from 4.5 μm to 3.55 μm over a length of 5 cm, resulting in a phase-matching range for idler wavelengths covering 4-7 μm, although we only expect high transmission for wavelengths up to 5.5 μm. According to our calculation, a peak power of >180 kW for each of the two pumps would fulfill the adiabatic condition, Eq. (5), across this entire bandwidth. We note, while we employed a linear taper rate in this study, a nonlinear taper could be employed as well. In either case, a rule for achieving high conversion efficiency is adherence to Eq. (5) for every frequency in the pulse, where Eq. (5) is satisfied for each frequency independently and is evaluated locally in the fiber where its wave-vector mismatch crosses zero.

The input pulse characteristics were chosen to be realizable using common fiber laser technology. The pumps were chosen as a 10-ps full-width at half maximum (FWHM) TL Gaussian pulse at 2.0-μm wavelength and its second harmonic, a 7.1-ps FWHM TL Gaussian pulse at 1.0 μm, each having peak power of 110 kW (which is slightly lower than the ideal power and was chosen to avoid strong parasitic FWM found at higher peak powers). We chose to employ picosecond pump pulse durations because of three reasons. 1) The group-velocity walk-off between the pump and signal pulses through the simulated fiber is $\sim$ 1 ps. 2) Pumps with picosecond TL durations excite fewer parasitic nonlinear effects compared to femtosecond pulses, due to their narrower bandwidth. We note that the pump bandwidth is broadened due to SPM/XPM during the interaction, and care must be taken to keep it appropriately narrow (i.e., to avoid parasitic effects that can be identified through the simulation) during the interaction. 3) Given the peak power needed to fulfill the adiabatic condition, the fiber damage threshold prevents the use of pulse durations $\gg$ 10 ps. The signal pulse was a chirped 2-ps FWHM Gaussian pulse spanning 1360-1440 nm, with a peak power of 10 kW. The corresponding idler range spans 4250-5140 nm. We simulated the nonlinear propagation of the three waves through the optical fiber, each in their respective fundamental mode. At each longitudinal fiber position, the nonlinear coupling coefficient (overlap factor) γ_{int} in Eq. (10) was evaluated from the overlap integral calculated based on the effective areas determined by finite element method at the center frequencies of the four waves of the intended AFWM. The obtained value was used for a constant γ_{int} over the entire simulated frequency grid at the corresponding longitudinal position, while its value changes as a function of tapered fiber core diameter as the waves propagate through the full fiber length.

Figure. 6 shows numerical solution of the (1+1)-D GNLSE for the parameters discussed above. Figure. 6(a) shows the power spectral density evolution of the 4-5.5 μm mid-IR region as the three input pulses propagate through the 5-cm-long tapered fiber. The generated idler wave inherits the Gaussian spectral profile of the signal wave. PCR evolution for selected wavelengths is shown in Fig. 6(b). Each mid-IR wavelength is produced with evolution dynamics typical of RAP, and with longitudinally varying conversion position, as expected due to the variation in core size where the $\Delta k_{\mathrm{eff}} = 0$ condition is encountered for different wavelengths. The PCR at the fiber exit is shown in Fig. 6(c) for the full idler bandwidth, spanning 4.2-5.2 μm, and is above 0.7 for the full range. The generated mid-IR pulse is centered at 4.7 μm and has an output energy of 5.5 nJ, with chirped $\sim$2 ps FWHM duration and $\sim$3 kW peak power. If fully compressed to its $\sim$43 fs TL duration, the sub-3-cycle mid-IR pulse can reach a peak power of 94 kW, thus indicating a new route to high peak power, fiber-based few-cycle pulse sources.

To further investigate the adiabatic character of the conversion and the influence of parasitic
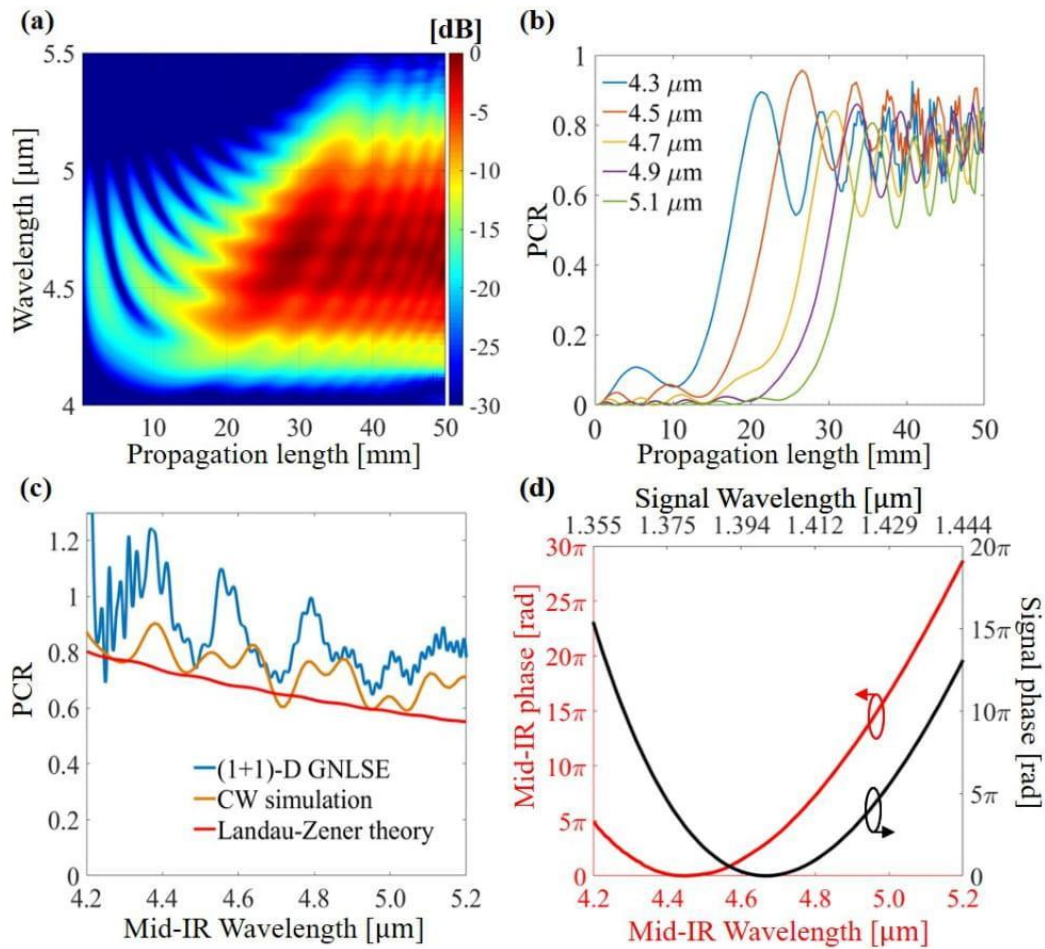
Fig. 6. Mid-IR generation via AFWM in InF$_3$ SIF with core radius tapered from 4.5 to 3.55 μm over a 5-cm length. **(a)** Mid-IR beam spectral density evolution along the propagation axis, given a Gaussian input signal spectrum. AFWM can be observed for 4.2-5.2 μm. **(b)** Evolution of PCR for selected wavelengths. **(c)** PCR at the fiber exit vs. idler wavelength. Due to parasitic FWM amplification of the input signal, PCR determined by solution of the GNLSE is higher than that predicted by the cw simulation and includes values greater than 1. **(d)** Comparison between the spectral phases of the output mid-IR and input signal waves indicates the coherence of the generated wave. The idler's phase consists of a conversion phase due to the wavelength-dependent conversion position (which is largely an effective third-order dispersion) plus the initial linear chirp (parabolic phase) of the signal pulse.

FWM, Fig. 6(c) includes for comparison both an analytical calculation of the expected conversion efficiency based on Landau-Zener theory of adiabatic transition probability [47,48], and numerical integration of the GNLSE for each signal-idler pair under the approximation that they are cw and that the AFWM interaction of Scheme 1 is the only FWM interaction. The cw simulation thus excludes pulse propagation, parasitic FWM, and SPM/XPM. It can be observed from Fig. 6(c) that the PCR expected from Landau-Zener theory matches the cw simulation well. Oscillations in PCR in the cw simulation result from non-apodized coupling (low-amplitude conversion-backconversion cycles) between signal and idler waves still existing at the fiber exit, as observed in Fig. 6(b). The PCR obtained from the full GNLSE simulation also matches the cw result well, but with slightly higher efficiency attributed to the parasitic process $\omega_A + \omega_B = \omega_{Sig} + \omega^*$, where ω^* is an unintended generated optical frequency. This parasitic process amplifies the input

signal by the strong pumps as if an optical parametric amplifier, resulting in a slightly amplified signal wave before its conversion to mid-IR takes place by AFWM. This process produces a PCR even greater than 1 for some wavelengths, a feature that potentially could be exploited in an application. However, fast oscillations in PCR appear at the short wavelength edge in Fig. 6(c) as a result of interference between the generated AFWM idler and parasitic cascaded FWM processes. We note that the relative weight of parasitic effects may be slightly higher than this model predicts, since the overlap factor for the intended AFWM process is slightly lower than that for FWM processes involving only visible and near-IR wavelengths.

Finally, the spectral phases of the input signal and output idler waves are presented in Fig. 6(d), showing coherent idler generation through AFWM. The quadratic phase of the chirped input signal is transferred to the mid-IR idler. An effective third-order dispersion can be observed, which is due to the longitudinally varying wavelength-dependent conversion position.

5. Summary and outlook

In this article, we introduced the concept of adiabatic four-wave mixing frequency conversion, a concept that should enable tunable, broadband, efficient, robust, and energetic frequency conversion in cubic nonlinear media for a broad range of applications. Theory and formula describing the analogy of RAP in SU(2)-symmetric FWM schemes were presented, culminating in the presentation of an adiabatic condition for FWM frequency conversion. Illustrating the wide applicability of the concept, two very different waveguided optical platforms were explored, using numerical modeling that captures the effects of broadband pulse propagation with longitudinally changing waveguide dimensions and a wide range of phase-matched nonlinear processes.

In silicon photonics devices, AFWM frequency conversion could be used for on-chip devices for applications such as conversion between lossless and dispersionless bands, sensing, computational manipulations and encryptions. A possible realization for an on-chip waveguide was suggested and simulated, with standard height for a silicon platform as well as standard sized widths, allowing a structure that could be incorporated easily as an on-chip device. We demonstrated a solution that suggests an efficient, robust, and broadband frequency conversion, with a bandwidth of up to 70 nm centered at 1820 nm, which is the first solution to our knowledge for such wide spectral widths. We have demonstrated this via simulation for an incoming broadband signal centered at 1680 nm and an outgoing idler of the same bandwidth centered at 1820 nm, with a PCR over 0.9. Similar structures could be easily designed to fit any desired signal-idler wavelength pairs desired on-chip without changing the overall size and geometry of the device.

In a step-index fiber platform, AFWM can be realized by using a tapered fiber. It was shown that a ZDW positioned in the middle of the four wavelengths is optimal for broadband phase matching of AFWM frequency conversion. A tapered InF_3 fiber was numerically simulated with a (1+1)-D nonlinear Schrödinger equation model. A broad 4.2-5.2 μm mid-IR bandwidth with flat PCR close to 1 was demonstrated. The proposed AFWM experimental parameters can be realized potentially in an all-fiber based system pumped by a Er-doped master oscillator. Pulse generation at the 2-μm pump wavelength with similar pulse duration and peak power has been reported, using a multi-stage thulium-doped fiber amplifier chain [49]. Pulses with bandwidth and center wavelength corresponding to the signal (1360-1440 nm, 2-ps chirped pulses) have been demonstrated using soliton self-frequency shift and dispersive wave generation using a 1550-nm Er-doped fiber source and highly nonlinear fiber [50]. The entire pulsed laser system might consist of an Er-doped fiber master oscillator front end used to pump soliton self-frequency shift as well as supercontinuum generation in highly nonlinear fiber to generate a 2-μm component that can be used to seed a multi-stage thulium-doped fiber amplifier. The high-energy 1-μm pump can be obtained by second harmonic generation of the 2-μm pump, or, alternatively, by using the supercontinuum to seed a multi-stage Ytterbium-doped fiber amplifier. The source and AFWM stage could therefore be an all-fiber based system.

While the simulated SIF platform can be tuned for the phase matching of other frequencies by an adjustment of the material type and dimensions of the tapered fiber, other fiber platforms may offer advantages for a specific spectral range and for other power levels. For example, our initial calculations predict hollow core fibers, including hollow core PCFs and microstructured fibers, to be potential platforms for AFWM. These fibers can handle orders-of-magnitude higher intensity than SIF due to their gaseous core, and typically have a much wider transmission window than solid core fibers [51]. Furthermore, the dispersion of hollow core fibers can be flexibly controlled by fiber geometry design, and thus may offer a flexible approach to the design of a waveguide that fits the needs of a particular application. The introduction of gases into holey fibers can also be used to tune their nonlinearity and dispersion, and pressure gradients might be used as another means for controlling the longitudinal variation of parameters used to fulfill the adiabatic condition. Therefore, we expect HCFs to provide an important platform for high power and high energy frequency conversion through AFWM processes.

We note that the FWM-BS scheme simulated in the examples of Section 4 is widely used for applications ranging from tunable wavelength conversion in the telecom band to quantum frequency conversion [35, 52–54], and recent work has reported broadband frequency conversion with a preserved pulse shape [43]. In recent years, FWM-BS has become an actively studied scheme for low-noise preparation and translation of single-photon states [36, 55–57]. In each of the above contexts, use of the adiabatic counterpart of the FWM-BS scheme may bring significant value by broadening the effective conversion band while also providing robust and high conversion efficiency and a linear phase transfer.

More generally, the ubiquitous presence of cubic nonlinearity potentially opens the AFWM concept to any waveguided optical platform that can handle the typical field strengths needed for FWM. While not all media can be expected to offer an opportunity for broadband conversion in a single device, not all relevant applications would require it. One might envision, for example, a frequency domain wavelength multiplexing scheme with a device tailored for each channel. In such an application, the robust and efficient qualities of adiabatic conversion – back-conversion free and signal intensity independent conversion with near-100% efficiency – could be beneficial. The expanded bandwidth of AFWM compared to conventional FWM can be expected to have a strong impact in many areas, such as up-conversion detection for sensing, spectroscopy, and imaging, or for the efficient generation of a hyperspectral range of wavelengths in an ultrafast laser system, potentially covering frequencies from UV to far-IR. Moreover, the linearized transfer function of amplitude and phase of a 1-to-1 photon up-conversion or down-conversion scheme such as this when pump pulse bandwidths are significantly narrower than those of the signal and idler – already demonstrated for octave-spanning conversion in adiabatic three-wave mixing processes [12] – may be used to greatly simplify dispersion management, expand the effective bandwidth of pulse shapers, or be utilized to preserve information in sensing, communications, or encryption applications.

Funding

Acknowledgments

2.2 Coherent control of the non-instantaneous nonlinear power-law response in resonant nanostructures

Coherent control of the noninstantaneous nonlinear power-law response in resonant nanostructures

Eyal Bahar ⓞ,[*] Uri Arieli, Michael Mrejen, and Haim Suchowski

School of Physics and Astronomy, Tel-Aviv University, Tel-Aviv 6779801, Israel
and Center for Light-Matter Interaction, Tel-Aviv University, Tel-Aviv 6779801, Israel

We experimentally demonstrate coherent control of the nonlinear response of optical second harmonic generation in resonant nanostructures beyond the weak-field regime. Contrary to common perception, we show that maximizing the intensity of the pulse does not yield the strongest nonlinear power-law response. We show this effect emerges from the temporally asymmetric photoinduced response in a resonant mediated noninstantaneous interaction. We develop a novel theoretical approach which captures the photoinduced nonlinearities in resonant nanostructures beyond the two photon description and give an intuitive picture to the observed noninstantaneous phenomena.

Nanostructures (NS) have revolutionized light matter interaction allowing for on demand control of unique optical [1,2], electrical [3,4], and mechanical properties [5], both in linear and nonlinear regimes [6–9]. In the past decade, much research has been performed on the optical nonlinearity of NSs emerging from their energy confinement [10] and geometrical architecture [11,12] contributing in both their single and collective responses [13–15]. Commonly enhanced by resonant NSs, the photoinduced nonlinear interaction in NSs has been mostly studied within the framework of the instantaneous response of these materials [16–18], meaning that the nonlinear medium interacts simultaneously with all interacting waves. While this instantaneous picture has provided a model describing the observations of rich nonlinear phenomena, it does not capture the full nonlinear dynamical response, which is fundamentally noninstantaneous. This is apparent in current research frontiers, where the study of the ultrafast, out-of-equilibrium, electronic dynamics in NSs has gained much attention [19–28]. However, the noninstantaneous contribution inherent to *resonant* interaction in these systems has been so far mostly overlooked.

The noninstantaneous contribution inherent to nonlinear resonant dynamics is well known in atomic and molecular systems, which is of particular importance in multiphoton processes [29]. Enhancement by orders of magnitude of electronic transitions in atomic systems [30,31], as well as for large organic molecules [32,33], has been enabled by spectrally shaping the pulse to be compatible with the noninstantaneous response in resonant mediated interactions, via coherent control schemes. However, for resonant NSs, applying such pulse shaping methods to enhance nonlinear processes have been so far limited, since these require the interacting pulse spectrum to be much broader than the resonant linewidth, which is typically not fulfilled for NSs. Therefore, pulse shaping has been mostly shown for controlling the *linear* response in plasmonic systems [34–38] or for multicolor

second harmonic generation (SHG) imaging [39]. As the resonant mediated noninstantaneous process also contributes to the power-law response, it is expected that this fundamental characteristic of the nonlinear dynamical response will play a major role in nonlinear interaction. Yet, to date, no experimental work has been performed demonstrating control over the noninstantaneous nonlinear power-law response in resonant NSs.

In this paper we experimentally demonstrate coherent control of the noninstantaneous nonlinear power-law response in resonant NSs. We show that, counterintuitively, the highest peak intensity does not yield the strongest optical nonlinearity, where the nonlinear response decreases significantly below the standard quadratic response. Furthermore, when approaching the strong field regime, we reveal an asymmetric temporal evolution accompanied with an unconventional decrease in the nonlinear power-law response, deviating from 2 to 1.6. Finally, we devise a theoretical framework and provide an intuitive picture for the noninstantaneous effects. Our proposed model, based on a resonant three-level system [40], solved to the fourth order in a perturbative expansion, captures noninstantaneous resonant phenomena beyond the weak-field two-photon description. In this framework, phase differences in the excitations of the localized surface plasmonic resonance (LSPR), captured as phase differences between second and fourth order contributions, lead to a dynamically rich nonlinear response which we observe experimentally. These effects are not captured in traditional nonlinear models including the well-known Miller rule [41], which has shown great accuracy in describing nonresonant nonlinearities in bulk media. Though our experimental observations were focused on plasmonic NSs, we believe the resonant three-level model is critical in analyzing strong light-matter interaction with any resonant process in NSs, including excitonic, electronic, or phononic excitations in semiconductor NSs and two-dimensional (2D) materials.

In our experimental demonstration of the noninstantaneous response, we use gold NSs in a split ring resonator (SRR) configuration, which is the most common geometrical structure

---

[*]Eyalb@mail.tau.ac.il
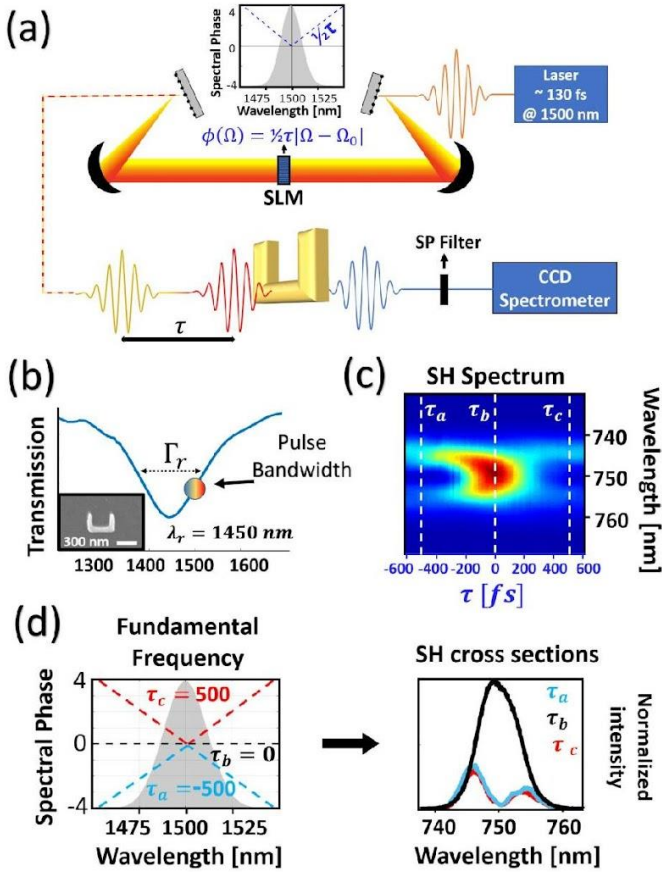
FIG. 1. Coherent control of SHG in plasmonic NSs. (a) The experimental apparatus is composed of a spatial light modulator (SLM) used as a spectral phase mask. Light passes through a 4f pulse shaper SLM in a double-pass configuration. The coherently altered pulse interacts with a gold NS, SHG is collected. (b) NS transmission measurement showing the LSPR wavelength and linewidth. Inset: The measured image of a SRR by a scanning electron microscope. (c) A normalized map of the measured SHG spectrum as a function of the spectral phase is placed as example of a weak-field reference when observing the power-law response map. The horizontal axis of the SH map is the delay between the spectrally split pulses, corresponding to the slope of an absolute value phase function centered about the central frequency of the pulse. (d) Cross sections of the SH map showing the SHG for large delays and with no delay (TL pulse).

with inherent SHG. In all experiments we have used a 130-fs laser fixed at 1500 nm focused on a SRR array with LSPR in the vicinity of the lasers central wavelength [see Figs. 1(a) and 1(b)]. For the coherent control experiment, we have assembled a pulse shaper consisting of a spatial light modulator (SLM) based in a double-pass 4f setup. When performing SLM-based experiments in NSs by a *single-pass* setup, one should be aware of the potential spatial shifts and distortions of the beam due to spatiotemporal couplings in the 4f system. The *double-pass* configuration was found to be indeed crucial to obtain accurate SLM-based measurements [42]. In our experiments, we apply a variable absolute valued spectral phase mask spectrally splitting the incoming pulse. By Fourier transform, the magnitude of the slope of the absolute valued phase function $\tau/2$ is directly related to the temporal interval
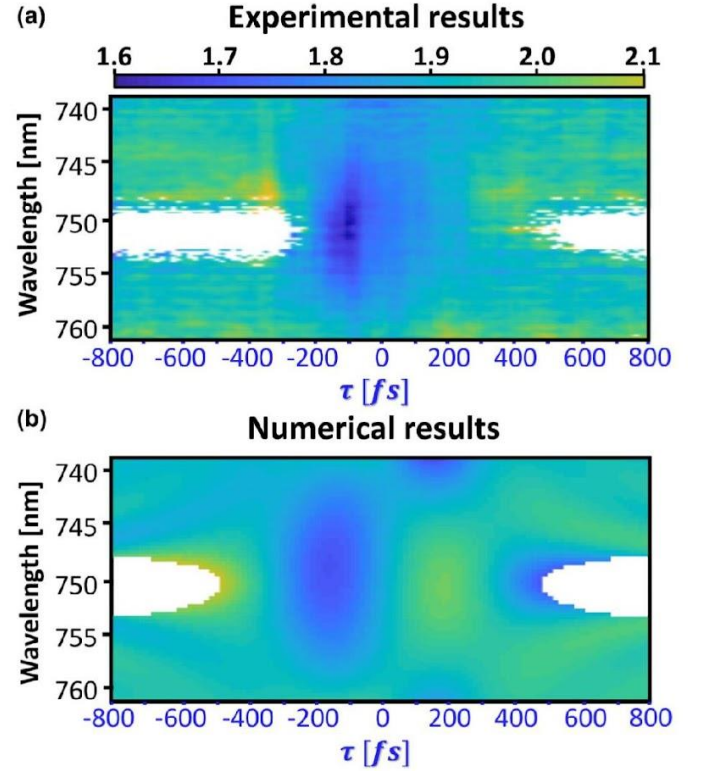
FIG. 2. Nonlinear noninstantaneous response of SH in gold NSs. Map of the power-law response $P(\lambda, \tau)$ (color coded) as a function of the delay between the pulses (x axis) and wavelength (y axis). (a) Experimental data: For a 100 fs negative delay, we observe that the nonlinear response decreases to 1.6 when shorter wavelengths arrive first (negative τ), while in the case of swapping the order of arrival, such that longer wavelengths are first to arrive (positive τ), this effect is absent. (b) Simulation results of the resonant three-level model. The main feature of a decrease in nonlinear response is predicted, as well as an overall well agreement with experiment. We note that both images have the same color bar.

between the spectrally separated pulses. The sign of the slope, positive or negative, corresponds to the order of arrival of the spectrally separated pulses where positive dictates longer wavelengths arrive first. This enables us to perform an SLM based, semidegenerate coherent pump-probe SHG process and create a map emphasizing the noninstantaneous nature of the interaction. A typical scan is placed in Fig. 1(c) to provide a weak-field reference for later analysis of the power-law response. When the delay between the spectrally split pulses is large enough, the spectrally separated pulses can be considered as noninteracting and perform conventional SHG within their own frequencies, while SHG by frequency mixing between the pulses is very weak or nonexistent [see Fig. 1(d)]. However, for short delays, the pulses temporally overlap leading to SHG by frequency mixing between the pulses yielding a broader SHG spectrum, as would be expected from a second order nonlinear process.

The experiment is repeated for different intensities to produce a pixel-by-pixel map showing the nonlinear power law as a function of wavelength and slope value in terms of delay [see Fig. 2(a)]. Appearing as white background in

these plots, areas in which the SHG intensities are weak, such that they are comparable with the noise level (1/100 for simulations), are considered irrelevant for power-law characterization, and therefore are cut out of the data. In our results, we see that unlike a conventional nonlinear crystal where the perturbative picture can be robustly modeled as I^P (experimentally verified, BBO), we find the power-law response shows a complex, dynamical nature, which depends on delay and wavelength such that $P \rightarrow P(\lambda, \tau)$. We point out three key features we observe in experiment: The nonlinear response is not symmetric in terms of delays, meaning that the order of arrival of the different pulses, each containing different spectral components, affects the power-law response for SHG. Furthermore, although peak intensity is higher for very short delays, the power-law response decreases to a minimal value of 1.6, which is significantly smaller than the conventional quadratic response expected in a second order process. Moreover, for zero delay, where the pulse is Fourier transform limited (TL), peak intensity is at its highest yet the nonlinear response is not the strongest and is only ~1.75, which implies that this effect could not be described by a saturation mechanism. In a broader view, we observe that for small delays the nonlinear response is dynamical and sensitive to the order of arrival of pulses (sign of τ). When shorter wavelengths are first to arrive, the nonlinear response decreases, gradually recovering as the delays shorten and fully recovers after 100 fs with longer wavelengths arriving first. Interestingly, for small delays, where the pulses overlap and peak intensity is at its highest, the power-law response is lower, suggesting the two photon picture is no longer suitable for describing the interaction process for these intensities.

Our attempts to model the experimental results with the nonlinear oscillator model and its perturbative solution fails to predict the observed properties, such as the decrease in the SH power-law response. However, we find that modeling the nonlinear response as a resonant three-level system can effectively predict the noninstantaneous properties emerging in experiment. These include, for the intermediate strength regime, a decrease in nonlinearity originating from the higher orders in the perturbative expansion. This attribute is not included in the nonlinear oscillator model, with susceptibility prescribed by Miller's rule [41], where the nonlinearity is monotonically increasing when considering higher orders in the perturbative approach.

In our model, we ascribe the intermediate level as the LSPR frequency. The excited state as the SH excitation frequency and ground state as the relaxed state of the system. We note that in the limit of a highly detuned resonant level, our solution approaches the known instantaneous solution found in nonresonant nonlinear optics [41]. By perturbative expansion, we solve up to the fourth order. In the case of a sub-half octave spanning bandwidth, due to energy conservation, third order terms do not contribute to the excitation. Including the fourth order enables us to capture intermediate field strength effects that impact the power-law response. We note that in our calculation of the fourth order pathways, terms which can be interpreted as cascaded processes with an effective coupling coefficient are included. The equations we obtain from this analysis are as follows:

$$I_{\text{SHG}}(\omega) \propto |\bar{\kappa}^2 E^{(2)} + \bar{\kappa}^4 E^{(4)}|^2, \tag{1a}$$

$$E^{(2)}(\omega) = \int \frac{E(\omega - \Omega)E(\Omega)}{\omega_r - \Omega + i\Gamma_r} d\Omega, \tag{1b}$$

$$E^{(4)}(\omega) = \int \frac{E(\Omega_2)E(\Omega_3)E(\Omega_4)E(\omega - \Omega_2 - \Omega_3 - \Omega_4)}{(\omega_r - \Omega_2 + i\Gamma_r)[\omega - (\Omega_4 + \omega_r + i\Gamma_r)](\Omega_2 + \Omega_3 - \omega - i\Gamma_{\text{Au}})} d\Omega_2 d\Omega_3 d\Omega_4$$
$$+ \int \frac{E(\Omega_2)E(\Omega_3)E(\Omega_4)E(\omega - \Omega_2 - \Omega_3 - \Omega_4)}{(\omega_r - \Omega_2 + i\Gamma_r)[\omega - (\Omega_4 + \omega_r + i\Gamma_r)](\Omega_2 + \Omega_3 - i\Gamma_{\text{Au}})} d\Omega_2 d\Omega_3 d\Omega_4, \tag{1c}$$

where $E^{(2)}$ and $E^{(4)}$ are the second and fourth order contributions of the perturbative expansion. $\Omega_{2,3,4}$ are frequencies integrated over in the multiphoton process illustrated as arrows showing interaction pathways in Fig. 3(a). ω_r is the measured LSPR frequency [see Fig. 1(b)]. $\bar{\kappa}$, a parameter indicating coupling strength of the modes with the electric field that should depend on geometry and free electron contribution in such a process, was fitted to give the best agreement with the data. $E(\Omega) = E_0 e^{i\phi(\Omega)}$ is the electric field, where E_0 and $\phi(\Omega)$ are the measured electric field strength and spectral phase, accordingly. In our experiment, the electric field strengths are in the order of 0.1 $[\frac{V}{nm}]$. The linewidths are introduced into the calculation as suggested by Refs. [43,44], where Γ_r is the linewidth of the NS array acquired by transmission measurements and Γ_{Au} is the collision rate related to the electron's mean free path for a gold NS approximated according to Ref. [45]. It is insightful to point out that $E^{(4)}$ is decomposed into two terms, each describing a different excitation process as illustrated in the pathway energy diagram in Fig. 3(a). For simplicity, their coupling strengths were approximated to be equal. Our simulation results are presented in Fig. 2(b), predicting the main feature of a decrease in nonlinearity, in an asymmetric temporal response and with the same timescale. In our simulations we see that timescales are determined by the LSPR's linewidth and Au collision rate. The results are relatively robust in terms of positive/negative detuning, where the sign of the detuning mostly affects the wavelength of the power-law's minimum. The simulations also predict that TL pulses do not yield the strongest power-law response and show other similar features observed in experiment. We see noticeable differences between the experiment and predicted results such as a 5% decrease in both $\tau = 200$ and $\tau = -130$ relative to the simulations. We attribute these differences to the spectral response of the NS's compared to the ideal

70

(a)

(b)
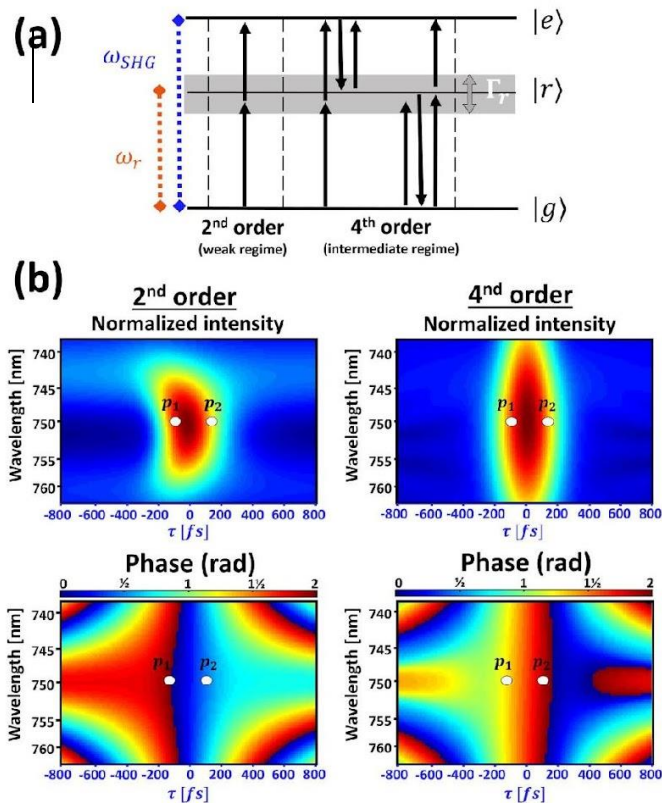
FIG. 3. The resonant three-level system perturbative solution and analysis beyond second order contributions. (a) Energy level diagram with second and fourth order interactions illustrated. ω_r and Γ_r are the resonant frequency and linewidth of the nonlinear system, accordingly. Arrows represent the coupling of levels by the electric field, where opposite pointing arrows correspond to a conjugated electric field. (b) Second and fourth order intensity and phase plots, with intensities each normalized separately for clarity of the intensity structure. p_1 and p_2 are points later referred to with further analysis.

Lorentzian shape of the three-level system, which become more significant for higher order excitation leading to a decreased power-law response.

When including terms beyond second order contributions in the three-level model, the next order's contribution is, as expected, initially small and becomes dominant with increased power. Surprisingly, the power-law response decreases, for the intermediate regime, due to phase difference with higher order excitations, effectively suppressing the excitation which corresponds to SHG. The intensity and phase of the second and fourth orders are plotted in Fig. 3(b). Although the direct ascertainment of the nonlinear behavior depends on both intensity and phase, observing the areas which are differently phased gives insight to the effect emerging in the nonlinear response. To unravel this connection, we perform analysis in the complex plane. For a specific wavelength and spectral shape, we plot the intensity (magnitude) and phase (angle) of the second and fourth order contributions separately and their sum. We further repeat this calculation with increased intensities.

We show two examples from our analysis (Fig. 4). For p_1, the phase between the second and fourth order leads to destructive interference resulting in a nonlinear response
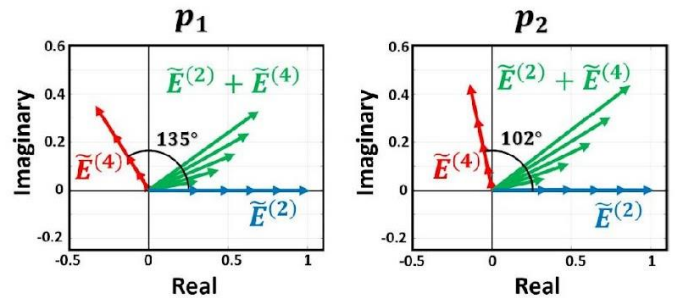
FIG. 4. The importance of relative phase in strong field SHG. Complex plane representation of the second, fourth, and summed contributions for different intensities showing how relative phase and intensity affects the nonlinear response. These are plotted for a specific wavelength and delays marked p_1 and p_2 in Fig. 3(b). The local evolution of the magnitude of the summed contribution would be the power-law response exhibited for each process. Each plot is rotated such that $E^{(2)}$ is pointing in the real direction, and normalized by $E^{(2)}$'s maximal value. By changing the order of arrival of the excitation pulses (negative to positive τ), the relative phase decreases and the intensity drives the system past its minimal nonlinear response to yield a stronger response.

which is smaller than quadratic. For p_2, the smaller phase difference is sufficient for the fourth order intensity to drive the combined sum past its minimal point towards fourth order nonlinearity resulting in an effectively restored quadratic nonlinearity. In order to fully appreciate the impact of the relative phase on the power-law's response, we verified and discuss here the ideal cases of minimal and maximal phase differences. In the case of no phase difference, the combined contributions' magnitude would be, for low intensities, comparable to the second order contribution, increasing similarly. For high intensities, it would increase similarly to the fourth order contribution. Here the rate of increase in magnitude, which is proportional to the power-law response, would increase *monotonically*. The transition from second to fourth order response still occurs when a phase difference exists. However, for the intermediate regime, the increase in magnitude is exchanged for rotation, resulting in a weaker power-law response. In the opposite case of a 180° phase difference, the contributions completely interfere destructively, leading to smaller than quadratic response for the intermediate regime. Here the power-law response would initially decrease, passing its minimal point, monotonically approaching towards fourth order nonlinearity. In our simulations, these phase differences in the SH excitation are the origin for the dynamical response and we believe describes the dynamical nonlinear response of the differently phased excitation of the LSPR found by experiment.

To conclude, by coherent control we experimentally unravel the ultrafast dynamical, noninstantaneous nonlinear response in resonant NSs. We see a pronounced decrease in the power-law response when shorter wavelengths arrive prior to longer wavelengths. We show experimentally that TL pulses do not yield the strongest nonlinearity when approaching strong field regime. We introduce a novel theoretical approach, which capture effects beyond the weak-field two-photon regime and describes our experimental observations in an intuitive picture. Since this model is based on the

general behavior of any system with a resonant level it may be used to describe other nonlinear dynamical observations such as the noninstantaneous SHG measured near a resonant intraband transition [46] or the observed deviations of LSPR dephasing times from the ideal harmonic oscillator model [47]. Furthermore, it could be applied to study other systems such as resonant excitonic and polaritonic couplings, SHG

in van der Waals materials [48], or for coherent two-photon luminescence in NSs [49].

[1] O. Avayu, E. Almeida, Y. Prior, and T. Ellenbogen, Nat. Commun. **8**, 14992 (2017).

[2] Z. Yang, P. Chak, A. D. Bristow, H. M. van Driel, R. Iyer, J. S. Aitchison, A. L. Smirl, and J. Sipe, Opt. Lett. **32**, 826 (2007).

[3] T. Rybka, M. Ludwig, M. F. Schmalz, V. Knittel, D. Brida, and A. Leitenstorfer, Nat. Photon. **10**, 667 (2016).

[4] R. W. Newson, J.-M. Ménard, C. Sames, M. Betz, and H. M. v. Driel, Nano Lett. **8**, 1586 (2008).

[5] A. Liu, W. Zhu, D. Tsai, and N. I. Zheludev, J. Opt. **14**, 114009 (2012).

[6] R. Camacho-Morales, M. Rahmani, S. Kruk, L. Wang, L. Xu, D. A. Smirnova, A. S. Solntsev, A. Miroshnichenko, H. H. Tan, F. Karouta *et al.*, Nano Lett. **16**, 7191 (2016).

[7] G. Li, S. Zhang, and T. Zentgraf, Nat. Rev. Mater. **2**, 17010 (2017).

[8] A. Hasan, M. Morshed, A. Memic, S. Hassan, T. J. Webster, and H. E.-S. Marei, Int. J. Nanomed. **13**, 5637 (2018).

[9] L. Catherine and P. Olivier, *Gold Nanoparticles for Physics, Chemistry and Biology* (World Scientific, Singapore, 2017).

[10] A. Krasnok, M. Tymchenko, and A. Alu, Mater. Today **21**, 8 (2018).

[11] K. O'Brien, H. Suchowski, J. Rho, A. Salandrino, B. Kante, X. Yin, and X. Zhang, Nat. Mater. **14**, 379 (2015).

[12] H. Husu, R. Siikanen, J. Makitalo, J. Lehtolahti, J. Laukkanen, M. Kuittinen, and M. Kauranen, Nano Lett. **12**, 673 (2012).

[13] A. I. Fernández-Domínguez, F. J. García-Vidal, and L. Martín-Moreno, Nat. Photon. **11**, 8 (2017).

[14] L. Michaeli, S. Keren-Zur, O. Avayu, H. Suchowski, and T. Ellenbogen, Phys. Rev. Lett. **118**, 243904 (2017).

[15] V. Valev, N. Smisdom, A. Silhanek, B. De Clercq, W. Gillijns, M. Ameloot, V. Moshchalkov, and T. Verbiest, Nano Lett. **9**, 3945 (2009).

[16] S. Liu, M. B. Sinclair, S. Saravi, G. A. Keeler, Y. Yang, J. Reno, G. M. Peake, F. Setzpfandt, I. Staude, T. Pertsch *et al.*, Nano Lett. **16**, 5426 (2016).

[17] M. Kauranen and A. V. Zayats, Nat. Photon. **6**, 737 (2012).

[18] V. Amendola, R. Pilot, M. Frasconi, O. M. Marago, and M. A. Iati, J. Phys.: Condens. Matter **29**, 203002 (2017).

[19] P. Lang, B. Ji, X. Song, Y. Dou, H. Tao, X. Gao, Z. Hao, and J. Lin, Opt. Lett. **43**, 5721 (2018).

[20] E.-M. Roller, L. V. Besteiro, C. Pupp, L. K. Khorashad, A. O. Govorov, and T. Liedl, Nat. Phys. **13**, 761 (2017).

[21] W. P. Putnam, R. G. Hobbs, P. D. Keathley, K. K. Berggren, and F. X. Kärtner, Nat. Phys. **13**, 335 (2017).

[22] C. M. Lazzarini, L. Tadzio, J. M. Fitzgerald, J. A. Sánchez-Gil, and V. Giannini, Phys. Rev. B **96**, 235407 (2017).

[23] L. Roloff, P. Klemm, I. Gronwald, R. Huber, J. M. Lupton, and S. Bange, Nano Lett. **17**, 7914 (2017).

[24] B. Born, S. Geoffroy-Gagnon, J. D. Krupa, I. R. Hristovski, C. M. Collier, and J. F. Holzman, ACS Photon. **3**, 1095 (2016).

[25] J.-S. Huang and Y. Kivshar, Special issue nonlinear and ultrafast nanophotonics, 1333 (2016).

[26] M. R. Shcherbakov, P. P. Vabishchevich, A. S. Shorokhov, K. E. Chong, D.-Y. Choi, I. Staude, A. E. Miroshnichenko, D. N. Neshev, A. A. Fedyanin, and Y. S. Kivshar, Nano Lett. **15**, 6985 (2015).

[27] H. Harutyunyan, A. B. Martinson, D. Rosenmann, L. K. Khorashad, L. V. Besteiro, A. O. Govorov, and G. P. Wiederrecht, Nat. Nanotechnol. **10**, 770 (2015).

[28] M. L. Brongersma, N. J. Halas, and P. Nordlander, Nat. Nanotechnol. **10**, 25 (2015).

[29] M. Shapiro and P. Brumer, *Principles of the Quantum Control of Molecular Processes* (Wiley-VCH, Berlin, 2003).

[30] N. Dudovich, B. Dayan, S. M. Gallagher Faeder, and Y. Silberberg, Phys. Rev. Lett. **86**, 47 (2001).

[31] L. Levin, W. Skomorowski, L. Rybak, R. Kosloff, C. P. Koch, and Z. Amitay, Phys. Rev. Lett. **114**, 233003 (2015).

[32] V. V. Lozovoy, I. Pastirk, K. A. Walowicz, and M. Dantus, J. Chem. Phys. **118**, 3187 (2003).

[33] D. Oron, N. Dudovich, D. Yelin, and Y. Silberberg, Phys. Rev. A **65**, 043408 (2002).

[34] M. I. Stockman, S. V. Faleev, and D. J. Bergman, Phys. Rev. Lett. **88**, 067402 (2002).

[35] D. Brinks, M. Castro-Lopez, R. Hildner, and N. F. van Hulst, Proc. Natl. Acad. Sci. USA **110**, 18386 (2013).

[36] S. Onishi, K. Matsuishi, J. Oi, T. Harada, M. Kusaba, K. Hirosawa, and F. Kannari, Opt. Express **21**, 26631 (2013).

[37] G. Volpe, G. Molina-Terriza, and R. Quidant, Phys. Rev. Lett. **105**, 216802 (2010).

[38] Y. Kojima, Y. Masaki, and F. Kannari, J. Opt. Soc. Am. B **33**, 2437 (2016).

[39] N. Accanto, L. Piatkowski, I. M. Hancu, J. Renger, and N. F. van Hulst, Appl. Phys. Lett. **108**, 083115 (2016).

[40] A. Yariv, *Optical Electronics* (Saunders College Publ., Fort Worth, TX, 1991), Chap. 13.

[41] R. W. Boyd, *Nonlinear Optics* (Elsevier, Amsterdam, 2003).

[42] D. Brinks, R. Hildner, F. D. Stefani, and N. F. van Hulst, Opt. Express **19**, 26486 (2011).

[43] V. Weisskopf, Z. Phys. **63**, 54 (1930).

[44] H. B. Bebb and A. Gold, Phys. Rev. **143**, 1 (1966).

[45] W. Cai and V. Shalaev, *Optical Metamaterials: Fundamentals and Applications* (Springer Science & Business Media, New York, 2009), Chap. 1, p. 24.

[46] C. Guo, G. Rodriguez, and A. J. Taylor, Phys. Rev. Lett. **86**, 1638 (2001).

[47] A. Anderson, K. S. Deryckx, X. G. Xu, G. Steinmeyer, and M. B. Raschke, Nano Lett. **10**, 2519 (2010).

[48] K.-Q. Lin, S. Bange, and J. M. Lupton, Nat. Phys. **15**, 242 (2019).

[49] V. Remesh, M. Stührenberg, L. Saemisch, N. Accanto, and N. F. van Hulst, Appl. Phys. Lett. **113**, 211101 (2018).

2.3 Unlocking coherent control of the ultrafast plasmonic interaction

Unlocking Coherent Control of Ultrafast Plasmonic Interaction

Eyal Bahar,* Uri Arieli, Maayan Vizner Stern, and Haim Suchowski*

Striking a metallic nanostructure with a short and intense pulse of light excites a complex out-of-equilibrium distribution of electrons that rapidly interact and lose their mutual coherent motion. Due to the highly nonlinear dynamics, the photo-excited nanostructures can generate energetic photons beyond the spectrum of the incident beam, where the shortest pulse duration is traditionally expected to induce the greatest nonlinear emission. Here, these photo-induced extreme ultrafast dynamics are coherently controlled by spectrally shaping a sub-10 fs pulse within the timescale of coherent plasmon excitations. Contrary to the common perception, it is shown that stretching the pulse to match its internal phase with the plasmon-resonance increases the second-order nonlinear emission by >25%. The enhancement is observed only when shaping extreme-ultrashort pulses (<20 fs), thus signifying the coherent electronic nature as a crucial source of the effect. A detailed theoretical framework that reveals the optimal pulse shapes for enhanced nonlinear emission regarding the nanostructures' plasmonic-resonances is provided. The demonstrated truly-coherent plasma control paves the way to engineer rapid out-of-equilibrium response in solids state systems and light-harvesting applications.

1. Introduction

Coherent control (CC) is an interference-based approach where the phase-correlations of electromagnetic fields are mutually manipulated to steer dynamical processes in matter. It offers many capabilities across scientific disciplines that include control of chemical reactions,[1–3] study of biological dynamics,[4,5] enhancement of attosecond physics,[6] and steering of quantum

E. Bahar, U. Arieli, M. V. Stern, H. Suchowski
Condensed Matter Physics Department
School of Physics and Astronomy, Faculty of Exact Sciences
Tel Aviv University
Tel Aviv 69978, Israel
E-mail: eyalb@tauex.tau.ac.il; haimsu@tauex.tau.ac.il
E. Bahar, M. V. Stern, H. Suchowski
Center for Light-Matter Interaction
Tel-Aviv University
Tel-Aviv 6779801, Israel

The ORCID identification number(s) for the author(s) of this article can be found under https://doi.org/10.1002/lpor.202100467

information processing.[7–9,10] CC in the optical regime is commonly established by tailoring the temporal shape of a short laser pulse. In the past two decades, the pulse-shaping approach has been extensively used to study and tune the coherent evolution of photo-excited carriers in atomic and molecular systems.[1,11–14] Owing to their long coherence time (hundreds of femtoseconds (fs)), these systems provide comfortable playgrounds to steer the electronic pathways by quantum interference. In turn, CC-induced interference was used to profoundly impact the system's response, including the linear and nonlinear optical emissions.[1–3] Such demonstrations include a surprising fundamental effect in atomic and molecular systems found by Dudovich et. al,[13] showing that resonant excitation is not optimized by maximally compressed pulses due to destructive interference of quantum-pathways in the multiphoton process. In particular, on-demand manipulation and significant enhancement of optical nonlinearities were shown.[1,3,13]

On the other hand, many solid-state systems de-cohere very rapidly. Plasmonic nanostructures, which hold the promise to confine, route, and control light at the nanoscale, constitute such a rapidly de-cohering system. In these nanostructures, the manipulation of the geometrical parameters have enabled the observation of extraordinary linear and nonlinear optical properties.[15–23] Also, the highly-dense radiation initiates complex local dynamics on several time scales (see **Figure 1**a).[24,25] First, it excites a collective coherent electronic redistribution (localized plasmons). These de-cohere in 20–30 fs into nonthermal electrons in a highly energetic out-of-equilibrium state. Then, internal collisions among the electrons bring the excited electronic distribution to a fully thermalized state (after few picoseconds). Lastly, relaxation to the lattice temperature is established by *e*-phonon collisions. Substantial observations of the photo-excited ultrafast relaxation evolution have revealed profound phenomena.[24,26–29] In addition, pulse shaping has recently been used, as a further tool to study plasmonic systems,[30–37] revealing novel spatio-temporal effects[38–41] as well as utilizing their nonlinear optical response for subwavelength control,[42] pulse phase retrieval nonlinear optical generation,[43] polarization-based phenomena,[41,44] and nonlinear multicolor imaging.[31,34,45] However, coherent control of ultrafast plasmon-dynamics

ADVANCED
SCIENCE NEWS
www.advancedsciencenews.com

LASER
& PHOTONICS
REVIEWS

www.lpr-journal.org

Figure 1. Coherent control of the photo-induced extreme ultrafast plasmonic excitation. a) The four stages of the photo-excited electronic dynamics 1) collective coherent electronic motion, plasmons, that de-phase in few femtoseconds into a 2) nonthermal electronic state where electron-electron relaxation occurs by the energetic carriers, 3) the electrons become hot and interact with the cold lattice to reach thermal electron-lattice equilibrium, and the 4) lattice-environment equilibration. During carrier excitation, collective electronic multiphoton excitations are induced and can produce second harmonic emission. Out-of-equilibrium dynamics spans up to the third stage. b) The nanostructure's resonance frequency and linewidth, denoted as ω_r and Γ_{int}, can be illuminated by (Upper panel) a sub-10 fs pulse, with much broader than the nanostructure's bandwidth (BW), or (Lower panel) pulse with narrower BW than the nanostructure's linewidth. c) The experimental setup. A sub-10 fs pulse passes through a 4f pulse shaper consisting of a spatial light modulator (SLM, See Inset). The shaped pulses interact with an array of gold nanostructures, producing SHG emission. The mirror-based setup frees the SLM from dispersion management of the pulse and is used only for CC. d) The interaction can be coherently controlled externally by manipulating the pulse's spectral phase to reroute the accumulative excitation-pathways to constructively interfere. A properly induced stretch pulse, despite having a lower intensity than the transform-limited, may lead to a stronger nonlinear plasmonic excitation and produces more SHG emission.

requires pulse shaping within the short-lived plasmonic coherent evolution, a challenging task so far due to the metals' dephasing time (∼20 fs for Gold). During the past decade, unexpected enhancement in plasmonic interaction by pulse stretching have been studied, raising many fundamental questions about the origin and mechanism of such enhancements in plasmonic hot spots.[46] In recent research from the Van Hulst's group,[31,47] closed loop based coherent control has shown the importance of pure phase control in optimizing the optical nonlinear response for two-photon photoluminescence (TPPL) in plasmonic nanostructures. However, while such TPPL enhancement, mediated by photon absorption, has been observed,[47] an enhancement of a parametric second harmonic generation with direct resonant based interference of pure photon-plasmon interaction is still lacking. Such coherent control, which may allow unprecedented nonlinear optical enhancement in plasmonic systems, as it has in the atomic realm, has however remained elusive.

Here, we demonstrate coherent control of collective electronic dynamics and its direct effect on generated optical nonlinearities. We use sub-10 fs pulse-shaping to match our few-cycle pulse with the internal dynamics of ultrashort plasmonics excitation. We show that, contrary to the common perception, stretching (chirping) the pulse leads to a significant enhancement in the generated second-order optical response exceeding by >25% of the generation at the maximally compressed ("transform-limited") pulse. We further measure the second-order generation (SHG) as a function of the chirp parameter and find that the optimal pulse chirp is asymmetrical in time and depends on the nanostructure's geometrical configuration. We devise a theoretical framework that focuses on the dynamics of broad spectral width pulses to efficiently match the broad electronic resonance (Figure 1b). The theory suggests that the coherently enhanced nonlinearity stems from the constructive interference of excitation pathways driven by the shaped pulse. We present a direct connection

**ADVANCED
SCIENCE NEWS**

www.advancedsciencenews.com

**LASER
&PHOTONICS
REVIEWS**

www.lpr-journal.org
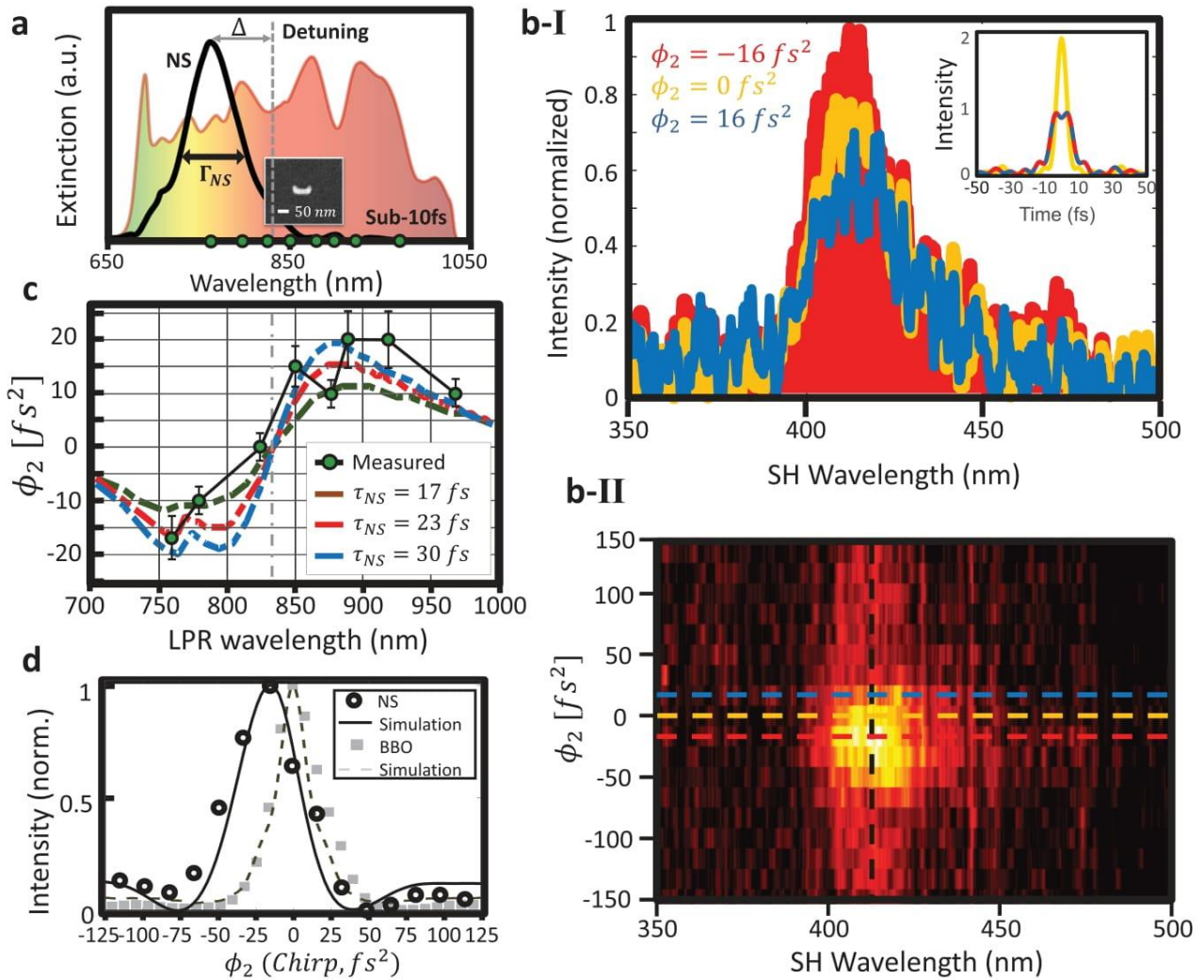
Figure 2. Enhanced nonlinear second harmonic generation by coherent control. a) Measured laser spectrum (colorful, logarithmic) and measured extinction cross-section of the LPR (black line). Inset: A SEM image of a single nanostructure. b-I) Normalized SHG emission for a positive chirp (dashed blue), unshaped transform-limited pulse (yellow) and negative chirp (red) showing an increase of more than 25% compared to the unshaped pulse and enhanced by 50% compared to the opposite-sign chirped pulse. The inset illustrates the pulses' temporal intensity profiles that is maximal for an unshaped pulse and is equal for both chirp signs. b-II) The SHG emission of plasmonic nanostructure as a function of the linear chirp parameter ϕ_2, controlled via the SLM. In stark contrast to the nonlinear instantaneous interaction, maximal nonlinear emission is obtained $\phi_2 = -16\,fs^2$, and not at the highest pulse's intensity. The horizontal dashed lines are cross-sections presented in (b-I). c) Experimental (black dots) measurements of the optimal chirp parameter as a function of the nanostructures resonant wavelengths. Simulation results (dashed) are plotted for several plasmonic decoherence times, τ_{NS}. As seen, the simulated value of $\tau_{NS} \sim 23\,fs$ best match the experimental results. d) Comparison of SHG emitted by plasmonic nanostructures (circles) and by a BBO crystal (squares) as a function of the chirp parameter. The maximal nonlinear response in plasmonic excitation is negatively shifted due to a non-instantaneous response to the interaction, in contrast to the symmetrically centered instantaneous response measured for a BBO crystal. The experimental results coincide with a numerical simulation based on a 3 level model, our theoretical approach to predict dynamical nonlinear plasmonic excitation.

between the optimal pulse durations and the extreme ultrafast plasmonic decoherence. In particular, as our theory relies on the coherent interference of the multiphoton interaction with a coherent resonant mode, it is based on the individual nanostructures localized plasmonic resonance (LPR)'s frequency and linewidth in a perturbative regime. In our simulations, we show that our model is sensitive to variation in plasmonic decoherence on the few-femtosecond scale. Such nonlinear optical enhancement not only provides a clear demonstration for its coherent

manipulation but also expands the current understanding of nonlinear plasmonics enhancement, which has been relaying so far on geometrical manipulation of the nanostructures.[15–18,27,48]

In our experiments, we use ultrashort pulses with a temporal resolution of sub-10 fs pulse, spanning a bandwidth of more than 300 nm (Venteon Dual, Laser-Quantum, measured linear spectrum in **Figure 2**a). The pulses illuminate arrays of U-shaped gold nanostructures, each with different localized plasmon resonance (LPR) (spectral extinction cross-section in Figure 2a, see

**ADVANCED
SCIENCE NEWS**

www.advancedsciencenews.com

LASER
& PHOTONICS
REVIEWS

www.lpr-journal.org

Supporting Information for more details). Normal incidence second harmonic generation (SHG) was measured for each spectral phase applied to the spatial light modulator (SLM). In our experiments, the ultrashort pulses' spectral bandwidth exceeds the resonance linewidth of the nanostructures' LPR, (~70 nm Full width-half-max, FWHM). This allows us to simultaneously excite the entire bandwidth of the metallic nanostructure's LPR response, a requirement for coherent control, in addition to enable to reach shorter timescales. This is unlike most previous ultrafast or nonlinear plasmonic experiments that operate with much narrower pulse bandwidths.

We coherently alter the driving pulse shape, using a homemade dispersionless pulse shaper based SLM. The pulse shaper was carefully designed to effectively free the SLM from dispersion management of few-cycle pulses, critically needed for high-fidelity shaping within the plasmonic lifetimes (Supporting Information). We have verified that the pulse at the illumination plane is maximally compressed in terms of its linear chirp. Any additional spectral phase applied by the SLM results in a shaped (chirped) pulse with broader temporal width and decreased intensity.

2. Results

Figure 2b shows the measured SHG emission from a plasmonic nanostructure with a resonant wavelength of 760 nm as a function of the quadratic spectral phase parameter, ϕ_2 (a.k.a linear chirp). While the pulse spectrum is centered at 850 nm, the plasmonic mediated SHG is slightly blue shifted. This effect, also observed in previous works, is caused by the plasmonic spectral shape of absorption and scattering cross-section.[31] The SHG spectrum induced by the transform-limited pulse ($\phi_2 = 0$) is shown in yellow.

We note that transform-limited pulse, which has zero-chirp and thus with any pulse's highest peak-intensity is usually expected to induce a maximal nonlinear optical response. Illuminating the nanostructures with positive linear chirp ($\phi_2 = 16\ \text{fs}^2$, blue) results, as expected by a stretched pulse, in reduced SHG emission (positive chirp corresponds to a pulse where its higher frequencies arrive first). However, negative linear chirp ($\phi_2 = -16\ \text{fs}^2$, red) shows an increased nonlinear emission of >25% in the accumulated SHG compared to the transform-limited pulse. In Figure 2b(II), we introduce a map of the measured SHG emission for a larger range of linear chirp ($-150\ \text{fs}^2$ to $150\ \text{fs}^2$ respectively), confirming clear maxima at $\phi_2 = -16\ \text{fs}^2$. Note, the pulse duration spans from sub-10 fs (at $\phi_2 = 0$, maximal pulse peak intensity) to ~155 fs at $\phi_2 = \pm150\ \text{fs}^2$ (see Supporting Information for more details). Contrary to common perception, in plasmonic nanostructures, the maximal nonlinear generation does not occur when maximizing the peak intensity of the pulse (i.e., the shortest pulse).

We compare the results with the SHG signal from a commonly used Beta-Barium-Borate (BBO) nonlinear crystal (see Figure 2d), which has an instantaneous nonlinear response as it is lossless and dispersionless in the near-infrared and optical regime (as dictated by the Kramers–Kronig relations). As expected, in BBO, the maximal SHG is obtained with a transform-limited pulse illumination. We also observe that in distinction to the sign-symmetrical intensity profile found in the BBO crystal,

in plasmonic nanostructures, the nonlinear excitation is asymmetrical in relation to the chirp parameter. As can be observed, the nonlinear response has an asymmetrical shape in relation to the chirp phase's sign. The asymmetry highlights that the plasmonic excitation process consists of a nontrivial coherent response that contributes to the multiphoton structure of the nonlinear interaction that is crucial in the first few femtoseconds of the excitation.

To deepen the understanding of the extreme ultrafast excitation, we study plasmonic nanostructures ranging in their effective lengths, from 130 to 300 nm (correspond to LPR's wavelengths 770 to 970 nm, respectively). We find a correlation between the optimal linear chirp with the LPR wavelength of the U-shaped nanostructures (see Figure 2c). Importantly, we see that the optimal linear chirp sign is inversely related to detuning, which is defined by the relative location of the plasmonic resonance to the pulse's central wavelength (See Figure 2a). Thus, in positively detuned interactions, where the plasmonic resonant frequency (wavelength) is higher (lower) than the central frequency (wavelength) of the incoming pulse, the optimal linear chirp is negative.

We utilize a theoretical and numerical approach that predicts the influence of pulse shaping on the measured optical nonlinear response in nanostructures, which allows to analyze the evolution of the interaction process capturing the inner dynamics in the multiphoton excitation. Our model aims to describe the ultrafast plasmonic dynamics of an isolated nanostructure during the effective timescale for plasmonic dephasing and ignores lattice scattering effects, strong-field effects or other effects that might be induced by the array. In a nutshell, we have considered the interaction as a three-level resonant model solved to the second-order in a time-dependent perturbation framework. The nonlinear polarization reads as follow:

$$P_{NL}^{(2)}(\Omega) \propto \sum_{\omega} \chi_{\text{eff}}^{(2)}(\omega, \omega_{NS}, \Gamma_{NS})\, E(\omega)\, E(\Omega - \omega)$$

$$= \sum_{\omega} \chi^{(2)} A(\omega) A(\Omega - \omega) \frac{e^{i[\phi(\omega)+\phi(\Omega-\omega)]}}{\omega - \omega_{NS} + i\Gamma_{NS}} \tag{1}$$

where $P_{NL}^{(2)}(\Omega)$ is the nonlinear polarization at frequency Ω, $E(\omega)$ and $E(\Omega - \omega)$ are the linear fields of the fundamental mode, where the generated frequency follows $\Omega = \omega + (\Omega - \omega)$ and $\chi_{\text{eff}}^{(2)}(\omega, \omega_{NS}, \Gamma_{NS}) \approx \frac{\chi^{(2)}}{\omega - \omega_{NS} + i\Gamma_{NS}}$ is the spectral-dependent local nonlinear susceptibility that depends on the nanostructures parameters ω_{NS} and Γ_{NS}. The $\chi^{(2)}(\omega, \omega_{NS}, \Gamma_{NS})$ expands the known geometrical-dependent-only $\chi^{(2)}$ term, which results in a generalized nonlinear emission $E_{SHG}(\Omega) \propto \int P_{NL}^{(2)}(\Omega) \times E(\Omega)$.[18] Our findings spotlight the importance of ultrafast phenomena in analyzing resonant nanostructures, appending to the ongoing efforts in understanding the crucial role of the dynamics in the interaction with singular nanostructures and collective arrays.[19,27,49,50] Our method for analysis of the multispectral interaction is captured in the schematic illustration depicted in **Figure 3**a, which directly reflects the theoretical model presented in Equation (1) (See Supporting Information for more information). As portrayed in Figure 3a, the induced second-order interaction can be viewed as a summation of complimentary frequency-pairs that add-up to the energy of the second harmonic frequency

ADVANCED
SCIENCE NEWS
www.advancedsciencenews.com

LASER
& PHOTONICS
REVIEWS

www.lpr-journal.org

a Resonant 3-level multi-pathways resonant interaction

b Geometrical representation multi-pathways interference

c
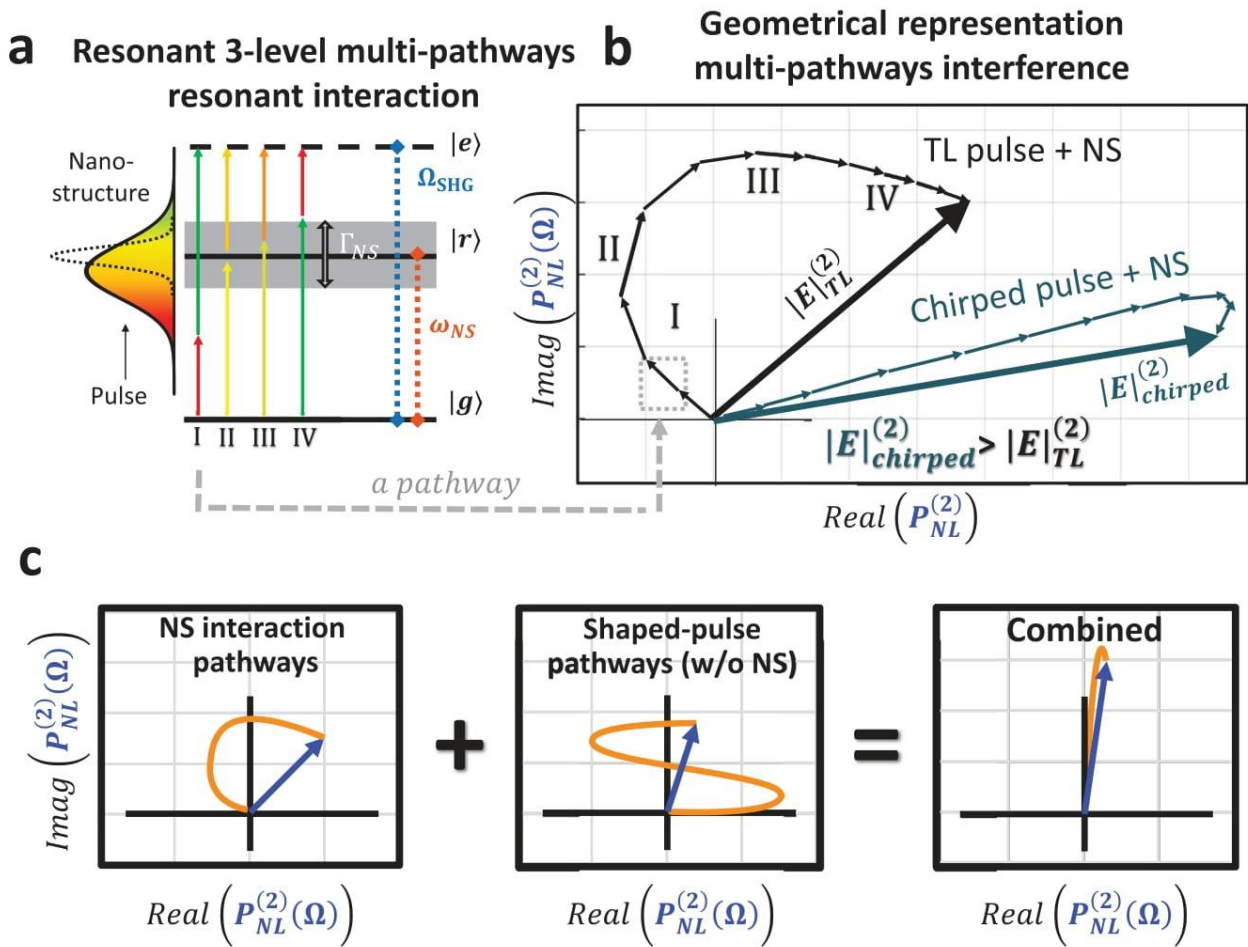
Figure 3. The plasmonic-mediated second order interaction as the 3-level. a) An energy level diagram of the pulse-nanostructure interaction. The broadband interaction induces multiple excitation pathways (Feynman paths, four possible pathways are shown) that result in SHG emission. The interference between these interaction pathways can be coherently controlled via spectral pulse shaping. b) Complex valued representation of the Feynman paths of the plasmonic-mediated second-order excitation $P_{NL}^{(2)}$. The broadband interaction induces multiple pathways for excitation (small arrows in the diagram). Each interaction can be represented by the interference of multiple pathways, where the orientation of each arrow stems from the combined phase of both the pulse and nanostructure. The accumulated amplitude, represented by a large arrow, corresponds to the measured intensity of the nonlinear plasmonic excitation. The Feynman diagram of $P_{NL}^{(2)}(\Omega)$ for a maximally compressed pulse, E_{TL} and a chirped pulse, E_{chirp} are illustrated. The chirped pulse enhances the interaction by rerouting the accumulative pathways to constructively interfere. Marked along the trajectory, I–IV, correspond to 4 possible pathways illustrated in Figure 3a. c) The Feynman diagram for the nonlinear ultrafast electronic excitation in the case of (left) a transform limited pulse. (middle) the optimal phase function predicted by the 3-level model without the nanostructures contribution and (right) the combined spectral contribution of both pulse and nanostructure, maximally elongating the amplitude of the interaction according to the 3-level model.

energy, illustrated by the excited state $|e\rangle$, which corresponds to the second harmonic frequency generated at that energy. The broadband pulse induces various sum frequency events, varying in the composition of their commentary frequency-pairs (illustrated by vertical arrows in Figure 3a). Due to the resonant nature of the interaction, each frequency-pair that interacts with the nanostructure contributes in both in amplitude and phase according to the detuning from the plasmonic resonate level $|r\rangle$. The accumulation of the complex-valued events coherently interferes and determines the total measured second harmonic outcome.

From the theory, we find that the nonlinear interaction's coherent structure consists of two contributions: the spectral phase of the ultrafast pulse and the nanostructure's inherent resonant

phase. The pulse contribution, controlled at will by the SLM, serves as a probe to study dynamical interactions. The nanostructure's contribution is composed of the amplitude and phase of the spectrally dependent plasmonic response, stemming from the collective electron dynamics, which also incorporate effects of geometry and environment.

To further gain an intuitive physical understanding of the interaction process, we use the pictorial representation in the complex plane along with the numerical simulations. The complex plane representation portrays all spectral components' accumulative contributions in the interaction and is calculated based on a three-level system approach, illustrated in Figure 3a and further described in Figure 3b (see more details in the Supporting Information). Our coherent control demonstrations can be

78

ADVANCED
SCIENCE NEWS

www.advancedsciencenews.com

LASER
& PHOTONICS
REVIEWS

www.lpr-journal.org

intuitively explained by the interfering pathways picture on the complex plane (see Figure 3b). Each excited nonlinear frequency is generated by the coherent accumulation of multiple individual pathways. Each pathway is set by a frequency pair in the driving pulse $\{\omega, \Omega_{SHG} - \omega\}$, dictating $\Omega_{SHG} = \omega + (\Omega_{SHG} - \omega)$. An example for four pathways, set by four frequency pairs, illustrated as paths I to IV.

Inherent to the nanostructures' excitation dynamics, the plasmonic response induces self-interfering pathways to the excitation (Figure 3c, left). However, a properly shaped pulse will induce constructive interference between the accumulated pathways, rearranging the trajectory to maximize the nonlinear excitation (Figure 3c, right). Since the unaltered pathways consist of the intrinsic destructive interference inherent to the interaction, a reciprocal manipulation of the ultrashort pulse leads to constructive interference in the interaction and to an enhanced excitation beyond any other pulse shapes, including the maximally compressed, transform-limited pulse. Our simulations that agree well with the experimental results provide a complimentary and intuitive understanding for the observed coherently controlled interaction.

3. Discussion

We utilize our numerical simulations and compare them with the experimental results of the optimal linear chirp for a variety of nanostructures across the spectral landscape. Such simulations offer a window to variations in the ultrafast plasmonic response and offer a way to determine the lifetime of the coherent excitation, τ_{NS}, which is inversely related to the effective nanostructures linewidth Γ_{NS}. We assume that Γ_{NS}, which takes an inherent part in the coherent excitation process, is based on the individual plasmonic nanostructure (see Refs. [51, 52, 53] for more information on the complexity of linewidths in plasmonic metasurfaces). It can differ from the experimental linewidth value extracted by far-field measurements, which might be broader as a result of inhomogeneity in the array. Γ_{NS} is related to the plasmonic damping factor derived for localized plasmonic resonance taking into consideration the shortened mean free path of electrons in gold nanostructures (see Section 2.3 for more information[19]). We also note that the contribution of electronic loss to the coherent collective dynamics in ultrafast timescales is yet to be fully understood. It consists of processes such as electron–electron scattering, nonthermalized electron formation, and evolution, which are not trivially contributing to the few-femtosecond regime.[51,52] A summary of our simulations is presented in Figure 2c. The optimal chirp parameter is plotted as a function of the nanostructure's LPR for three plasmonic decoherence timescales, 17, 23, and 30 fs, which can be derived for plasmonic nanostructures based on common literature or measured in similar configurations,[19,48,54,55] viewing the plasmonic lifetime based on free electron absorption and geometry. As seen, the numerical simulations provide very high sensitivity to variations in decoherence times. Worth noting that in the numerical analysis, the effective interaction linewidth γ_{NS} is the only parameter that is not determined experimentally.

Using our theoretical analysis, which allows predicting the nonlinear excitation leading to SHG for any pulse shape, detuning, and coherence time parameters, we find the optimal pulse shape that globally maximizes the nonlinear interaction. More specifically, we find that for plasmonic nanostructures, the optimal spectral phase is $\tan^{-1}(\frac{\Gamma_{atan}}{\omega - \omega_{atan}})$, where Γ_{atan} and ω_{atan} determine the width and the central frequency of the inverse tangent function, accordingly. Maximal enhancement of SHG for a specific design is obtained when the characteristics of the plasmonic nanostructure set the parameters $\Gamma_{atan} = \Gamma_{NS}$ and $\omega_{atan} = \omega_{NS}$ (see **Figure 4**). Since the optical nonlinearity is produced separately for each frequency in the manifold of target second harmonic excitations, the optimal pulse shape prediction requires analysis of a range of frequencies (see Supporting Information for more details).

We have verified our predictions experimentally and consistently observe maximal enhancement for the predicted optimal phases. Interestingly, by setting different parameters to the inverse tangent spectral phase, we can uniformly suppress the SHG emission for the central emission profile, maintaining constant profiles of the emission spectra in the generated signal. Taking advantage of this quality, we are able to continuously vary the inverse tangent function to distinctly yet simultaneously facilitate coherent control capabilities in a single-shot. Such control allows contrastingly manipulating to enhance, maintain, or suppress specific components in the induced nonlinear spectrum. In order to demonstrate these effects, we selectively manipulate the central spectral profile of the nonlinear emission while effectively maintaining a general form of the emission profile. For example, by setting the parameters to $\omega_{atan} = \omega_{NS}$ and $\Gamma_{atan} = -\Gamma_{NS}$, we demonstrate variations in the intensity of up to 200% over the intensity of the SHG emission for particular frequencies while maintaining a constant emission profile for other frequencies. The ability to induce differential control, which is shown to suppress only the central profile of the nonlinear emission, stems from the interference of pathways that correspond to the excited frequency Ω_{SHG}. Therefore, as the interference for each excited nonlinear frequency has a different accumulated composition, the interaction process is effectively manipulated separately for each of the second harmonic frequency components.

4. Conclusion

To conclude, by ultrafast pulse shaping within the coherence time of the plasmonic evolutions, we unlock fundamental coherent control capabilities and enable the steering and enhancement of the nonlinear optical generation in plasmonic nanostructures. We demonstrate a fundamental effect of coherent control in resonant media[13] for localized plasmonic nanostructures. Such realization, which requires pulse shaping capabilities in the single-cycle regime, expands the concept to extreme limits. While coherent excitation in systems with high loss, such as LPRs, are commonly overlooked due to their short-lived, out-of-equilibrium nature, we show that by properly shaping the incoming pulse, the induced excitation can be coherently manipulated throughout the interaction. Notably, such control substantially modifies the nonlinear electronic dynamics with only subtle modifications to the temporal pulse shape and width. Also, the experimental results show that competing processes in the interaction, such as the formation of highly energetic non-thermalized electrons, do not play a significant role in
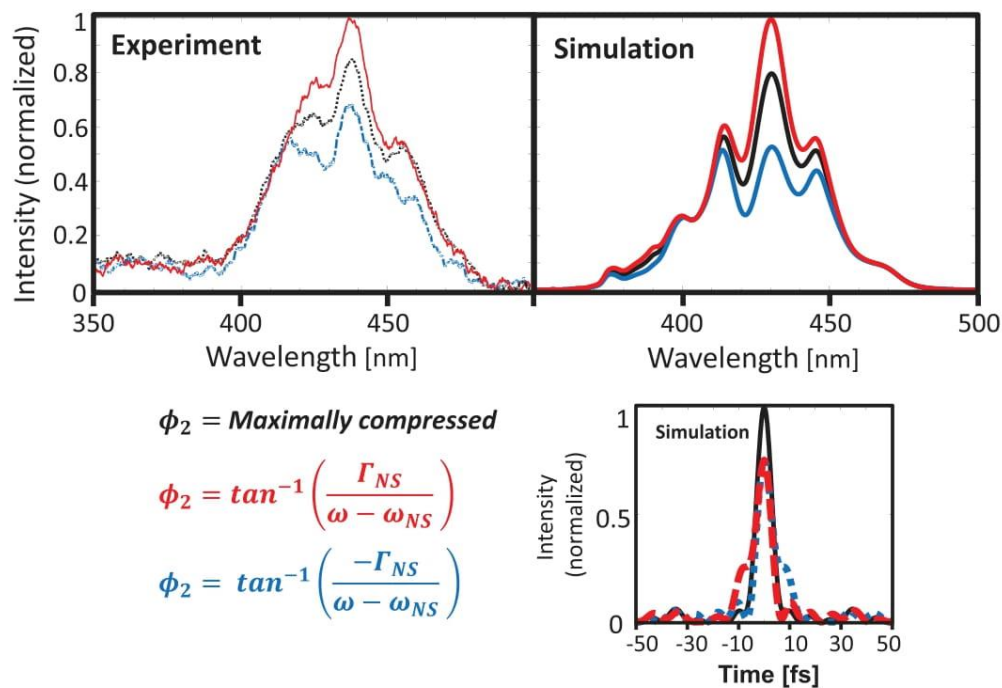
Figure 4. Optimal nonlinear plasmonic excitation by manipulation the pathways interference. Measured (upper left) and simulated (upper right) SHG induced by the plasmonic excitation with LSP resonance of $\lambda_r = 890$ nm for the three pulse shapes: (red) The optimal pulse shape, which is obtained by a spectral phase of an inverse tangent phase function—as predicted by the 3-level model, (black) an unshaped, maximally compressed pulse, and (blue) an example of differentialy suppressing pulse shape, diminishing the central profile of the generated spectrum while maintaining a constant emission frame. The spectral phase of the inverse tangent function, which is applied by the SLM, can be continuously tuned by changing the value of Γ_{atan}, to produce pulse shapes that vary the generated nonlinear plasmonic excitation spectrum. As dictated by Fourier-transform, the pulse shapes are only slightly deformed in their temporal profiles (lower right) yet have a dramatic effect in the generation of the nonlinear signal.

hindering the initial coherence of the plasmonic state. Based on the accumulative interference of the individual spectral components, our theoretical framework is found suitable to explain the experimental results and predict the optimal pulse for maximal global nonlinear enhancement. We believe that our coherent control demonstration will promote a paradigm shift in the view of nanoscale nonlinearities, where the origin of optical nonlinearity in nanostructures does not stem only from the enhanced absorption but can rather be dominated by coherent interference.

Furthermore, our fundamental demonstration links the manipulation of photo-excited nanostructure evolution to the vast coherent control schemes explored in atomic and molecular systems. Thus, opening a doorway to implement ultrafast control based on intrinsic plasmonic dynamics is expected to unlock entirely new capabilities desirable in active spatiotemporal metasurfaces at extreme ultrafast speeds.[50] Beyond the significant contribution to fundamental research, we expect that coherent control at extreme ultrafast timescales will provide novel control methods in metamaterials-based applications in nonlinear microscopy, electronic and excitonic dynamics in 2D metamaterials, cancer phototherapy as well as artificial and natural light-harvesting complexes.

Supporting Information

Supporting Information is available from the Wiley Online Library or from the author.

Conflict of Interest

The authors declare no conflict of interest.

Data Availability Statement

The data that support the findings of this study are available from the corresponding author upon reasonable request.

80

[1] T. Brixner, G. Gerber, *ChemPhysChem* **2003**, *4*, 418.

[2] M. Shapiro, P. Brumer, *Principles of Quantum Control of Molecular Processes*, Wiley, Hoboken, NJ **2003**.

[3] Y. Silberberg, *Annu. Rev. Phys. Chem.* **2009**, *60*, 277.

[4] W. Wohlleben, T. Buckup, J. L. Herek, M. Motzkus, *ChemPhysChem* **2005**, *6*, 850.

[5] I. I. Rabi, J. R. Zacharias, S. Millman, P. Kusch, *Phys. Rev.* **1938**, *53*, 318.

[6] H. Katsuki, N. Takei, C. Sommer, K. Ohmori, *Acc. Chem. Res.* **2018**, *51*, 1174.

[7] C. P. Koch, *J. Phys. Condens. Matter* **2016**, *28*, 213001.

[8] J. N. Becker, J. Görlitz, C. Arend, M. Markham, C. Becher, *Nat. Commun.* **2016**, *7*, 1.

[9] M. Kues, C. Reimer, P. Roztocki, L. R. Cortés, S. Sciara, B. Wetzel, Y. Zhang, A. Cino, S. T. Chu, B. E. Little, D. J. Moss, L. Caspani, J. Azaña, R. Morandotti, *Nature* **2017**, *546*, 622.

[10] E. Shahmoon, S. Levit, R. Ozeri, *Phys. Rev. A - At. Mol. Opt. Phys.* **2009**, *80*, 033803.

[11] C. P. Koch, M. Lemeshko, D. Sugny, *Rev. Mod. Phys.* **2019**, *91*, 035005.

[12] A. P. Heberle, J. J. Baumberg, K. Köhler, *Phys. Rev. Lett.* **1995**, *75*, 2598.

[13] N. Dudovich, B. Dayan, S. M. Gallagher Faeder, Y. Silberberg, *Phys. Rev. Lett.* **2001**, *86*, 47.

[14] L. Levin, W. Skomorowski, L. Rybak, R. Kosloff, C. P. Koch, Z. Amitay, *Phys. Rev. Lett.* **2015**, *114*, 233003.

[15] M. Kauranen, A. V. Zayats, *Nat. Photonics* **2012**, *6*, 737.

[16] S. Keren-Zur, O. Avayu, L. Michaeli, T. Ellenbogen, *ACS Photonics* **2016**, *3*, 117.

[17] X. Ni, N. K. Emani, A. V. Kildishev, A. Boltasseva, V. M. Shalaev, *Science (80-.)* **2012**, *335*, 427.

[18] K. O'Brien, H. Suchowski, J. Rho, A. Salandrino, B. Kante, X. Yin, X. Zhang, *Nat. Mater.* **2015**, *14*, 379.

[19] W. Cai, V. Shalaev, O. Metamaterials, *Fundamentals and Applications*, Springer, New York **2010**.

[20] N. C. Panoiu, W. E. I. Sha, D. Y. Lei, G. C. Li, *J. Opt.* **2018**, *20*, 083001.

[21] C. Ciracì, E. Poutrina, M. Scalora, D. R. Smith, *Phys. Rev. B - Condens. Matter Mater. Phys.* **2012**, *86*, 115451.

[22] C. Li, X. Lu, A. Srivastava, S. D. Storm, R. Gelfand, M. Pelton, M. Sukharev, H. Harutyunyan, *Nano Lett.* **2021**, *21*, 1599.

[23] E. Drobnyh, M. Sukharev, *J. Chem. Phys.* **2020**, *152*, 094706.

[24] S. Kumar, A. K. Sood, *ArXiv* **2018**, 131.

[25] G. V. Hartland, *Chem. Rev.* **2011**, *111*, 3858.

[26] T. Stoll, P. Maioli, A. Crut, N. Del Fatti, F. Vallé, *Eur. Phys. J. B* **2014**, *87*, 23.

[27] G. Li, S. Zhang, T. Zentgraf, *Nat. Rev. Mater.* **2017**, *2*, 1.

[28] Y. Cho, D. J. Wu, W. Ponizovskaya, E. Chaturvedi, P. Bratkovsky, A. M. Wang, S. Y. Zhang, X. Wang, F. Shen, *Opt. Express* **2009**, *17*, 17652.

[29] D. Bayer, C. Wiemann, O. Gaier, M. Bauer, M. Aeschlimann, *J. Nanomater.* **2008**, *2008*, 249514.

[30] P. Tuchscherer, C. Rewitz, D. V. Voronine, F. J. García de Abajo, W. Pfeiffer, T. Brixner, *Opt. Express* **2009**, *17*, 14235.

[31] L. Piatkowski, N. Accanto, N. F. Van Hulst, *ACS Photonics* **2016**, *3*, 1401.

[32] J. S. Huang, D. V. Voronine, P. Tuchscherer, T. Brixner, B. Hecht, *Phys. Rev. B - Condens. Matter Mater. Phys.* **2009**, *79*, 195441.

[33] T. Rybka, M. Ludwig, M. F. Schmalz, V. Knittel, D. Brida, A. Leitenstorfer, **2016**.

[34] V. Remesh, M. Stührenberg, L. Saemisch, N. Accanto, N. F. Van Hulst, *Appl. Phys. Lett.* **2018**, *113*, 211101.

[35] E. Bahar, U. Arieli, M. Mrejen, H. Suchowski, *Phys. Rev. B* **2020**, *101*, 035141.

[36] T. Utikal, M. I. Stockman, A. P. Heberle, M. Lippitz, H. Giessen, *Phys. Rev. Lett* **2010**, *104*, 113903.

[37] T. W. Lee, S. K. Gray, *Phys. Rev. B - Condens. Matter Mater. Phys.* **2005**, *71*, 035423.

[38] D. Brinks, R. Hildner, F. D. Stefani, N. F. van Hulst, *Opt. Express* **2011**, *19*, 26486.

[39] N. Accanto, L. Piatkowski, J. Renger, N. F. Van Hulst, *Nano Lett.* **2014**, *14*, 4078.

[40] J. A. Maytorena, W. L. Mochán, *Phys. Rev. B* **1998**, *57*, 2580.

[41] H. Maekawa, E. Drobnyh, C. A. Lancaster, N. Large, G. C. Schatz, J. S. Shumaker-Parry, M. Sukharev, N. H. Ge, *J. Phys. Chem. C* **2020**, *124*, 20424.

[42] M. Aeschlimann, M. Bauer, D. Bayer, T. Brixner, F. J. García De Abajo, W. Pfeiffer, M. Rohmer, C. Spindler, F. Steeb, *Nat. 2007 4467133* **2007**, *446*, 301.

[43] N. Accanto, J. B. Nieder, L. Piatkowski, M. Castro-Lopez, F. Pastorelli, D. Brinks, N. F. Van Hulst, *Light Sci. Appl.* **2014**, *3*, e143.

[44] M. Aeschlimann, M. Bauer, D. Bayer, T. Brixner, S. Cunovic, F. Dimler, A. Fischer, W. Pfeiffer, M. Rohmer, C. Schneider, F. Steeb, C. Strüber, D. V. Voronine, *Proc. Natl. Acad. Sci* **2010**, *107*, 5329.

[45] N. Accanto, L. Piatkowski, I. M. Hancu, J. Renger, N. F. Van Hulst, *Appl. Phys. Lett.* **2016**, *108*, 083115.

[46] M. Aeschlimann, T. Brixner, S. Cunovic, A. Fischer, P. Melchior, W. Pfeiffer, M. Rohmer, C. Schneider, C. Strüber, P. Tuchscherer, D. V. Voronine, *IEEE J. Sel. Top. Quantum Electron.* **2012**, *18*, 275.

[47] N. Accanto, P. M. De Roque, M. Galvan-Sosa, I. M. Hancu, N. F. Van Hulst, *Nanophotonics* **2021**, *10*, 597.

[48] N. Del Fatti, F. Vallée, *Appl. Phys. B Lasers Opt.* **2001**, *73*, 383.

[49] L. Michaeli, S. Keren-Zur, O. Avayu, H. Suchowski, T. Ellenbogen, *Phys. Rev. Lett.* **2017**, *118*, 243904.

[50] A. M. Shaltout, V. M. Shalaev, M. L. Brongersma, *Science* **2019**, *364*, eaat3100.

[51] M. Quinten, Optical Properties of Nanoparticle Systems: Mie and Beyond **2011** - See sections 3.1.3, 5.3.2.2, 5.3.2.3 and 8.2.

[52] F. Vallée, N. Del Fatti, *Plasmon. Theory Appl.* **2013**, 167 -.

[53] L. Michaeli, H. Suchowski, T. Ellenbogen, *Laser Photon. Rev.* **2020**, *14*, 1900204.

[54] C. Sönnichsen, T. Franzl, T. Wilk, G. von Plessen, J. Feldmann, O. Wilson, P. Mulvaney, *Phys. Rev. Lett.* **2002**, *88*, 077402.

[55] Y. Nishiyama, K. Imaeda, K. Imura, H. Okamoto, *J. Phys. Chem. C* **2015**, *119*, 16215.

3 Outlook

Ultrafast and nonlinear optics have revolutionized our understanding of the structure and dynamics of light-matter interaction (*29*, *165*). Naturally, ultrafast pulse shaping is a powerful tool for controlling ultrafast nonlinear phenomena. State-the-art capabilities of pulse-shaping schemes in nanophotonic systems are emerging in applications for neuroscience, high harmonic generation, and quantum information processing. However, despite coherent control's great success in research of atomic and molecular systems, coherent control is still in its infancy for systems that exhibit complex spatiotemporal dynamics such as nanophotonics and atomic layered materials. As an outlook to the research and observations made during my PhD, I hope to motivate others to continue utilizing coherent control and pulse shaping nonlinear optical interaction in nanophotonics and 2D materials. I have faith that my work provides the observations and ground basis for coherent control application in plasmonic or atmoic layered materials systems.

There are many possible research directions for utilizing coherent control of nonlinear ultrafast phenomena by spectrally shaping the excitation pulse. Here, I will briefly mention two immediate outlooks. The first, is applying coherent control on the exciton resonance in monolayer WSe2, a project continuing the line of coherent control over resonant interaction in metamaterials. The project is already in process, showing promising preliminary experimental results. The second research direction regards the strong spatio-temporal couplings we have encountered in applying our pulse shaping apparatus. We suggest to research this phenomenon, which is usually considered parasitic, for finding a route to use it as a novel tool for spatio-temporal coherent control.

3.1 Nonlinear resonant optical interaction in 2D layered materials

Since the experimental apparatus built for the application of coherent control schemes in plasmonic systems is highly versatile, it is suitable for a wide range of nanometer or larger length scales as well as for timescales spanning femtoseconds to picoseconds. In addition, other ultrafast nonlinear phenomena such as FWM or third harmonic generation can be examined by this coherent control apparatus. The theoretical framework we developed

relies on a generalized view of resonant interaction and can be applicable for many other systems with a resonant mode.

Hence, an immediate research direction is to study other nanoscale resonant interaction with more complex resonant structure, such as resonant excitons in transition-metal-dichalcogenide (TMD) materials. Materials such as Graphene, Layered hBN, WSe2 and more are currently gaining much attention thanks to their nonlinear properties and their long lived coherences making them very attractive for quantum information processing research.

In the past few months, jointly with Omri Meron, we have been able to show coherent control of the A-exciton resonance in monolayer WSe2. Utilizing our ultra-broadband pulse-shaper, we coherently controlled the third-order nonlinear response and showed a 2.3-fold enhancement beyond a maximally compressed pulse. Initial results from our work have been presented by Omri Meron in a peer-reviewed poster presentation entitled "Coherent control of the excitonic resonance in WSe2" (Nanometa 2022).

3.2 Spatiotemporal control

Optical pulse shaping is a fundamental tool for coherent control of light-matter interaction. While such control enables the measurement of ultrafast temporal dynamics, simultaneous spatio-temporal control is required for studying non-local ultrafast charge dynamics at the nanoscale. However, obtaining accurate spatial control at a sub-wavelength resolution with conventional optical elements poses significant difficulty.

During the construction of various ultrafast 4f SLM-based pulse shapers I have built throughout my PhD, we have encountered strong spatio-temporal couplings in such systems. For example, while assembling the single pulse shaper towards the realization of the research described in the second article of this dissertation, we observed a spatial splitting of the outgoing beam when we apply a V-shape phase mask. Meaning that the V-shape phase, which we apply to induce a temporal split to the pulse, also leads to a spatial splitting of the outgoing beam. This observation was a strong motivation in constructing the double-pass configuration that removed the unwanted effect in the experiment. However, while these effects are usually regarded as parasitic, these observations spiked the idea to explore these effects as a tool to study spatio-temporal coherent control schemes in the fs-nanometer scale.

Induced by light-matter interaction, 2D materials such as single\bilayer Graphene, hBN or stacked materials forming super lattices, display spatio-temporal phenomena on the fs and nanometer scales. Fs nanometer spatio-temporal coherent control could deepen the understanding of ultrafast dynamics in systems where the mean free path can be up to several μm (*166–168*), including processes such as Bloch oscillations, Landau-Zener tunneling in super lattices or electron transport in graphene.

While spatio-temporal coupling effects found in 4f systems have long been thought of as parasitic effects reducing the precision of control of the spatial and temporal profile (*162*), making use of the spatio-temporal modulation produced by a single pass 4f-SLM system can be explored as a tool to study such spatio-temporal phenomena.

A first step based on these ideas has been already taken, in a project lead by Mr. Shlomi Korman, a Master student in our team. Our mutual work, led by Shlomi, was recently published a paper entitled "Spatio-temporal ultrafast pulse shaping at the femtosecond-nanometer scale", Optics Letters 47.17 (2022): 4279-4282 (*169*). In the manuscript, we experimentally demonstrate spatial steering at the sub-micron scale of SHG from NSs. A Figure from the manuscript is present here (Figure 11), illustrating the
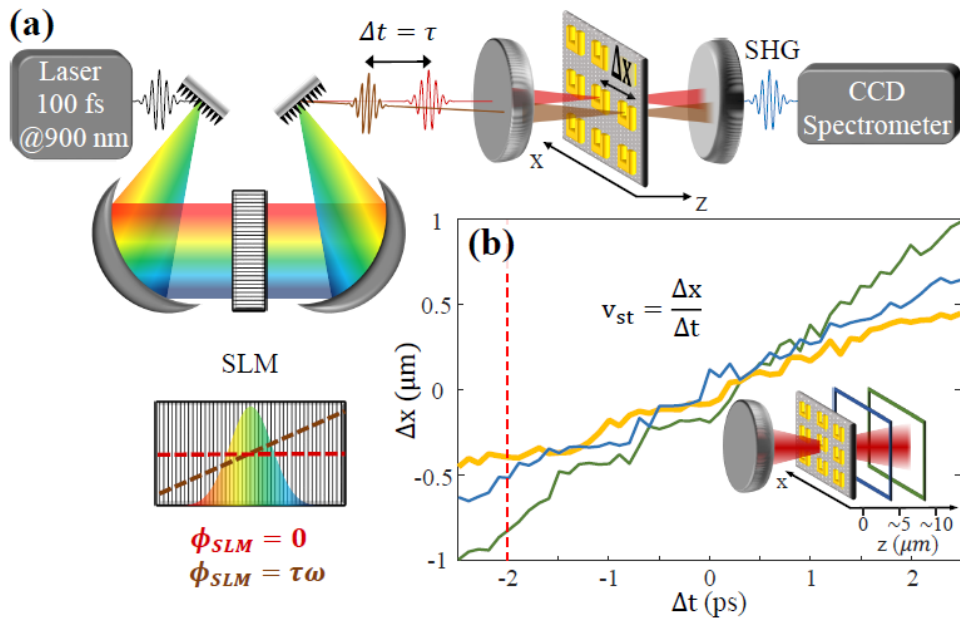
Figure 11. Illustration of a 4f SLM-based spatio-temporal control in nanostructures. (a) The experimental apparatus is composed of 100 fs laser pulses passing through an SLM-based single-pass pulse shaper. The shaped pulses interact with gold NS's and SHG is collected. The applied spectral phase, e.g. a linear phase $\phi = \tau\omega$ debited in brown, shapes the pulse both temporally and spatially, enabling to shift the position and delay of the pulse interaction (b) The beam displacement as a function of applied linear phase, at the experimental focus (orange) and of two other focus planes further in the optical axis. Figure adopted from Ref. [169].

general setup and observations of spatial steering at the sub-micron scale of SHG from NSs.

The introduced scheme for tunable spatiotemporal pump-probe experiments serves as the first step in developing a richer controllable SLM-based spatio-temporal pulse shaper. Future exploration of the relation between the spectral phase and spatio-temporal shape can provide a rich basis for coherent control experiments of ultrafast transport phenomena and non-localized resonant interaction.

4 תקציר

בעשורים האחרונים נעשתה התקדמות יוצאת דופן ביכולת שלנו לשלוט ולעצב אינטראקציה של אור וחומר. אחד מהתורמים המרכזיים שקידמו את התחום הוא השימוש בלייזרים אולטרא-מהירים וחומרים אופטיים מלאכותיים - על מנת להעצים ולשפר את האינטראקציה. על ידי עיצוב התצורה הגיאומטרית, החומרים והסביבה של ננו-חלקיקים, ניתן לשלוט על העוצמה, הפאזה והתדרים האלקטרומגנטיים הנוצרים באינטראקציה ננו-אופטית, כפי שהודגם באופן נרחב בצורה ניסיונית. את הננו-חלקיקים ניתן לשבץ למערכים, המכונים מטא-משטחים, וכך להציע משטחים עם תגובת תדרים מהונדסת, בעלי תכונות מרחביות הנובעות מהעיצוב דמוי הסריג ובחתך רוחב אינטראקציה משופר. לפיכך, משטחים אלה בעצם מציעים את האפשרות למזער אלמנטים אופטיים מסורתיים ולממש פונקציות חדישות. בנוסף, החופש לעצב את התצורה הגיאומטרית שלהן מספק מגרש משחקים עצום לחקור תופעות פיזיקליות חדשות באינטראקציה אופטית ננומטרית. למרות ההתקדמות המרשימה, רוב המטא-משטחים המשמשים כיום במחקר ובתעשייה, מתוכננים בצורה כזו שהתכונות האופטיות שלהם למעשה נקבעות ברגע ייצור ואינן משתנות לאחר מכן. יחד עם זאת, האפשרות לשלוט באופן אקטיבי בתגובה האופטית של מטא-חומרים זוכה לתשומת לב רבה בשנים האחרונות. מטא חומרים המאפשרים מניפולציה לפי דרישה של אינטראקציית האור-חומר, יאפשרו מימד חדש של שליטה ותופעות פיזיקליות מסקרנות.

בתזה זו, אנו חוקרים באופן תיאורטי וניסיוני היבטים של שליטה קוהרנטית באינטראקציה אופטית לא ליניארית במטא-חומרים ומערכות מצב מוצק ננו אופטיות. אנו חוקרים תועפות חדשות עבור שליטה בתהליכים אופטיים לא ליניארים הנוצרים בשילוב פולסים אולטרא-מהירים במערכות ננו-אופטיות כגון מוליכי גל סיליקון פוטונים וננומבנים פלזמוניים ומתרכזים במניפולציה של הדינמיקה הקוהרנטית בעזרת מודולציה מרחבית וזמנית על האינטראקציה.

שליטה קוהרנטית היא שיטה מבוססת מכניקת קוונטים המאפשרת לשלוט בתהליכים דינמיים על ידי אור. במהותה, תחום השליטה הקוהרנטית נועד לפתור את הבעיה של ניתוב יעיל של מערכת קוונטית ממצב התחלתי למצב סופי. במערכות אטומיות ומולקולריות שליטה קוהרנטית מיושמת באופן נרחב ומאפשר הגברה עצומה של תופעות לא ליניאריות על ידי שליטה על הנתיבים האפשריים לעירור, הקיימים באינטראקציה מרובת מצבעים עצמיים. דרך מרכזית לממש ניתוב אופטימלי למצב רצוי עבור עירור לא ליניארי, היא להתאים את הפאזה של פולס לייזר קצר במיוחד, על ידי שיטות של עיצוב פולסים, וכך לשלוט ולתמרן את ההתאבכות בין מספר הנתיבים של האינטראקציה. מעבר לעירעור לא ליניארי לרמה אלקטרונית, שליטה קוהרנטית הודגמה גם עבור המרת תדרים לא ליניארית על ידי עיצוב התצורה הגיאומטרית של מוליך גל וכך לנתב את תוצאת האינטראקציה המוכתבת על ידי התאבכות בהתאמת פאזות של התדרים הנוצרים לאורך המוליך גל.

תזה זאת מורכבת באופן הבא: בפרק הראשון אנו סוקרים ומספקים רקע נדרש עבור רעיונות מרכזיים השזורים בתהליך המחקר המוצג בתזה זאת. בפתיחת הפרק הראשון אנחנו מציגים נושאים של אופטיקה לא ליניארית, ערבוב לא ליניארי מסדר שלישי של ארבע-גלים (סעיף 1.1), מטא-משטחים (סעיף 1.2) שליטה

קוונטית קוהרנטית בפלסמוניקה (סעיף 1.3) ואת השיטות הניסיוניות, החישוביות וההנדסיות שנעשה בהם שימוש עבור המחקר (סעיף 1.4). בפרק 2, אשר מהווה את הגוף המרכזי בתזת המאמרים הזאת, אנו מציגים שלושה מאמרים אשר עברו ביקורת עמיתים והתפרסמו, כאשר כל אחד מהמאמרים מתרכז באופן אחר של שילוב שליטה קוהרנטית בננו-אופטיקה אולטרא מהירה. בפרק 3, אנחנו מסתכלים קדימה ומציעים כיווני מחקר עתידי הממשיכים את הממצאים המוצגים לאורך התזה.

במאמר **הראשון**, אנחנו מציגים את ההישגים שלנו בהמרת תדר לא לינארית במובילי גלים, שיטה להמרת תדר עבור פולסים מהירים במיוחד, רחבי פס, באמצעות שליטה הקוהרנטית. אנו מציגים את מושג המרת התדר האדיאבטית באינטראקציה לא לינארית מסדר שלישי (ערבוב ארבעה-גלים). גישה זו מיישמת שליטה קוהרנטית באמצעות עיצוב מרחבי עבור המרת תדר לא לינארית במוליכי גל מחומרים צנטרוסימטריים. שיטה זו מציעה נתיב לעקוף את הגבלת היעילות אל מול רוחב הפס, אשר מתקבלת בסכמות המרת תדרים מקובלות במחקר ותעשייה. בנוסף, אנחנו מיישם את התיאוריה שלנו עבור יישום מוכללות המתאימה ליישום נרחב במכשירי סיליקון-פוטונים ובסיבים אופטיים. **במאמר השני,** אנחנו מציגים את הניסויים והתאוריה שלנו בשליטה קוהרנטית בננו מבנים על ידי עיצוב פולסים צרי סרט. במקרה של פולסים צרי סרט, אנחנו מדגימים שליטה קוהרנטית על ידי הטבעה של פאזות ספקטרליות מתצורת וי (V-shaped) כאשר האינטראקציה מבצעת עבור שדות הנושקים לאינטראקציית שדה חזק. אנו מראים, בעזרת שליטה קוהרנטית, שהתגובה המעריכית הלא לינארית היא מורכבת ובעל מבנה אשר מושפע באופן משמעותי מסדר הגעת התדרים בפולסים. לבסוף, **במאמר השלישי,** אנחנו מתרכזים באתגר עיקרי ביישום שליטה קוהרנטית בננו-מבנים מתכתיים - זמן הקוהרנטיות האולטרה-מהיר שלהם, אשר קצר מ-20 פמטו-שניות. עובדה זו הפכה את השליטה הקוהרנטית במבנים פלסמוניים על ידי עיצוב פולסים למאוד מוגבלת. הדגמה של סכמות שליטה קוהרנטיות מרכזיות מעולם השליטה הקוהרנטית במערכות קוונטיות אטומיות, כגון שיפור של עירור לא לינארי באמצעות התאבכות של נתיבי האינטראקציה, נותרו עד כה בלתי מושגות. בעזרת עיצוב פולסים קצרים מ-10 פמטו-שניות, אנו מאפשרים לבצע שליטה קוהרנטית בננו-מבנים פלזמונים ומראים שהעירעור הפלזמוני הלא לינארי האופטימי אינו מתקבל על דחיסה זמנית מקסימלית של הפולסים. הפולסים דווקא צריכים להיות מתוחים בהתאם לרזוננס הפלזמוני ורוחב הסרט של הלייזר. בנוסף להדגמה הניסיונית שלנו, אנו גם מספקים תאוריה אשר מתארת את ההגברה ליצירת הרמוניה שניה ומנבאת את תצורת הפולס האופטימלי, אשר נקבע על ידי הרזוננס הפלזמוני, רוחב הסרט שלו, ומאפייני הלייזר. תצורת הפולס הזאת מספקת ביצועים יעילים יותר מאשר פולס שהוא מוגבל-טרנספורם-פוריה אשר מכווץ זמנית בצורה מקסימלית.

הממצאים והפיתוחים בתזה זו מאפשרים מחקר חדש ומרגש כמו גם יישומים והדמנויות חדשות באופטיקה אולטרה מהירה וננופוטוניקה.

חיבור לשם קבלת התואר "דוקטור לפילוסופיה"

שליטה קוהרנטית באינטראקציה לא לינארית של פולסים אולטרה-מהירים במטא-חומרים

הוגש לסנאט של אוניברסיטת תל-אביב

אייל בכר

יולי 2022

References

1.   J. Kerr, XL. *A new relation between electricity and light: Dielectrified media birefringent. London, Edinburgh, Dublin Philos. Mag. J. Sci.* **50**, 337–348 (1875).

2.   E. A. Manykin, A. M. Afanas'ev, "On One Possibility of Making a Medium Transparent by Multiquantum Resonance" (1967).

3.   M. Shapiro, P. Brumer, Principles of the quantum control of molecular processes. *Princ. Quantum Control Mol. Process. by Moshe Shapiro, Paul Brum. pp. 250. ISBN 0-471-24184-9. Wiley-VCH, Febr. 2003.*, 250 (2003).

4.   I. I. Rabi, J. R. Zacharias, S. Millman, P. Kusch, A new method of measuring nuclear magnetic moment. *Phys. Rev.* **53** (1938), p. 318.

5.   Y. Silberberg, Quantum Coherent Control for Nonlinear Spectroscopy and Microscopy. *Annu. Rev. Phys. Chem.* **60**, 277–292 (2009).

6.   W. S. Warren, H. Rabitz, M. Dahleh, Coherent control of quantum dynamics: The dream is alive. *Science (80-.).* **259**, 1581–1589 (1993).

7.   W. Wohlleben, T. Buckup, J. L. Herek, M. Motzkus, Coherent Control for Spectroscopy and Manipulation of Biological Dynamics. *ChemPhysChem.* **6**, 850–857 (2005).

8.   R. Atanasov, A. Haché, J. L. P. Hughes, H. M. van Driel, J. E. Sipe, Coherent Control of Photocurrent Generation in Bulk Semiconductors. *Phys. Rev. Lett.* **76**, 1703–1706 (1996).

9.   V. Remesh, M. Stührenberg, L. Saemisch, N. Accanto, N. F. van Hulst, Phase control of plasmon enhanced two-photon photoluminescence in resonant gold nanoantennas. *Appl. Phys. Lett.* **113**, 211101 (2018).

10.   J. I. J. Wang, D. Rodan-Legrain, L. Bretheau, D. L. Campbell, B. Kannan, D. Kim, M. Kjaergaard, P. Krantz, G. O. Samach, F. Yan, J. L. Yoder, K. Watanabe, T. Taniguchi, T. P. Orlando, S. Gustavsson, P. Jarillo-Herrero, W. D. Oliver, Coherent control of a hybrid superconducting circuit made with graphene-based van der Waals heterostructures. *Nat. Nanotechnol.* **14**, 120–125 (2019).

11.   M. Kues, C. Reimer, P. Roztocki, L. Cortés, S. S.- Nature, undefined 2017, On-chip generation of high-dimensional entangled quantum states and their coherent control. *nature.com.*

12.   M. Kues, C. Reimer, P. Roztocki, L. R. Cortés, S. Sciara, B. Wetzel, Y. Zhang, A. Cino, S. T. Chu, B. E. Little, D. J. Moss, L. Caspani, J. Azaña, R. Morandotti, On-chip generation of high-dimensional entangled quantum states and their coherent control. *Nature.* **546**, 622–626 (2017).

13.   J. F. Wang, F. F. Yan, Q. Li, Z. H. Liu, H. Liu, G. P. Guo, L. P. Guo, X. Zhou, J. M. Cui, J. Wang, Z. Q. Zhou, X. Y. Xu, J. S. Xu, C. F. Li, G. C. Guo, Coherent Control of Nitrogen-Vacancy Center Spins in Silicon Carbide at Room Temperature. *Phys. Rev. Lett.* **124**, 223601 (2020).

14.   A. Espinosa-Soria, E. Pinilla-Cienfuegos, F. J. Díaz-Fernández, A. Griol, J. Martí, A. Martínez, Coherent Control of a Plasmonic Nanoantenna Integrated on a Silicon Chip. *ACS Photonics.* **5**, 2712–2717 (2018).

15.   H. Shin, J. A. Cox, R. Jarecki, A. Starbuck, Z. Wang, P. T. Rakich, Control of coherent information via on-chip photonic–phononic emitter–receivers. *Nat. Commun. 2015 61.* **6**, 1–8 (2015).

16.   D. Brinks, M. Castro-Lopez, R. Hildner, N. F. Van Hulst, Plasmonic antennas as design elements for coherent ultrafast nanophotonics. *Proc. Natl. Acad. Sci. U. S. A.* **110**, 18386–18390 (2013).

17.   A. Dahan, A. Levanon, M. Katz, H. Suchowski, Ultrafast adiabatic second harmonic generation. *J. Phys. Condens. Matter.* **29**, 084004 (2017).

18.   H. Suchowski, D. Oron, A. Arie, Y. Silberberg, Geometrical representation of sum frequency generation and adiabatic frequency conversion. *Phys. Rev. A.* **78**, 63821 (2008).

19.   H. Suchowski, V. Prabhudesai, D. Oron, A. Arie, Y. Silberberg, Robust adiabatic sum frequency conversion. *Opt. Express.* **17**, 12731–12740 (2009).

20.   E. Bahar, U. Arieli, M. Mrejen, H. Suchowski, Coherent control of the noninstantaneous nonlinear power-law response in resonant nanostructures. *Phys. Rev. B.* **101**, 035141 (2020).

21.   E. Bahar, U. Arieli, M. V. Stern, H. Suchowski, Unlocking Coherent Control of Ultrafast Plasmonic Interaction. *Laser Photon. Rev.*, 2100467 (2022).

22.   E. Bahar, X. Ding, A. Dahan, H. Suchowski, J. Moses, Adiabatic four-wave mixing frequency conversion. *Opt. Express.* **26**, 25582 (2018).

23.   J. A. Armstrong, N. Bloembergen, J. Ducuing, P. S. Pershan, Interactions between Light Waves in a Nonlinear Dielectric. *Phys. Rev.* **127**, 1918–1939 (1962).

24.   C. L. Tang, W. R. Bosenberg, T. Ukachi, R. J. Lane, L. K. Cheng, Optical parametric oscillators. *Proc. IEEE.* **80**, 365–374 (1992).

25.   A. M. Zheltikov, Let there be white light: supercontinuum generation by ultrashort laser pulses.

Physics-Uspekhi. **49** (2006), p. 605.

26. A. P. Vandevender, P. G. Kwiat, High efficiency single photon detection via frequency up-conversion. *J. Mod. Opt.* (2009).

27. T. Schneider, *Nonlinear Optics in Telecommunications* (Springer Science & Business Media, 2013).

28. M. Dantus, Coherent Nonlinear Spectroscopy: From Femtosecond Dynamics to Control. *http://dx.doi.org/10.1146/annurev.physchem.52.1.639*. **52**, 639–679 (2003).

29. V. Parodi, E. Jacchetti, R. Osellame, G. Cerullo, D. Polli, M. T. Raimondi, Nonlinear Optical Microscopy: From Fundamentals to Applications in Live Bioimaging. *Front. Bioeng. Biotechnol.* **8**, 1174 (2020).

30. R. W. Boyd, *Nonlinear optics* (Academic Press, 3rd Editio., 2008).

31. J. M. Liu, Nicolaas Bloembergen as a scientist and a mentor. *Nat. Photonics 2018 123*. **12**, 118–121 (2018).

32. J. B. Pendry, A. J. Holden, D. J. Robbins, W. J. Stewart, Magnetism from conductors and enhanced nonlinear phenomena. *IEEE Trans. Microw. Theory Tech.* **47**, 2075–2084 (1999).

33. M. T. and A. A. Alexander Krasnok, Nonlinear metasurfaces: a paradigm shift in nonlinear optics. *Mater. Today* (2017), doi:https://doi.org/10.1016/j.mattod.2017.06.007.

34. C. M. Soukoulis, S. Linden, M. Wegener, Negative refractive index at optical wavelengths. *Science (80-.).* **315** (2007), pp. 47–49.

35. P. Strobbia, E. R. Languirand, B. M. Cullum, Recent advances in plasmonic nanostructures for sensing: a review. *https://doi.org/10.1117/1.OE.54.10.100902*. **54**, 100902 (2015).

36. N. C. Panoiu, W. E. I. Sha, D. Y. Lei, G. C. Li, Nonlinear optics in plasmonic nanostructures. *J. Opt.* **20**, 083001 (2018).

37. N. I. Zheludev, Y. S. Kivshar, From metamaterials to metadevices. *Nat. Mater.* **11**, 917–924 (2012).

38. T. F. Heinz, Second-Order Nonlinear Optical Effects at Surfaces and Interfaces. *Mod. Probl. Condens. Matter Sci.* **29**, 353–416 (1991).

39. R. C. Miller, Optical Second Harmonic Generation In Piezoelectric Crystals. *Appl. Phys. Lett.* **5**, 17–19 (1964).

40. M. A. Foster, A. C. Turner, R. Salem, M. Lipson, A. L. Gaeta, Broad-band continuous-wave parametric wavelength conversion in silicon nanowaveguides. *Opt. Express*. **15**, 12949–12958 (2007).

41. J. Leuthold, C. Koos, W. Freude, Nonlinear silicon photonics. *Nat. Photonics*. **4**, 535–544 (2010).

42. M. G. Allen, Diode laser absorption sensors for gas-dynamic and combustion flows. *Meas. Sci. Technol.* **9**, 545–562 (1998).

43. J. Wang, J. Sun, Q. Sun, Proposal for all-optical switchable OR/XOR logic gates using sum-frequency generation. *IEEE Photonics Technol. Lett.* **19**, 541–543 (2007).

44. D. Polli, P. Altoè, O. Weingart, K. M. Spillane, C. Manzoni, D. Brida, G. Tomasello, G. Orlandi, P. Kukura, R. A. Mathies, M. Garavelli, G. Cerullo, Conical intersection dynamics of the primary photoisomerization event in vision. *Nature*. **467**, 440–443 (2010).

45. T. Popmintchev, M.-C. Chen, D. Popmintchev, P. Arpin, S. Brown, S. Ališauskas, G. Andriukaitis, T. Balčiunas, O. D. Mücke, A. Pugzlys, A. Baltuška, B. Shim, S. E. Schrauth, A. Gaeta, C. Hernández-Garc\'\ia, L. Plaja, A. Becker, A. Jaron-Becker, M. M. Murnane, H. C. Kapteyn, Bright Coherent Ultrahigh Harmonics in the keV X-ray Regime from Mid-Infrared Femtosecond Lasers. *Science (80-.).* **336**, 1287–1291 (2012).

46. H. Suchowski, B. D. Bruner, A. Ganany-Padowicz, I. Juwiler, A. Arie, Y. Silberberg, Adiabatic frequency conversion of ultrafast pulses. *Appl. Phys. B*. **105**, 697–702 (2011).

47. J. Moses, H. Suchowski, F. X. Kärtner, Fully efficient adiabatic frequency conversion of broadband Ti: sapphire oscillator pulses. *Opt. Lett.* **37**, 1589–1591 (2012).

48. H. Suchowski, P. R. Krogen, S.-W. Huang, F. X. Kärtner, J. Moses, Octave-spanning coherent mid-IR generation via adiabatic difference frequency conversion. *Opt. Express*. **21**, 28892–28901 (2013).

49. P. Krogen, H. Suchowski, H. Liang, N. Flemens, K.-H. Hong, F. X. Kärtner, J. Moses, Generation and multi-octave shaping of mid-infrared intense single-cycle pulses. *Nat. Photonics*. **11**, 222–226 (2017).

50. M. A. Foster, A. C. Turner, J. E. Sharping, B. S. Schmidt, M. Lipson, A. L. Gaeta, Broad-band optical parametric gain on a silicon photonic chip. *Nature*. **441**, 960–963 (2006).

51. Y. Ding, J. Xu, H. Ou, C. Peucheret, Mode-selective wavelength conversion based on four-wave mixing in a multimode silicon waveguide. *Opt. Express*. **22**, 127–135 (2014).

52. I. Agha, M. Davanço, B. Thurston, K. Srinivasan, Low-noise chip-based frequency conversion by four-wave-mixing Bragg scattering in SiNx waveguides. *Opt. Lett.* **37**, 2997–2999 (2012).

53. S. Coen, A. H. L. Chau, R. Leonhardt, J. D. Harvey, J. C. Knight, W. J. Wadsworth, P. S. J. Russell,

Supercontinuum generation by stimulated Raman scattering and parametric four-wave mixing in photonic crystal fibers. *J. Opt. Soc. Am. B.* **19**, 753–764 (2002).

54. C. R. Petersen, U. Møller, I. Kubat, B. Zhou, S. Dupont, J. Ramsay, T. Benson, S. Sujecki, N. Abdel-Moneim, Z. Tang, D. Furniss, A. Seddon, O. Bang, Mid-infrared supercontinuum covering the 1.4--13.3 μm molecular fingerprint region using ultra-high NA chalcogenide step-index fibre. *Nat. Photonics.* **8**, 830–834 (2014).

55. K. Yin, B. Zhang, L. Yang, J. Hou, 15.2 W spectrally flat all-fiber supercontinuum laser source with> 1 W power beyond 3.8 μm. *Opt. Lett.* **42**, 2334–2337 (2017).

56. C. Y. Wang, T. Herr, P. Del'Haye, A. Schliesser, J. Hofer, R. Holzwarth, T. W. Hänsch, N. Picqué, T. J. Kippenberg, Mid-infrared optical frequency combs at 2.5 μm based on crystalline microresonators. *Nat. Commun.* **4**, 1345 (2013).

57. P. Del'Haye, O. Arcizet, A. Schliesser, R. Holzwarth, T. J. Kippenberg, Full stabilization of a microresonator-based optical frequency comb. *Phys. Rev. Lett.* **101**, 53903 (2008).

58. A. G. Griffith, R. K. W. Lau, J. Cardenas, Y. Okawachi, A. Mohanty, R. Fain, Y. H. D. Lee, M. Yu, C. T. Phare, C. B. Poitras, A. L. Gaeta, M. Lipson, Silicon-chip mid-infrared frequency comb generation. *Nat. Commun.* **6**, 6299 (2015).

59. S. B. Papp, K. Beha, P. Del'Haye, F. Quinlan, H. Lee, K. J. Vahala, S. A. Diddams, Microresonator frequency comb optical clock. *Optica.* **1**, 10–14 (2014).

60. M. Nisoli, S. De Silvestri, O. Svelto, Generation of high energy 10 fs pulses by a new pulse compression technique. *Appl. Phys. Lett.* **68**, 2793–2795 (1996).

61. D. Faccio, A. Grün, P. K. Bates, O. Chalus, J. Biegert, Optical amplification in the near-infrared in gas-filled hollow-core fibers. *Opt. Lett.* **34**, 2918–2920 (2009).

62. J. Fatome, S. Pitois, G. Millot, 20-GHz-to-1-THz repetition rate pulse sources based on multiple four-wave mixing in optical fibers. *IEEE J. Quantum Electron.* **42**, 1038–1046 (2006).

63. C. J. McKinstrie, S. Radic, M. G. Raymer, L. Schenato, Unimpaired phase-sensitive amplification by vector four-wave mixing near the zero-dispersion frequency. *Opt. Express.* **15**, 2178–2189 (2007).

64. A. C. S Jr, J. M. C. Boggio, A. A. Rieznik, H. E. Hernandez-Figueroa, H. L. Fragnito, J. C. Knight, Highly efficient generation of broadband cascaded four-wave mixing products. *Opt. Express.* **16**, 2816–2828 (2008).

65. T. T. Ng, J. L. Blows, J. T. Mok, R. W. McKerracher, B. J. Eggleton, Cascaded four-wave mixing in fiber optical parametric amplifiers: application to residual dispersion monitoring. *J. Light. Technol.* **23**, 818–826 (2005).

66. H. Suchowski, G. Porat, A. Arie, Adiabatic processes in frequency conversion. *Laser Photon. Rev.* **8**, 333–367 (2014).

67. N. B. Baranova, M. A. Bolshtyanskii, B. Y. Zel'dovich, Adiabatic energy transfer from a pump wave to its second harmonic. *Quantum Electron.* **25**, 638–640 (1995).

68. C. R. Phillips, M. M. Fejer, Efficiency and phase of optical parametric amplification in chirped quasi-phase-matched gratings. *Opt. Lett. Vol. 35, Issue 18, pp. 3093-3095.* **35**, 3093–3095 (2010).

69. C. Langrock, C. R. Phillips, D. Chang, L. Gallmann, M. M. Fejer, Y. W. Lin, Apodization of chirped quasi-phasematching devices. *JOSA B, Vol. 30, Issue 6, pp. 1551-1568.* **30**, 1551–1568 (2013).

70. C. Heese, C. R. Phillips, L. Gallmann, M. M. Fejer, U. Keller, Ultrabroadband, highly flexible amplifier for ultrashort midinfrared laser pulses based on aperiodically poled Mg:LiNbO₃. *Opt. Lett. Vol. 35, Issue 14, pp. 2340-2342.* **35**, 2340–2342 (2010).

71. C. Heese, C. R. Phillips, L. Gallmann, M. M. Fejer, U. Keller, D. Brida, C. Manzoni, G. Cirmi, M. Marangoni, S. Bonora, P. Villoresi, S. De Silvestri, G. Cerullo, Role of apodization in optical parametric amplifiers based on aperiodic quasi-phasematching gratings. *Opt. Express, Vol. 20, Issue 16, pp. 18066-18071.* **20**, 18066–18071 (2012).

72. C. Heese, C. R. Phillips, B. W. Mayer, L. Gallmann, M. M. Fejer, U. Keller, A. D. Shiner, C. Trallero-Herrero, N. Kajumba, H. C. Bandulet, D. Comtois, F. Légaré, M. Giguère, J. C. Kieffer, P. B. Corkum, D. M. Villeneuve, K. D. Schultz, C. I. Blaga, R. Chirla, P. Colosimo, J. Cryan, A. M. March, C. Roedig, E. Sistrunk, J. Tate, J. Wheeler, P. Agostini, S. Baker, J. S. Robinson, C. A. Haworth, H. Teng, R. A. Smith, C. C. Chirilă, M. Lein, J. W. G Tisch, C. Vozzi, R. Torres, M. Negro, L. Brugnera, T. Siegel, C. Altucci, R. Velotta, F. Frassetto, L. Poletto, P. Villoresi, S. De Silvestri, S. Stagira, J. P. Marangos, T. Metzger, A. Baltuška, N. Forget, D. Kaplan, A. Galvanauskas, 75 MW few-cycle mid-infrared pulses from a collinear apodized APPLN-based OPCPA. *Opt. Express, Vol. 20, Issue 24, pp. 26888-26894.* **20**, 26888–26894 (2012).

73. O. Yaakobi, L. Caspani, M. Clerici, F. Vidal, R. Morandotti, M. D. Ashkezari, M. Baquero-Ruiz, W. Bertsche, P. D. Bowe, E. Butler, C. L. Cesar, S. Chapman, M. Charlton, A. Deller, S. Eriksson, J. Fajans, T. Friesen, M. C. Fujiwara, D. R. Gill, A. Gutierrez, J. S. Hangst, W. N. Hardy, M. E.

Hayden, A. J. Humphries, R. Hydomako, M. J. Jenkins, S. Jonsell, L. V Jorgensen, L. Kurchaninov, N. Madsen, S. Menary, P. Nolan, K. Olchanski, A. Olin, A. Povilus, P. Pusa, F. Robicheaux, E. Sarid, S. Seif el Nasr, D. M. Silveira, C. So, J. W. Storey, R. I. Thompson, D. P. van der Werf, J. S. Wurtele, Y. Yamazaki, Complete energy conversion by autoresonant three-wave mixing in nonuniform media. *Opt. Express, Vol. 21, Issue 2, pp. 1623-1632*. **21**, 1623–1632 (2013).

74. H. Suchowski, P. R. Krogen, S.-W. Huang, F. X. Kärtner, J. Moses, D. Brida, M. Marangoni, C. Manzoni, S. D. Silvestri, G. Cerullo, Octave-spanning coherent mid-IR generation via adiabatic difference frequency conversion. *Opt. Express, Vol. 21, Issue 23, pp. 28892-28901*. **21**, 28892–28901 (2013).

75. A. Arie, G. Porat, Efficient, broadband, and robust frequency conversion by fully nonlinear adiabatic three-wave mixing. *JOSA B, Vol. 30, Issue 5, pp. 1342-1351*. **30**, 1342–1351 (2013).

76. A. Dahan., thesis, Tel Aviv University.

77. A. Nagler, A. Dahan, A. Levanon, E. Lifshitz, E. Bahar, H. Suchowski, M. Mrejen, Pulse shaping of broadband adiabatic SHG from a Ti-sapphire oscillator. *Opt. Lett. Vol. 42, Issue 15, pp. 2992-2995*. **42**, 2992–2995 (2017).

78. Y. Ding, J. Xu, H. Ou, C. Peucheret, S. R. Ryf, A. H. Randel, C. Gnauck, R.-J. Bolle, P. J. Essiambre, D. W. Winzer, A. Peckham, R. Mccurdy, N. K. Randel, M. Fontaine, E. Montoliu, S. Burrows, A. H. Chandrasekhar, R.-J. Xie, R. Winzer, P. Delbue, A. Pupalaikis, Y. Sureka, L. Sun, R. V Grüner-Nielsen, R. Jensen, H. Gabrielli, D. Liu, S. G. Johnson, M. Lipson, Mode-selective wavelength conversion based on four-wave mixing in a multimode silicon waveguide. *Opt. Express, Vol. 22, Issue 1, pp. 127-135*. **22**, 127–135 (2014).

79. S. Diez, C. Schmidt, R. Ludwig, H. G. Weber, K. Obermann, S. Kindt, I. Koltchanov, K. Petermann, Four-wave mixing in semiconductor optical amplifiers for frequency conversion and fast optical switching. *IEEE J. Sel. Top. Quantum Electron.* **3**, 1131–1144 (1997).

80. A. Melloni, F. Morichetti, M. Martinelli, Four-wave mixing and wavelength conversion in coupled-resonator optical waveguides. *JOSA B, Vol. 25, Issue 12, pp. C87-C97*. **25**, C87–C97 (2008).

81. A. H. L. Chau, J. D. Harvey, J. C. Knight, P. S. J. Russell, R. Leonhardt, S. Coen, W. J. Wadsworth, Supercontinuum generation by stimulated Raman scattering and parametric four-wave mixing in photonic crystal fibers. *JOSA B, Vol. 19, Issue 4, pp. 753-764*. **19**, 753–764 (2002).

82. L. Allen, J. H. Eberly, Physics, Optical Resonance and Two-Level Atoms (Dover Books on Physics), 256 (1987).

83. M. Kauranen, A. V. Zayats, Nonlinear plasmonics. *Nat. Photonics*. **6** (2012), pp. 737–748.

84. M. W. Klein, C. Enrich, M. Wegener, S. Linden, Second-harmonic generation from magnetic metamaterials. *Science (80-.).* **313**, 502–4 (2006).

85. K. O'Brien, H. Suchowski, J. Rho, A. Salandrino, B. Kante, X. Yin, X. Zhang, Predicting nonlinear properties of metamaterials from the linear response. *Nat. Mater.* **14**, 379–383 (2015).

86. N. Segal, S. Keren-Zur, N. Hendler, T. Ellenbogen, Controlling light with metamaterial-based nonlinear photonic crystals. *Nat. Photonics*. **9**, 180–184 (2015).

87. L. Michaeli, S. Keren-Zur, O. Avayu, H. Suchowski, T. Ellenbogen, Nonlinear Surface Lattice Resonance in Plasmonic Nanoparticle Arrays. *Phys. Rev. Lett.* **118**, 243904 (2017).

88. S. Ayas, H. Güner, B. Türker, O. Ö. Ekiz, F. Dirisaglik, A. K. Okyay, A. Dâna, Raman enhancement on a broadband meta-surface. *ACS Nano* (2012), doi:10.1021/nn301665a.

89. N. Zhang, K. Liu, Z. Liu, H. Song, X. Zeng, D. Ji, A. Cheney, S. Jiang, Q. Gan, Ultrabroadband Metasurface for Efficient Light Trapping and Localization: A Universal Surface-Enhanced Raman Spectroscopy Substrate for "All" Excitation Wavelengths. *Adv. Mater. Interfaces* (2015), doi:10.1002/admi.201500142.

90. S. Romano, G. Zito, S. Managò, G. Calafiore, E. Penzo, S. Cabrini, A. C. De Luca, V. Mocella, Surface-Enhanced Raman and Fluorescence Spectroscopy with an All-Dielectric Metasurface. *J. Phys. Chem. C* (2018), doi:10.1021/acs.jpcc.8b03190.

91. P. Anger, P. Bharadwaj, L. Novotny, Enhancement and quenching of single-molecule fluorescence. *Phys. Rev. Lett.* (2006), doi:10.1103/PhysRevLett.96.113002.

92. A. Rose, T. B. Hoang, F. McGuire, J. J. Mock, C. Ciracì, D. R. Smith, M. H. Mikkelsen, Control of radiative processes using tunable plasmonic nanopatch antennas. *Nano Lett.* (2014), doi:10.1021/nl501976f.

93. S. Yuan, X. Qiu, C. Cui, L. Zhu, Y. Wang, Y. Li, J. Song, Q. Huang, J. Xia, Strong Photoluminescence Enhancement in All-Dielectric Fano Metasurface with High Quality Factor. *ACS Nano* (2017), doi:10.1021/acsnano.7b04810.

94. E. Hendry, T. Carpy, J. Johnston, M. Popland, R. V. Mikhaylovskiy, A. J. Lapthorn, S. M. Kelly, L. D. Barron, N. Gadegaard, M. Kadodwala, Ultrasensitive detection and characterization of biomolecules using superchiral fields. *Nat. Nanotechnol.* (2010), doi:10.1038/nnano.2010.209.

95. W. Ma, H. Kuang, L. Xu, L. Ding, C. Xu, L. Wang, N. A. Kotov, Attomolar DNA detection with chiral nanorod assemblies. *Nat. Commun.* (2013), doi:10.1038/ncomms3689.

96. R. Schreiber, N. Luong, Z. Fan, A. Kuzyk, P. C. Nickels, T. Zhang, D. M. Smith, B. Yurke, W. Kuang, A. O. Govorov, T. Liedl, Chiral plasmonic DNA nanostructures with switchable circular dichroism. *Nat. Commun.* (2013), doi:10.1038/ncomms3948.

97. P. Törmä, W. L. Barnes, Strong coupling between surface plasmon polaritons and emitters: a review. *Reports Prog. Phys.* **78**, 013901 (2015).

98. E. Eizner, O. Avayu, R. Ditcovski, T. Ellenbogen, Aluminum Nanoantenna Complexes for Strong Coupling between Excitons and Localized Surface Plasmons. *Nano Lett.* **15**, 6215–6221 (2015).

99. G. Hajisalem, M. S. Nezami, R. Gordon, Probing the Quantum Tunneling Limit of Plasmonic Enhancement by Third Harmonic Generation. *Nano Lett.* **14**, 6651–6654 (2014).

100. W. Zhu, R. Esteban, A. G. Borisov, J. J. Baumberg, P. Nordlander, H. J. Lezec, J. Aizpurua, K. B. Crozier, Quantum mechanical effects in plasmonic structures with subnanometre gaps. *Nat. Commun.* **7** (2016), doi:10.1038/ncomms11495.

101. P. Roelli, C. Galland, N. Piro, T. J. Kippenberg, Molecular cavity optomechanics as a theory of plasmon-enhanced Raman scattering (2016), doi:10.1038/NNANO.2015.264.

102. R. Chikkaraddy, B. De Nijs, F. Benz, S. J. Barrow, O. A. Scherman, E. Rosta, A. Demetriadou, P. Fox, O. Hess, J. J. Baumberg, Single-molecule strong coupling at room temperature in plasmonic nanocavities. *Nature.* **535** (2016), doi:10.1038/nature17974.

103. R. A. Shelby, D. R. Smith, S. Schultz, Experimental Verification of a Negative Index of Refraction. *Science (80-.).* **292**, 77–79 (2001).

104. S. A. Maier, Plasmonics: Fundamentals and applications. *Plasmon. Fundam. Appl.*, 1–223 (2007).

105. P. Biagioni, J.-S. Huang, B. Hecht, Nanoantennas for visible and infrared radiation. *Rep. Prog. Phys.* **75**, 024402 (2012).

106. C. F. Bohren, D. R. Huffman, *Absorption and scattering of light by small particles* (Wiley, 2004).

107. L. Catherine, P. Olivier, *Gold nanoparticles for physics, chemistry and biology* (World Scientific, 2017).

108. L. Novotny, N. van Hulst, Antennas for light. *Nat. Photonics.* **5**, 83–90 (2011).

109. H. Harutyunyan, A. B. F. Martinson, D. Rosenmann, L. K. Khorashad, L. V Besteiro, A. O. Govorov, G. P. Wiederrecht, Anomalous ultrafast dynamics of hot plasmonic electrons in nanostructures with hot spots. *Nat. Nanotechnol.* **10**, 770 (2015).

110. G. V. Hartland, Optical studies of dynamics in noble metal nanostructures. *Chem. Rev.* **111** (2011), pp. 3858–3887.

111. C. Voisin, N. Del Fatti, D. Christofilos, F. Vallée, Ultrafast Electron Dynamics and Optical Nonlinearities in Metal Nanoparticles. *J. Phys. Chem. B.* **105**, 2264–2280 (2001).

112. A. Manjavacas, J. G. Liu, V. Kulkarni, P. Nordlander, Plasmon-Induced Hot Carriers in Metallic Nanoparticles. *ACS Nano.* **8**, 7630–7638 (2014).

113. P. Shapiro, Moshe; Brumer, Principles of the Quantum Control of Molecular Processes.

114. A. Yariv, Optical Electronics 4th edn, Ch 13 (1991).

115. C. Liu, W. Liu, S. Wang, H. Li, Z. Lv, F. Zhang, D. Zhang, J. Teng, T. Zheng, D. Li, M. Zhang, P. Xu, Q. Gong, Super-resolution nanoscopy by coherent control on nanoparticle emission. *Sci. Adv.* **6**, eaaw6579 (2020).

116. T. Sikorsky, Z. Meir, R. Ben-Shlomi, N. Akerman, R. Ozeri, Spin-controlled atom-ion chemistry. *Nat. Commun.* **9** (2018), doi:10.1038/s41467-018-03373-y.

117. M. Aeschlimann, M. Bauer, D. Bayer, T. Brixner, S. Cunovic, F. Dimler, A. Fischer, W. Pfeiffer, M. Rohmer, C. Schneider, F. Steeb, C. Strüber, D. V. Voronine, Spatiotemporal control of nanooptical excitations. *Proc. Natl. Acad. Sci.* **107**, 5329–5333 (2010).

118. T. Brixner, G. Gerber, Quantum control of gas-phase and liquid-phase femtochemistry. *ChemPhysChem.* **4** (2003), pp. 418–438.

119. N. Accanto, J. B. Nieder, L. Piatkowski, M. Castro-Lopez, F. Pastorelli, D. Brinks, N. F. Van Hulst, Phase control of femtosecond pulses on the nanoscale using second harmonic nanoparticles. *Light Sci. Appl. 2014 31.* **3**, e143–e143 (2014).

120. T. Brixner, J. Stenger, H. M. Vaswani, M. Cho, R. E. Blankenship, G. R. Fleming, Two-dimensional spectroscopy of electronic couplings in photosynthesis. *Nature.* **434**, 625–628 (2005).

121. C. Bäuerle, D. Christian Glattli, T. Meunier, F. Portier, P. Roche, P. Roulleau, S. Takada, X. Waintal, Coherent control of single electrons: A review of current progress. *Reports Prog. Phys.* **81** (2018), p. 056503.

122. N. Dudovich, B. Dayan, S. M. G. Faeder, Y. Silberberg, Transform-limited pulses are not optimal for resonant multiphoton transitions. *Phys. Rev. Lett.* **86**, 47 (2001).

123. T. Stoll, P. Maioli, A. Crut, N. Del Fatti, F. Vall??e, Advances in femto-nano-optics: ultrafast

nonlinearity of metal nanoparticles. *Eur. Phys. J. B*. **87**, 23–25 (2014).

124. J. N. Becker, J. Görlitz, C. Arend, M. Markham, C. Becher, Ultrafast all-optical coherent control of single silicon vacancy colour centres in diamond. *Nat. Commun.* **7**, 1–6 (2016).

125. L. Allen, J. H. Eberly, Physics, Optical Resonance and Two-Level Atoms (Dover Books on Physics), 256 (1987).

126. P. Tuchscherer, C. Rewitz, D. V. Voronine, F. Javier García de Abajo, W. Pfeiffer, T. Brixner, Analytic coherent control of plasmon propagation in nanostructures. *Opt. Express*. **17**, 14235 (2009).

127. L. Piatkowski, N. Accanto, N. F. Van Hulst, Ultrafast Meets Ultrasmall: Controlling Nanoantennas and Molecules. *ACS Photonics*. **3** (2016), pp. 1401–1414.

128. J. S. Huang, D. V. Voronine, P. Tuchscherer, T. Brixner, B. Hecht, Deterministic spatiotemporal control of optical fields in nanoantennas and plasmonic circuits. *Phys. Rev. B - Condens. Matter Mater. Phys.* **79**, 195441 (2009).

129. T. Rybka, M. Ludwig, M. F. Schmalz, V. Knittel, D. Brida, A. Leitenstorfer, Sub-cycle optical phase control of nanotunnelling in the single-electron regime (2016), doi:10.1038/NPHOTON.2016.174.

130. V. Remesh, M. Stührenberg, L. Saemisch, N. Accanto, N. F. Van Hulst, Phase control of plasmon enhanced two-photon photoluminescence in resonant gold nanoantennas. *Appl. Phys. Lett.* **113**, 211101 (2018).

131. T. W. Lee, S. K. Gray, Controlled spatiotemporal excitation of metal nanoparticles with picosecond optical pulses. *Phys. Rev. B - Condens. Matter Mater. Phys.* **71**, 035423 (2005).

132. T. Utikal, M. I. Stockman, A. P. Heberle, M. Lippitz, H. Giessen, All-optical control of the ultrafast dynamics of a hybrid plasmonic system. *Phys. Rev. Lett.* **104**, 113903 (2010).

133. D. Brinks, R. Hildner, F. D. Stefani, N. F. van Hulst, Beating spatio-temporal coupling: implications for pulse shaping and coherent control experiments. *Opt. Express*. **19**, 26486 (2011).

134. N. Accanto, L. Piatkowski, J. Renger, N. F. Van Hulst, Capturing the optical phase response of nanoantennas by coherent second-harmonic microscopy. *Nano Lett.* **14**, 4078–4082 (2014).

135. J. A. Maytorena, W. L. Mochán, Hydrodynamic model for sum and difference frequency generation at metal surfaces. *Phys. Rev. B*. **57**, 2580 (1998).

136. H. Maekawa, E. Drobnyh, C. A. Lancaster, N. Large, G. C. Schatz, J. S. Shumaker-Parry, M. Sukharev, N. H. Ge, Wavelength and Polarization Dependence of Second-Harmonic Responses from Gold Nanocrescent Arrays. *J. Phys. Chem. C*. **124**, 20424–20435 (2020).

137. O. Avayu, E. Almeida, Y. Prior, T. Ellenbogen, Composite functional metasurfaces for multispectral achromatic optics. *Nat. Commun.* **8**, 14992 (2017).

138. T. Rybka, M. Ludwig, M. F. Schmalz, V. Knittel, D. Brida, A. Leitenstorfer, Sub-cycle optical phase control of nanotunnelling in the single-electron regime. *Nat. Photonics*. **10**, 667 (2016).

139. A. Q. Liu, W. M. Zhu, D. P. Tsai, N. I. Zheludev, Micromachined tunable metamaterials: a review. *J. Opt.* **14**, 114009 (2012).

140. R. Camacho-Morales, M. Rahmani, S. Kruk, L. Wang, L. Xu, D. A. Smirnova, A. S. Solntsev, A. Miroshnichenko, H. H. Tan, F. Karouta, others, Nonlinear generation of vector beams from AlGaAs nanoantennas. *Nano Lett.* **16**, 7191–7197 (2016).

141. G. Li, S. Zhang, T. Zentgraf, Nonlinear photonic metasurfaces. *Nat. Rev. Mater.* **2**, 17010 (2017).

142. A. Hasan, M. Morshed, A. Memic, S. Hassan, T. J. Webster, H. E.-S. Marei, Nanoparticles in tissue engineering: applications, challenges and prospects. *Int. J. Nanomedicine*. **13**, 5637 (2018).

143. P. K. Jain, X. Huang, I. H. El-Sayed, M. A. El-Sayed, Review of some interesting surface plasmon resonance-enhanced properties of noble metal nanoparticles and their applications to biosystems. *Plasmonics*. **2**, 107–118 (2007).

144. L. Levin, W. Skomorowski, L. Rybak, R. Kosloff, C. P. Koch, Z. Amitay, Coherent control of bond making. *Phys. Rev. Lett.* **114**, 233003 (2015).

145. M. Gentile, M. Hentschel, R. Taubert, H. Guo, H. Giessen, M. Fiebig, Investigation of the nonlinear optical properties of metamaterials by second harmonic generation. *Appl. Phys. B*. **105**, 149–162 (2011).

146. N. I. Zheludev, A Roadmap for Metamaterials. *Opt. Photonics News*. **22**, 30 (2011).

147. B. Luk'yanchuk, N. I. Zheludev, S. A. Maier, N. J. Halas, P. Nordlander, H. Giessen, C. T. Chong, The Fano resonance in plasmonic nanostructures and metamaterials. *Nat. Mater.* **9**, 707–715 (2010).

148. V. V Lozovoy, I. Pastirk, K. A. Walowicz, M. Dantus, Multiphoton intrapulse interference. II. Control of two-and three-photon laser induced fluorescence with shaped pulses. *J. Chem. Phys.* **118**, 3187–3196 (2003).

149. N. Dudovich, D. Oron, Y. Silberberg, Coherent transient enhancement of optically induced resonant transitions. *Phys. Rev. Lett.* **88**, 123004 (2002).

150. M. I. Stockman, S. V Faleev, D. J. Bergman, Coherent control of femtosecond energy localization in nanosystems. *Phys. Rev. Lett.* **88**, 67402 (2002).

151. D. Brinks, M. Castro-Lopez, R. Hildner, N. F. van Hulst, Plasmonic antennas as design elements for coherent ultrafast nanophotonics. *Proc. Natl. Acad. Sci.* **110**, 18386–18390 (2013).

152. S. Onishi, K. Matsuishi, J. Oi, T. Harada, M. Kusaba, K. Hirosawa, F. Kannari, Spatiotemporal control of femtosecond plasmon using plasmon response functions measured by near-field scanning optical microscopy (NSOM). *Opt. Express.* **21**, 26631–26641 (2013).

153. G. Volpe, G. Molina-Terriza, R. Quidant, Deterministic subwavelength control of light confinement in nanostructures. *Phys. Rev. Lett.* **105**, 216802 (2010).

154. Y. Kojima, Y. Masaki, F. Kannari, Control of ultrafast plasmon pulses by spatiotemporally phase-shaped laser pulses. *JOSA B*. **33**, 2437–2444 (2016).

155. N. Accanto, L. Piatkowski, I. M. Hancu, J. Renger, N. F. van Hulst, Resonant plasmonic nanoparticles for multicolor second harmonic imaging. *Appl. Phys. Lett.* **108**, 83115 (2016).

156. O. E. Martinez, J. P. Gordon, R. L. Fork, Negative group-velocity dispersion using refraction. *J. Opt. Soc. Am. A*. **1**, 1003 (1984).

157. O. E. Martinez, Grating and prism compressors in the case of finite beam size. *J. Opt. Soc. Am. B*. **3**, 929 (1986).

158. A. M. Weiner, Femtosecond pulse shaping using spatial light modulators. *Rev. Sci. Instrum.* **71**, 1929 (2000).

159. A. M. Weiner, Cite as. *Rev. Sci. Instrum.* **71**, 1929 (1929).

160. O. Martinez, Design of high-power ultrashort pulse amplifiers by expansion and recompression. *IEEE J. Quantum Electron.* **23**, 1385–1387 (1987).

161. D. Strickland, G. Mourou, Compression of amplified chirped optical pulses. *Opt. Commun.* **55**, 447–449 (1985).

162. D. Brinks, R. Hildner, F. D. Stefani, N. F. van Hulst, Beating spatio-temporal coupling: implications for pulse shaping and coherent control experiments. *Opt. Express*. **19**, 26486–26499 (2011).

163. R. Trebino, *Frequency-Resolved Optical Gating: The Measurement of Ultrashort Laser Pulses* (Springer US, 2011).

164. Trebino, Frequency-resolved optical gating.

165. M. Maiuri, M. Garavelli, G. Cerullo, Ultrafast Spectroscopy: State of the Art and Open Challenges. *J. Am. Chem. Soc.* **142**, 3–15 (2020).

166. V. G. Lyssenko, in *Spectroscopy of Systems with Spatially Confined Structures* (Springer Netherlands, Dordrecht, 2003), pp. 323–356.

167. B. Di Bartolo, *Spectroscopy of systems with spatially confined structures : Proceedings of the NATO Advanced Study Institute on Spectroscopy of Systems with Spatially Confined Structures Erice, Sicily, Italy 15-30 June 2001* (Springer, 2003).

168. A. S. Mayorov, R. V. Gorbachev, S. V. Morozov, L. Britnell, R. Jalil, L. A. Ponomarenko, P. Blake, K. S. Novoselov, K. Watanabe, T. Taniguchi, A. K. Geim, Micrometer-Scale Ballistic Transport in Encapsulated Graphene at Room Temperature. *Nano Lett.* **11**, 2396–2399 (2011).

169. S. Korman, E. Bahar, U. Arieli, H. Suchowski, Spatio-temporal ultrafast pulse shaping at the femtosecond-nanometer scale. *Opt. Lett.* (2022).

Appendix

Appendix A - Adiabatic FWM simulation:

```
-------------------------------------------------------
close all
clear all
clc

%% Draft Approximation is inserted to simulation
N_QPM=1; % This should be not relavent for us for 4wm%% What order of quasi phase
matching. ( start with 1 get plan, if not good enough for production so expand allways
odd)
Lc=20*1e-3; % what units is this [meter]
width=[1.5 1.55]; %x specify minmax edges for choosing scale factor for scale*cos(kg)
qeff_median=qeff_median_function(width);

lambda_pump_A=2200*1e-9;
lambda_pump_B=2000*1e-9;
lambda_signal_min=1650*1e-9;
lambda_signal_max=1720*1e-9;


Material= 'Neff' %;%Si_1550_2000';% 'SLT'; % Chose 'SLT' for SLT, 'Mgcln' for Mgcln,
'KTP' for KTP; for 4wm i would want silicon ask haim if confused refracive.com
[P,order] =
Grating_Draft_Approx(width,N_QPM,Lc,lambda_signal_min,lambda_signal_max,lambda_pump_A,
lambda_pump_B,Material);
% look at asaf word p = a_k and order == n;

% now we have our crytal desgin ( intial geuss)

%% input parametes for the grating design inserted
% Kg_spline=polyval(P,z_norm_modified)
% z_norm=((z_old./(Lcr/2)*alpha+1)/2).^gamma;
% Kg=(polyval(P,z_norm)+beta);

alpha=0.6;%1; %0.6;%1%%%0.6%%%%;%0.6  less means Sterching the imagsec
beta=-11000;%1700;%-11000;%-4000%%%-11000%%%%;%8000;%-550 10*1e-3; % Translates  -
minus means right (move window) ( -1000 moves graph left)% less means move
gamma=0.45;%1; %0.45;%1%%%0.45%%%%%;%0.3; % [1-1.2 ]
% alpha=1.5;%  Sterching
% beta=5.6*1e5;%10*1e-3; %
% gamma=1; % [1-1.2 ]
% Scale is the change in amplitude (1-Max/med)
scale=(max(Deff(width))/qeff_median)-1;  % DO NOT CHANGE THIS FOR TESTING. THIS SHOULD
BE CHANGED ONLY AT THE END WHEN YOU KNOW\DECIED IT

span_s_min=lambda_signal_min-0*1e-9;
span_s_max=lambda_signal_max+0*1e-9; % show more of the edge for understanding the
edges
% so guess for lambdasmin----lmabdsmax but checking for more colores.
%%

[ Conversion_curve,lambda_s ] = Run_sim(
alpha,beta,gamma,scale,qeff_median,N_QPM,Lc,P,order,span_s_min,span_s_max,lambda_pump_
A,lambda_pump_B,Material)

%% Showing results :
% figure(2);
% subplot(3,1,2)
%  plot(lambda_s./1e-9,smooth(Conversion_curve,3,'sgolay'),'LineWidth',3);
```

```matlab
%  xlabel('\lambda_s [nm]','FontSize',16);
%  set(gca,'FontSize',16);
%  set(gca,'LineWidth',2);
%  xlim([span_s_min./1e-9, span_s_max./1e-9]);
%  title(['Conversion efficiency \eta[%]   ','I_p=1','[GW/cm^2]']);
%  grid on;
%  hold on;

 %% Calculating and plotting the design
z=linspace(-Lc/2,Lc/2,10000);
z_old=z;
z_norm=((z_old./(Lc/2)*alpha+1)/2).^gamma;
Kg=(polyval(P,z_norm)+beta); % There was a 100* here but i dropped it caus it
different units now
qeff_cos = scale.*cos((Kg.*z_old));
qeff_tot=(1+qeff_cos)*qeff_median;
width=qeff_to_width(qeff_tot); % in microns
width=width*1e-6; % meter
figure(2715711)
plot(z,width,'bo')
xlabel('z [meter]')
ylabel('y [micrometer]')
title('crystal width')

 ----------------------------------------------------
function [ Conversion_curve,lambda_s ] =
Run_sim(alpha,beta,gamma,scale,qeff_median,N_QPM,Lc,P,order,span_s_min,span_s_max,lamb
da_pump_A,lambda_pump_B,Material,String)
%% List of deimentions:
%[fs] = [c/lambda] = [1/s]
%Lambda = [1/m]
%[c] = [m/s]
% eta= [Ohm]
% Xai_3 = [m/V]
% Pump_A_Intensity=[W/m]

%% Deciding Variables and Resolution:
%% Controled parameters
%%%%%%%%%% Resolution   %%%%%%%%%%%%%%%%
calc_per_mm=100; % should be 1000 for this simulation % 100 calculation per mm of the
crystal.  IMPORTANT RESSSSSS
Ns_res = 1;% 0.1; % resolution of wavelengths in nm of simluation ( the higher the
better)
%%%%%%%%%%%%%%%%%%%%%%%%%%%%%%%%%%%%%%
%% Do not change this : Your controled(above) parameters define these other resolution
parametrs:
calc_per_meter=calc_per_mm*1e3;
N=ceil(calc_per_meter*Lc); % number of Total calculations
z=linspace(-Lc/2,Lc/2,N);

%% Set initial intesity
% A=sqrt(2*power);


ApA0=10;% [Watt]
ApB0=10;% [Watt]
As0=3; %  % [Watt] [This power is for for each wave length! ]
Ai0=0;% [Watt]

Is0=As0;
%% Defining coefficients
Cai_3=2.5*1e-19; % foud this value. this is the mean of cai 3 in the range we ar
wroking 1500-2100 nm %Journal of Applied Physics 110, 011301 (2011); doi:
http://dx.doi.org/10.1063/1.3592270
%Cai_3=8.38*1e-20; % [m/V] API JAP 74 4710 ( sudarson gave me )
c=3*1e8;   % [m/s]
```

```matlab
eta_0=377; % [Ohm]   wavelength impedance;


beta_i=0*1e-2./1e9;
beta_pA=0*1e-2./1e9;
beta_pB=0*1e-2./1e9;
beta_s=0*1e-2./1e9;


%% Signal Grid - The same as the Pump one - SHG case
Ns_res =Ns_res; % 0.1; % resolution in nm of simluation
Ns=ceil(Ns_res*(span_s_max-span_s_min)./(1e-9)); % number of spectral point
Msg= ['Number of spectral points is :' num2str(Ns)]
Ni=Ns;
NpA=Ns;
NpB=Ns;

fs_min=c./span_s_max; % [fs] = [c/lambda] = [1/s]
fs_max=c./span_s_min;
fs=linspace(fs_min,fs_max,Ns)';
lambda_s=c./fs;
%% Pump Grid
fpA=c./lambda_pump_A';
fpB=c./lambda_pump_B';
%% Idler Grid
type1='SU(1,1) PumpA + PumpB - Signal'; % Conserved is the diffrence ai^2-as^2
type2='SU(2) PumpA + Signal - PumpB'; % Conserved is the sum ai^2+as^2
Nonlinear_procces_type = type2;

switch Nonlinear_procces_type
    case 'SU(1,1) PumpA + PumpB - Signal'
%          fi_min=fpA+fpB-fs_max; % 4wm
%          fi_max=fpA+fpB-fs_min; % 4wm
    case 'SU(2) PumpA + Signal - PumpB'
        %   delta_k=(ki+kpB-(ks+kpA));
            fi_max=-fpB+fpA+fs_max; % 4wm
            fi_min=fpA-fpB+fs_min; % 4wm
end


fi=linspace(fi_min,fi_max,Ni)';
lambda_i=c./fi;
%% Index of refraction definition

if strcmp(Material,'SLT')
   npA=n_SLT(lambda_pump_A./1e-6,25);  % Index(wavelength[micrometer],temperture)% The
/1e-6 takes it from meter to micrometers
   npB=n_SLT(lambda_pump_B./1e-6,25);
   ns=n_SLT(lambda_s./1e-6,25);
   ni=n_SLT(lambda_i./1e-6,25);
elseif strcmp(Material,'Mgcln')
   npA=n_mgcln5(lambda_pump_A./1e-6,25);  % Index(wavelength,temperture)
   npB=n_mgcln5(lambda_pump_B./1e-6,25);
   ns=n_mgcln5(lambda_s./1e-6,25);
   ni=n_mgcln5(lambda_i./1e-6,25);
elseif strcmp(Material,'KTP')
   npA=n_ktp_5gaab(lambda_pump_A./1e-6);  % Index(wavelength,temperture)
   npB=n_ktp_5gaab(lambda_pump_B./1e-6);
   ns=n_ktp_5gaab(lambda_s./1e-6);
   ni=n_ktp_5gaab(lambda_i./1e-6);
elseif strcmp(Material,'Si_1550_2000')
   npA=n_eff_Si_width_380nm_1550_2000(lambda_pump_A./1e-6);  %
Index(wavelength,temperture)
   npB=n_eff_Si_width_380nm_1550_2000(lambda_pump_B./1e-6);
   ns=n_eff_Si_width_380nm_1550_2000(lambda_s./1e-6);
   ni=n_eff_Si_width_380nm_1550_2000(lambda_i./1e-6);
```

```matlab
elseif strcmp(Material,'Neff')
msg='for not overloading memory - calculate per step'
%% Initial value of intex for calculating A0s at the moemnt its 1
npA=1;  % Index(wavelength,temperture)
   npB=1;
   ns=1;
   ni=1;

end

%% Pump - We'll assume flat spectral shape - Remember -
Apump_A0=ApA0;%  [Watt]
Apump_B0=ApB0; % [Watt]
%% Signal
SSignal_Intensity=ones(size(lambda_s));
As0=As0*SSignal_Intensity;

%% Idler Spectrum

Ai0=Ai0;% [Watt]

%% Now we can start simulating the pulse
% Defining the Grid struct:
Grids.fs=fs;
Grids.fpA=fpA;
Grids.fpB=fpB;
Grids.fi=fi;
% Defining the refractive Index struct
neff.ns=ns;
neff.npA=npA;
neff.npB=npB;
neff.ni=ni;
% Defining Simulation Parameters struct
Sim_params.Cai_3=Cai_3;
Sim_params.Lc=Lc;
Sim_params.Ns=Ns;
Sim_params.Ni=Ni;
Sim_params.NpA=NpA;
Sim_params.NpB=NpB;
Sim_params.beta_i=beta_i;
Sim_params.beta_pA=beta_pA;
Sim_params.beta_pB=beta_pB;
Sim_params.beta_s=beta_s;
Sim_params.alpha=alpha;
Sim_params.beta=beta;
Sim_params.gamma=gamma;
Sim_params.scale=scale;
Sim_params.N_QPM=N_QPM;
Sim_params.P=P;
Sim_params.order=order;
Sim_params.Material=Material;
Sim_params.qeff_median=qeff_median;
if exist('String','var')
    Sim_params.String=String;
end
% Defining The Signals struct


Signals.As=zeros(Ns,N,'single');
Signals.ApA=zeros(NpA,N,'single');
Signals.ApB=zeros(NpB,N,'single');
Signals.Ai=zeros(Ni,N,'single');

Signals.As(:,1)=As0;
Signals.ApA(:,1)=Apump_A0;
Signals.ApB(:,1)=Apump_B0;
```

```
Signals.Ai(:,1)=Ai0;
Signals.z=z;

[Signals]=Iter(Signals,Sim_params,neff,Grids); % this is actually the calucltion for
CW simluations

%%

z=Signals.z;
As=Signals.As;
ApA=Signals.ApA;
ApB=Signals.ApB;
Ai=Signals.Ai;

Ps=sum(abs(As).^2)./2; % (2*eta_0./ns_v),1);
Pi=sum(abs(Ai).^2)./2; % (2*eta_0./ni_v),1);
PpA=sum(abs(ApA).^2)./2; % (2*eta_0./npA_v),1);
PpB=sum(abs(ApB).^2)./2; % (2*eta_0./npB_v),1);


-------------------------------------------------------

-------------------------------------------------------
function [Signals]=Iter(Signals,Sim_params,neff,Grids)
% Signals - The Signals to modified

% Forth order Runga-Kutta
A=[ 0   0   0 0;
    0.5 0   0 0;
    0   0.5 0 0;
    0   0   1 0];
c=[0 0.5 0.5 1]';
bz=[1/6 , 1/3 , 1/3 , 1/6]';
n_K=4;

% Second order Runga-Kutta
% A=[0   0;
%    0.5 0];
%
% c=[0 0.5]';
% bz=[0, 1]';
% n_K=2;

% Retrieving Data from struct

Ns=Sim_params.Ns;
Ni=Sim_params.Ni;
NpA=Sim_params.NpA;
NpB=Sim_params.NpB;

As=Signals.As;
ApA=Signals.ApA;
ApB=Signals.ApB;
Ai=Signals.Ai;
z=Signals.z;

h=z(2)-z(1);
N=length(z);
M=10;
hM=h/M;

%% Initializing the next places in ApA for calcluation
        % Explanation : ApA is a 1x1000 vector, but it should interact
        % with all signal colores (effectivly the simuplation is running for all
signal colors seperatly one by one
        % so in order to make sure initial conidtions are held for all
```

```matlab
        % we initialize them manually at this stage:
    ApA(1:Ns,:)=ones(Ns,length(ApA)).*ApA;
    ApB(1:Ns,:)=ones(Ns,length(ApB)).*ApB;

%% End of Retrieving data from Signals struct
  if Ns==Ni
%         for wavelength_index=1:Ns


        for i=2:N

            if rem(10*(i/N),1)==0
                calc_step=100*(i/N);
                disp(['Step = ' num2str(calc_step) '%'])
%                 disp(['calc_step=' num2str(calc_step) ' -  wavelength left='
num2str(wavelength_index) '/' num2str(Ns) ])
            end

            As_temp=As(:,i-1);
            ApA_temp=ApA(:,i-1);
            ApB_temp=ApB(:,i-1);
            Ai_temp=Ai(:,i-1);


                for j=1:M

                        Ks=zeros(Ns,n_K);
                        KpA=zeros(NpA,n_K);
                        KpB=zeros(NpB,n_K);
                        Ki=zeros(Ns,n_K);

                        for m=1:n_K
                                [Ks(:,m),KpA(:,m),KpB(:,m),Ki(:,m),
delta_k_plus_kg, delta_k_minus_kg,
delta_k,parasitic_delta_k_mkg,parasitic_delta_k_pkg] = ...
                                matrix_ODE_BPM_1(As_temp
+hM*sum(bsxfun(@times,Ks,A(m,:)),2),...
                                                    ApA_temp
+hM*sum(bsxfun(@times,KpA,A(m,:)),2),...
                                                    ApB_temp
+hM*sum(bsxfun(@times,KpB,A(m,:)),2),...
                                                    Ai_temp
+hM*sum(bsxfun(@times,Ki,A(m,:)),2),...
                                                    z(i-1)+hM*(j-
1)+c(m)*hM,Sim_params,neff,Grids);


                        end

                        As_temp=As_temp+hM*sum(bsxfun(@times,Ks,bz'),2);
                        ApA_temp=ApA_temp+hM*sum(bsxfun(@times,KpA,bz'),2);
                        ApB_temp=ApB_temp+hM*sum(bsxfun(@times,KpB,bz'),2);
                        Ai_temp=Ai_temp+hM*sum(bsxfun(@times,Ki,bz'),2);
                %
                    end
%% testing code -

dkplus(:,i-1)=delta_k_plus_kg;
dkminus(:,i-1)=delta_k_minus_kg;
parasitic_delta_k_m(:,i-1)=parasitic_delta_k_mkg;
parasitic_delta_k_p(:,i-1)=parasitic_delta_k_pkg;
delta_k_tot(:,i-1)=delta_k;
% end of testing code
%%

            As(:,i)=As_temp;
```

```matlab
                    ApA(:,i)=ApA_temp;
                    ApB(:,i)=ApB_temp;
                    Ai(:,i)=Ai_temp;

            end
%       end
%% testing code -
figure(2);
subplot(2,2,4)
plot(z(2:end),dkplus,'b',z(2:end),dkminus,'r',z(2:end),delta_k_tot,'g')
title('dk plus - b dk minus -r  dk - g')
%% testing code -
figure;
plot(z(2:end),parasitic_delta_k_m,'b',z(2:end),parasitic_delta_k_p,'r',z(2:end),delta_
k_tot,'g')
title('parasitic +-(wa-wb) -->dk minus - b dk plus -r  dk - g')

% surf(1:Ns,2:N,dkplus)
%% Saving the modified signals into the signals structure
Signals.As=As;
Signals.ApA=ApA;
Signals.ApB=ApB;
Signals.Ai=Ai;


%% tmp delete after use
%% defining factors
%
% alpha=Sim_params.alpha;
% beta=Sim_params.beta;
% gamma=Sim_params.gamma;
% N_QPM=Sim_params.N_QPM;
% P=Sim_params.P;
% Lc=Sim_params.Lc;
%
%
% if isfield(Sim_params,'String')
%     eval(Sim_params.String);
% else
%     z_old=z./N_QPM;
%     Lcr=(Lc/N_QPM);
%     z_norm=((z_old./(Lcr/2)*alpha+1)/2).^gamma; %%% Why??  why is it changing the
the z?
%     Kg=100*(polyval(P,z_norm)+beta);
% %     deff=sign(cos(Kg.*z_old)); this is what asaf had
%     deff =cos(Kg.*z_old);
% end


  else
    errordlg('Ni is not equal Ns --> This means that you must change the code.','File
Error');
  end
end


-------------------------------------------------------

-------------------------------------------------------


function [dA_s,dA_pA,dA_pB,dA_i delta_k_plus_kg delta_k_minus_kg delta_k
parasitic_delta_k_mkg parasitic_delta_k_pkg] =
matrix_ODE_BPM_1(As,ApA,ApB,Ai,z,Sim_params,neff,Grids)
%% List of deimentions:
%[fs] = [c/lambda] = [1/s]
%Lambda = [1/m]
%[c] = [m/s]
```

```matlab
% eta= [Ohm]
% Xai_3 = [m/V]
% Pump_A_Intensity=[W/m]
% [kg]= [1/lambda]


c=3*1e8;
% Retrieving data
Cai_3=Sim_params.Cai_3;
Ns=Sim_params.Ns;
Ni=Sim_params.Ni;
NpA=Sim_params.NpA;
NpB=Sim_params.NpB;
beta_i=Sim_params.beta_i;
beta_pA=Sim_params.beta_pA;
beta_pB=Sim_params.beta_pB;
beta_s=Sim_params.beta_s;
qeff_median=Sim_params.qeff_median;
fs=Grids.fs;
fpA=Grids.fpA;
fpB=Grids.fpB;
fi=Grids.fi;
%% converting to wavelength (in meters)
lambda_s=c./fs;
lambda_pA=c./fpA;
lambda_pB=c./fpB;
lambda_i=c./fi;
%delta=Sim_params.delta;
%% defining factors
alpha=Sim_params.alpha;
beta=Sim_params.beta;
gamma=Sim_params.gamma;
scale=Sim_params.scale;
N_QPM=Sim_params.N_QPM;
P=Sim_params.P;
Lc=Sim_params.Lc;


%% Old asaf code
if isfield(Sim_params,'String')
    eval(Sim_params.String);
else
    z_old=z./N_QPM;
    Lcr=(Lc/N_QPM);
    z_norm=((z_old./(Lcr/2)*alpha+1)/2).^gamma;
    Kg=(polyval(P,z_norm)+beta); % There was a 100* here but i dropped it caus it
different units now

%% change for it to be 4wm
modulation_type = 'adiabatic';%
switch modulation_type
    case 'adiabatic'
         qeff_cos = scale.*cos((Kg.*z_old));
    case 'QPM'
        QPMKg=(polyval(P,0))+beta;
        qeff_cos = scale.*cos((QPMKg.*z_old));
        Kg=QPMKg;
    case 'bulk'
        Kg=0;
        qeff_cos = scale;
end

end
%%% end of old asafs code

%% Calculate(find) width
```

```matlab
qeff_tot=(1+qeff_cos)*qeff_median;
width=qeff_to_width(qeff_tot); % in microns
width=width*1e-6; % meter


%% Calculate index
    if strcmp(Sim_params.Material,'Neff')
        % [Neff] = Neff_width_lambda(xx,yy)
        % yy wis width (micrometer)
        % xx is wavelength ( meter )
        ns= Neff_width_lambda(lambda_s,width*1e6)';
        npA=Neff_width_lambda(lambda_pA,width*1e6);
        npB=Neff_width_lambda(lambda_pB,width*1e6);
        ni=Neff_width_lambda(lambda_i,width*1e6)';
    else
        % ns=neff.ns(wavelength_index);
        ns=neff.ns;
        npA=neff.npA;
        npB=neff.npB;
        ni=neff.ni;
    end

% End of retrieving data

%% defining propogation constants
ks=(2*pi*fs/c).*ns;
kpA=(2*pi*fpA/c).*npA;
kpB=(2*pi*fpB/c).*npB;
ki=(2*pi*fi/c).*ni;


%% Parameters :

epsilon0=8.854187817.*1e-12; % [Farad]/[meter]; Wikipedia
Cai_3;


normilization=1;


factor=epsilon0*Cai_3*qeff_tot*normilization;
% normilized_factor=(4./(fi+fs+fpA+fpB)).*(1+qeff_cos);
% factor=normilized_factor*8*1e-15;

% kan habibi



%% equations
type1='SU(1,1) PumpA + PumpB - Signal'; % Conserved is the diffrence ai^2-as^2
type2='SU(2) PumpA + Signal - PumpB'; % Conserved is the sum ai^2+as^2
Nonlinear_procces_type = type2;
switch Nonlinear_procces_type
    case 'SU(1,1) PumpA + PumpB - Signal'

        dA_i=-
1i.*factor*fi.*((0.5*(abs(Ai).^2)+abs(ApA).^2+abs(ApB).^2+abs(As).^2).*Ai  +
(conj(As).*ApA.*ApB).*exp(1i*(ki+ks-kpA-kpB).*z));

        dA_s=-
1i.*factor*fs.*((0.5*(abs(As).^2)+abs(ApA).^2+abs(ApB).^2+abs(Ai).^2).*As  +
(conj(Ai).*ApA.*ApB).*exp(1i*(ki+ks-kpA-kpB).*z));

        dA_pA=-
1i.*factor*fpA.*((0.5*(abs(ApA).^2)+abs(Ai).^2+abs(ApB).^2+abs(As).^2).*ApA  +
(conj(ApB).*As.*Ai).*exp(1i*(kpA+kpB-ki-ks).*z));
```

```matlab
        dA_pB=-
1i.*factor*fpB.*((0.5*(abs(ApB).^2)+abs(ApA).^2+abs(Ai).^2+abs(As).^2).*ApB  +
(conj(ApA).*As.*Ai).*exp(1i*(kpA+kpB-ki-ks).*z));
            msg='not taking into account in the moment any TPA effects';


    case 'SU(2) PumpA + Signal - PumpB'
        delta_k=(ki+kpB-(ks+kpA));

            dA_i=-
1i.*factor.*fi.*((0.5*(abs(Ai).^2)+abs(ApA).^2+abs(ApB).^2+abs(As).^2).*Ai  +
(conj(ApB).*As.*ApA).*exp(1i*delta_k.*z));

            dA_s=-
1i.*factor.*fs.*((0.5*(abs(As).^2)+abs(ApA).^2+abs(ApB).^2+abs(Ai).^2).*As  +
(conj(ApA).*Ai.*ApB).*exp(-1i*delta_k.*z));

            dA_pA=-
1i.*factor.*fpA.*((0.5*(abs(ApA).^2)+abs(Ai).^2+abs(ApB).^2+abs(As).^2).*ApA  +
(conj(As).*ApB.*Ai).*exp(-1i*delta_k.*z));

            dA_pB=-
1i.*factor.*fpB.*((0.5*(abs(ApB).^2)+abs(ApA).^2+abs(Ai).^2+abs(As).^2).*ApB  +
(conj(Ai).*ApA.*As).*exp(1i*delta_k.*z));
            msg='not taking into account in the moment any TPA effects';
 %% Testing code -
gamma_intesitiy_moduluation=(factor.*((fpA*abs(ApA).^2-fpB*abs(ApB).^2))/2);
% should add gamma in some way
 delta_k_minus_kg=delta_k-Kg+gamma_intesitiy_moduluation;
 delta_k_plus_kg=delta_k+Kg-gamma_intesitiy_moduluation;

 parasitic_delta_k_mkg=(ki-kpB-(ks-kpA))-Kg;
 parasitic_delta_k_pkg=(ki-kpB-(ks-kpA))+Kg;

end




end
-------------------------------------------------------

-------------------------------------------------------
function [P,order] =
Grating_Draft_Approx(width,N_QPM,Lc,lambda_signal_min,lambda_signal_max,lambda_pump_A,
lambda_pump_B,Material)

% lambda = [meter]
% k = [1/meter]
% L = [meter]
%% Setting approximat coeeficiant of additional phase :
% For simplicity, assuming both pumpA and pumpB are same strength and
% calculating gamma

Ip=1;% This will eventually be intesity of a GW/cm^2 But units are still gonna be w/m
!
Cai_3=2.5*1e-19; %   foud this value. this is the mean of cai 3 in the range we ar
wroking 1500-2100 nm %Journal of Applied Physics 110, 011301 (2011); doi:
http://dx.doi.org/10.1063/1.3592270
eta_0=377;
epsilon0=8.854187817.*1e-12 ; % [Farad]/[meter]
Pump_Intensity=Ip*(1e9/(1e-2).^2);
c=3*1e8;
```

```matlab
L=(Lc/N_QPM); % see High_Order_QPM.ppt for understading why this is the meaning.
%% Setting parameters for calculation
lambda_s=linspace(lambda_signal_min,lambda_signal_max,1000);
lambda_pA=lambda_pump_A;
lambda_pB=lambda_pump_B;

%% Creating space (:
z=linspace(-L/2,L/2,500); % [meter]
% lambda_i=1./(1./lambda_s-1./lambda_p); %TWM DFG
%lambda_i=1./(1./lambda_s+1./lambda_p); %TWM SFG

%% Chossing interaction type
type1='SU(1,1) PumpA + PumpB - Signal'; % Conserved is the diffrence ai^2-as^2
type2='SU(2) PumpA + Signal - PumpB'; % Conserved is the sum ai^2+as^2


Nonlinear_procces_type = type2;
switch Nonlinear_procces_type
    case 'SU(1,1) PumpA + PumpB - Signal'
        lambda_i=1./(1./lambda_pB+1./lambda_pA-1./lambda_s); %4wm
    case 'SU(2) PumpA + Signal - PumpB'
     lambda_i=1./(1./lambda_pA+1./lambda_s-1./lambda_pB); %4wm
end


%% Index of refraction definition
%% converting lambda to micrometer: caus thats what they like
lambda_s=linspace(lambda_signal_min,lambda_signal_max,1000).*(1e6);
lambda_pA=lambda_pump_A.*(1e6);
lambda_pB=lambda_pump_B.*(1e6);
lambda_i=lambda_i.*1e6;
if strcmp(Material,'SLT')
   npA=n_SLT(lambda_pA,25);  % Index(wavelength[micrometer],temperture)
   npB=n_SLT(lambda_pB,25);
   ns=n_SLT(lambda_s,25);
   ni=n_SLT(lambda_i,25);
elseif strcmp(Material,'Mgcln')
   npA=n_mgcln5(lambda_pA,25);  % Index(wavelength,temperture)
   npB=n_mgcln5(lambda_pB,25);
   ns=n_mgcln5(lambda_s,25);
   ni=n_mgcln5(lambda_i,25);
elseif strcmp(Material,'KTP')
   npA=n_ktp_5gaab(lambda_pA);  % Index(wavelength,temperture)
   npB=n_ktp_5gaab(lambda_pB);
   ns=n_ktp_5gaab(lambda_s);
   ni=n_ktp_5gaab(lambda_i);
elseif strcmp(Material,'Si_1550_2000')
   npA=n_eff_Si_width_380nm_1550_2000(lambda_pA);  % Index(wavelength,temperture)
   npB=n_eff_Si_width_380nm_1550_2000(lambda_pB);
   ns=n_eff_Si_width_380nm_1550_2000(lambda_s);
   ni=n_eff_Si_width_380nm_1550_2000(lambda_i);
elseif strcmp(Material,'Neff')
    median_width=0.7*0.5*(max(width)+min(width))
   npA=Neff_width_lambda(lambda_pA*1e-6,median_width);  % Index(wavelength,temperture)
   npB=Neff_width_lambda(lambda_pB*1e-6,median_width);
   ns=Neff_width_lambda(lambda_s*1e-6,median_width)';
   ni=Neff_width_lambda(lambda_i*1e-6,median_width)';

end
%% converting lambda to micrometer: caus we work in meter !!
lambda_s=lambda_s.*(1e-6);
lambda_pA=lambda_pA.*(1e-6);
lambda_pB=lambda_pB.*(1e-6);
lambda_i=lambda_i.*1e-6;
 %% end of building index
```

```matlab
 %% Parameters to calculate gamma : phase shift due to kerr effect
Ap0=sqrt(Pump_Intensity*2*eta_0./npA);
% factor=epsilon0*Cai_3*qeff_median_function(width);
% normilized_factor=(4/(fi+fs+fpA+fpB)).*(1+deff);
normilization=1e-14;


factor=epsilon0*Cai_3*qeff_median_function(width)*normilization;
% fpA=c./lambda_pA;
% fpB=c./lambda_pB;
% normilized_factor=(4./(fi+fs+fpA+fpB));
% factor=normilized_factor*8*1e-15;

%%

% lambda = [meter]
% k = [1/meter]
ks=(2*pi./lambda_s).*ns;
kpA=(2*pi./lambda_pA).*npA;
kpB=(2*pi./lambda_pB).*npB;
ki=(2*pi./lambda_i).*ni;

%% Calculating gamma the auto and cross modulation for pumpA=pumpB intesity
     fi=c./lambda_i;
     fs=c./lambda_s;
     [Wis Wis_index]=max(abs(fi-fs));
     Wis=Wis*sign(fi(Wis_index)-fs(Wis_index));
gamma=(factor.*Wis/2)*abs(Ap0).^2;
%%
%% tmp
gamma=gamma;



%% Chossing interactiong Type :

switch Nonlinear_procces_type
    case 'SU(1,1) PumpA + PumpB - Signal'
        msgbox('Error in Grating_Draft_Approx line 64, Delta_k mismatch no defied
yet!')
%         delta_k=(ki-(kpA+kpB-ks)); %4wm %%

    case 'SU(2) PumpA + Signal - PumpB'
     delta_k=(ki+kpB-(ks+kpA)); %4wm %%

end


%delta_k=(ki-(ks+kpA))/1; %SFG
% delta_k=ks-(ki+kp); %DFG


%% Kgnom definition - Muamad Rishoni !
lambda_Adi_max=0.4*max(2*pi./(delta_k+gamma)); % Called lambda_A_max for historic
reasons  - i would of called it lambda_tmp
lambda_Adi_min=1.7*min(2*pi./(delta_k+gamma));
lambda_mid=(lambda_Adi_max+lambda_Adi_min)/2;
delta_lambda=(lambda_Adi_max-lambda_Adi_min);
lambda=(lambda_mid+(delta_lambda./L).*z);
Kg_nom=2*pi./lambda; %% muamad rishoni
if min((delta_k+gamma))<0
    msg='delta k is negative, im unsure what this means- -   check this in grating
draft approx'
end

z_norm=(z./((L/2))+1)/2;
```

```
order=0;
Delta=10;
while Delta>1.001
    order=order+1;
    P=polyfit(z_norm,Kg_nom,order); % a_k
    Kg_sp=polyval(P,z_norm); % Kg_spline - the value of Kg when using this polyfit
    Delta=max(Kg_sp./Kg_nom)  % error between fit and wanted. if its small thne yofi.
continue.
end
end
```

Appendix B – GUI script and simulation of spectral pulse shaping second harmonic generation in resonant interaction

```
function varargout = slm_simulation_fig_non_instan_option(varargin)
set(groot,'DefaultFigureColormap',jet)
% SLM_SIMULATION_FIG_NON_INSTAN_OPTION MATLAB code for
slm_simulation_fig_non_instan_option.fig
%      SLM_SIMULATION_FIG_NON_INSTAN_OPTION, by itself, creates a new
SLM_SIMULATION_FIG_NON_INSTAN_OPTION or raises the existing
%      singleton*.
%
%      H = SLM_SIMULATION_FIG_NON_INSTAN_OPTION returns the handle to a new
SLM_SIMULATION_FIG_NON_INSTAN_OPTION or the handle to
%      the existing singleton*.
%
%      SLM_SIMULATION_FIG_NON_INSTAN_OPTION('CALLBACK',hObject,eventData,handles,...)
calls the local
%      function named CALLBACK in SLM_SIMULATION_FIG_NON_INSTAN_OPTION.M with the
given input arguments.
%
%      SLM_SIMULATION_FIG_NON_INSTAN_OPTION('Property','Value',...) creates a new
SLM_SIMULATION_FIG_NON_INSTAN_OPTION or raises the
%      existing singleton*.  Starting from the left, property value pairs are
%      applied to the GUI before slm_simulation_fig_non_instan_option_OpeningFcn gets
called.  An
%      unrecognized property name or invalid value makes property application
%      stop.  All inputs are passed to slm_simulation_fig_non_instan_option_OpeningFcn
via varargin.
%
%      *See GUI Options on GUIDE's Tools menu.  Choose "GUI allows only one
%      instance to run (singleton)".
%
% See also: GUIDE, GUIDATA, GUIHANDLES

% Edit the above text to modify the response to help
slm_simulation_fig_non_instan_option

% Last Modified by GUIDE v2.5 26-Jul-2020 12:25:25

% Begin initialization code - DO NOT EDIT
gui_Singleton = 1;
gui_State = struct('gui_Name',        mfilename, ...
                   'gui_Singleton',  gui_Singleton, ...
                   'gui_OpeningFcn', @slm_simulation_fig_non_instan_option_OpeningFcn,
...
                   'gui_OutputFcn',  @slm_simulation_fig_non_instan_option_OutputFcn,
...
                   'gui_LayoutFcn',  [] , ...
                   'gui_Callback',   []);
if nargin && ischar(varargin{1})
    gui_State.gui_Callback = str2func(varargin{1});
end

if nargout
    [varargout{1:nargout}] = gui_mainfcn(gui_State, varargin{:});
else
    gui_mainfcn(gui_State, varargin{:});
end
% End initialization code - DO NOT EDIT


% --- Executes just before slm_simulation_fig_non_instan_option is made visible.
function slm_simulation_fig_non_instan_option_OpeningFcn(hObject, eventdata, handles,
varargin)
% This function has no output args, see OutputFcn.
```

```
% hObject    handle to figure
% eventdata  reserved - to be defined in a future version of MATLAB
% handles    structure with handles and user data (see GUIDATA)
% varargin   command line arguments to slm_simulation_fig_non_instan_option (see
VARARGIN)

% Choose default command line output for slm_simulation_fig_non_instan_option
handles.output = hObject;

% Update handles structure
guidata(hObject, handles);

% UIWAIT makes slm_simulation_fig_non_instan_option wait for user response (see
UIRESUME)
% uiwait(handles.figure1);

%% perhaps this is needed:
% paths:
% addpath 'C:\Users\eyalb\Dropbox\Eyal Bahar\Masters - Tel
Aviv\Research\Matlab_simulations\noninstantanous'
%
%
%
%
%


% --- Outputs from this function are returned to the command line.
function varargout = slm_simulation_fig_non_instan_option_OutputFcn(hObject,
eventdata, handles)
% varargout  cell array for returning output args (see VARARGOUT);
% hObject    handle to figure
% eventdata  reserved - to be defined in a future version of MATLAB
% handles    structure with handles and user data (see GUIDATA)

% Get default command line output from handles structure
varargout{1} = handles.output;


% --------------------------------------------------------------------
function Untitled_1_Callback(hObject, eventdata, handles)
% hObject    handle to Untitled_1 (see GCBO)
% eventdata  reserved - to be defined in a future version of MATLAB
% handles    structure with handles and user data (see GUIDATA)



function eb_lambda0_Callback(hObject, eventdata, handles)
% hObject    handle to eb_lambda0 (see GCBO)
% eventdata  reserved - to be defined in a future version of MATLAB
% handles    structure with handles and user data (see GUIDATA)

% Hints: get(hObject,'String') returns contents of eb_lambda0 as text
%        str2double(get(hObject,'String')) returns contents of eb_lambda0 as a double


% --- Executes during object creation, after setting all properties.
lambda0 = str2double(get(handles.eb_lambda0_input,'String'));

function eb_lambda0_CreateFcn(hObject, eventdata, handles)
% hObject    handle to eb_lambda0 (see GCBO)
% eventdata  reserved - to be defined in a future version of MATLAB
% handles    empty - handles not created until after all CreateFcns called

% Hint: edit controls usually have a white background on Windows.
%       See ISPC and COMPUTER.
```

```matlab
if ispc && isequal(get(hObject,'BackgroundColor'),
get(0,'defaultUicontrolBackgroundColor'))
    set(hObject,'BackgroundColor','white');
end




function eb_lambda_fwhm_Callback(hObject, eventdata, handles)
% hObject    handle to eb_lambda_fwhm (see GCBO)
% eventdata  reserved - to be defined in a future version of MATLAB
% handles    structure with handles and user data (see GUIDATA)

% Hints: get(hObject,'String') returns contents of eb_lambda_fwhm as text
%        str2double(get(hObject,'String')) returns contents of eb_lambda_fwhm as a
double


% --- Executes during object creation, after setting all properties.
function eb_lambda_fwhm_CreateFcn(hObject, eventdata, handles)
% hObject    handle to eb_lambda_fwhm (see GCBO)
% eventdata  reserved - to be defined in a future version of MATLAB
% handles    empty - handles not created until after all CreateFcns called

% Hint: edit controls usually have a white background on Windows.
%       See ISPC and COMPUTER.
if ispc && isequal(get(hObject,'BackgroundColor'),
get(0,'defaultUicontrolBackgroundColor'))
    set(hObject,'BackgroundColor','white');
end




function res = eb_res_Callback(hObject, eventdata, handles)
% hObject    handle to eb_res (see GCBO)
% eventdata  reserved - to be defined in a future version of MATLAB
% handles    structure with handles and user data (see GUIDATA)

% Hints: get(hObject,'String') returns contents of eb_res as text
%        str2double(get(hObject,'String')) returns contents of eb_res as a double




% --- Executes during object creation, after setting all properties.
function eb_res_CreateFcn(hObject, eventdata, handles)
% hObject    handle to eb_res (see GCBO)
% eventdata  reserved - to be defined in a future version of MATLAB
% handles    empty - handles not created until after all CreateFcns called

% Hint: edit controls usually have a white background on Windows.
%       See ISPC and COMPUTER.
if ispc && isequal(get(hObject,'BackgroundColor'),
get(0,'defaultUicontrolBackgroundColor'))
    set(hObject,'BackgroundColor','white');
end


% --- Executes on button press in pb_run_simluation_gaus.
function pb_run_simluation_gaus_Callback(hObject, eventdata, handles)
% hObject    handle to pb_run_simluation_gaus (see GCBO)
% eventdata  reserved - to be defined in a future version of MATLAB
% handles    structure with handles and user data (see GUIDATA)

%% Get Data for simulation
lambda0 = str2double(get(handles.eb_lambda0,'String')); % lambda0 of pulse
res= str2double(get(handles.eb_res,'String'));
```

```matlab
lambda_fwhm= str2double(get(handles.eb_lambda_fwhm,'String'));


c=2.99792458e17; %met/sec -> nm\sec
% converting
w0=2*pi*c/lambda0; % frequaancy w0=2*pi*f0 % wo of pulse
t_fwhm = lambda0^2/c/lambda_fwhm*0.441*1e15; % fs
%% Getting t_fwhm of original pulse for showing in gui
textLabel = num2str(t_fwhm);
set(handles.tb_time_fwhm, 'String', textLabel);
%% creating pulse
% checking if spectrum is loaded or artificial
checkbox_value= get(handles.cb_use_load, 'Value');
switch checkbox_value
    case 1
            filne_name_direct=get(handles.eb_load_spectra_name,'String');
            filename_to_load=['D:\Dropbox\Eyal Bahar\Masters - Tel
Aviv\Research\spectras\' filne_name_direct];
            try
               loded_spectra=load(filename_to_load);
            catch
                 try
                 filename_to_load=['C:\Users\User\Dropbox\Eyal Bahar\Masters - Tel
Aviv\Research\spectras\' filne_name_direct];
                  loded_spectra=load(filename_to_load);
                  catch
%                      C:\Users\eyalb\Dropbox\Eyal Bahar\Masters - Tel
Aviv\Research\spectras\spectra\2020-07-26\loded_spectra_20200726T120757.mat
                    % laptop - work
                    filename_to_load=['C:\Users\eyalb\Dropbox\Eyal Bahar\Masters -
Tel Aviv\Research\spectras\' filne_name_direct];
                  loded_spectra=load(filename_to_load);
                end
            end
            w=2*pi*c./loded_spectra.current_data(:,1);
            gaussian_data=loded_spectra.current_data(:,2);
            lambda=2*pi*c./w;
            [max_of_loded_spectra_value
max_of_loded_spectra_index]=max(gaussian_data);
           %w0=w(max_of_loded_spectra_index);
            gaussian_w=gaussian_data./(max_of_loded_spectra_value)
             lambda0=2*pi*c/w0;
% Updating GUI info
          textLabel2='NaN - Loded data'
         set(handles.eb_lambda0,'String',num2str(lambda0));
          res = length(w);
          set(handles.eb_res,'String',num2str(res));
          set(handles.eb_lambda_fwhm,'String',textLabel2);
          set(handles.tb_time_fwhm, 'String', textLabel2);


    case 0
    [gaussian_w, w, lambda]=gaussian_pulse(res,lambda0,lambda_fwhm );
end

%% checking for variables to make sense in the future:
% This is here because after using loded data
tf = strcmp(get(handles.eb_lambda_fwhm,'String'),'NaN - Loded data');
if tf
    lambda_fwhm=66;
    time_fwhm=666;
end
%% getting mask

switch get(get(handles.bg_how_many_phases,'SelectedObject'),'Tag')   % Get Tag of
selected object.
```

```matlab
case 'rb_how_many_phases_1'

        %%%%%%%%%%%%%%%%%%%%%%%%%%%%%%%%%%%%%%%%%%%%%%%%%%%
        %%%%%%%%%%%%%%%%% Building  singal phase %%%%%%%%%%%%%%%
        %%%%%%%%%%%%%%%%%%%%%%%%%%%%%%%%%%%%%%%%%%%%%%%%%%%%
        %% Getting parameteres
        % From SLM Phase parameters
        phase_str_from_eb=get(handles.eb_phase,'String');
        a=str2double(get(handles.eb_mask_param_a,'String'));
        b=str2double(get(handles.eb_mask_param_b,'String'));
        d=str2double(get(handles.eb_mask_param_d,'String'));
        w0=2*pi*c/str2double(get(handles.eb_mask_param_lambda0,'String'));  % is
given as lambda0 but translated into w0. this is the mask parameter
        w02=2*pi*c/str2double(get(handles.eb_mask_param_lambda02,'String'));
        % From non-instantanous parameters
        gamma=eval((get(handles.eb_gamma,'String')));

        %% building phase
        phase=eval(get(handles.eb_phase,'String'));
        mask_f= mask(phase);


    case 'rb_how_many_phases_2'
        %%%%%%%%%%%%%%%%%%%%%%%%%%%%%%%%%%%%%%%%%%%%%%%%%%%%%%
        %%%%%%%%%%%%%%%%% Building multiphase phase (2) %%%%%%
        %%%%%%%%%%%%%%%%%%%%%%%%%%%%%%%%%%%%%%%%%%%%%%%%%%%%%%
        %% intializing Transform limited pulse
            transform_limited_phase=zeros(1,length(w));
            mask_f= mask(transform_limited_phase);



    %% Finding relavent places for range1
            % so first handling range 2 because w and lambda work backwards.
            % understand where the last jump is ( in this case its the only jump)


        % finding range for first two phase ( in terms of w, w_s(start), w_e(end))

            % note s<->e changes part because lambda and w are shitty

range1_s=2*pi*c/str2double(get(handles.eb_multiphase_one_range_e,'String'));

range1_e=2*pi*c/str2double(get(handles.eb_multiphase_one_range_s,'String'));
            range_1=rangefunc(range1_s,range1_e,w);
        % IMPORTANT NOTE: at range_2_e i imforced one_range_e so it would never overlap

range2_s=2*pi*c/str2double(get(handles.eb_multiphase_two_range_e,'String'));

range2_e=2*pi*c/str2double(get(handles.eb_multiphase_one_range_e,'String'));
            % here is inforcment for the txt bok :
                textLabel = (get(handles.eb_multiphase_one_range_e,'String'));
                set(handles.sb_multiphase_two_range_s, 'String', textLabel);
            eb_multiphase_two_range_s=str2double(textLabel)
            range_2=rangefunc(range2_s,range2_e,w);


        %% building phases
            % Shared :
            w0=2*pi*c/str2double(get(handles.eb_mask_param_lambda0,'String'));
            gamma=eval((get(handles.eb_gamma,'String')));

    %%%%%% First range box %%%%%
            a1=str2double(get(handles.eb_mask_param_a_multiphase_one,'String'));
            b1=str2double(get(handles.eb_mask_param_b_multiphase_one,'String'));
            d1=str2double(get(handles.eb_mask_param_d_multiphase_one,'String'));
```

```matlab
            w02_1=2*pi*c/str2double(get(handles.eb_mask_param_lambda02_1,'String'));

            % Setting this string for future use
            phase_str_from_eb=get(handles.eb_multiphase_one,'String');

            % setting the parameters so eval could use them!
            a=a1;
            b=b1;
            d=d1;
            w1=w02_1;


            % Building phase 1
            phase=eval(get(handles.eb_multiphase_one,'String'));
            phase1=phase;
            mask_1= mask(phase);
%%
    %%%%% Second range box %%%%


range2=eb_multiphase_two_range_s;%str2double(get(handles.eb_multiphase_two_range_s,'St
ring'));
            a2=str2double(get(handles.eb_mask_param_a_multiphase_two,'String'));
            b2=str2double(get(handles.eb_mask_param_b_multiphase_two,'String'));
            d2=str2double(get(handles.eb_mask_param_d_multiphase_two,'String')); ;
            w02_2=2*pi*c/str2double(get(handles.eb_mask_param_lambda02_2,'String'));

            % Setting this string for future use
            phase_str_from_eb=get(handles.eb_multiphase_two,'String');

            % setting the parameters so eval could use them!
            a=a2;
            b=b2;
            d=d2;
            w2=w02_2;

            % Building phase 2
            phase=eval(get(handles.eb_multiphase_two,'String'));
            phase2=phase;
            mask_2= mask(phase);

%%
        %%%%%%%%%%%%%%%%%%%%%%%%%%%%%%%%%%%%%%%
        %%%%%%%%%%%%   Total phase      %%%%%%%%%%
        %%%%%%%%%%%%%%%%%%%%%%%%%%%%%%%%%%%%%%%

%write here the multiphase blabla éù ôä ð÷åãä òãéðä ìâáé äúôéøä
            phase=range_1.*phase1+range_2.*phase2;

            mask_f=mask_1.*range_1+mask_2.*range_2;

          %finding empty parts and making then unity:
           mask_zero_index=find(mask_f==0);
           mask_f(mask_zero_index)=1;



    case 'rb_make_window'
        %% tmp for calculationg and adding ones to mask

        %% intialize parameters
        gamma=eval((get(handles.eb_gamma,'String')));
        transform_limited_phase=zeros(1,length(w));
        mask_f= mask(transform_limited_phase);
        phase=mask_f;
        %% make action
```

```matlab
        lambda_open=eval(get(handles.eb_lambda_open,'String'));
        lambda_close=eval(get(handles.eb_lambda_close,'String'));
        [mask_f phase]= make_windwon(w,mask_f,c,phase,lambda_open,lambda_close);

end

%% acting on gaussian

        Ew=mask_f.*sqrt(gaussian_w);



%% SFG
    %% Instantanousun
        [Iw_sfg,w_sfg,lambda_sfg] = iw_sfg(Ew,w,lambda);


    %% Non instantanous
        if get(handles.rb_non_instan,'Value')
        %% parameters for non instantanous resonance
        lambda0_ns=eval(get(handles.eb_lambda0_ns,'String'));
        [Iw_sfg_non_instan_with_phase Iw_sfg_non_instan_TL]=
sfg_simulation_non_instantanous(gaussian_w,w,transpose(mask_f),lambda0_ns,gamma,lambda
0,w0,lambda_fwhm);
        lambda_sfg = lambda_sfg + 25;
        end
        if get(handles.rb_miller_boyd,'Value')
        %% parameters for non instantanous resonance
        lambda0_ns=eval(get(handles.eb_lambda0_ns,'String'));
        [Iw_sfg_miller_boyd_with_phase Iw_sfg_miller_boyd_TL]=
sfg_simulation_miller_boyd(gaussian_w,w,transpose(mask_f),lambda0_ns,gamma,lambda0,w0,
lambda_fwhm);
        end

%% FFT to get time signal
        Et=fftshift(ifft(fftshift(Ew))).^2;

        dw = w(2)-w(1);
        Fst = 2*pi*1/dw;
        dft = Fst/length(w);
        t = -Fst/2:dft:Fst/2-dft;  % the effective dt = 1/(w(end)-w(1))
%%
%%%%%%%%%%%%%%%%%%%%%%%%%%%%%%%%%%%%%%%%%%%%%
%%%%                  Plotting               %%%%%
%%%%%%%%%%%%%%%%%%%%%%%%%%%%%%%%%%%%%%%%%%%%%%%
    if a==666
        ['stop here']
    end
        %%%%%%%%%%%%%%%% PLOT FF(t) %%%%%%%%%%%%%%%%
                h=plot(handles.plot_ff_t,1e15*t,abs(Et)/max(abs(Et)),'o-');
                title(handles.plot_ff_t, 'I(t) after mask')
                %finding relavent places to plot
                field=abs(Et)/max(abs(Et));
                t_relav_s=find(field-0.001>0,1,'first');% finds fist index which is
relavent
                t_relav_e=find(field-0.001>0,1,'last'); % find last index thats
relavent

                if length(t_relav_s)==0
                    t_relav_s=1;
                end
                if length(t_relav_e)==0
                    t_relav_e=length(field);
                end
                try
```

```
                        axis(handles.plot_ff_t, [1e15*t(t_relav_s) 1e15*t(t_relav_e) -inf
inf]);
                end
                try
                        axis(handles.plot_ff_t, [-1e15*t(t_relav_s) -1e15*t(t_relav_e) -
inf inf]);
                end
                %  axis(handles.plot_ff_w, [-1e3 1e3 -inf inf]);
                xlabel(handles.plot_ff_t,'t [fs]')
                ylabel(handles.plot_ff_t,'Normilized intensity a.ref.')


%%
        %%%%%%%%%%%%%% Plot SFG   %%%%%%%%%%%%%
%% plotting instantnous or non instantanous or both !

        if get(handles.cb_show_TL_non_instan_and_masked_instan,'Value') % if check box
for show TL is marked
            if get(handles.rb_non_instan,'Value')

plot(handles.plot_iw_sfg,lambda_sfg,Iw_sfg_non_instan_TL,'b',lambda_sfg,Iw_sfg_non_ins
tan_with_phase,'--r')
                title(handles.plot_iw_sfg, '                     SFG - TL vs masked non
instan')
                xlabel(handles.plot_iw_sfg,' \lambda  [nm]')
                ylabel(handles.plot_iw_sfg,'intensity a.u.')
                xlim(handles.plot_iw_sfg,[0.5*lambda0-1.5*lambda_fwhm
0.5*lambda0+1.5*lambda_fwhm])
                lgd=legend(handles.plot_iw_sfg,'TL - non instantanous', 'with mask
non-instantanous');
                set(lgd,'position',[   0.365    0.362    0.1767    0.0592])
                lgd.FontSize = 8;
                    if b==666 % plot outside
                        figure(222)
%                       hold on
                        norm_fac= 1;
%max(max(max(Iw_sfg_non_instan_TL)),max(max(Iw_sfg_non_instan_with_phase)));

plot(lambda_sfg,Iw_sfg_non_instan_TL./norm_fac,'b',lambda_sfg,Iw_sfg_non_instan_with_p
hase./norm_fac,'-g')
                        title( '                   SFG - TL vs masked non instan')
                        xlabel(' \lambda  [nm]')
                        ylabel('intensity a.u.')
                        xlim([0.5*lambda0-1.5*lambda_fwhm
0.5*lambda0+1.5*lambda_fwhm])
                        lgd=legend('TL - non instantanous', 'with mask non-
instantanous');
                        set(lgd,'position',[   0.365    0.362    0.1767    0.0592])
                        lgd.FontSize = 8;
                    end
            else
                if get(handles.rb_miller_boyd,'Value')

plot(handles.plot_iw_sfg,lambda_sfg,Iw_sfg_miller_boyd_TL,'b',lambda_sfg,Iw_sfg_miller
_boyd_with_phase,'--r')
                title(handles.plot_iw_sfg, '                     SFG - TL vs masked non
instan')
                xlabel(handles.plot_iw_sfg,' \lambda  [nm]')
                ylabel(handles.plot_iw_sfg,'intensity a.u.')
                xlim(handles.plot_iw_sfg,[0.5*lambda0-1.5*lambda_fwhm
0.5*lambda0+1.5*lambda_fwhm])
                lgd=legend(handles.plot_iw_sfg,'TL - miller_boyd', 'with mask
miller_boyd');
                set(lgd,'position',[   0.365    0.362    0.1767    0.0592])
                lgd.FontSize = 8;
```

```
                else
%                   errordlg('Cant disply if non instantanous interaction radio button
is not chosed','File Error')
                        if get(handles.rb_instan,'Value') % checking wich radio button
is switch on - instan or non isntan
                            plot(handles.plot_iw_sfg,lambda_sfg,Iw_sfg,'b')
                            title(handles.plot_iw_sfg, 'SFG - instantanous')
                            xlabel(handles.plot_iw_sfg,' \lambda  [nm]')
                            ylabel(handles.plot_iw_sfg,'intensity a.u.')
                            xlim(handles.plot_iw_sfg,[0.5*lambda0-1.5*lambda_fwhm
0.5*lambda0+1.5*lambda_fwhm])
                        end
                end
            end
        else

        if get(handles.rb_instan,'Value') % checking wich radio button is switch on -
instan or non isntan
            plot(handles.plot_iw_sfg,lambda_sfg,Iw_sfg,'b')
            title(handles.plot_iw_sfg, 'SFG - instantanous')
            xlabel(handles.plot_iw_sfg,' \lambda  [nm]')
            ylabel(handles.plot_iw_sfg,'intensity a.u.')
            xlim(handles.plot_iw_sfg,[0.5*lambda0-1.5*lambda_fwhm
0.5*lambda0+1.5*lambda_fwhm])
        end

        if get(handles.rb_non_instan,'Value') % checking wich radio button is switch
on - instan or non isntan
            plot(handles.plot_iw_sfg,lambda_sfg,Iw_sfg_non_instan_with_phase,'--r')
            title(handles.plot_iw_sfg, 'SFG - non instantanous')
            xlabel(handles.plot_iw_sfg,' \lambda  [nm]')
            ylabel(handles.plot_iw_sfg,'intensity a.u.')
            xlim(handles.plot_iw_sfg,[0.5*lambda0-1.5*lambda_fwhm
0.5*lambda0+1.5*lambda_fwhm])
        end

         if get(handles.rb_miller_boyd,'Value') % checking wich radio button is
switch on - instan or non isntan
            plot(handles.plot_iw_sfg,lambda_sfg,Iw_sfg_miller_boyd_with_phase,'--r')
            title(handles.plot_iw_sfg, 'SFG - miller-boyd')
            xlabel(handles.plot_iw_sfg,' \lambda  [nm]')
            ylabel(handles.plot_iw_sfg,'intensity a.u.')
            xlim(handles.plot_iw_sfg,[0.5*lambda0-1.5*lambda_fwhm
0.5*lambda0+1.5*lambda_fwhm])
         end

        end




%%
        %%%%%%%%%%%%% Plot FF  %%%%%%%%%%%%%
            x=lambda;
            y1 = phase./pi;
            y2 = abs(Ew).^2;
% Create a plot with 2 y axes using the plotyy function
xlim(handles.plot_ff_w,[lambda0-2*lambda_fwhm lambda0+2.5*lambda_fwhm])
            [ax, h1, h2] = plotyy(handles.plot_ff_w,x, y2, x, y1,'plot');
%% This section is only for outplotting Ew phase plots
%
% y2
% x
% y1
```

```matlab
%
% % %
% % % figure(16052019)
% % % yyaxis left
% % % plot(2*pi*c./x,y2,'black','linewidth',3)
% % % ylabel('Normilized intensity')
% % % yyaxis right
% % % plot(2*pi*c./x,y1,':b','linewidth',5)
% % % ylim([0 1])
% % % ylabel('Phase [rad]')
% % % xlabel('\omega - Angular frequnacy')
% % % xlim(1e15.*[1.15 1.35])
% % % set(gca,'FontSize',20)
% % %


%%
            xlabel(handles.plot_ff_w,'\lambda  [nm]')
            title(handles.plot_ff_w, 'FF')
            set(h1,'LineStyle','--')
            set(h2,'MarkerSize',0.5)
            set(h2,'linestyle','none','marker','o');

        if get(handles.rb_make_window,'Value')
            set(h2,'linestyle','none','color','g');
        end
%smtng weird!!!! (handles.plot_ff_w,[lambda0-1.5*lambda_fwhm lambda0+1.5*lambda_fwhm])


        % Use the axis handles to set the labels of the y axes
        set(get(ax(1), 'Ylabel'), 'String', 'intensity a.u.');
        set(get(ax(2), 'Ylabel'), 'String', 'Phase (in units of \pi');

        if min(y1)~=max(y1) % just making sure plot minmax make sense
        %     set(ax(2),'ylim',[-pi/3*max(abs(y1)) pi/3*max(abs(y1))]);
        % set(ha(1),'ylim',[0 60],'ytick',[20 40]);
        end
        %%%% export plot figure - for article
% % % % % % figure(661092018)
% % % % %
% % % % %             [ax, h1, h2] = plotyy(x, y2, x, y1,'plot');
% % % % %              xlabel('\lambda  [nm]')
% % % % %              title('FF')
% % % % %              set(h1,'Linewidth',8)
% % % % %              set(h2,'LineStyle','-.')
% % % % %              set(h2,'Linewidth',4)
% % % % %              xlim(ax(1),[1300 1700])
% % % % %              xlim(ax(2),[1300 1700])
% % % % %              ylim(ax(2),[-10 10])
% % % % % %            set(h2,'linestyle','none','marker','o');
% % % % %
% % % % %          % Use the axis handles to set the labels of the y axes
% % % % %          set(get(ax(1), 'Ylabel'), 'String', 'intensity a.u.');
% % % % %          set(get(ax(2), 'Ylabel'), 'String', 'Phase (in units of \pi');
% % % % %
% % % % % % figure(661092019)
% % % % %                  h1=plot(1e15*t,abs(Et).^2/max(abs(Et)).^2,'-');
% % % % %
% % % % %                  %finding relavent places to plot
% % % % %                  xlim([-1000 1000])
% % % % %                  set(h1,'Linewidth',8)
%%%%%%%%%%%%%%%%%%%%%%%%%%%%%%%%%%%%

disp(['Done master - ended @ ' datestr(now)])
```

```matlab
function tb_time_fwhm_CreateFcn(hObject, eventdata, handles)
function eb_mask_param_a_Callback(hObject, eventdata, handles)
function eb_mask_param_a_CreateFcn(hObject, eventdata, handles)

if ispc && isequal(get(hObject,'BackgroundColor'),
get(0,'defaultUicontrolBackgroundColor'))
    set(hObject,'BackgroundColor','white');
end
function eb_phase_Callback(hObject, eventdata, handles)
function eb_phase_CreateFcn(hObject, eventdata, handles)
if ispc && isequal(get(hObject,'BackgroundColor'),
get(0,'defaultUicontrolBackgroundColor'))
    set(hObject,'BackgroundColor','white');
end
function eb_mask_param_b_Callback(hObject, eventdata, handles)
function eb_mask_param_b_CreateFcn(hObject, eventdata, handles)
if ispc && isequal(get(hObject,'BackgroundColor'),
get(0,'defaultUicontrolBackgroundColor'))
    set(hObject,'BackgroundColor','white');
end
function eb_mask_param_d_Callback(hObject, eventdata, handles)
function eb_mask_param_d_CreateFcn(hObject, eventdata, handles)
if ispc && isequal(get(hObject,'BackgroundColor'),
get(0,'defaultUicontrolBackgroundColor'))
    set(hObject,'BackgroundColor','white');
end
function eb_mask_param_lambda02_Callback(hObject, eventdata, handles)
function eb_mask_param_lambda02_CreateFcn(hObject, eventdata, handles)
if ispc && isequal(get(hObject,'BackgroundColor'),
get(0,'defaultUicontrolBackgroundColor'))
    set(hObject,'BackgroundColor','white');
end
function eb_mask_param_lambda0_CreateFcn(hObject, eventdata, handles)
if ispc && isequal(get(hObject,'BackgroundColor'),
get(0,'defaultUicontrolBackgroundColor'))
    set(hObject,'BackgroundColor','white');
end
function eb_multiphase_one_Callback(hObject, eventdata, handles)
function eb_multiphase_one_CreateFcn(hObject, eventdata, handles)
if ispc && isequal(get(hObject,'BackgroundColor'),
get(0,'defaultUicontrolBackgroundColor'))
    set(hObject,'BackgroundColor','white');
end
function eb_multiphase_two_Callback(hObject, eventdata, handles)
function eb_multiphase_two_CreateFcn(hObject, eventdata, handles)
if ispc && isequal(get(hObject,'BackgroundColor'),
get(0,'defaultUicontrolBackgroundColor'))
    set(hObject,'BackgroundColor','white');
end
function eb_mask_param_lambda0_Callback(hObject, eventdata, handles)
function eb_multiphase_one_range_s_Callback(hObject, eventdata, handles)
function eb_multiphase_one_range_s_CreateFcn(hObject, eventdata, handles)
if ispc && isequal(get(hObject,'BackgroundColor'),
get(0,'defaultUicontrolBackgroundColor'))
    set(hObject,'BackgroundColor','white');
end
function eb_multiphase_two_range_s_Callback(hObject, eventdata, handles)
function eb_multiphase_two_range_s_CreateFcn(hObject, eventdata, handles)
if ispc && isequal(get(hObject,'BackgroundColor'),
get(0,'defaultUicontrolBackgroundColor'))
    set(hObject,'BackgroundColor','white');
end
function bg_how_many_phases_CreateFcn(hObject, eventdata, handles)
function bg_how_many_phases_SelectionChangedFcn(hObject, eventdata, handles)
```

```matlab
function rb_how_many_phases_1_CreateFcn(hObject, eventdata, handles)
function rb_how_many_phases_1_Callback(hObject, eventdata, handles)
function eb_multiphase_one_range_e_Callback(hObject, eventdata, handles)
function eb_multiphase_one_range_e_CreateFcn(hObject, eventdata, handles)
if ispc && isequal(get(hObject,'BackgroundColor'),
get(0,'defaultUicontrolBackgroundColor'))
    set(hObject,'BackgroundColor','white');
end
function eb_multiphase_two_range_e_Callback(hObject, eventdata, handles)
function eb_multiphase_two_range_e_CreateFcn(hObject, eventdata, handles)
if ispc && isequal(get(hObject,'BackgroundColor'),
get(0,'defaultUicontrolBackgroundColor'))
    set(hObject,'BackgroundColor','white');
end
function eb_mask_param_b_multiphase_one_Callback(hObject, eventdata, handles)
function eb_mask_param_b_multiphase_one_CreateFcn(hObject, eventdata, handles)
if ispc && isequal(get(hObject,'BackgroundColor'),
get(0,'defaultUicontrolBackgroundColor'))
    set(hObject,'BackgroundColor','white');
end
function eb_mask_param_d_multiphase_one_Callback(hObject, eventdata, handles)
function eb_mask_param_d_multiphase_one_CreateFcn(hObject, eventdata, handles)
if ispc && isequal(get(hObject,'BackgroundColor'),
get(0,'defaultUicontrolBackgroundColor'))
    set(hObject,'BackgroundColor','white');
end
function eb_mask_param_lambda02_1_Callback(hObject, eventdata, handles)
function eb_mask_param_lambda02_1_CreateFcn(hObject, eventdata, handles)
if ispc && isequal(get(hObject,'BackgroundColor'),
get(0,'defaultUicontrolBackgroundColor'))
    set(hObject,'BackgroundColor','white');
end
function eb_mask_param_b_multiphase_two_Callback(hObject, eventdata, handles)
function eb_mask_param_b_multiphase_two_CreateFcn(hObject, eventdata, handles)
if ispc && isequal(get(hObject,'BackgroundColor'),
get(0,'defaultUicontrolBackgroundColor'))
    set(hObject,'BackgroundColor','white');
end
function eb_mask_param_d_multiphase_two_Callback(hObject, eventdata, handles)
function eb_mask_param_d_multiphase_two_CreateFcn(hObject, eventdata, handles)
if ispc && isequal(get(hObject,'BackgroundColor'),
get(0,'defaultUicontrolBackgroundColor'))
    set(hObject,'BackgroundColor','white');
end
function eb_mask_param_lambda02_2_Callback(hObject, eventdata, handles)
function eb_mask_param_lambda02_2_CreateFcn(hObject, eventdata, handles)
if ispc && isequal(get(hObject,'BackgroundColor'),
get(0,'defaultUicontrolBackgroundColor'))
    set(hObject,'BackgroundColor','white');
end
function eb_mask_param_a_multiphase_one_Callback(hObject, eventdata, handles)
function eb_mask_param_a_multiphase_one_CreateFcn(hObject, eventdata, handles)
if ispc && isequal(get(hObject,'BackgroundColor'),
get(0,'defaultUicontrolBackgroundColor'))
    set(hObject,'BackgroundColor','white');
end
function eb_mask_param_a_multiphase_two_Callback(hObject, eventdata, handles)
function eb_mask_param_a_multiphase_two_CreateFcn(hObject, eventdata, handles)
if ispc && isequal(get(hObject,'BackgroundColor'),
get(0,'defaultUicontrolBackgroundColor'))
    set(hObject,'BackgroundColor','white');
end
function sb_multiphase_two_range_s_CreateFcn(hObject, eventdata, handles)
function eb_run_range_mask_param_a_s_Callback(hObject, eventdata, handles)
function eb_run_range_mask_param_a_s_CreateFcn(hObject, eventdata, handles)
```

```matlab
if ispc && isequal(get(hObject,'BackgroundColor'),
get(0,'defaultUicontrolBackgroundColor'))
    set(hObject,'BackgroundColor','white');
end
function eb_run_range_mask_param_a_e_Callback(hObject, eventdata, handles)
function eb_run_range_mask_param_a_e_CreateFcn(hObject, eventdata, handles)
if ispc && isequal(get(hObject,'BackgroundColor'),
get(0,'defaultUicontrolBackgroundColor'))
    set(hObject,'BackgroundColor','white');
end
function eb_run_range_mask_param_a_res_Callback(hObject, eventdata, handles)
function eb_run_range_mask_param_a_res_CreateFcn(hObject, eventdata, handles)
if ispc && isequal(get(hObject,'BackgroundColor'),
get(0,'defaultUicontrolBackgroundColor'))
    set(hObject,'BackgroundColor','white');
end
function pb_run_range_CreateFcn(hObject, eventdata, handles)
function pb_run_range_Callback(hObject, eventdata, handles)
%% Get Data for simulation
        %% closing old figure
% % %        surf_fig=figure(2246);
% % %        close 2246
%% More re-editing from here.
phase_ranger_choise=get(handles.rb_run_range_phase1,'Value') ; % for now. when want to
change add this
%% loading parameters from gui
c=2.99792458e17; %met/sec -> nm\sec
lambda0 = str2double(get(handles.eb_lambda0,'String')); % of pulse
w0=2*pi*c/lambda0; % frequaancy w0=2*pi*f0 % of pulse
res= str2double(get(handles.eb_res,'String'));
lambda_fwhm= str2double(get(handles.eb_lambda_fwhm,'String'));
% % %
% % % t_fwhm = lambda0^2/c/lambda_fwhm*0.441*1e15; % fs
% % % %% Getting t_fwhm of original pulse for showing in gui
% % % textLabel = num2str(t_fwhm);
% % % set(handles.tb_time_fwhm, 'String', textLabel);
%% creating pulse
% load spectrum or not?
checkbox_value= get(handles.cb_use_load, 'Value');

if checkbox_value
            filne_name_direct=get(handles.eb_load_spectra_name,'String');

            try
                filename_to_load=['D:\Dropbox\Eyal Bahar\Masters - Tel
Aviv\Research\spectras\' filne_name_direct];
                loded_spectra=load(filename_to_load);
            catch
                try
                filename_to_load=['C:\Users\User\Dropbox\Eyal Bahar\Masters - Tel
Aviv\Research\spectras\' filne_name_direct];
                loded_spectra=load(filename_to_load);
                 catch

%                    C:\Users\eyalb\Dropbox\Eyal Bahar\Masters - Tel
Aviv\Research\spectras\spectra\2020-07-26\loded_spectra_20200726T120757.mat
                    % laptop - work
                    filename_to_load=['C:\Users\eyalb\Dropbox\Eyal Bahar\Masters -
Tel Aviv\Research\spectras\' filne_name_direct];
                    loded_spectra=load(filename_to_load);
                end
            end
            loded_spectra=load(filename_to_load);
    w=2*pi*c./loded_spectra.current_data(:,1);
    gaussian_data=loded_spectra.current_data(:,2);
    lambda=2*pi*c./w;
```

```matlab
    [max_of_loded_spectra_value max_of_loded_spectra_index]=max(gaussian_data);
     w0=w(max_of_loded_spectra_index);
    gaussian_w=gaussian_data./max_of_loded_spectra_value;
      lambda0=2*pi*c/w0;
       % Updating GUI info
   textLabel2='NaN - Loded data'
   set(handles.eb_lambda0,'String',num2str(lambda0));
    res = length(w);
    set(handles.eb_res,'String',num2str(res));
    set(handles.eb_lambda_fwhm,'String',textLabel2);
    set(handles.tb_time_fwhm, 'String', textLabel2);


else
    [gaussian_w, w, lambda]=gaussian_pulse(res,lambda0,lambda_fwhm );
    gaussian_w=transpose(gaussian_w);
    w=transpose(w);
    lambda=transpose(lambda);
end
% [gaussian_w, w, lambda]=gaussian_pulse(res,lambda0,lambda_fwhm );
%[gaussian_w,w,lambda]=gaussian_pulse(res,lambda0,lambda_fwhm )

%% getting mask
% phase parameters
%%%%%%%%%%%%%%%%%%%%%%%%%%%%%%%%%%%%%%%%%%%%%%%%%%%%%%%%%%%%%%%%
%%%%%%%%%%%%%%%%% Building  singal phase %%%%%%%%%%%%%%%%%%%%%%%%%
%%%%%%%%%%%%%%%%%%%%%%%%%%%%%%%%%%%%%%%%%%%%%%%%%%%%%%%%%%%%%%%%

%%%%%%%%%%%%%%%% running parameters %%%%%%%%%%%%%%%%%%%%%
a_s=str2double(get(handles.eb_run_range_mask_param_a_s,'String'));
a_e=str2double(get(handles.eb_run_range_mask_param_a_e,'String'));
a_res=str2double(get(handles.eb_run_range_mask_param_a_res,'String'));
a=linspace(a_s,a_e,a_res);

%% choosing if interaction is instantanous or non instantnouc
interaction_type=get(handles.bg_choose_instan,'SelectedObject');
interaction_type=get(interaction_type,'Tag');
 switch interaction_type
     case 'rb_instan'
                %% calculating Iw_sfg
                for ii=1:length(a)
                [w_sfg Iw_sfgn phase_txt_for_disply_in_figure_surf
b]=run_slm_inner(a(ii),phase_ranger_choise,hObject, eventdata, handles);
                Iw_sfg_instan(ii,:)=Iw_sfgn;
                end
                       %% plotting this case
                       %%%%%%%%%%%%%%%%%%%%%%%%%%
                       %%% Plotting surf %%%%%
                       %%%%%%%%%%%%%%%%%%%%%%%%

w0_mask_param=2*pi*c/str2double(get(handles.eb_mask_param_lambda0,'String'));  % is
given as lambda0 but translated into w0
                       figure(2246)
                       if get(handles.cb_plot_as_lambda,'Value')
%                         a_in_term_of_lambda=2*pi*c./a
                          lambda_sfg=2*pi*c./w_sfg;
                       h=surf(lambda_sfg,a,Iw_sfg_instan);
%                        xlim([0.5*lambda0*0.9 0.5*lambda0*1.1])
                       xlabel('\lambda')
                       else
                       h=surf(w_sfg,a,Iw_sfg_instan);
                       xlim([2*w0*0.9 2*w0*1.1])
                       xlabel('w')
                       end
%                         h=surf(w_sfg,a,Iw_sfg_instan)
                       set(h,'LineStyle','none')
```

```
                                view(0,90)
                                w0_txt_for_surf_plot_info = sprintf('%.5g', w0_mask_param);
                                title(['SFG instantanous ' phase_txt_for_disply_in_figure_surf
'      w0 = ' w0_txt_for_surf_plot_info '     b=' num2str(b) ])
                                %%tmp
% % % %                             figure(512020)
% % % %                             where=4500;
% % % %
h=surf(lambda_sfg(where:end),a,Iw_sfg_instan(:,where:end));
% % % %                                         set(h,'LineStyle','none')
% % % %                             view(0,90)


                                %%
                                ylabel('a')
                                zlabel('I')
                                disp(['Master Bahar, i am done running Range calculations @ '
datestr(now)])
%                       disp(['ended @ ' datestr(now)])
        case 'rb_non_instan'

                    %% calculating Iw_sfg
                            lambda0_ns=eval(get(handles.eb_lambda0_ns,'string'));
                            gamma=eval(get(handles.eb_gamma,'string'));


                             for ii=1:length(a)
                            [mask_f(ii,:) phase(ii,:) phase_txt_for_disply_in_figure_surf
b] = create_ranged_phase(a(ii),phase_ranger_choise,hObject, eventdata, handles);
                            [Iw_sfg_non_instan_with_phase_ii Iw_sfg_non_instan_TL]=
sfg_simulation_non_instantanous(transpose(gaussian_w),transpose(w),transpose(mask_f(ii
,:)),lambda0_ns,gamma,lambda0,w0,lambda_fwhm);

Iw_sfg_non_instan_with_phase(ii,:)=Iw_sfg_non_instan_with_phase_ii;
                            end

                             %% creating lambda_Sfg
                             w_sfg=linspace(2*w(1),2*w(end),2*length(w)-1);
                             lambda_sfg=2*pi*c./w_sfg;
                            %% plotting this case
                            %%%%%%%%%%%%%%%%%%%%%%%%
                            %%% Plotting surf %%%%%
                              %%%%%%%%%%%%%%%%%%%%%%%

w0_mask_param=2*pi*c/str2double(get(handles.eb_mask_param_lambda0,'String'));  % is
given as lambda0 but translated into w0
                            lambda_0_mask_param =
(get(handles.eb_mask_param_lambda0,'String'));
                            figure(2246)
                            if get(handles.cb_plot_as_lambda,'Value')
%                             a_in_term_of_lambda=2*pi*c./a
                            surfin=Iw_sfg_non_instan_with_phase;
                            surfin=surfin.*1e24;
                            surfin=surfin;

                            mean=100;

                            surfin=movmean(surfin',mean)';
                            surfin=surfin./max(max(surfin));
                            h=surf(15+lambda_sfg,a,surfin,'LineStyle','none');
                            colormap parula
                            try
                                xlim([300 500])
                            catch
                                xlim([0.5*lambda(1) 0.5*lambda(end)])
```

123

```matlab
                        xlim([300 500])
                    end
                    xlabel('\lambda')
                else
                    h=surf(w_sfg,a,Iw_sfg_non_instan_with_phase);
                    xlim([2*w0*0.9 2*w0*1.1])
                    xlabel('w')
                end
                set(h,'LineStyle','none')
                view(0,90)
                w0_txt_for_surf_plot_info = sprintf('%.4g', w0_mask_param);
                gamma_for_title = sprintf('%.4g',gamma)

                %% for paper
                colorbar
                if b==666
                    caxis_min=str2num(get(handles.eb_mask_param_d,'string'));

                caxis([caxis_min max(max((surfin)))])
                end
                title({['SFG-non instantanous  '
phase_txt_for_disply_in_figure_surf ],[' w_r=' num2str(lambda0_ns) '    w_0 = '
lambda_0_mask_param ],[' \Gamma = 2*pi*c*1e-7* '  num2str(gamma./(2*pi*c*1e-7)) 'nm  =
' num2str(round(2./gamma*1e15,1)) ' fs '], num2str(mean)})
%                   title({['SFG-non instantanous  '
phase_txt_for_disply_in_figure_surf ],[' w_0=' w0_txt_for_surf_plot_info '    b='
num2str(b) '    \Gamma ='  gamma_for_title ]})
                %%
                ylabel('a')
                zlabel('I')
                disp(['Master Bahar, i am done running Range calculations @ '
datestr(now)])


                %T temporary    only to get cross setcion
%
get_crossection(a,w_sfg,Iw_sfg_non_instan_with_phase,750,'lambda',0.5*lambda);
                %get_crossection(a,w,I,where,a_or_w_or_lambda,lambda)

%                   figure(666)

%                   plot(a,Iw_sfg_non_instan_with_phase(:,length(gaussian_w)/2))
        case 'rb_miller_boyd'

            %% calculating Iw_sfg
                lambda0_ns=eval(get(handles.eb_lambda0_ns,'string'));
                gamma=eval(get(handles.eb_gamma,'string'));


                for ii=1:length(a)
                [mask_f(ii,:) phase(ii,:) phase_txt_for_disply_in_figure_surf
b] = create_ranged_phase(a(ii),phase_ranger_choise,hObject, eventdata, handles);
                [Iw_sfg_miller_boyd_with_phase_ii Iw_sfg_miller_boyd_TL]=
sfg_simulation_miller_boyd(transpose(gaussian_w),transpose(w),transpose(mask_f(ii,:)),
lambda0_ns,gamma,lambda0,w0,lambda_fwhm);

Iw_sfg_miller_boyd_with_phase(ii,:)=Iw_sfg_miller_boyd_with_phase_ii;
                end

                %% creating lambda_Sfg
                w_sfg=linspace(2*w(1),2*w(end),2*length(w)-1);
                lambda_sfg=2*pi*c./w_sfg;
                %% plotting this case
                %%%%%%%%%%%%%%%%%%%%%%
                %%% Plotting surf %%%%%
                 %%%%%%%%%%%%%%%%%%%%%%
```

```matlab
w0_mask_param=2*pi*c/str2double(get(handles.eb_mask_param_lambda0,'String'));  % is
given as lambda0 but translated into w0
                        figure(2246)
                        if get(handles.cb_plot_as_lambda,'Value')
%                           a_in_term_of_lambda=2*pi*c./a
                        h=surf(lambda_sfg,a,Iw_sfg_miller_boyd_with_phase);
                        try
                            xlim([0.5*lambda(1) 0.5*lambda(end)])
%xlim([0.5*lambda0*0.97 0.5*lambda0*1.025])
                        catch
                            xlim([0.5*lambda(end) 0.5*lambda(1)])
%xlim([0.5*lambda0*0.97 0.5*lambda0*1.025])
                        end

                        xlabel('\lambda')
                        else
                        h=surf(w_sfg,a,Iw_sfg_miller_boyd_with_phase);
                        xlim([2*w0*0.9 2*w0*1.1])
                        xlabel('w')
                        end
                        set(h,'LineStyle','none')
                        view(0,90)
                        w0_txt_for_surf_plot_info = sprintf('%.4g', w0_mask_param);
                        gamma_for_title = sprintf('%.4g',gamma);
                        title(['SFG-miller-boyd  ' phase_txt_for_disply_in_figure_surf
'   w_0=' w0_txt_for_surf_plot_info '    b=' num2str(b) '    \Gamma ='
gamma_for_title ])

                        ylabel('a')
                        zlabel('I')
%                         disp('Done Range master')
%                         disp(['ended @ ' datestr(now)])
                        disp(['Master Bahar, i am done running Range calculations @ '
datestr(now)])

                        if 0; % plot cross_section
                            ii_start=find(lambda_sfg-765<0,1);
                            ii_end=find(lambda_sfg-740<0,1);
                            ii_765=find(lambda_sfg-765<0,1);
                            ii_760=find(lambda_sfg-760<0,1);
                            ii_757=find(lambda_sfg-757<0,1);
                            ii_750=find(lambda_sfg-750<0,1);
                            ii_745=find(lambda_sfg-745<0,1);
                            ii_list=[ii_765,ii_760,ii_757,ii_750,ii_745];
%                             jj=1;
                            for ii=ii_list% ii_start:300:ii_end
                                figure(2247)
                                hold on

plot(a,Iw_sfg_miller_boyd_with_phase(:,ii)./max(Iw_sfg_miller_boyd_with_phase(:,ii)),'
DisplayName',num2str(lambda_sfg(ii)))
%                                 legend_entry(jj)={num2str(lambda_sfg(ii))};

%                                 jj=jj+1;
%                                 pause()
                            end
                            legend show
                        end
 end
 figure(2246)
 if get(handles.cb_view_side,'Value')
 view([90 0])
 end
```

```matlab
% --- Executes on button press in pb_load_spectrum.
function pb_load_spectrum_Callback(hObject, eventdata, handles)
% hObject    handle to pb_load_spectrum (see GCBO)
% eventdata  reserved - to be defined in a future version of MATLAB
% handles    structure with handles and user data (see GUIDATA)
%[intn w] = spectrumexmpl(100,1.1*1e15,1.4*1e15)
[filename1,filepath1]=uigetfile({'*.*','All Files'},...
  'Select Data File 1');
  cd(filepath1);
  try
            load(filename1)
        counts=file_struct.data.spectral_data;
          spectrum=file_struct.data.spectrum;
           w=spectrum;
          intn=counts;
            current_data(:,1)=w;
            current_data(:,2)= intn;
            filename = ['loded_spectra_' datestr(now,30) '.mat'];

  mkdir(['spectra\' datestr(now,29)]);
    % get the new path
    FolderDestination=strcat(['spectra\' datestr(now,29)]);
  %%%%%%%%%%%%%%%%%%%%%%
  % saves if need
%
%% option to save :
save([FolderDestination '\' filename],'current_data')
  catch
  current_data = xlsread(filename1);
  w=current_data(:,1)
  intn=current_data(:,2)
    filename = ['loded_spectra_' datestr(now,30) '.mat'];

  mkdir(['spectra\' datestr(now,29)]);
    % get the new path
    FolderDestination=strcat(['spectra\' datestr(now,29)]);
  %%%%%%%%%%%%%%%%%%%%%%
  % saves if need
%
%% option to save :
save([FolderDestination '\' filename],'current_data')

  end


set(handles.eb_load_spectra_name,'String',['spectra\' datestr(now,29) '\' filename] )

plot(handles.plot_load_spectrum,w,intn,'o-');

%%% here should be added load file .....
%%%%%%
%%%%%%
%%%%%%
%%%%%%
%%%%%%
%%%%%%
%%%%%%
%%%%%%


% --- Executes on button press in cb_use_load.
function cb_use_load_Callback(hObject, eventdata, handles)
% hObject    handle to cb_use_load (see GCBO)
% eventdata  reserved - to be defined in a future version of MATLAB
% handles    structure with handles and user data (see GUIDATA)
```

```matlab
% Hint: get(hObject,'Value') returns toggle state of cb_use_load


% --- Executes during object creation, after setting all properties.
function cb_use_load_CreateFcn(hObject, eventdata, handles)
% hObject    handle to cb_use_load (see GCBO)
% eventdata  reserved - to be defined in a future version of MATLAB
% handles    empty - handles not created until after all CreateFcns called


% --- Executes during object creation, after setting all properties.
function pb_load_spectrum_CreateFcn(hObject, eventdata, handles)
% hObject    handle to pb_load_spectrum (see GCBO)
% eventdata  reserved - to be defined in a future version of MATLAB
% handles    empty - handles not created until after all CreateFcns called



function eb_load_spectra_name_Callback(hObject, eventdata, handles)
% hObject    handle to eb_load_spectra_name (see GCBO)
% eventdata  reserved - to be defined in a future version of MATLAB
% handles    structure with handles and user data (see GUIDATA)

% Hints: get(hObject,'String') returns contents of eb_load_spectra_name as text
%        str2double(get(hObject,'String')) returns contents of eb_load_spectra_name as
a double


% --- Executes during object creation, after setting all properties.
function eb_load_spectra_name_CreateFcn(hObject, eventdata, handles)
% hObject    handle to eb_load_spectra_name (see GCBO)
% eventdata  reserved - to be defined in a future version of MATLAB
% handles    empty - handles not created until after all CreateFcns called

% Hint: edit controls usually have a white background on Windows.
%       See ISPC and COMPUTER.
if ispc && isequal(get(hObject,'BackgroundColor'),
get(0,'defaultUicontrolBackgroundColor'))
    set(hObject,'BackgroundColor','white');
end

function [w_sfg Iw_sfg phase_txt_for_disply_in_figure_surf b] =
run_slm_inner(a,phase_ranger_choise,hObject, eventdata, handles)%% Get Data for
simulation
lambda0 = str2double(get(handles.eb_lambda0,'String'));
res= str2double(get(handles.eb_res,'String'));
lambda_fwhm= str2double(get(handles.eb_lambda_fwhm,'String'));

c=2.99792458e17; %met/sec -> nm\sec
% lambda0=1500;% [nm]
% lambda_fwhm=40;
w0=2*pi*c/lambda0; % frequaancy w0=2*pi*f0
t_fwhm = lambda0^2/c/lambda_fwhm*0.441*1e15; % fs
%% Getting t_fwhm of original pulse for showing in gui
textLabel = num2str(t_fwhm);
set(handles.tb_time_fwhm, 'String', textLabel);
%% creating pulse
%[gaussian_w, w, lambda]=gaussian_pulse(res,lambda0,lambda_fwhm );
%[gaussian_w,w,lambda]=gaussian_pulse(res,lambda0,lambda_fwhm )

% checking if spectrum is loaded or artificial
checkbox_value= get(handles.cb_use_load, 'Value');
if checkbox_value
    file_name_itself=get(handles.eb_load_spectra_name,'String');
            try
```

```matlab
                    loded_spectra=load(['D:\Dropbox\Eyal Bahar\Masters - Tel
Aviv\Research\spectras\' file_name_itself]);
                catch
                    try
                        filename_to_load=['C:\Users\User\Dropbox\Eyal Bahar\Masters - Tel
Aviv\Research\spectras\' file_name_itself];
                        loded_spectra=load(filename_to_load);
                    catch

%                        C:\Users\eyalb\Dropbox\Eyal Bahar\Masters - Tel
Aviv\Research\spectras\spectra\2020-07-26\loded_spectra_20200726T120757.mat
                        % laptop - work
                        filename_to_load=['C:\Users\eyalb\Dropbox\Eyal Bahar\Masters -
Tel Aviv\Research\spectras\' file_name_itself];
                        loded_spectra=load(filename_to_load);
                    end
                end
        w=2*pi*c./loded_spectra.current_data(:,1);
        gaussian_w=loded_spectra.current_data(:,2);
        lambda=2*pi*c./w;
       [max_of_loded_spectra_value, max_of_loded_spectra_index]=max(gaussian_w);
        w0=w(max_of_loded_spectra_index);

        lambda0=2*pi*c/w0;
        % Updating GUI info
    textLabel2='NaN - Loded data'
    set(handles.eb_lambda0,'String',num2str(lambda0));
     res = length(w);
     set(handles.eb_res,'String',num2str(res));
     set(handles.eb_lambda_fwhm,'String',textLabel2);
     set(handles.tb_time_fwhm, 'String', textLabel2);


else
    [gaussian_w, w, lambda]=gaussian_pulse(res,lambda0,lambda_fwhm );
end
% checking for variables to make sense in the future:
tf = strcmp(get(handles.eb_lambda_fwhm,'String'),'NaN - Loded data');
if tf
    % random values just for code to work
%     lambda_fwhm=50;
%     time_fwhm=80e15;
end
%% getting mask
% phase parameters
% for exapmle a*sin(b(w-w0)+c)
% a=0*1.5;
% b=5.9*1e-12;
% c=0;
%phase= a*sin(b*(w-w0)+c);
% % % a= 1*1e-27;
% % % % set(handles.rb_howmanyphase, 'SelectionChangeFcn',
@rb_howmanyphase_SelectionChangeFcn);
% % % % % get(handles.rb_howmanyphase_value,
% % % % if handles.rb_howmanyphase_value=1
%%%%%%%%%%%%%%%%%%%%%%%%%%%%%%%%%%%%%%%%%%%%%%%%%%%%%%%%%%%%%%%%%%
%%%%%%%%%%%%%%%%%%%%% setting handle for multiule choise of phase #######
%%%%%%%%%%%%%%%%%%%%%%%%%%%%%%%%%%%%%%%%%%%%%%%%%%%%%%%%%%%
% if get(eventdata.NewValue,'Value')


% if get(handles.rb_how_many_phases_1,'Value')
 if get(handles.rb_how_many_phases_1,'Value') % Get Tag of selected object.
%  display('Radio button 1');


%%%%%%%%%%%%%%%%%%%%%%%%%%%%%%%%%%%%%%%%%%%%%%%%%
```

```
%%%%%%%%%%%%%% Building  singal phase %%%%%%%%%%%%%%%%%%%%%
%%%%%%%%%%%%%%%%%%%%%%%%%%%%%%%%%%%%%%%%%%%%%%%%%%%%%
%phase=pi_setp(w,w0+w0/100); % pi_setp(w,ws)
%phase=a.*(w-w0).^2
b=str2double(get(handles.eb_mask_param_b,'String'));
d=str2double(get(handles.eb_mask_param_d,'String'));
% x=w
% x0=w0;
    w0_mask_param=2*pi*c/str2double(get(handles.eb_mask_param_lambda0,'String'));  %
is given as lambda0 but translated into w0
w02=2*pi*c/str2double(get(handles.eb_mask_param_lambda02,'String'));
phase_str_from_eb=get(handles.eb_phase,'String');
fun = str2func(['@(a,b,d,w,w0,w02)',phase_str_from_eb]);
phase=fun(a,b,d,w,w0_mask_param,w02);
mask_f= mask(phase);
phase_txt_for_disply_in_figure_surf=phase_str_from_eb;
 end


%%%%%%%%%%%%%%%%%%%%%%%%%%%%%%%%%%%%%%%%%%%%%%%%%%
%%%%%%%%%%%%%%%% Building multiphase phase (2) %%%%%%%%%%%%%%%%%%%%%%
%%%%%%%%%%%%%%%%%%%%%%%%%%%%%%%%%%%%%%%%%%%%%%%%%%
  if get(handles.rb_how_many_phases_2,'Value')
%% Finding relavent places for range1
% so firt handling range 2 because w and lambda work backwards.
% understand where the last jump is ( in this case its the only jump)


%%intializing Transform limited pulse
transform_limied_phase=zeros(1,length(w));
mask_f= mask(transform_limied_phase);
%% finding range for first two phase ( in terms of w, w_s(start), w_e(end))
% note s<->e changes part because lambda and w are shitty
range1_s=2*pi*c/str2double(get(handles.eb_multiphase_one_range_e,'String'));
range1_e=2*pi*c/str2double(get(handles.eb_multiphase_one_range_s,'String'));
range_1=rangefunc(range1_s,range1_e,w);
%% IMPORTANT NOTE: at range_2_e i imforced one_range_e so it would never overlap
range2_s=2*pi*c/str2double(get(handles.eb_multiphase_two_range_e,'String'));
range2_e=2*pi*c/str2double(get(handles.eb_multiphase_one_range_e,'String'));
% here is inforcment :  clc
textLabel = (get(handles.eb_multiphase_one_range_e,'String'));
set(handles.sb_multiphase_two_range_s, 'String', textLabel);
eb_multiphase_two_range_s=str2double(textLabel)
range_2=rangefunc(range2_s,range2_e,w);
% range1=2*pi*c/str2double(get(handles.eb_multiphase_one_range_s,'String')); % w -
this should tell you max wavlength ( min freq )
% w_minimal_range_index=find(w-range1>=0,1); % gives the index of min w where this
range should live.
%% building phases
% Shared :
w0_mask_param=2*pi*c/str2double(get(handles.eb_mask_param_lambda0,'String'));
%%%%%% First range %%%%%
if phase_ranger_choise==1
a1=a;
else
a1=str2double(get(handles.eb_mask_param_a_multiphase_one,'String'));
end
b1=str2double(get(handles.eb_mask_param_b_multiphase_one,'String'));

d=str2double(get(handles.eb_mask_param_d_multiphase_one,'String'));
w02_1=2*pi*c/str2double(get(handles.eb_mask_param_lambda02_1,'String'));

phase_str_from_eb=get(handles.eb_multiphase_one,'String');
fun = str2func(['@(a,b,c,w,w0,w1)',phase_str_from_eb]);
phase=fun(a1,b1,d,w,w0_mask_param,w02_1);
phase1=phase;
mask_1= mask(phase);
```

```
phase_txt_for_disply_in_figure_surf='Still need to code this';
% mask_f(w_minimal_range_index+1:end)=mask_range_1(w_minimal_range_index+1:end);
%%%%%%%%%%%%%%%%%%%%%%%%%%%%%%%%%%%%%%%%%%%55
%%%% Second Range %%%%%
  % is given as lambda0 but translated into w0
range2=eb_multiphase_two_range_s;%str2double(get(handles.eb_multiphase_two_range_s,'St
ring'));
if phase_ranger_choise==0
a2=a;
else
a2=str2double(get(handles.eb_mask_param_a_multiphase_two,'String'));
end

b2=str2double(get(handles.eb_mask_param_b_multiphase_two,'String'));
b=b
d=str2double(get(handles.eb_mask_param_d_multiphase_two,'String'));
w02_2=2*pi*c/str2double(get(handles.eb_mask_param_lambda02_2,'String'));

phase_str_from_eb=get(handles.eb_multiphase_two,'String');
fun = str2func(['@(a,b,c,w,w0,w2)',phase_str_from_eb]);
phase=fun(a2,b2,d,w,w0_mask_param,w02_2);
phase2=phase;
mask_2= mask(phase);
% phase_txt_for_disply_in_figure_surf=[phase_txt_for_disply_in_figure_surf1
phase_str_from_eb];
phase_txt_for_disply_in_figure_surf='Still need to code this';
% mask_f(1:w_minimal_range_index)= mask_range_2(1:w_minimal_range_index);
%%
%%%%%%%%%%%%%%%%%%%%%%%%%%%%%%%%%%%%

%%%%%%%%%%%%    Total phase        %%%%%%%%%%%

        %%%%%%%%%%%%%%%%%%%%%%%%%%%%

%write here the multiphase blabla éù ôä ð÷åãä òãéðä ìâáé äúôéøä
phase=range_1.*phase1+range_2.*phase2;
mask_f=mask_1.*range_1+mask_2.*range_2;
% finding emmpty parts and making then unity:
mask_zero_index=find(mask_f==0);
mask_f(mask_zero_index)=1;

            %%%%%%%%%%%%%%%%%%%%%%%%%%%%%
                %%%%%%%%%%%%%%%%%%%%%%%%%%%%%%%%
 end
%% acting on gaussian

Ew=mask_f.*gaussian_w;

%% Creating SFG




[Iw_sfg,w_sfg,lambda_sfg] = iw_sfg(Ew,w,lambda);


% disp('Done with inner function too master')
% disp(['Master Bahar, Calculation ended @ ' datestr(now) ])


% --- Executes during object creation, after setting all properties.
function latex_tb_lmabda0_CreateFcn(hObject, eventdata, handles)
% hObject    handle to latex_tb_lmabda0 (see GCBO)
% eventdata  reserved - to be defined in a future version of MATLAB
% handles    empty - handles not created until after all CreateFcns called
```

```
function eb_gamma_Callback(hObject, eventdata, handles)
% hObject    handle to eb_gamma (see GCBO)
% eventdata  reserved - to be defined in a future version of MATLAB
% handles    structure with handles and user data (see GUIDATA)

% Hints: get(hObject,'String') returns contents of eb_gamma as text
%        str2double(get(hObject,'String')) returns contents of eb_gamma as a double


% --- Executes during object creation, after setting all properties.
function eb_gamma_CreateFcn(hObject, eventdata, handles)
% hObject    handle to eb_gamma (see GCBO)
% eventdata  reserved - to be defined in a future version of MATLAB
% handles    empty - handles not created until after all CreateFcns called

% Hint: edit controls usually have a white background on Windows.
%       See ISPC and COMPUTER.
if ispc && isequal(get(hObject,'BackgroundColor'),
get(0,'defaultUicontrolBackgroundColor'))
    set(hObject,'BackgroundColor','white');
end



function eb_lambda0_ns_Callback(hObject, eventdata, handles)
% hObject    handle to eb_lambda0_ns (see GCBO)
% eventdata  reserved - to be defined in a future version of MATLAB
% handles    structure with handles and user data (see GUIDATA)

% Hints: get(hObject,'String') returns contents of eb_lambda0_ns as text
%        str2double(get(hObject,'String')) returns contents of eb_lambda0_ns as a
double


% --- Executes during object creation, after setting all properties.
function eb_lambda0_ns_CreateFcn(hObject, eventdata, handles)
% hObject    handle to eb_lambda0_ns (see GCBO)
% eventdata  reserved - to be defined in a future version of MATLAB
% handles    empty - handles not created until after all CreateFcns called

% Hint: edit controls usually have a white background on Windows.
%       See ISPC and COMPUTER.
if ispc && isequal(get(hObject,'BackgroundColor'),
get(0,'defaultUicontrolBackgroundColor'))
    set(hObject,'BackgroundColor','white');
end


% --- Executes on button press in cb_show_TL_non_instan_and_masked_instan.
function cb_show_TL_non_instan_and_masked_instan_Callback(hObject, eventdata, handles)
% hObject    handle to cb_show_TL_non_instan_and_masked_instan (see GCBO)
% eventdata  reserved - to be defined in a future version of MATLAB
% handles    structure with handles and user data (see GUIDATA)

% Hint: get(hObject,'Value') returns toggle state of
cb_show_TL_non_instan_and_masked_instan



% function eb_mask_param_d_multiphase_one_Callback(hObject, eventdata, handles)
% % hObject    handle to eb_mask_param_d_multiphase_one (see GCBO)
% % eventdata  reserved - to be defined in a future version of MATLAB
% % handles    structure with handles and user data (see GUIDATA)
%
```

```matlab
% % Hints: get(hObject,'String') returns contents of eb_mask_param_d_multiphase_one as
text
% %        str2double(get(hObject,'String')) returns contents of
eb_mask_param_d_multiphase_one as a double


% --- Executes during object creation, after setting all properties.
% function eb_mask_param_d_multiphase_one_CreateFcn(hObject, eventdata, handles)
% % hObject    handle to eb_mask_param_d_multiphase_one (see GCBO)
% % eventdata  reserved - to be defined in a future version of MATLAB
% % handles    empty - handles not created until after all CreateFcns called
%
% % Hint: edit controls usually have a white background on Windows.
% %       See ISPC and COMPUTER.
% if ispc && isequal(get(hObject,'BackgroundColor'),
get(0,'defaultUicontrolBackgroundColor'))
%     set(hObject,'BackgroundColor','white');
% end


% function eb_mask_param_d_multiphase_two_Callback(hObject, eventdata, handles)
% % hObject    handle to eb_mask_param_d_multiphase_two (see GCBO)
% % eventdata  reserved - to be defined in a future version of MATLAB
% % handles    structure with handles and user data (see GUIDATA)
%
% % Hints: get(hObject,'String') returns contents of eb_mask_param_d_multiphase_two as
text
% %        str2double(get(hObject,'String')) returns contents of
eb_mask_param_d_multiphase_two as a double


% --- Executes during object creation, after setting all properties.
% function eb_mask_param_d_multiphase_two_CreateFcn(hObject, eventdata, handles)
% % hObject    handle to eb_mask_param_d_multiphase_two (see GCBO)
% % eventdata  reserved - to be defined in a future version of MATLAB
% % handles    empty - handles not created until after all CreateFcns called
%
% % Hint: edit controls usually have a white background on Windows.
% %       See ISPC and COMPUTER.
% if ispc && isequal(get(hObject,'BackgroundColor'),
get(0,'defaultUicontrolBackgroundColor'))
%     set(hObject,'BackgroundColor','white');
% end


% --- Executes on button press in cb_block_amplitude.
function cb_block_amplitude_Callback(hObject, eventdata, handles)
% hObject    handle to cb_block_amplitude (see GCBO)
% eventdata  reserved - to be defined in a future version of MATLAB
% handles    structure with handles and user data (see GUIDATA)

% Hint: get(hObject,'Value') returns toggle state of cb_block_amplitude


function eb_lambda_open_Callback(hObject, eventdata, handles)
% hObject    handle to eb_lambda_open (see GCBO)
% eventdata  reserved - to be defined in a future version of MATLAB
% handles    structure with handles and user data (see GUIDATA)

% Hints: get(hObject,'String') returns contents of eb_lambda_open as text
%        str2double(get(hObject,'String')) returns contents of eb_lambda_open as a
double
```

```matlab
% --- Executes during object creation, after setting all properties.
function eb_lambda_open_CreateFcn(hObject, eventdata, handles)
% hObject    handle to eb_lambda_open (see GCBO)
% eventdata  reserved - to be defined in a future version of MATLAB
% handles    empty - handles not created until after all CreateFcns called

% Hint: edit controls usually have a white background on Windows.
%       See ISPC and COMPUTER.
if ispc && isequal(get(hObject,'BackgroundColor'),
get(0,'defaultUicontrolBackgroundColor'))
    set(hObject,'BackgroundColor','white');
end


function eb_lambda_close_Callback(hObject, eventdata, handles)
% hObject    handle to eb_lambda_close (see GCBO)
% eventdata  reserved - to be defined in a future version of MATLAB
% handles    structure with handles and user data (see GUIDATA)

% Hints: get(hObject,'String') returns contents of eb_lambda_close as text
%        str2double(get(hObject,'String')) returns contents of eb_lambda_close as a
double


% --- Executes during object creation, after setting all properties.
function eb_lambda_close_CreateFcn(hObject, eventdata, handles)
% hObject    handle to eb_lambda_close (see GCBO)
% eventdata  reserved - to be defined in a future version of MATLAB
% handles    empty - handles not created until after all CreateFcns called

% Hint: edit controls usually have a white background on Windows.
%       See ISPC and COMPUTER.
if ispc && isequal(get(hObject,'BackgroundColor'),
get(0,'defaultUicontrolBackgroundColor'))
    set(hObject,'BackgroundColor','white');
end


% --- Executes during object creation, after setting all properties.

% --- Executes during object creation, after setting all properties.
function plot_iw_sfg_CreateFcn(hObject, eventdata, handles)
% hObject    handle to plot_iw_sfg (see GCBO)
% eventdata  reserved - to be defined in a future version of MATLAB
% handles    empty - handles not created until after all CreateFcns called

% Hint: place code in OpeningFcn to populate plot_iw_sfg


% --- Executes during object creation, after setting all properties.
function ivan_CreateFcn(hObject, eventdata, handles)
% hObject    handle to ivan (see GCBO)
% eventdata  reserved - to be defined in a future version of MATLAB
% handles    empty - handles not created until after all CreateFcns called

% Hint: place code in OpeningFcn to populate ivan


% --- Executes during object creation, after setting all properties.
function plot_tmp_CreateFcn(hObject, eventdata, handles)
% hObject    handle to plot_ff_w (see GCBO)
% eventdata  reserved - to be defined in a future version of MATLAB
% handles    empty - handles not created until after all CreateFcns called

% Hint: place code in OpeningFcn to populate plot_ff_w
```

```
% --- Executes on button press in cb_plot_as_lambda.
function cb_plot_as_lambda_Callback(hObject, eventdata, handles)
% hObject    handle to cb_plot_as_lambda (see GCBO)
% eventdata  reserved - to be defined in a future version of MATLAB
% handles    structure with handles and user data (see GUIDATA)

% Hint: get(hObject,'Value') returns toggle state of cb_plot_as_lambda


% --- Executes during object creation, after setting all properties.
function plot_load_spectrum_CreateFcn(hObject, eventdata, handles)
% hObject    handle to plot_load_spectrum (see GCBO)
% eventdata  reserved - to be defined in a future version of MATLAB
% handles    empty - handles not created until after all CreateFcns called

% Hint: place code in OpeningFcn to populate plot_load_spectrum

function plot_ff_t_CreateFcn(hObject, eventdata, handles)
% hObject    handle to plot_ff_w (see GCBO)
% eventdata  reserved - to be defined in a future version of MATLAB
% handles    empty - handles not created until after all CreateFcns called

% Hint: place code in OpeningFcn to populate plot_ff_w


% --- Executes during object deletion, before destroying properties.


% --- Executes during object creation, after setting all properties.
function plot_ff_w_CreateFcn(hObject, eventdata, handles)
% hObject    handle to plot_ff_w (see GCBO)
% eventdata  reserved - to be defined in a future version of MATLAB
% handles    empty - handles not created until after all CreateFcns called

% Hint: place code in OpeningFcn to populate plot_ff_w


% --- Executes on button press in rb_miller_boyd.
function rb_miller_boyd_Callback(hObject, eventdata, handles)
% hObject    handle to rb_miller_boyd (see GCBO)
% eventdata  reserved - to be defined in a future version of MATLAB
% handles    structure with handles and user data (see GUIDATA)

% Hint: get(hObject,'Value') returns toggle state of rb_miller_boyd

% --- Executes when figure1 is resized.
function figure1_SizeChangedFcn(hObject, eventdata, handles)
% hObject    handle to figure1 (see GCBO)
% eventdata  reserved - to be defined in a future version of MATLAB
% handles    structure with handles and user data (see GUIDATA)

% --- Executes on button press in cb_view_side.
function cb_view_side_Callback(hObject, eventdata, handles)
% hObject    handle to cb_view_side (see GCBO)
% eventdata  reserved - to be defined in a future version of MATLAB
% handles    structure with handles and user data (see GUIDATA)

% Hint: get(hObject,'Value') returns toggle state of cb_view_side
```